Electrochemical safety of neural implants: in vitro study of platinum electrodes behaviour near Shannon's safe stimulation limit

Thomas Niederhoffer

A dissertation submitted in partial fulfillment

of the requirements for the degree of

Doctor of Philosophy

of

University College London.

Department of Medical Physics and Biomedical Engineering

University College London

November 7, 2024

I, Thomas Niederhoffer, confirm that the work presented in this thesis is my own. Where information has been derived from other sources, I confirm that this has been indicated in the work.

Abstract

In neural electrical stimulation, safe stimulation guidelines are crucial for effective treatment while avoiding neural damage and electrode degradation. Shannon's parameter k sets conditions on stimulation parameters to prevent neural damage, though the underlying mechanisms remain unclear. An experimental approach was designed to explore the electrochemical mechanisms involved in the charge injection behaviour of platinum electrodes near Shannon's safe limit. A custom stimulator was developed to deliver biphasic, cathodic-first, charge-balanced, asymmetric, current-controlled pulse trains, while monitoring electrode potential. The pulse trains were calibrated to approach and exceed Shannon's limit. A characterisation and conditioning sequence, including electrochemical impedance spectroscopy and cyclic voltammetry, was implemented to ensure repeatability. The influence of various experimental parameters was investigated, such as electrode design (recess, electrode size, electrode shape), stimulation protocol (pulse width), and electrolyte composition (pH, ionic strength, density, buffer system, dissolved gas). Initial results in saline confirmed previous findings: positive potential ratcheting from irreversible charge injection linked to molecular oxygen reduction, and correlation of Shannon's limit with oxide-mediated platinum dissolution. This mechanism held consistent despite parameter variations, though the onset k-value differed. Changes in electrode design affected current density distribution and diffusion profile; variations in pulse width influenced polarisation due to longer diffusion times; electrolyte composition changes impacted ionic interactions, including double-layer capacitance, faradaic mechanisms, and diffusion. Double-layer

capacitance and diffusion profile emerged as key factors determining oxide-mediated platinum dissolution threshold and rate. Future research should further examine how the *in vivo* environment impacts these parameters and work towards developing a standardised characterisation method for stimulation electrodes.

Impact Statement

This thesis examines safety guidelines for electrical stimulation, focusing on the maximum safe charge that can be injected during a stimulation pulse without triggering harmful electrochemical reactions. Safety criteria include the onset of water electrolysis or Shannon's limit, which was studied in this work. After implantation, the electrode state is inaccessible, therefore, the maximal injectable charge is assessed *in vitro* in a body-mimicking solution.

The findings presented here provide a better understanding of Shannon's damage limit and provide compelling arguments for an update of safety guidelines. First, the electrochemical mechanism suggested here to correlate with Shannon's limit confirms previous findings, but the invariability of the mechanism despite the broadness of experimental parameters anchors it as the primary candidate. Although the correlation with neural damage could not directly be established in this study, the suggested dissolution mechanism does generate electrode degradation, which should be avoided for long-lasting treatment. Therefore, my thesis provides a supporting argument to reconsider the safe injectable charge criteria that are used inside and outside of academia for electrode characterisation as they are proven to be insufficient to avoid electrode degradation. Moreover, I highlighted the complementarity of common characterisation techniques and provided an analysis method with a record of determining the electrode state. Thus, this work may impact the neural engineering community as other researchers may adopt a similar research framework and use findings from fundamental electrochemistry like I did to understand electrode behaviour better.

An important part of this thesis concerns the accuracy of characterisation methods, and how experimental rigour is crucial to produce valuable results for the community. I highlighted the role of many experimental parameters on the accuracy of measurements, which may sometimes be overlooked or misunderstood, such as electrode conditioning and characterisation parameters. On a few instances, I also demonstrated how the apparent measurement may not reflect the real electrode state and how it can be accounted for. A compelling point was made on a common saline characterisation solution, showing that the neural engineering community should consider using a more accurate solution for electrode characterisation. Overall, this thesis aims at opening mentalities and providing elements towards more comprehensive, standardised reporting strategies for better academic collaboration and to enhance the outcomes of biomedical research. By identifying discrepancies in established methods, the thesis encourages researchers to critically evaluate their methodologies for more reliable results.

Finally, I touched on novel topics in my research, highlighting the key parameters affecting electrode degradation during stimulation. These findings indicate the future directions towards the creation of an accurate body model to be used for *in vitro* electrode characterisation prior to implantation. Therefore, my research provides a new lens on research methodology, highlights a proven technique for better reliability, and paves the road towards a better understanding of charge injection and electrode degradation during electrical stimulation. With reliable and accurate characterisation methods, the success rate and development of novel implants will be tremendously enhanced, which will in turn improve the quality of life of millions of patients.

Acknowledgements

First and foremost I am extremely grateful to my supervisors, Dr. Henry Lancashire and Prof. Anne Vanhoestenberghe for their invaluable advice, unwavering support, and patience during my PhD study. From helping with the technical aspects of experiments to deeply discussing theoretical concepts, they have helped me develop as a rigorous and thorough researcher, but also as a person. A special thanks to both of them as well for proofreading my various papers and mainly my PhD dissertation, and for pushing me to participate in various conferences and events, which greatly inspired me through my project. Then, I would like to thank the Department of Medical Physics and Biomedical Engineering for funding my studentship. I would also like to thank the whole IDG team for welcoming me and for helping me with my various electronic design problems. My special thanks to Ahmad Shah Idil, my colleague and fellow PhD student, for the technical guidance and emotional support from start to finish. I would like to thank Prof. Sara Ghoreishizadeh for examining my upgrade report and providing valuable feedback. I would also like to express gratitude to Dr Prabhav Nadipi Reddy and Dr Henry Lancashire for giving me the opportunity to teach as a postgraduate teaching assistant, which greatly developed my pedagogic and interpersonal skills. Special thanks to Henry for pushing me to apply for Associate Fellowship in Higher Education Awards and to Dr Sarah Massey for reviewing my application. I would like to extend my gratitude to the EIT research group for the fruitful discussions and collaborations, and for adopting me for the time of a conference in Baltimore. Finally, I would like to express my sincere gratitude to my parents and my

partner, who have been close to me this whole time, for providing unwavering support and believing in me through highs and lows. Without their patience and continuous encouragement over the past few years, it would have been impossible for me to complete my study.

List of research contributions

Conference abstracts

T. Niederhoffer, A. Vanhoestenberghe, H. Lancashire. Influence of Aspect Ratio on the Current Density Profile of Recessed Electrodes. *International Society of Electrochemistry 71st Annual Meeting*, online, August 31 - September 5, 2020.

A. Vanhoestenberghe, D. Jiang, H. Lancashire, T. Niederhoffer, N. Donaldson. Charge Balancing Strategies: Electronics Design Impact on Safety and Electrode Stability. *10th International IEEE/EMBS Conference on Neural Engineering (NER)*, online, May 4 - 6, 2021.

T. Niederhoffer, H. Lancashire, A. Vanhoestenberghe. Unsafe Electrical Stimulation Correlates with Oxide Reduction Onset in Unbuffered Saline, *44th Annual International Conference of IEEE EMBS (EMBC)*, Glasgow, UK, July 11 - 15, 2022.

T. Niederhoffer, A. Vanhoestenberghe, H. Lancashire. Influence of Extracellular Matrix-Mimicking Gel Electrolyte on Electrode Charge Injection, *11th International IEEE/EMBS Conference on Neural Engineering (NER)*, Baltimore, MD, USA, April 25 - 27, 2023.

Conference full papers

T. Niederhoffer, A. Vanhoestenberghe, H. Lancashire. Effect of pH and gel electrolyte on safe charge injection and electrode degradation of platinum electrodes, *IEEE BioSensors Conference*, London, UK, July 31 - August 1, 2023.

I. Ali, F. Xue, C. Henrique, T. Niederhoffer, A. Shah Idil, D. Jiang, H. Lancashire. Initial Life Test of Silicone Encapsulated FR4 Printed Circuit Boards for Pre-Clinical Active Implants, *24th European Microelectronics and Packaging Conference & Exhibition (EMPC)*, Cambridge, UK, September 11 - 14, 2023.

Journal papers

T. Niederhoffer, A. Vanhoestenberghe, and H. Lancashire. Methods of poly (3, 4)-ethylenedioxithiophene (pedot) electrodeposition on metal electrodes for neural stimulation and recording. *Journal of neural engineering*, 20(1): 011002, 2023.

T. Niederhoffer, A. Vanhoestenberghe, and H. Lancashire. Extending the understanding of Shannon's safe stimulation limit for platinum electrodes: biphasic charge-balanced pulse trains in unbuffered saline at ph= 1 to ph= 12. *Journal of Neural Engineering*, 2024.

In preparation: T. Niederhoffer, A. Vanhoestenberghe, and H. Lancashire. Extending the understanding of Shannon's safe stimulation limit for platinum electrodes: influence of buffer and dissolved gases during biphasic charge-balanced pulse trains

Contents

List of Figures

List of Tables

List of abbreviations

AR - Aspect ratio

AS - Active site

BBB - Blood brain barrier

BJT - Bipolar junction transistor

CBS - Carbonate-buffered solution

C_{dl} - Double-layer capacitance

CE - Counter electrode

CIL - Charge-injection limit

CPE - Constant phase element

CMOS - Complementary metal oxide semiconductor

CNS - Central nervous system

CP - Chronopotentiometry

CSC - Charge storage capacity

CSF - Cerebro-spinal fluid

CV - Cyclic voltammetry/cyclic voltammogram

DIW - Deionised water

DL - Double layer

ECM - Extracellular matrix

EIS - Electrical impedance spectroscopy

EIT - Electrical impedance tomography

ESA - Electrochemical surface area

FBR - Foreign body reaction

IC - Integrated circuit

ISF - Interstitial fluid

NHE/RHE/SHE - Normal/Reversible/Standard hydrogen electrode

OCP - Open-circuit potential

PBS - Phosphate-buffered saline

(P)EDOT - (Poly)-(3,4)-ethylene dioxithiophene

PNS - Peripheral nervous system

R_A - Access resistance

RE - Reference electrode

rms - Root main square

ROS - Reactive oxygen species

SCE - Saturated calomel electrode

SIDNE - Stimulation-induced depression of neuronal excitability

SIROF - Sputtered iridium oxide film

WE - Working electrode

Chapter 1

Introduction

1.1 Neural stimulation principles

1.1.1 Fundamentals of neural stimulation

Electrical stimulation, neural stimulation, or neuromodulation, is a therapeutic technique used to treat pathologies or impairments of the nervous system through the injection of electrical current stimuli. Neural stimulation is used to treat a range of conditions including epilepsy, Parkinson's disease, chronic pain, depression, movement disorders, foot drop, incontinence, blindness, and deafness (Fig. 1.1). Neural stimulation is also used to improve the quality of life of patients with paralysis, spinal cord injuries, or amputees through the use of brain-computer interfaces (BCI) or bionic prostheses. For optimal integration with patients, BCIs and bionic prostheses aim to directly read neural signals from the brain or nerves and bypass the impaired area to transmit the signal to healthy parts of the nervous system.

Neural stimulation stands out by its ability to target specific faulty brain areas, pathways or networks, and it can be programmed to change depending on clinical response. Neural stimulation is invaluable to treat drug-resistant pathologies, or conditions for which pharmacological therapies do not exist. Neuromodulation is also a useful alternative to pharmacological treatments which can engender tolerance, addiction, toxicity and side effects [Davis and Gaitanis, 2020, Leichsenring et al., 2022, Howes et al., 2022, Hickey and Stacy,

2016]. The targeted nature of neural stimulation limits the scope of its side effects, as opposed to many pharmacological treatments which cause systemic adverse effects as they spread through the gastrointestinal tract and/or bloodstream. For example, deep brain stimulation, for Parkinson's disease, offers greater consistency in efficacy compared to medications which wear off at different times during the day [Denison and Morrell, 2022].

Neural stimulation is delivered through electrodes, which are implanted in the brain, spinal cord or peripheral nerves, tissues which include bioelectric cells — neurons — responsible for the transmission of neural signals.

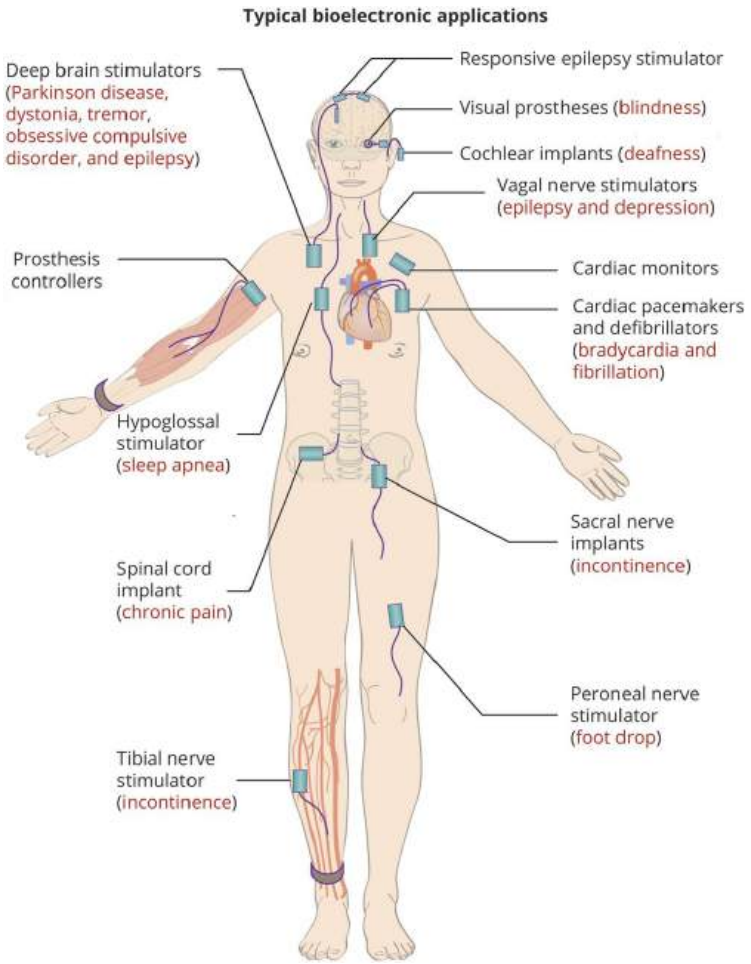

Figure 1.1: *Schematic of applications of bioelectronic medicine, reproduced from Denison and Morrell [2022] under the CC BY 4.0 license.*

The nervous system can be divided into two units: the central nervous system (CNS) grouping the brain and the spinal cord, and the peripheral nervous sys-

tem (PNS) comprising all the peripheral nerves. Neural signals are transmitted through both units of the nervous system via neurons. Neurons constitute a cell body containing the cell nucleus, synapses, which allow neurons to communicate via neurotransmitter exchanges, dendrites, which transmit synaptic signals to the cell body (afferent), and axons which carry the neural signal away from the cell body (efferent). Each neuron may have several synapses and dendrites but only one axon, which may branch at its end to connect to several neurons or organs. Neural signals are transmitted from the brain to the rest of the body via axons running through the spinal cord, which connect to peripheral nerves, which further relay the neural signal. Peripheral nerves consist of fascicles which are bundles of axons, which carry signals from the dorsal root of the spinal cord to muscles (motoneurons) and from sensory terminals back to the ventral root of the spinal cord (sensory neurons). The membranes of axons are polarised due to different ionic concentrations inside and outside of the cell (with a typical resting potential of -70 mV) [Cuevas, 2007]. The transmission of neural signals along the axon occurs through local depolarisation of the membrane which propagates along the axon. The profile of the axon signal has a specific shape called an action potential (AP), which consists of a depolarisation first reaching $\approx$ +40 mV, followed by a repolarisation of the membrane, which becomes slightly hyperpolarised at $\approx$ -80 mV before returning to resting potential. A neural AP typically lasts for 0.5 ms [Brink and Mackel, 1993], and the different phases are determined by the exchange rates of ions (mainly K^+ and Na^+) through transmembrane ion channels [Buzsáki et al., 2012]. The duration and amplitude of an AP cannot be altered, and neurons are not able to fire (send an AP) before the previous AP is finished, due to inactivation of Na^+ ion channels.

Neural stimulation aims to generate or modulate neural signals by causing membrane depolarisation, to initiate an AP, or local hyperpolarisation, to reduce neuron excitability. Electrical stimuli engender changes in ionic concentrations outside the cell, which change the potential across the membrane,

and when the potential difference reaches a threshold of ≈-55 mV, an AP is generated. APs follow an all-or-nothing principle, meaning that subthreshold stimuli do not elicit an AP and suprathreshold stimuli elicit an AP of characteristic amplitude, independently of the stimuli strength [Buzsáki et al., 2012]. The threshold of membrane depolarisation was correlated to electrical stimulus parameters (strength I and duration d) in equations derived by Weiss $Q = I_R(d + d_c)$ and Lapicque $I = I_R(1 + \frac{d_c}{d})$, which introduce parameters I_R and d_c described in the following paragraph. Stimulation pulses of various strengths (current amplitude) and of various durations (pulse width) were delivered and threshold values for the generation of an AP or innervated muscle contraction were reported on a stimulus strength (intensity) against stimulus duration plot — the Weiss-Lapicque strength-duration curve [Geddes and Bourland, 1985].

Studies of nerve activation threshold showed a hyperbolic trend, with a horizontal intensity asymptote for high stimulus durations, which represents the minimum current able to elicit membrane depolarisation, called the rheobase (I_R). Strength-duration curves provide another key stimulation parameter: the chronaxie (d_c), which is the pulse duration eliciting depolarisation for a current equal to double the rheobase. Chronaxie represents an optimal pulse duration for electrical stimulation as the point of minimal pulse energy (Fig. 1.2) [Geddes and Bourland, 1985].

Electrical stimulation is considered a more proportionate and targeted treatment for neuropathologies than pharmaceuticals [Leichsenring et al., 2022, Howes et al., 2022] since it only targets electrically active cells, and the spatial zone of activation can be adjusted, therefore, secondary effects are less systemic with electrical stimulation. However, electrical stimulation protocols' efficiency relies on the optimisation of many parameters including electrode positioning, stimulation duration (frequency, pulse width respecting chronaxie) and stimulation intensity, which are a compromise between stimulating only the targeted neuron population and delivering sufficient charge to reach the

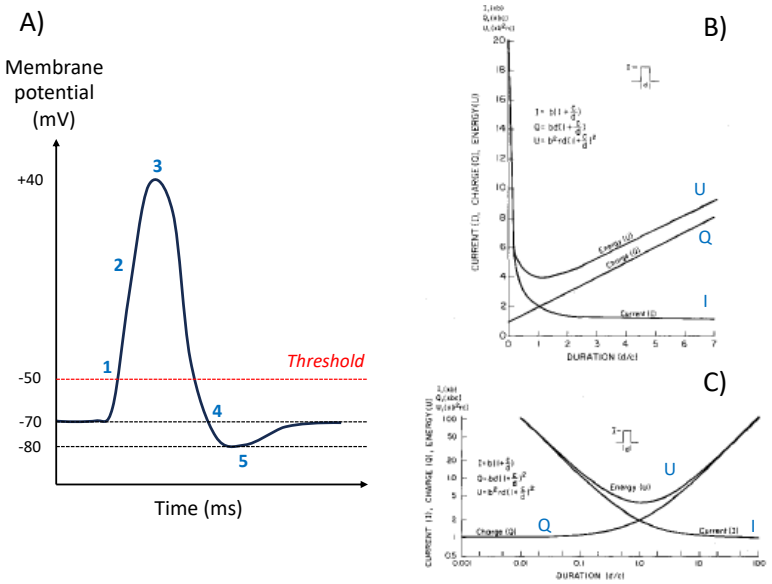

Figure 1.2: *A) Shape of a transmembrane action potential with threshold potentials (timescale 3.5 ms). 1 - 5 represent the transmembrane ion gated channels phases: 1- Na^+ gates open letting Na^+ inside the cell, 2- K^+ gates open letting K^+ outside the cell, 3- Na^+ gates become refractory, Na^+ flow stops, 4- K^+ channels close, Na^+ channels reset, 5- residual K^+ outside the cell diffuse away and is removed by active transmembrane transport. B) Strength-duration curve reproduced from Geddes and Bourland [1985], demonstrating the dependence nerve activation threshold on current (I), charge (Q) and energy (U) with pulse duration (d) normalised to chronaxie (c). C) The same strength-duration curves on an x-axis logarithmic scale, which clearly shows how the point of minimal energy corresponds to chronaxie (c). © 1985 IEEE*

activation threshold. Besides the design of stimulation protocols, the design of the electrodes delivering the stimuli is as important for treatment efficiency and safety. In the following section 1.1.2, I will explain what electrodes are and how they operate.

1.1.2 Neural electrodes

Electrodes are the common name given to the terminals delivering electrical stimuli. An electrode is an interface between an electronic conductor and an ionic conductor [Bard et al., 2022]. The name electrode is commonly given to the electronic conductor, while the ionic conductor is called the electrolyte. In this thesis, I will use the word electrode to describe the electron-conducting terminal, as it is most used in the neural engineering community, and I will

use electrode-electrolyte interface to describe the interface between conducting media.

Electrodes are mostly made out of metals, because of their high electrical conductivity and easy manufacturing options [Navarro et al., 2005]. Suitable materials for electrodes need to be corrosion-resistant to avoid short-time failure of neural implants and toxic metallic particle release. Thus, noble metals such as gold, platinum (Pt), iridium, and their alloys are used for their relative chemical inertness. Tungsten, which was also used in a few applications, was recently demonstrated unsuitable for stimulation purposes [Idil and Donaldson, 2018]. Stainless steel represents an accessible low-cost electrode material, but it is rather used for large surface area electrodes as it is prone to corrosion [Mortimer et al., 1980]. Originally, electrodes had quite large dimensions (cm^2 to mm^2): to reduce the physical tissue damage due to the implantation of a relatively large, stiff material in the body, and to target small populations of neurons accurately, electrode sizes have been drastically reduced (down to μm^2). However, reducing the electrode surface area greatly increases the impedance across the electrode-electrolyte interface and results in higher charge densities during stimulation, which translates to a high resistance to charge transfer through the interface, and higher electrode polarisation voltages during stimulation, which may be harmful.

In recent decades, several directions have been explored to circumvent challenges associated with charge transfer at ever smaller electrodes. Texturing the electrode surface by laser roughening [Green et al., 2012a], chemical etching or metal electrodeposition (Pt black [Arcot Desai et al., 2010], Pt nanograss [Boehler et al., 2017a]) increases the surface roughness, therefore increases the electrochemically available area for reactions to take place, reducing electrode impedance. Therefore, two measurements of electrode surface area are considered: the geometric surface area (GSA), which takes the physical dimensions of the electrode into account, and the electrochemical surface area (ESA), which factors in roughness and can be determined through electrochem-

ical techniques. The distinction between surface areas is crucial for electrode performance analysis. Metal electrodes have also been coated with conductive coatings to enhance their performance, for instance with iridium oxide (IrOx) [Weiland and Anderson, 2000, Cogan et al., 2004b, Negi et al., 2010] or poly-(3,4)-ethylenedioxithiophene (PEDOT) [Cui and Martin, 2003, Ludwig et al., 2011], a conductive polymer. IrOx and PEDOT, the most common coatings in neural engineering, increase the electrode ESA and change charge transfer mechanisms at the interface. Despite significant advances around these materials, key challenges still need to be addressed before IrOx and PEDOT can be used as reliable electrode materials for long-term applications. Both coatings are unstable mechanically and suffer delamination after moderate stimulation intensity [Cogan et al., 2004a, Cui and Zhou, 2007], and the toxicity of those materials still remains a grey area. IrOx also requires an electrode voltage bias to maximise its performance, which is difficult to deliver when implanted without creating risks for the patient.

Moreover, coated or uncoated metal electrodes still induce tissue damage around the implantation site due to their mechanical stiffness [Sharafkhani et al., 2022]. Indeed, metals and solid polymers such as PDMS (Polydimethylsiloxane) have a Young's modulus around between 3 and 5 orders of magnitude larger than that of brain tissues (10^{11} Pa for metals, 1 to 3 $\times 10^6$ Pa for PDMS, 10^2 to 10^4 Pa for the brain [Hong et al., 2018]). Therefore, flexible electrodes have been developed using thin-film technology and hydrogels to reduce the mechanical mismatch and reduce the foreign body response around implants, which improves the long-term performance of electrodes [Kim et al., 2018, Pimenta et al., 2021].

Various electrode array designs have been developed for a range of applications and implantation sites, which can be more or less invasive. More invasive electrode arrays offer better selectivity and higher proximity to the targeted neurons, which allows a better signal transmission from electrode to neuron and vice versa, but the implantation is more traumatic and difficult [Navarro et al.,

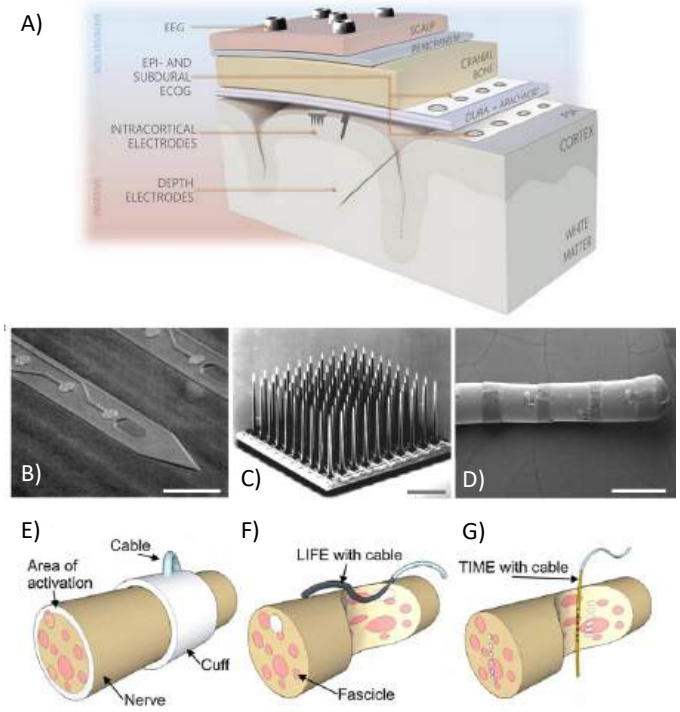

Figure 1.3: *A) Schematic showing the implantation sites of various electrode array designs, reproduced from Campbell and Wu [2018]. B)-D) show scanning electron microscopy images of brain electrodes, reproduced from Salatino et al. [2017] with permission: B) Michigan probe, C) Utah electrode array, D) DBS lead. E)-G) show schematics of peripheral nerve electrodes with their stimulation zone, reproduced from Boretius et al. [2010] with permission: E) cuff electrode, F) LIFE electrode, G) TIME electrode.*

2005]. Figure 1.3 shows various electrode array designs and implantation sites. Placed on the surface of the brain epidurally or subdurally without penetrating it are electrocorticography (ECoG) electrodes, which are an array of surface electrodes mainly used for neural signal recording. To interface more closely with the cortex, which is the outer part of the brain, penetrating electrodes may take several forms. Michigan probes (Fig. 1.3 B) consist of a rigid silicon body along which electrode contacts are distributed to interface with neurons at various depths. Utah electrode array (UEA, Fig. 1.3 C) consists of an array of silicon probes, the tips of which have been coated with metal to interface with neurons. Whereas Michigan probes have contacts along an axis at several depths, UEA have numerous contacts across a plane which allow stimulation

of a larger population of neurons within a given cortical layer. To couple UEA breadth with Michigan probes' depth, the Utah slanted electrode array was developed with each row of the UEA penetrating at a different depth. Some therapies including deep brain stimulation (DBS) require interfacing with deeper brain structures. DBS leads (Fig. 1.3 D) consist of a wire at the end of which several cylindrical zones have been deinsulated and constitute active electrode sites. The implantation of such depth electrodes is challenging and requires great precision to position the electrode in the right zone with minimal damage for example through stereotactic surgery [Binder et al., 2005, Qin et al., 2017].

Interfacing peripheral nerve electrodes (PNE) demands different designs as PNE interfaces with parallel axons rather than whole neuron populations like in the brain. Nerves group several fascicles, which communicate with specific motor or sensory targets, therefore, precisely targeting fascicles greatly influences the therapy's success. A widely-used PNE design is cuff electrodes (Fig. 1.3 E) consisting of a tubular design made out of insulator with metal electrode contacts, which wraps around the nerve [Veraart et al., 1993]. Various cuff designs have been optimised to deal with the challenges presented by peripheral nerves. First, nerves have various thicknesses throughout the body and optimal contact is required to produce efficient stimulation, so adjustable-size cuffs were developed with flexible electrode contacts. Second, fascicle distribution inside nerves is highly variable and changes over the length of the nerve, and cuff electrodes primarily stimulate axons on the periphery of nerves. To address that nerve-shaping designs were developed such as the FINE [Tyler and Durand, 2003], which mechanically shapes the nerve in a flattened rectangle shape, thereby spreading axons, and is able to stimulate across that distribution with several laterally-distributed contacts. Some studies suggest FINE design causes mechanical trauma to the nerve, however, some evidence shows that the tissue is able to adapt and recover [Tyler and Durand, 2003]. To achieve further selectivity, penetrating PNEs were designed, such as the

LIFE (longitudinal intrafasciular electrode) [Lawrence et al., 2004] and TIME (transverse intrafascicular multichannel electrode)[Boretius et al., 2010]. LIFE (Fig. 1.3 F) has a similar concept to DBS leads: a wire electrode with several disc-shaped active sites which is implanted longitudinally inside the nerve or even inside a fascicle. TIME electrodes (Fig. 1.3 G) resemble Michigan probes, with vertically-distributed active sites along a shank-shaped electrode body implanted transversally across the nerve. The active electrode site distribution allows to selectively stimulate several fascicles, and using flexible substrates and thin-film technologies reduced implantation trauma. The electrical field around electrode active sites, which determines which neurons are stimulated is shown in figure 1.3 E), F), and G). Active site size and shape (two-dimensional and three-dimensional) influence the electrical field and charge injection properties, which will be discussed next.

Charge injection across the electrode-electrolyte interface requires transfer of charge from an electronic conductor to an ionic conductor. Most electrolytes including body extracellular fluids are aqueous (water-based), a polar solvent which helps with salts solubilisation, salts which are the main current-carrying ions. The molecular arrangements and ion concentrations which arise in the electrode's vicinity have been described in aqueous electrolytes as the combination of two layers, the compact Helmholtz layer at the electrode surface and the diffuse Gouy-Chapman layer between the Helmholtz layer and the solution bulk (Fig. 1.4. When a piece of metal is immersed in an aqueous electrolyte, electrons in the metal migrate towards the interface and water molecules align on the electrolyte side of the interface with their positive charge barycentre (hydrogen atoms) towards the electrode. As a consequence, the negative charge barycentre (oxygen atom) aligns the other way, attracting positively-charged ions (cations) towards the interface to preserve charge neutrality. This layer of water molecules and cations at the electrode surface is called the Helmholtz layer or double layer (DL) and does not require any applied electrode voltage to form. Since the cations are solvated, the positive charge plane (cations,

"outer Helmholtz plane") and the negative charge plane (oxygen atoms in water molecules, "inner Helmholtz plane") are separated by some distance, creating a capacitor, which can be charged or discharged. At a further distance from the electrode is the Gouy-Chapman layer, which describes a more diffuse region where ions are free to migrate and ion concentrations (anion or cation depending on the electrode polarisation) converge towards the bulk electrolyte concentrations as distance to the electrode increases [Oldham, 2008, Doblhoff-Dier and Koper, 2021].

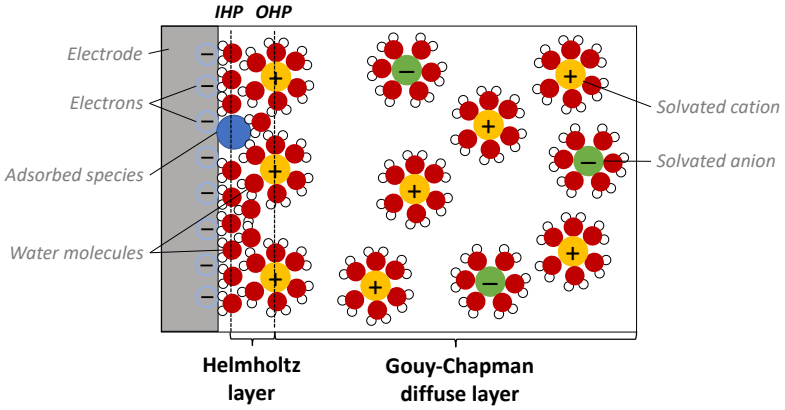

Figure 1.4: *Schematic showing molecular arrangements at the electrode-electrolyte interface in an aqueous electrolyte.*

The transfer of electrical charge from the electrode to the electrolyte is conveyed through two mechanisms: capacitive charge injection and faradaic charge injection. When no charge is driven through the interface, the potential across the DL due to charge separation is referred to as the resting potential, that can be described as the equilibrium potential of the interface, or open-circuit potential (OCP). When a potential is applied to the electrodes, charges accumulate at the interface without electrons crossing the interface, similar to a charging capacitor. The DL acts as a capacitance (C_{dl}), which contributes to charge injection until saturation, independently of stimulation conditions. C_{dl} depends on electrode material and electrode area. For smooth Pt in an aqueous solution, $C_{dl} = 20\ \mu F.mm^{-2}$ [Merrill et al., 2005]. In parallel to capacitive charge injection, direct electron exchanges occur as redox reactions through

the interface: faradaic reactions. Redox couple reactions are governed by thermodynamics laws, determining the electrochemical potential at which the reactions occur. The equilibrium potential E_{eq} or E^0 is the potential at which there is a balance between the reduction and oxidation reactions and no net current flows across the interface. Electrochemical reactions occur when the potential steers away from equilibrium beyond threshold potential delta called activation overpotential η_A, thus at $E < E_{eq} - \eta_{A,red}$, reduction is favoured, and at $E > E_{eq} + \eta_{A,ox}$ oxidation is favoured. Electrochemical reactions involve electron transfer with the electrode, which draws current flow through the system. It is important to note that even though a reaction is thermodynamically likely to happen, it may not be available for charge transfer as reaction kinetics or diffusion might limit the reaction rate. Therefore faradaic reactions depend on electrode potential, electrode material, electrolyte composition, reactant concentration, and all parameters that may influence reaction kinetics.

For a given redox couple, the electrode potential can be inferred from the concentrations of oxidised (C_O) and reduced (C_R) species following Nernst equation:

$$E = E^0 + \frac{RT}{nF} ln(\frac{C_O}{C_R}) \tag{1.1}$$

In Nernst equation 1.1, E is the electrode potential, E^0 the standard potential for the redox reaction, n the number of electrons involved in the electrode reaction, F the Faraday constant, R universal gas constant, and T the temperature. In the presence of several redox couples, the electrode potential is a combination of the contributions of each couple, which is rarely calculable in practice. Where no clearly identifiable redox couple is present at an electrode surface, the electrode potential may take a range of values at rest and the potential must be experimentally determined as the open-circuit potential (OCP). From Nernst equation, several relationships can be derived to infer current flow and changes in potential at the electrode-electrolyte interface.

The relationship between electrical current and voltage difference applied to the electrode is described by the Butler-Volmer equation:

$$j = j_0 [exp(\frac{\alpha_a nF\eta}{RT}) - exp(-\frac{\alpha_c nF\eta}{RT})] \tag{1.2}$$

In Eq. 1.2, j is the electrode current density, j_0 the exchange current density (the current density in the absence of overpotential, $\eta = 0$, i.e. at equilibrium, when the forward and backward reactions are equal [Xing et al., 2023]), α_a and α_c the anodic and cathodic charge transfer coefficients, η the activation overpotential ($\eta = E - E_{eq}$, E electrode potential, E_{eq} equilibrium potential). To account for mass transport, the Butler-Volmer equation can be modified by factoring in the normalised time-dependent reactant concentration at the electrode surface $\frac{c(0,t)}{c^*}$, where c^* is the bulk concentration, in the extended Butler-Volmer equation:

$$j = j_0 [\frac{c_o(0,t)}{c_o^*} exp(\frac{\alpha_a nF\eta}{RT}) - \frac{c_r(0,t)}{c_r^*} exp(-\frac{\alpha_c nF\eta}{RT})] \tag{1.3}$$

The Butler-Volmer equation 1.3 has two limiting regimes: the low overpotential region and the high overpotential region. In the low overpotential region, where $E \approx E_{eq}$, $\eta \simeq 0$, the current density is directly proportional to the overpotential $j = j_0 \frac{zF}{RT}\eta$. In the high overpotential region, where $E - E_{eq} >> 1$ or $E - E_{eq} << 1$, the Butler-Volmer equation simplifies as the Tafel equation.

$$\text{For } E - E_{eq} >> 1$$

$$E - E_{eq} = a_a + b_a, \tag{1.4}$$

$$\text{For } E - E_{eq} << 1$$

$$E - E_{eq} = a_c - b_c, \tag{1.5}$$

a and b are Tafel constants for a given reaction and temperature and are different for cathodic and anodic reactions. b, the Tafel slope can be estimated as $b = [\frac{\partial E}{\partial ln|I_F|}]_{c_i,T,P}$, with I_F the faradaic current, sum of anodic and cathodic

currents; however, the Tafel slope is rather measured experimentally. For a single reaction, a more common form of the Tafel equation is used, which factors in the reactant concentration:

$$i = nkFC\, e^{\pm \frac{\alpha F \eta}{RT}} \tag{1.6}$$

In Eq. 1.6, k is the rate constant for the electrode reaction, C is the reactive species concentration at the electrode surface, and the sign in the exponential is determined whether it is a cathodic (negative) or anodic (positive) mechanism.

1.1.3 *In vivo* environment

The main focus in this thesis is on implanted stimulation electrodes interfacing directly with cells and tissue. Electrodes are implanted in the extra-cellular matrix, a support matrix consisting of various proteins including collagen, various cells, and extracellular fluid. Neurons in the CNS are surrounded by a conductive fluid called the cerebrospinal fluid (CSF), composed of ions and proteins, and in the PNS, the interstitial fluid (ISF), which slightly differs in composition. The main ions in CSF and ISF are sodium Na^+, chloride Cl^-, bicarbonate HCO_3^-, potassium K^+, phosphate HPO_4^-, calcium Ca^{2+}, magnesium Mg^{2+} and sulfate SO_4^{2-} [Cogan, 2008]. In addition, other molecules are present, including glucose, as well as free colloidal proteins, including mainly albumin, amino acids, and various cells. Gases are also present under a dissolved form as the product of respiration, with estimated interstitial percentages of 89% nitrogen, 6% carbon dioxide and 5% oxygen [Cogan, 2008]. The body needs to maintain a homeostatic pH of 7.4 for cells and body functions to work normally. There are three buffer systems regulating pH in the body: the phosphate buffer system ($H_2PO_4^-/HPO_4^{2-}$), the carbonate/bicarbonate buffer system (HCO_3^-/H_2CO_3 / CO_2^{2-}/HCO_3^-), and the protein buffer system, which relies on carboxyl ($-COO^-$) and amino groups ($-NH_2$) releasing and accepting H^+ ions capacity. pH buffering is crucial at a macroscopic scale for the body; however, it is possible that buffers become locally exhausted,

especially during neural stimulation [Ballestrasse et al., 1985, Huang et al., 2001], which will be explored in detail in section 6.1.

Implanted electrodes are foreign bodies inserted in the body against which the immune system will respond. First, in the case of electrodes implanted in the CNS, electrode implantation will damage blood vessels, which causes a breach of the blood brain barrier (BBB). The BBB is a border of endothelial cells which regulates the transmission of blood products to the brain, therefore, a breach of the BBB will trigger an immune response to protect the brain, on top of the foreign body response (FBR). The FBR evolves over a few weeks after implantation (up to 12 weeks) but it is triggered immediately following implantation (Fig. 1.5). First, in the first 12 hours, microglia, a support cell of the CNS, become activated and migrate towards the implant. Activated microglia contribute to activating astrocytes, which migrate towards the electrodes over the first few days of implantation. Microglia and astrocytes go on to form a protective sheath around a cortical implant, creating distance between neurons and the electrode and forming an electrically insulating barrier. After a few weeks, the sheath, which is called a glial scar, becomes denser and isolates the electrode from neurons, contributing to functional implant failure as signals cannot be transmitted efficiently anymore: amplitudes become too small for recording and effective stimulation thresholds become too high. In the PNS, a similar reaction occurs, with connective fibrous tissue insulating the electrode.

Aside from the fibrous encapsulation, which represents a challenge for long-term implantation, the *in vivo* environment may yield biotic failures. Highly reactive molecules, such as reactive oxygen species released by immune cells [Campbell and Wu, 2018] attack electrode materials and wire insulations, which may cause corrosion, insulation delamination or passivation, and result in implant failure [O'Malley et al., 2017]. Proteins are also known to adsorb onto the electrode surface, especially albumin, which blocks reaction sites for charge injection and results in reduced charge injection capacity and higher

electrode impedance [Newbold et al., 2010, Carnicer-Lombarte et al., 2017, Harris et al., 2021].

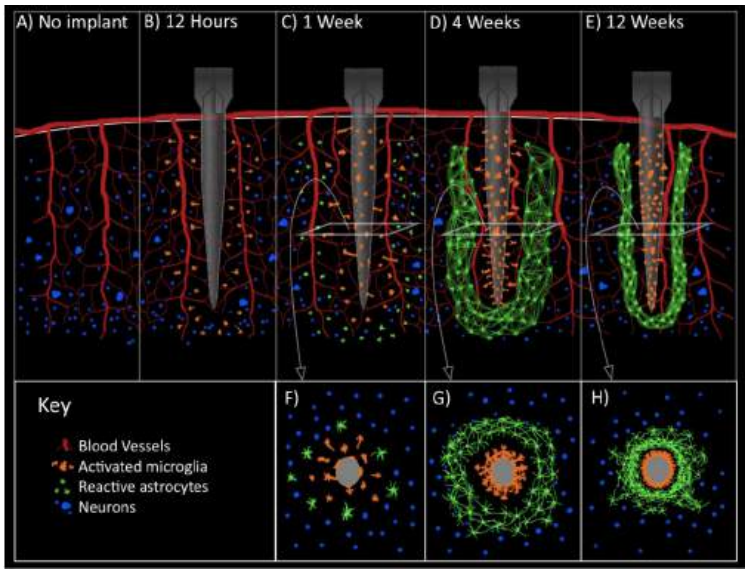

Figure 1.5: *Schematic of foreign body reaction in the brain at different times after implantation, reproduced from Campbell and Wu [2018]. F)-H) show cross-sectional views of the implant's surroundings.*

1.2 *In vitro* electrode characterisation

Electrode characterisation is conducted in electrolytes modelling the ionic composition of CSF and ISF, most commonly isotonic phosphate-buffered saline (PBS). At least two electrodes are needed for such characterisations: the electrode of interest, which is called the working electrode (WE), and a second electrode to close the current flowing loop called the counter electrode (CE), as shown in figure 1.6 B i). During current injection the WE and CE become polarised; therefore to accurately measure WE potential, a third electrode, the reference electrode (RE), is introduced, through which no current flows. The RE has a stable electrochemical potential based on a well-defined redox reaction and a constant ionic concentration [Bard et al., 2022]. Most common RE types are standard hydrogen electrode (SHE) or normal hydrogen electrode (NHE), based on hydrogen evolution ($Pt/H_2/H^+$) with all components at unit activity, which is the standard potential reference, reversible hydrogen

electrode (RHE), based on the same reaction with bubbled hydrogen gas (+0 mV vs NHE), silver-silver chloride ($Ag \mid AgCl$), based on Ag/AgCl/KCl (+197 mV vs NHE, saturated in AgCl), very commonly used in neural engineering, and saturated calomel electrode (SCE), based on Hg_2/Hg_2Cl_2/KCl (+242 mV vs NHE, saturated in Hg_2Cl_2), all potentials at room temperature [Bard et al., 2022]. The RE can act as the CE in a two-electrode setup, however, the current flowing through the RE will lead to polarisation. Therefore, for electrode characterisation a three-electrode setup is preferred, as in figure 1.6 B ii). Commonly the CE is made from any conductive material which remains stable in the electrolyte, including platinum, stainless steel or carbon. In the three-electrode arrangement the CE closes the current flow loop, while the RE probes the solution potential. In practice the CE should have a surface area at least ten times larger than the WE to minimise faradaic processes and polarisation occurring at the CE, which may influence the characterisation of the WE; with a larger surface area, the double-layer capacitance of the CE will be larger than the WE may support all the charge injected.

1.2.1 Electronic model of the electrode-electrolyte interface

The charge-injection behaviour of the electrode-electrolyte interface can be modelled by an equivalent electrode circuit. Randles [1947] proposed a model consisting C_{dl} in parallel with a faradaic impedance Z_F , both in series with a resistance R_A (Fig. 1.6 A.). The faradaic impedance has two main components: the mass transport phenomenon and the reaction impedance [Epelboin and Keddam, 1970]. The mass transport component, comprising diffusion and adsorption phenomena, considers the phenomena that affect the availability of redox reactants. The reaction component, comprising the kinetics and the complexity of a reaction, considers the physical factors possibly curbing a reaction, e.g. reactant concentration, temperature, or potential, and is proportional to the exchange current density (j_0 in the Butler-Volmer equation 1.2) [Guo, 2020]. The faradaic impedance has non-linear behaviour above a voltage,

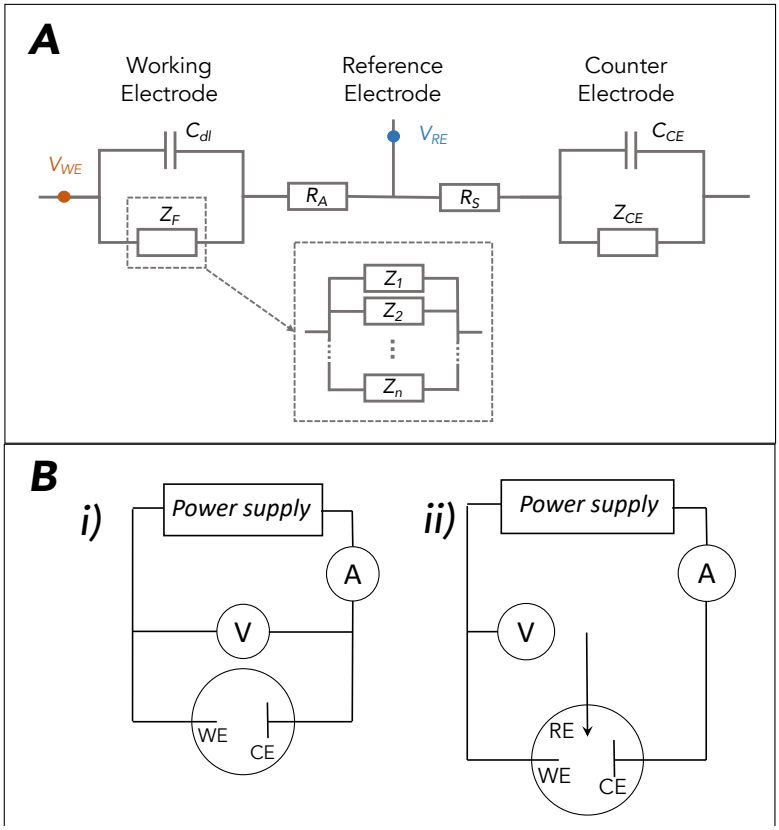

Figure 1.6: *A) Equivalent electronic circuit of a three-electrode setup, with C_{dl} the double-layer capacitance, Z_F the faradaic impedance, R_A the access resistance, and R_S the solution resistance. B) Electronic schematics of i) two-electrode setup, ii) three-electrode setup. Figure adapted from Niederhoffer et al. [2023b].*

which Schwan [1992] demonstrated is reached regularly during stimulation. An important component in the equivalent electrical circuit of the interface is the access resistance, R_A. R_A describes the voltage drop present between WE and RE, and is approximated as a constant resistance for a given electrode, depending only on solution conductivity and electrode geometry at frequencies relevant to neural stimulation electrodes [Newman, 1966, Hall, 1975]. For a flat disc electrode, Newman [1966] established $R_A = \frac{\rho}{4a}$, where ρ represents the electrolyte resistivity and a the electrode radius. For a hemispherical electrode, $R_A = \frac{\rho}{2\pi a}$ [Hall, 1975] . However, it can be difficult to separate R_A from voltage drops due to the circuit and cable resistance. R_A is neglected for CE, because it is substantially smaller than at WE, due to the dimensions of both surfaces, affecting only the required system compliance voltage, not the

measured voltage WE to RE.

Randle's circuit remains a coarse estimate of the electrode-electrolyte's interface behaviour, and due to frequency dispersion of possibly both R_A and C_{dl} [Gateman et al., 2022], a more versatile component was proposed: a constant-phase element (CPE), which impedance is defined as $Z_{CPE} = \frac{1}{(j\omega Q)^{\alpha}}$, with $0 \leq \alpha \leq 1$ (dimensionless) and Q expressed in $Fs^{\alpha-1}cm^{-2}$. A CPE presents a constant phase angle of $-90° \alpha$, and represents non-ideal double-layer capacitance and non-linear effects affecting the reaction impedance. Specific cases include $\alpha = 0$, which represents a pure resistive behaviour with Q=1/R, and $\alpha = 1$, which represents the ideal capacitance case with $Q = C_{dl}$. The effect of reactant diffusion may be represented using a Warburg element, which is a CPE with $\alpha = 1/2$ ($Z_W = \frac{A_W}{\sqrt{j\omega}}$, with $A_W = 1/\sqrt{Q}$), which has a constant phase of $-45°$ and a magnitude inversely proportional to the square root of the frequency.

1.2.2 Main characterisation techniques

1.2.2.1 Electrochemical impedance spectroscopy

Electrochemical impedance spectroscopy (EIS) is used to characterise the impedance of an electrode across a range of frequencies (Fig. 1.7 A). A sinusoidal voltage waveform of small amplitude (5 mV to 100 mV [Boehler et al., 2020a]) and varying frequency (typically 1 Hz to 100 kHz [Cogan, 2008]) is applied to the electrode and the resulting current is measured. EIS is usually conducted at equilibrium (or OCP) to avoid faradaic reactions. The small amplitude of the input signal is required to grant the principle of linearisation of equations when deriving the complex transfer function in Ohm's law. EIS is usually analysed in the form of a Nyquist plot (Fig. 1.7 Aii)), looking at the real and imaginary parts of the impedance, or in the form of a Bode plot (impedance module ($\mid Z \mid$, Ω) versus phase (ϕ, °)), Fig. 1.7 Aiii). Nyquist plots allow direct reading of the electronic modelling quantities, including R_A and C_{dl}, and may give clues on the faradaic behaviour of the electrode, for instance on the presence of a Warburg element. A Bode plot gives more direct

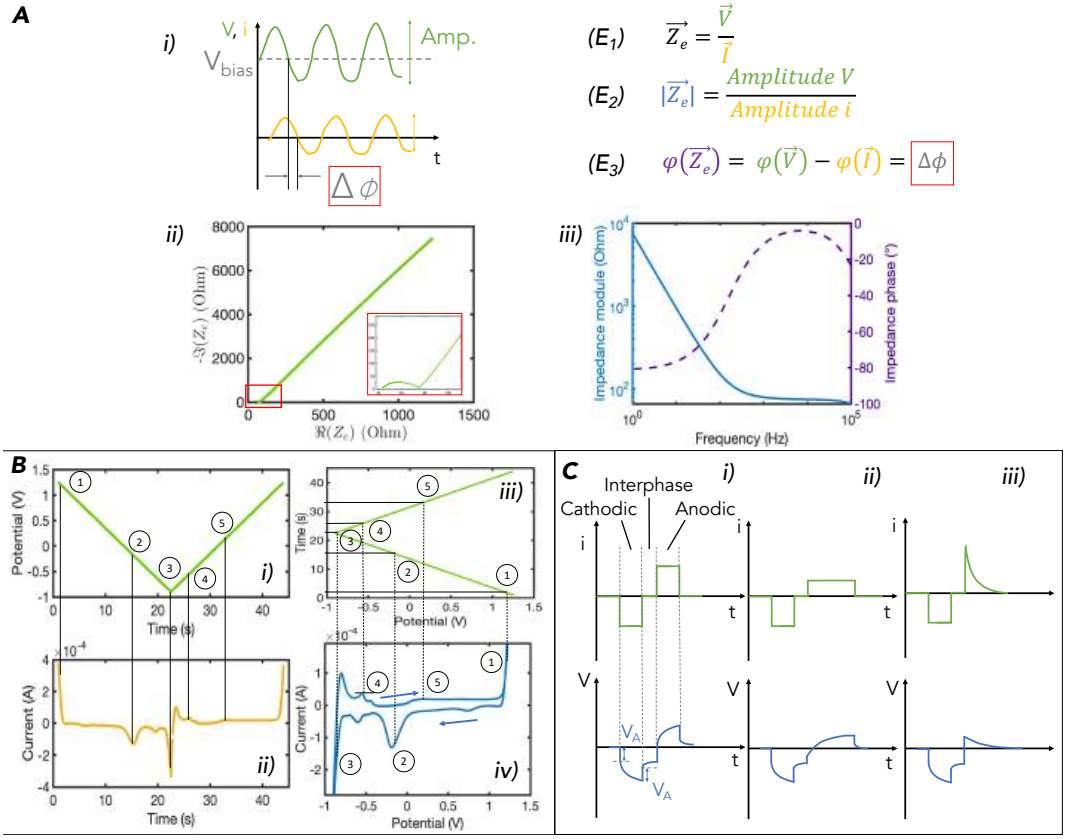

Figure 1.7: *A Electrochemical impedance spectroscopy i) Input voltage sine wave (green) and resulting current waveform (yellow), ii) Nyquist plot $\Im(Z_e)$ vs $\Re(Z_e)$, iii) Bode plot impedance module (equation (E_2)) and phase (equation (E_3)) vs frequency. B cyclic voltammetry i) Potential sweep vs time, ii) Resulting measured current vs time, iii) Transposed potential sweep, iv) Cyclic voltammogram: current vs potential. C chronopotentiometry waveforms, examples of biphasic, cathodic-first, charge-balanced pulses i) symmetric, ii) asymmetric square anodic phase, iii) asymmetric capacitor discharge anodic phase. Figure adapted from Niederhoffer et al. [2023b].*

information on the behaviour of the electrode at various frequencies with the phase indicating whether the electrode is more resistive ($\phi \approx 0°$) or capacitive ($\phi \approx -90°$). Electronic model quantities may be derived from a Bode plot: the module is usually a decreasing function of frequency [Ghazavi and Cogan, 2018], dominated by C_{dl} at low frequencies [Cogan, 2008, Harris and Wallace, 2019] and by R_A at high frequencies, making the impedance independent from electrode material at high frequencies [Ghazavi and Cogan, 2018]. Z_F dominates at very low frequency (< 1 Hz), but is often not observed for neural

electrode [Franks et al., 2005]. EIS should be reported over the full frequency range, rather than specifically at 1 kHz commonly reported in the neural interface literature, which only relates to common body frequencies [Gurney, 2014].

Limits: EIS presents several limitations possibly leading to an incomplete characterisation of the interface. First, the impedance transfer function is voltage-dependent, therefore, complete modelling of the electrode would require measuring EIS at various electrode potentials, to avoid wrong estimations of impedance and polarisation voltage [Harris and Wallace, 2019]. Another limitation regards the small voltage amplitudes, leading to small current amplitudes — especially for large impedances, which are prone to noise and error measurements and do not adequately represent the electrode response to large amplitude stimulation pulses.

1.2.2.2 Cyclic voltammetry

Cyclic voltammetry (CV) measures the current flow across the electrode-electrolyte interface when the electrode potential is varied cyclically. The electrode potential is cyclically swept across a potential range at a constant rate (Fig. 1.7 B i)), called the sweep rate, and the resulting current is measured (Fig. 1.7 B ii)). The resulting i-E curve (Fig. 1.7 B iv)) is called a voltammogram and depends on the reacting species at the interface, their concentration, the electrode area, and the sweep rate. The potential range is usually delimited by solvent electrolysis, called the "water window" for aqueous electrolytes. Faradaic reactions appear on the voltammograms as peaks, such as points 2 and 4, or wider shoulders, such as point 5. Capacitive charge injection is also visible on a voltammogram as a constant current ($i = C\frac{dV}{dt}$ with $\frac{dV}{dt} = \nu$, ν being the sweep rate), which is represented by the separation between the positive-going scan (anodic) and negative going scan (cathodic). Larger electrodes exhibit larger current amplitudes, because of a larger capacitance and a larger area for charge transfer. Using slow sweep rates shows the electrode behaviour in pseudo-steady-state conditions, which allow faradaic reactions to settle, and

the diffusion length to increase, letting reactants travel into less exposed areas, which increases the reactive surface while decreasing the current magnitude. At slower sweep rates, the faradaic peaks are less defined due to diffusion, but the charge passed increases, because the exposition time is larger [Harris et al., 2018b]. Fast-sweep rate CVs are performed to limit diffusion effects and characterise exposed surface areas only, however, the voltammogram shape is dominated by capacitive current, therefore faradaic peaks are more difficult to identify. An important neural electrode property to analyse from the voltammograms is the charge storage capacity (CSC), which corresponds to the total charge sunk by the electrode during the cathodal phase (current flowing from the cathode to the anode) and reversibly sourced during the anodal phase.

Cyclic voltammograms may present several overlapping peaks, which render the curve analysis more complex. Semiderivation is a deconvolution technique, which can be used to separate individual peak contributions and remove unwanted baselines [Pałys et al., 1991]. Semiintegration is another valuable technique, which gives access to a quantity proportional to the reactant concentration near the electrode surface [Mahon and Oldham, 2018]. In this thesis, semiderivation was used for faradaic peak deconvolution, but semiintegration was not used due to the complexity of the electrochemical system.

Limits: CV provides valuable knowledge about electrode behaviour at a pseudo-steady-state regime but does not accurately describe non-DC conditions with fast charge transfers, including stimulation pulses. During pulsing, the fast switching of current involves capacitive charge injection and faradaic reactions which have fast enough kinetics to occur during the pulse, which may not be the same as the reactions observed on a CV. Moreover, while most characterisations solely report the cathodic CSC, one would need to record both cathodic and anodic CSC because a different amount of charge can be injected in both parts, at least for the first CV cycles [Harris et al., 2018b, Harris and Wallace, 2019, Harris et al., 2019b].

1.2.2.3 Chronoamperometry and chronopotentiometry

Chronopotentiometry (CP) characterises the charge-injection regime and electrode polarisation during current-controlled pulses (Fig. 1.7 C). Biphasic current pulses are applied to the electrode and the potential excursions are measured. At the current switching points, ohmic drops due to the access resistance R_A are usually observed, which do not represent the potential at the electrode-electrolyte interface. Therefore, the ohmic voltage drop, also called access voltage V_A (Fig. 1.7 C i) is subtracted from the measured potential to obtain the electrode polarisation voltage. Ohmic drops also occur during CV, and are usually compensated for internally by most commercial potentiostats. To evaluate V_A for a "manual" ohmic compensation, the magnitude of the current step is increased gradually until the polarisation voltage during a pulse reaches unsafe potentials to define the safe charge injection limit (CIL). For a better estimate of the polarisation voltage and CIL, the access voltage should be subtracted from the measured voltage at the onset of the current pulse [Cogan, 2008]. R_A can be estimated from EIS data, determined empirically during an accurate measurement of the current and matching R_A to obtain a continuous polarisation curve [Kumsa et al., 2016b], or numerically identified through V_A as the maximum of the voltage derivative [Cisnal et al., 2018]. The biphasic current pulses used in CP should match the stimulation protocols used *in vivo* (if known) as safe CIL limits are specific for given pulse widths and waveforms.

Chronoamperometry (CA) uses the same principles as CP, but applies voltage-controlled pulses instead of current-controlled [Harris et al., 2018a]. CA enables control of electrode potential and measuring the amount of charge injected at the largest safe electrode potential; however, CA does not reflect the charge injection mode when using current-controlled stimuli.

Limits: First, identifying the charge-injection mechanisms from the voltage excursion curve is complex, including V_A calculation and decoupling faradaic and capacitive mechanisms, which may cause inaccuracies. The unsafe

potential limits determining the CIL are usually defined as the onset potentials of hydrogen and oxygen evolution (water window limits); however, neural damage may occur within these potential limits, and therefore, CIL may overestimate safe limits. Moreover, conducting CP in inaccurate body fluid models does not allow to accurately calculate the interface polarisation *in vivo*. Therefore, the CIL calculated during *in vitro* CP may not correspond to the CIL of the implanted electrode and determined maximum safe current amplitudes *in vitro* may be unsafe *in vivo* [Leung et al., 2014].

1.2.3 *In vitro* techniques accuracy

In vitro electrode characterisation aims to predict the performance of electrodes when implanted in body tissues, therefore, characterisation conditions should be as close as possible to *in vivo* conditions. Sulfuric acid has been used as a characterisation electrolyte [Kumsa et al., 2016b], as the main electrochemical reactions are available as in saline (bar the potential shift due to the different pH). However, pH influences the electrochemical reactions due to the higher proportion of H^+ ions, and is shown to enhance Pt dissolution processes [Topalov et al., 2014b]. PBS is the most used neural electrode characterisation electrolyte as PBS has a stable pH similar to the body and similar ions. In the body however, the phosphate buffer has a less prominent role, and studies showed that PBS's buffering capacity overestimates that of the body [Harris et al., 2018b]. After the protein buffer, the carbonate buffer system (CBS) is thought to be the second main buffering capacity, which is not reflected by the use of PBS. In interstitial fluid, the concentrations of proteins are low (traces), which makes the bicarbonate buffer the major buffer in the environment where electrodes are implanted [Chesler, 1990]. Some more realistic electrolytes have been developed such as artificial perilymph [Harris et al., 2018b] and model ISF [Cogan, 2008], which have ionic compositions close to real fluids, however, the CBS is still underrepresented and biological elements are missing, which leave a mismatch between the *in vitro* and *in vivo* performance [Hu et al., 2006, Harris et al., 2018b, 2021].

Indeed, several studies have compared electrode performance *in vitro* and *in vivo*, reporting a 1.1 to 24 times lower charge injection capacity *in vivo* [Hu et al., 2006, Kane et al., 2013, Terasawa et al., 2013, Leung et al., 2014, Vatsyayan et al., 2021], higher polarisation [Cogan, 2008], a different impedance spectrum [Cogan, 2008, Wei and Grill, 2009, Harris et al., 2022], and a CV showing a behaviour between PBS and artificial fluids, which suggest the reaction mechanisms may still differ. Cogan [2008] suggest protein adsorption or mass-transport restriction in tissue may explain observed discrepancies. In some cases, the *in vivo* environment contributes to mitigating harmful reactions through protein adsorption including stimulation-induced pH swings [Huang et al., 2001] and platinum dissolution [Shepherd et al., 1985, Hibbert et al., 2000]. Nonetheless, the discrepancy between *in vitro* characterisation and *in vivo* performance may yield unforeseen behaviours which may affect long-term efficiency and safety.

Finally, electrode characterisation greatly depends on experimental repeatability and precision. The influence of various parameters on the main characterisation techniques was mentioned in previous paragraphs, which highlights the importance of using wide characterisation ranges (corresponding to use conditions) reporting consistent quantities to produce comparable results, for instance, reporting a full EIS scan and a full CV than just the impedance at 1 kHz and the CSC [Harris et al., 2022, Boehler et al., 2020a]. Furthermore, electrode performance was shown to depend on initial state [Harris et al., 2019a, Doering et al., 2023], therefore, electrodes should be carefully preconditioned before characterisation but also before implantation. Differences in preconditioning sequence alter the recorded potential more than the presence of dissolved oxygen in solution, which is an important reactant in faradaic charge injection mechanisms [Doering et al., 2023]. Electrode cleaning is an important part of preconditioning which helps desorb contaminants from the electrode surface, activating the reaction sites through surface oxidation, and producing a pristine base state for reproducible results [Topalov et al., 2014b,

Harris et al., 2018b, Weltin and Kieninger, 2021].

1.3 Safe stimulation guidelines

1.3.1 Electrochemistry of platinum electrodes

Ideally, stimulation electrodes should rely on pure capacitive charge injection to avoid creating potentially harmful reaction products. However, except for some carefully designed electrode materials, such as titanium nitride (TiN), faradaic reactions will occur for most electrode materials within the water window. In this section, an overview of the main electrochemical reactions at platinum electrodes in traditional aqueous electrolytes is given. All potentials are given with respect to an $Ag \mid AgCl$ reference electrode (sat., 25° in pH 7.2 PBS from [Boehler et al., 2020a]

Hydrogen plating (H-plating) consists in hydrogen ions bonding with the Pt atoms of the electrode surface, Eq. 1.7. Hydrogen most likely diffuses in the first few layers of the metal to be more stable than in a monolayer film [Elam and Conway, 1987]. The adsorption-desorption of H atoms acts as a pseudo-capacitance, as it is fully reversible and is kinetically fast. H-plating is favoured in acidic solutions, due to a higher concentration of H^+ ions, but it also exists in alkaline solution, where H_2O becomes the proton donor.

$$Pt \; + \; H^+ \; + \; e^- \; \leftrightarrow \; Pt - H_{ads} \quad (E^0 = -0.5\,V) \tag{1.7}$$

$$\text{In basic electrolytes} : \; Pt \; + \; H_2O \; + \; e^- \; \leftrightarrow \; Pt - H_{ads} + OH^-$$

Similarly, hydroxide ions (OH^-) participate in charge injection by plating the electrode surface. A metastable OH-coverage is gradually formed, where the Pt-OH elements rearrange before reduction during the cathodic sweep, Eq. 1.8 [Angerstein-Kozlowska et al., 1973]. Pt-OH reduction is more complex than Pt-H, because it competes with other Pt oxide reduction reactions, and OH-plating is therefore less linear and reliable than H-plating. OH^- plating charge transfer is favoured in alkaline solutions, due to a higher concentration

of OH^- ions, but it also exists in acidic solutions, where H_2O becomes the proton acceptor.

$$Pt-OH_{ads} + e^- \leftrightarrow Pt + OH^- \quad (E^0 = +0.4V) \tag{1.8}$$

$$\text{In acidic electrolytes : } Pt-OH_{ads} + H^+ + e^- \leftrightarrow Pt + H_2O$$

Pt oxide formation 1.9 has been widely studied to determine whether it alters electrode performance and eventually leads to Pt dissolution [Brummer and Turner, 1977, Donaldson and Donaldson, 1986b, Hibbert et al., 2000, Topalov et al., 2014b, Kovach et al., 2016, Doering et al., 2022, Shah et al., 2024]. The Pt dissolution mechanism has not been precisely identified and can take the mechanistic routes shown in 1.10, 1.11 and 1.12, for which E^0 is difficult to determine. In the reduction reaction, several chemical paths are possible, leading to different products: either hydroxide groups are reduced and desorb from the surface, or deposited Pt-OH rearrange in deeper layers of the material, or PtO is formed and co-exists with partial PtOH films. Rearrangements within the material make the reverse reaction unavailable - or kinetically sluggish - altering the charge injection and the material [Angerstein-Kozlowska et al., 1973]. If a whole pocket of surface Pt atoms is separated from the bulk by those rearrangements, the surface is altered and Pt is released in the surroundings (electrode corrosion) [Topalov et al., 2014b].

$$PtO + 2H^+ + 2e^- \leftrightarrow Pt + H_2O \quad (E^0 = +0.2V) \tag{1.9}$$

$$\text{In basic electrolytes : } PtO + H_2O + 2e^- \leftrightarrow Pt + 2OH^-$$

$$PtO + 4H^+ + 2e- \leftrightarrow Pt^{2+} + 2H_2O + H_2 \tag{1.10}$$

$$PtO_2 + 4H^+ + 2e- \leftrightarrow Pt^{2+} + 2H_2O \tag{1.11}$$

$$Pt^{2+} + 2e^- \leftrightarrow Pt \tag{1.12}$$

Platinum also reacts with common ions found in most electrolytes, such as chloride ions Cl^- and phosphate species H_3PO_4/H_3PO_3, although these re-

actions are usually considered outside the water window. Hudak et al. [2010] extended the potential window typically used in cyclic voltammetry and observed peaks just outside the water window limits attributed to phosphate reduction ($E^0 = -0.75V$), a combined effect of phosphate and chloride oxidation ($E^0 \approx +1.6V$), and a peak attributed to chloride reduction inside the water window ($E^0 = +0.6V$). While phosphate reactions are not considered hazardous for the electrode, chloride is known to form platinum-chloride complexes, which may detach from the electrode surface upon oxidation, which results in platinum dissolution. Pt dissolution through chloride complexation may happen *in vitro*, and is enhanced by acidic conditions [Doering et al., 2022], however, this mechanism is less likely *in vivo*, as proteins such as albumin adsorb onto Cl^- reaction sites and prevent this phenomenon [Topalov et al., 2014b].

Possible reduction reaction for phosphate:

$$H_3PO_4 + 2\,H^+ + 2\,e^- \;\leftrightarrow\; H_3PO_3 + H_2O, \quad (E^0 = -0.91\,V) \tag{1.13}$$

Chloride adsorption:

$$Pt - Cl_{ads} + e^- \;\leftrightarrow\; Pt + Cl^- \tag{1.14}$$

Pt dissolution through chloride complexation:

$$Pt + 4\,Cl^- \;\rightarrow\; [PtCl_4]^{2-} + 2e^- \tag{1.15}$$

Dissolved oxygen (O_2) participates in charge injection as a cathodic reaction (sinking current). Molecular oxygen reduction is commonly observed on cyclic voltammograms with an onset at $E = 0\,V$ as a negative shift of the base current; however, the proportion of charge injection through molecular oxygen reduction during pulsing is uncertain [Cogan et al., 2010, Musa et al., 2011].

$$O_2 + 4H^+ + 4e^- \;\rightarrow\; 2H_2O \tag{1.16}$$

At extremes of potential, oxidation and reduction of the solvent can happen, the "electrolyte window". The oxidation and the reduction of water (respectively 1.17 and 1.18) are associated with large currents, due to the presence in abundance of the reactants, and production of gases and pH excursions, which can occasion serious damage in tissues. Because the evolved gases are unavailable for the reverse reactions, the electrolysis of water is irreversible. H^+ and OH^- ions are also produced, which result in important pH drifts that could be harmful for cells and tissues in the vicinity of the electrode [Cogan et al., 2016]

$$2H_2O + 2e^- \rightarrow H_2 + 2OH^- \quad (E^0 = -0.6\,V) \tag{1.17}$$

$$H_2O \rightarrow O_2 + 4H^+ + 4e^- \quad (E^0 = +0.8\,V) \tag{1.18}$$

The potential window delimited by oxidation and reduction of water, called the water window, is often considered as the safe potential window when characterising and using Pt electrodes. The potential values of the water window may vary due to several factors, including surface roughness or fouling, which may delay the onset of water electrolysis. The usual water window for platinum at neutral pH is [-0.6 V ; +0.8V] vs Ag|AgCl, Boehler et al. [2020b] report [-0.9 V; +1.2 V] vs Ag|AgCl in PBS at pH 7.2, and in this work an experimentally determined water window of [-0.9 V; +1.2 V] vs Ag|AgCl was determined.

The only safe faradaic charge-transfer mechanisms are commonly considered hydrogen plating [Hibbert et al., 2000, Merrill et al., 2005, Harris et al., 2018a], Pt oxide formation/reduction and hydroxide plating [Robblee et al., 1983, Shepherd et al., 1985, Leung et al., 2014]. Adsorption reactions also occur in solutions and in living tissue, including chloride and phosphate adsorption [Gencoglu and Minerick, 2009, Hudak et al., 2010, Harris et al., 2018b], adsorption of proteins [Huang et al., 2001, Harris et al., 2018b] and adsorption of amino acids [Hibbert et al., 2000]. Adsorption of proteins and nucleic acids are non-specific physisorption phenomena, relying on weak attraction forces,

which do not depend on electrode potential. The movement and reorientation of proteins and amino acids with their electrically charged groups form an electrical current, participating in charge injection. However the charge injection lasts only shortly after implantation and does not absorb-desorb cyclically, because there is no electron exchange with the electrode [Harris et al., 2018b].

1.3.2 Stimulation waveforms

Neural stimulation elicits neural signals through the depolarisation of neurons' membranes. Membrane depolarisation is more efficiently achieved with cathodic stimulation than anodic stimulation, therefore, most stimulation protocols emphasise cathodic first stimulation pulses [Mortimer and Bhadra, 2018]. Stimulation pulses may be current-controlled or voltage-controlled, however, the former option is usually preferred as it provides more control over the injected charge, to achieve the threshold described by the strength-duration curve [Cogan, 2008]. I will therefore focus this section on current-controlled, cathodic-first pulses (in the case of biphasic pulses, see below). While current-controlled pulses allow precise control of injected charge, safety concerns are raised as the electrode potential is left uncontrolled and may shift towards harmful electrochemical processes such as water electrolysis (1.17, 1.18). The following explores how the stimulation waveform may be designed to shape the electrode potential excursion during current-controlled pulses.

In monophasic cathodic pulses (Fig. 1.8 A), C_{dl} charges during the first pulse, remains charged during the interpulse period as there is no current flow, and charges further in the next pulses. In such a stimulation regime, which does not allow C_{dl} to discharge, the voltage drop across the double-layer capacitance increases as more charge is transmitted ($Q = CV$). As the electrode potential changes, favourable potentials for faradaic reactions are reached, so faradaic reactions contribute to successive charge injections, and at substantial overpotentials, the faradaic charge injection becomes the dominant charge injection mode. In monophasic cathodic pulses, the electrode potential is progressively driven more negative after each monophasic pulse through capacitive charge

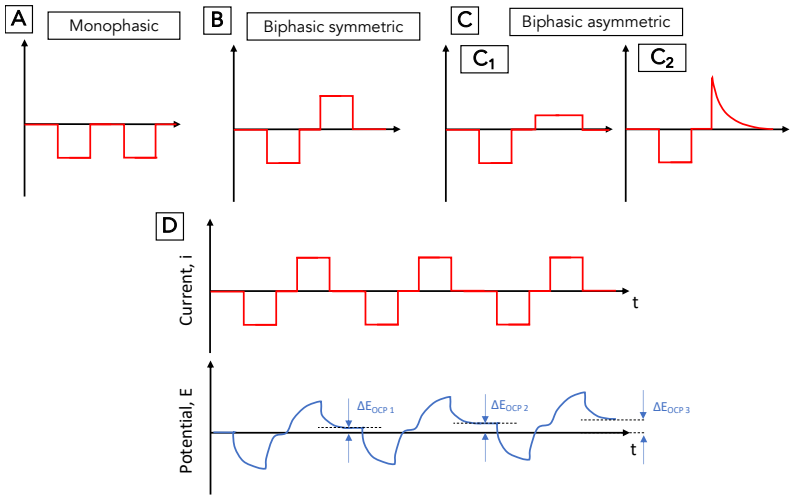

Figure 1.8: *Examples of stimulation waveforms. A) Monophasic stimulation, B) Biphasic charge-balanced square symmetric pulses C) Biphasic charge-balanced square asymmetric pulses (C_1 with square anodic phase, C_2 with anodic capacitive discharge). D) Schematic illustrating potential ratcheting in the voltage response to charge-balanced biphasic pulses due to irreversible cathodic charge injection.*

injection ($i = C_{dl}\frac{dV}{dt} \Leftrightarrow V = \frac{1}{C_{dl}}\int_t(i\,dt) = \frac{i\Delta t}{C_{dl}}$) and then through faradaic reactions, consuming one species of a redox couple, driving the potential further away from equilibrium according to Nernst equation, until hydrogen evolution onset is reached, which happens only after a few pulses [Merrill et al., 2005]. To keep the electrode potential within safe potential bounds, allowing more efficient long-term stimulation protocols, discharging the electrode between stimulation pulses is necessary. Passive techniques such as shorting electrodes between pulses effectively discharge C_{dl}, however, it results in a net DC current, which was demonstrated to be harmful [Gencoglu and Minerick, 2009, Cogan et al., 2016]. Therefore, active discharge strategies were introduced, including biphasic waveforms (Fig 1.8 B and C) following the idea of discharging C_{dl} and reversing faradaic reactions [Lilly et al., 1955, Merrill et al., 2005]. In biphasic pulses, a charge reversal phase (anodic) follows the stimulation phase (cathodic) to revert the changes induced at the interface during the first phase including C_{dl} charging. The anodic phase aims to reset the electrode's state to its pre-pulsing state, therefore, the anodic charge is equal to the cathodic charge, hence the terminology charge-balanced pulses. It is common to have

a zero-current interpulse delay phase between the cathodic and anodic phases to ensure a neural signal is triggered before the reversal anodic phase reestablishes the electrode-electrolyte interface's state, avoiding a too early reversal and possible AP blocking [Merrill et al., 2005]. Biphasic pulses often use identical cathodic and anodic phases, yielding charge-balanced symmetric pulses (Fig. 1.8 B), which is the most convenient to implement, and widely used on commercial stimulators.

However, charge-balanced pulses may not be fully efficient in reverting the interface to its initial state: the interface will return to its initial condition only if the electrochemical mechanisms involved in charge injection in both phases are reversible, such as C_{dl} charging, and are reversed. Some faradaic reactions are fully reversible, such as H-plating, but other reactions may not be fully reversible, due to reactants diffusing away from the electrode or unavailable reversal reactions. Therefore, despite ensuring electrical charge balance, the asymmetrical electrochemical charge injection leads to an imbalance in charge injection between phases, which results in an adjustment of the OCP called potential ratcheting, or potential slide-back [Donaldson and Donaldson, 1986a, Merrill et al., 2005], shown in figure 1.8 D. The OCP gradually changes until the quantity of irreversible electrochemical charge injection is equal in both phases, although the irreversibility in both phases may be attributed to different reactions, at which point the OCP stabilises, which happens after a few pulses [Merrill et al., 2005]. Positive potential ratcheting, as shown in figure 1.8 D, is the result of more cathodic irreversibility [Kumsa et al., 2016b, Harris et al., 2019a]. To avoid potential ratcheting, charge-imbalanced pulses are recommended by some researchers [Scheiner et al., 1990, Kumsa et al., 2019], provided that the cathodically-injected charge can be precisely measured and injected in the anodic phase. Alternatively, an asymmetric charge-balanced waveform can compensate the charge imbalance if it specifically reverses precise mechanisms. For example, stimulators comporting a blocking capacitor in series with the electrodes are able to anodically inject the cathodic charge in

the form of a capacitor discharge (Fig. 1.8 C2), where more charge is injected in the first microseconds compared to a square pulse, to reverse reactions where products otherwise diffuse quickly from the interface and would otherwise be irreversible during symmetric pulse stimulation [Gorman and Mortimer, 1983].

1.3.3 Neural damage caused by electrical stimulation

Neural implants are highly invasive, and the implantation of a foreign object in the body induces several sources of neural damage [Sahyouni et al., 2017]: first, the implantation surgery causes acute tissue damage similar to stab wounds [Eles et al., 2018], then, the FBR triggers an inflammatory response and a local depletion of neurons [Campbell and Wu, 2018, McConnell et al., 2009], which is chronically reactivated by implant micromotion relative to body tissues, constituting a major source of chronic damage leading to implant failure [Sharafkhani et al., 2022]. Besides the trauma caused by electrode implantation and electrode presence in tissue, electrical stimulation may also cause neural damage, however, the electrical damage mechanisms remain uncertain. This section focuses on reports of neural damage from electrical stimulation and explanatory theories.

Maintaining electrode potentials within the water window and avoiding irreversible charge injection aims to avoid electrochemically induced neural damage during stimulation. A series of studies on Pt electrodes implanted in cats' cortices [Pudenz et al., 1975, Yuen et al., 1981, Agnew et al., 1986, McCreery et al., 1988, 1990], cats' cochlea [Shepherd et al., 1985], cats' nerves [Agnew et al., 1989], monkeys' cerebellum [Brown et al., 1977], and monkeys' spinal cord [Swiontek et al., 1980] reported neural damage, despite using biphasic charge-balanced waveforms not exceeding safe potential limits (water window). Damage was observed mostly as neuron loss and changes in cell morphology (denatured neurons), but also sometimes as inflammation or oedema, presence of connective tissue, or electrode corrosion. The studies reported different stages of electrode and tissue damage, while using different electrode areas, stimulation intensities, stimulation durations, frequencies, and

pulse widths. Shannon [1992] devised a relationship discriminating empirically observed damaging and non-damaging stimulation protocols, despite the variety of animal models and stimulation strategies, which depends only on the charge per phase (Q) and the charge density per phase (D):

$$log(D) = k - log(Q) \tag{1.19}$$

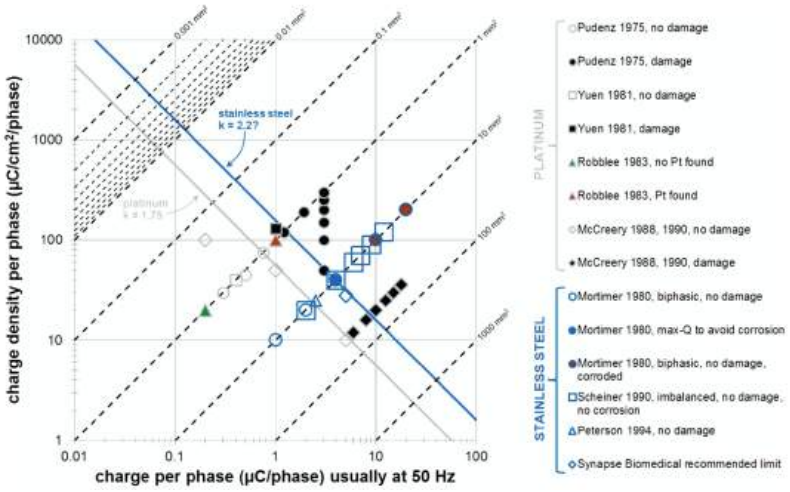

Figure 1.9: *Shannon's plot showing studies reporting damaging (filled markers) and non-damaging (void markers) stimulation and the safety limit line fork ≈ 1.75, reproduced from Kumsa et al. [2016b] under the CC BY 4.0 license.*

In Eq 1.19, k is Shannon's parameter, which defines a damage limit line diagonally in Shannon's plot (Fig. 1.9), the line k defines a threshold above which damage is observed. For Pt, $k \leq 1.75$ is commonly considered to be the damage limit; however, Shannon [1992] suggested a band within which the damage limit could be found $1.5 \leq k \leq 1.8$. A value of $k = 1$ would mean that charge is proportional to electrode area, whereas a k-value of 2 would result in charge proportional to electrode perimeter [Günter et al., 2019]. Shannon's equation was empirically inferred; however, the physical or physiological causes explaining the damage limit remain uncertain. Shannon's relationship underlines a safe stimulation threshold parameter with a good correlation to a few stimulation parameters but ignores some important parameters, including frequency

and duty cycle, which affect damage [Cogan et al., 2016]. Moreover, Shannon's relationship was established on Pt macroelectrodes ($\approx$ 1 mm diameter and larger) and only considered the geometrical surface area of electrodes, ignoring roughness. Therefore, Shannon's limit can only be used for Pt electrodes (until the damage mechanisms are fully understood), and further work was needed to extend the limit to microelectrodes (10 μm and smaller dimensions), which replaced macroelectrodes in most recent applications. While Kumsa et al. [2017] showed that electrodes with areas ranging from 0.2 mm^2 to 12.7 mm^2 followed the same damage threshold scaling with k, Butterwick et al. [2007] showed that macroelectrodes and microelectrodes had different damage threshold scaling, which pushed forward a new damage limit for microelectrodes, which only depends on charge per phase, a limit of 4 nC/phase [McCreery et al., 2010]. As modern electrode dimensions are two to three orders of magnitude smaller than those considered by Shannon [1992], charge density is proportionally larger, and the safe limit described by k can be approximated as a vertical line on the Shannon plot [Cogan et al., 2016, McCreery et al., 1994, 2010]. Roughness changes the available electrode area for electrochemical processes, thus changes the charge injection mechanisms. Electrodes with the same geometrical area but different roughnesses delivering similar charge per phase yield the same k, however, the charge injection mechanisms may differ, therefore, the damage limit may be different for rougher electrodes [Cogan et al., 2016, Carnicer-Lombarte et al., 2017]. Studies underlying Shannon's limit did not report electrode roughness, so it is not possible to adjust Shannon's limit for roughness; however, this suggests that the damage limit should be handled cautiously. Currently electrodes are used at stimulation levels well below Shannon's safe injection threshold to mitigate risks [DiLorenzo et al., 2014]. To optimize stimulation and with the development of microelectrodes where charge densities may exceed the limit k, a better understanding of the underlying mechanisms and safe stimulation guidelines are needed.

Two theories are presented to explain neural damage following neural

stimulation as observed above the limit k: neuron overstimulation leading to a loss of excitability of neurons (stimulation-induced depression of neuronal excitability or SIDNE); and production of harmful species through electrode degradation or other reactions at the electrode surface [Cogan et al., 2016, Kumsa et al., 2016b]. Rather than being opposed, both theories may occur simultaneously, and the observation of one of these mechanisms does not exclude the other [Cogan et al., 2016]. The theories relate to different ways of measuring damage: SIDNE corresponds to a functional evaluation of damage, where one measures the activity of neurons, while the electrochemical theory corresponds to a histological evaluation of damage, where tissues are visually and analytically inspected to find traces of damage, and both are usually mutually exclusive because they cannot be performed simultaneously [Cogan et al., 2016].

1.3.3.1 Neuron hyperstimulation

Stimulation-induced depression of neuronal excitability (SIDNE) may be explained by the mass action theory, which hypothesises that neurons saturate at a threshold stimulation rate, preventing the transmission of consistent action potentials. A too high stimulation rate leads to an abnormal intracellular concentration of Ca^{2+} ions, which are absorbed by the cell instead of Na^{+} to readjust the membrane potential [McCreery et al., 1990]. The abundant presence of Ca^{2+} inside the cell impairs function and can even lead to cell death. SIDNE was demonstrated in cats' cochlea with iridium electrodes stimulated at high frequency for a prolonged duration without observing neuron degeneration or inflammation, hinting that a high stimulation rate may induce functional damage without histological damage [McCreery et al., 1997]. However, the severity of the induced SIDNE was shown to highly depend on stimulus frequency and duty cycle (proportion of active stimulation time), which advocates for the mass action theory, which depends more on stimulation rate than intensity. In further work, frequency has been showed to influence damage thresholds on retinal cells [Butterwick et al., 2007] and in peripheral nerves

[McCreery et al., 1995]. The duty cycle was also addressed, showing no damage when the charge density remained low enough even close to 100% duty cycle (continuous stimulation) [Kuncel and Grill, 2004], but a decrease in neuron excitability is observed at higher charge densities [Tykocinski et al., 1995]. Frequency and duty cycle do not figure in Shannon's equation, which can be interpreted as Shannon's limit reporting a different damage mechanism than SIDNE. However, k is related to the product Q.D, which represents a cumulative effect of the proportion of triggered neurons with the activated volume of tissue, therefore, a proportionality to the total number of neurons activated [McCreery et al., 1990]. Therefore, Shannon's limit may relate to a too large number of triggered (saturated) neurons causing damage, which may explain why a reduction of stimulation frequency and duty cycle reduces damage.

A subsequent study McCreery et al. [1988] studied the histological damage caused to neurons in the vicinity of Pt electrodes (faradaic) and sintered tantalum pentoxide (capacitive) immediately and one week after stimulation, with a rationale to discriminate between damage attributable to harmful faradaic reactions vs stimulation rate, and to assess the recoverability of observed damage. It was shown that both types of electrodes yielded similar degrees of damage after a few hours of stimulation and that most of the injured neurons had recovered after a week. McCreery et al. [1988] concluded that observed histological damage, as observed in studies leading to Shannon's limit, is more likely to be correlated to current flow through the tissue rather than production of toxic species from faradaic reactions, however, prolonged stimulation protocol may have resulted in more irreversible damage.

1.3.3.2 Harmful faradaic reaction products

Platinum is relatively inert in saline in the potential regions observed during neural stimulation, compared to stainless steel for example, however, faradaic reactions occur and may yield harmful reaction products causing neural damage.

Platinum electrode corrosion, which releases platinum in the body was

suspected to cause the damage observed by McCreery et al. [1990] as traces of platinum were found at $k \geq 1.75$ *in vitro* [McHardy et al., 1980, Donaldson and Donaldson, 1986b] and *in vivo* [Robblee et al., 1983], and the injection of platinum salts in brain tissue caused damage similar to that observed during stimulation [Agnew et al., 1977]. Kumsa et al. [2016b] studied the charge injection of Pt disc electrodes in a repeated pulsing experiment with increasing k to determine what electrochemical phenomenon happens when k approaches 1.75. At these charge levels, the potential ratcheting due to unbalanced charge injection results in the electrode potential reaching the onset of repeated cycles of oxidation and reduction of Pt which is implicated in Pt dissolution. Pt salts have been proven to be harmful to neuronal cells and Pt dissolution therefore becomes a serious candidate for neural damage [Brummer and Turner, 1977]. *In vitro* studies showed reduced levels of Pt dissolution in the presence of proteins [Hibbert et al., 2000, Robblee et al., 1980], however, chronically stimulated Pt cochlear electrodes showed consistent levels of Pt dissolution, which were proportional to stimulation intensity, without observing neuronal loss or functional changes to the neuron population [Shepherd et al., 2019, 2020, 2021]. Pt particles were found in the vicinity of the electrode [Clark et al., 2014], triggering an enhanced FBR [Nadol Jr et al., 2014] and tissue necrosis [Shepherd et al., 2019].

Cl^- is known to adsorb onto Pt (1.14) and to enhance Pt dissolution through Pt-Cl complexes (1.15) or by blocking dissolved Pt redeposition, although the adsorption of proteins such as albumin may inhibit this behaviour *in vivo* [Topalov et al., 2014b, Hudak et al., 2017a, Doering et al., 2022]. More details on the Pt-Cl reactions are given in section 1.3.1.

Oxygen evolution reactions, especially the role of reactive oxygen species (ROS) including hydrogen peroxide (H_2O_2), are potentially harmful reactions at stimulation electrodes [Cogan et al., 2016]. ROS are highly reactive, which makes them likely to participate in dissolving electrode material and damaging encapsulation, resulting in electrode failure. ROS are also known to participate

in neural signal modulation, reducing neuronal activity through GABA receptor activation [Lamb and Webb, 1984, Ohashi et al., 2016]. Therefore, ROS action may be a factor in SIDNE if ROS is produced during neural stimulation. Reduction of molecular oxygen (Eq. 1.16) induces irreversibility in neural stimulation, which may cause interface changes resulting in harmful reactions [Merrill et al., 2005, Kumsa et al., 2016b].

Production of H^+ and OH^- ions cause large pH excursions at the electrode surface, which extend away from the electrode when the electrode dimension increased [Ballestrasse et al., 1985]. Moreover, pH was proven to vary in a wound area [Gupta et al., 2004], for instance following electrode implantation, which affects cell metabolism and charge injection [Brummer and Turner, 1977]. However, due to the body's buffer system, large concentrations gradients and the measured pH excursions remain minimal below 0.25 mC/phase [Huang et al., 2001]. The large excursions simulated by Ballestrasse et al. [1985] are likely to occur in the electrode vicinity and may remain undetected. While direct damage through pH is difficult to evaluate in this case, pH affects charge-injection reactions, which could translate into damage. Another possible cause of neural damage is the production of toxic substances from faradaic reactions. Dangerous redox reactions at Pt electrodes involve Pt dissolution releasing noxious Pt salts [Brummer and Turner, 1975], and oxidation/reduction of water.

1.4 Summary and research questions

Electrodes are used to deliver current-controlled pulses to elicit neural signals through electrochemical charge injection at the electrode-electrolyte interface. During pulses, the interface changes following those charge injection reactions despite safe stimulation strategies introduced to control the electrode's behaviour. Moreover, the electrode's environment changes over time as the body reacts to the implantation of a foreign body, which changes the electrode's properties. Therefore, electrode behaviour needs to be further evaluated, over

a range of conditions, in order to investigate the electrochemical mechanisms involved in charge injection *in vivo* which will enable more successful long-term stimulation and pave the way for new implant development. This thesis is focused on the behaviour of platinum electrodes during biphasic charge-balanced pulsatile stimulation, especially the electrochemical mechanisms involved in neural damage as reported by McCreery et al. [1990] and Shannon [1992]. The difference of behaviour *in vitro* and *in vivo* is pivotal to the understanding of neural damage, and parameters influencing charge injection need to be included in electrode testing setups for complete characterisation. Therefore, I chose to focus my work on answering the following questions emerging from my literature review:

- How do the electrochemical test methods influence measured electrode performance and how to best characterise stimulation electrodes' behaviour?

- How do materials and methods which do not figure in Shannon's equation influence platinum electrodes' behaviour in relationship to Shannon's parameter k?

- How do electrolyte characteristics influence platinum electrodes' behaviour in relationship to Shannon's parameter k, especially model body fluid conditions?

To address the first question, chapter 2 reports a systematic review characterising the influence of electrodeposition methods of a conductive polymer on electrode performance, which I supplemented with my own results for comparison. The conductive polymer (PEDOT) was chosen as subject for the review instead of platinum because it is a relatively new material in neural engineering and a review of the influence of methods was more relevant to the research community than a review about platinum, which has been extensively

characterised. Chapter 3 reports my design of an electrochemical setup to characterise platinum electrodes' behaviour during biphasic pulsing and study the implications of a variety of parameters. Electrode design considerations which may influence Shannon's limit were studied and reported in chapter 4 in three parts: electrode recess, electrode size, and electrode shape. The few studies on Shannon's limit varied k by varying the stimulation current, therefore, the effect of varying stimulation pulse width was studied in chapter 5. Finally, chapter 6 reports studies of electrolyte characteristics which are usually absent from traditional characterisation electrolytes, including pH, salinity, electrolyte structure (gelated vs fluid), buffer system, and dissolved gases. To conclude this work, a general discussion (chapter 7) considers the context of this work and possibilities for future work, and the general conclusions are given in the conclusive section.

Chapter 2

Characterising the influence of methods on electrode performance: the example of PEDOT

Out of interest for the influence of experimental methods on electrode performance, a thorough literature review was conducted on the electrodeposition methods of poly (3,4)-ethylene dioxithiophene (PEDOT), a conductive polymer used to improve metal electrodes' performances [Niederhoffer et al., 2023b]. The paper highlighted the multiplicity of experimental parameters used across studies, with a recrudescence of a few combinations of parameters, which pertained to a reproduction of previous protocols, rather than for a specific outcome. Despite the variability across studies, clear trends emerged: coating thickness and CSC increased linearly with deposition charge density, CIL increased with pulse width for different coating types [Green et al., 2011, 2012a, 2013] and with deposition charge density, as did surface roughness, although several parameters seemed to affect roughness. Impedance decreased with deposition charge density and the normalised 1 kHz impedance converged to a resistivity value equivalent to the resistivity of PBS, showing that the 1 kHz impedance is dominated by access resistance. Therefore, increasing de-

position charge density to deposit more PEDOT does not decrease the 1 kHz impedance lower than R_A. An important consideration from this work related to the choice of reported quantities and to the variability of characterisation parameters. The span of used characterisation parameters, for instance CV potential range and sweep rate, introduced substantial variability in results, preventing some direct comparisons. The observed trends were clear, proving the strength of the correlation, however, some volatility within the trends could be attributed to characterisation parameters variability, for example for CSC. Second, reported quantities such as CSC and impedance at 1 kHz do not provide sufficient information on the electrode behaviour, as demonstrated with the impedance, which was almost equal to R_A. Broader characterisation results are needed for a better understanding of the electrodes' behaviour and standardised characterisation for comparability. These considerations were taken into account in my own work, for the characterisation of a PEDOT-coated cuff electrode.

2.1 Context

An expandible cuff electrode was developed for electrical impedance tomography (EIT) [Chapman et al., 2018, Ravagli et al., 2020] and selective stimulation of the vagus nerve to reduce physical strain induced by traditional cuffs [Paggi et al., 2024, Aristovich et al., 2021]. Stainless steel was chosen for its fatigue resistance properties, however, electrical charge injection capacity needed to be improved, which was realised by coating the electrode with PEDOT:pTS. I performed a full electrochemical characterisation of a PEDOT-coated cuff and compared the performance to a non-coated platinum cuff, with 30 active sites (AS) each. Thus, I designed the characterisation protocol according to the application and stimulation conditions.

2.2 Methods

The electrodes were 15 pairs of 3 × 0.35 mm rectangles of 12.5 μm 304 stainless steel foil (Advent Research Materials, UK). The exposed stainless steel

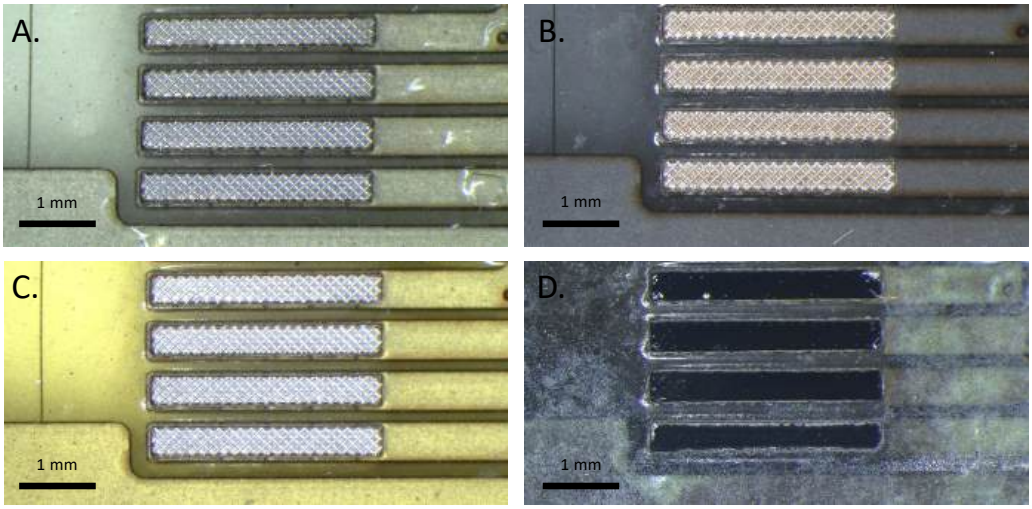

Figure 2.1: *Optical microscopy images of the cuff electrode active sites treatment. A. Laser patterning. B. Acid etching (not performed on the tested electrodes in this work). C. Gold plating. D. PEDOT:pTS electrodeposition.*

electrodes were laser-patterned using bidirectional cross-hatching with 0.1 mm gaps at ±45° to the length of the electrode (Fig.2.1 A.). The electrodes were then plated with gold using a gold strike pen (Spa plating) at 10 V for 30 s (≈ 200 mA) (Fig.2.1 C.). For the Pt electrode, the surface was tank-plated with Pt (Spa plating) for 60 s at 10 V. PEDOT electrodes were coated with PEDOT:pTS using a PalmSens potentiostat on galvanostatic mode at 2 $mA.cm^{-2}$ for 450 s, coating 14 electrodes simultaneously (total area 0.147 cm^2) yielding a 900 $mC.cm^{-2}$ deposition charge density (Fig.2.1 D.). The plating solution was prepared with 100 mM EDOT and 50 mM pTS mixed in acetonitrile, as reported in Chapman et al. [2018]. Therefore, the PEDOT-coated electrodes were compared to Pt-plated gold electrodes with the same dimensions and fabrication process. The fabrication process has similar elements to various previous designs: laser patterning like [Green et al., 2012a], square pads like [Castagnola et al., 2015], PEDOT:pTS on gold like Kayinamura et al. [2010], Chapman et al. [2018].

The characterisation methods were chosen to complete two objectives:

characterise at best the electrode behaviour during stimulation and produce comparable characterisation data with other PEDOT-coated electrodes. Therefore, the parameters used for the tests echoed the most frequently used parameter ranges found in the systematic review. Characterisation was performed in a three-electrode setup with an Ag|AgCl reference electrode (3.5 M) and a carbon rod counter-electrode with a Gamry Reference 600+ potentiostat.

EIS was performed from 1 Hz to 100 kHz at OCP with an amplitude of 5 mV. The frequency range covered a large enough range to characterise the electrode behaviour during stimulation, and a small amplitude improves the accuracy of the linearisation of Ohm's law. Additionally, EIS should be performed at OCP to avoid current flow interfering with the measurements. The impedance magnitude and phase at 1 kHz were reported as it is usually the case in electrode characterisation along with the full spectrum Bode plot, which more accurately defines the electrode behaviour. The access resistance was also reported.

CV was performed at a scan rate of 100 mV/s between -0.8 V and +0.6 V vs Ag|AgCl as both were the most-used parameters for CVs of PEDOT-coated electrodes [Niederhoffer et al., 2023b]. However, experimentally, the water window was observed between -0.8 V and +1 V vs Ag|AgCl. The charge storage capacity (CSC) was calculated as the integral of the cathodic CV scan.

Two pulse widths were to be used for stimulation, 50 μs and 1 ms, therefore, the maximum safe charge injection was determined for both pulse widths. Biphasic square cathodic-first charge-balanced pulses of increasing intensity were applied, and the maximum safe current was calculated when the electrode polarisation, which is the potential corrected for the ohmic drop (see 1.2.2), reached the potentials of water electrolysis. The theoretical limits are [-0.6 V ; +0.8 V] for Pt and [-0.9 V ; +0.6 V] for PEDOT, and I used the experimental water window for Pt as well [-0.8 V ; +1 V]. No experimental water window could be determined for PEDOT, therefore, only one CIL was reported, whereas for Pt, theoretical and experimental CIL are reported in figure

2.4 A. Figure 2.4 B shows the polarisation curves obtained for maximum safe currents for Pt (theoretical and experimental safe limits) and PEDOT. The maximum safe injected charge (or charge injection limit (CIL)) was calculated by multiplying the current by the pulse width.

CV was performed first to have a cleaning and activation action, then EIS, and CP with both pulse widths to complete the characterisation.

2.3 Results

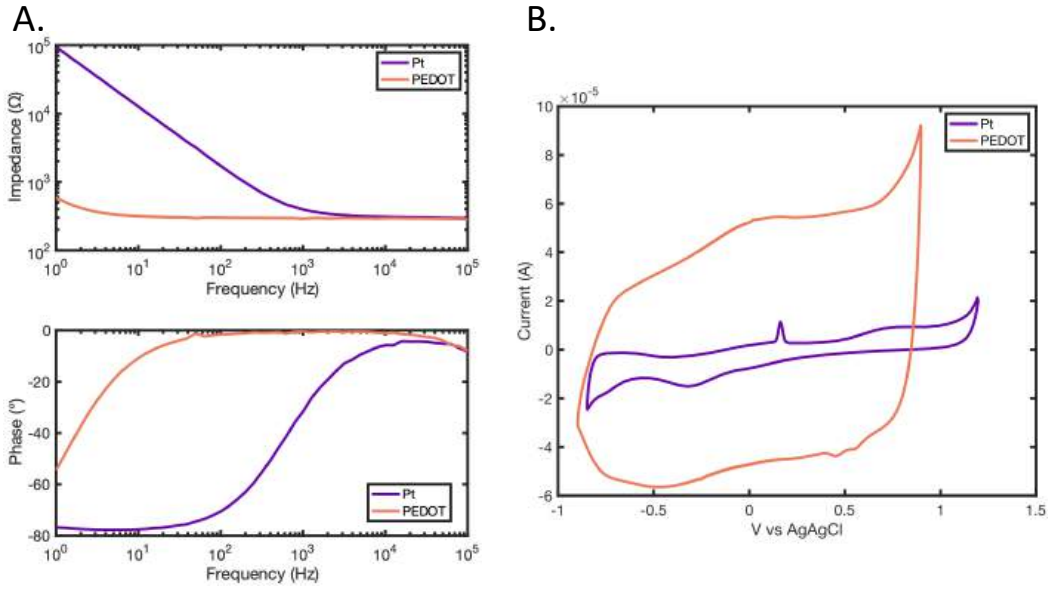

Figure 2.2: *A. Bode plot of EIS measurements comparing the Pt-plated (purple) and PEDOT-coated (orange) electrode impedance (top) and phase (bottom). B. CV comparison of the Pt-plated (purple) and PEDOT-coated (orange) electrode.*

PEDOT electrodeposition substantially changed the EIS and CV (Fig. 2.2). The high-frequency impedance was similar for bare Pt and PEDOT, however, the impedance remained flat for most of the frequency spectrum, with a transition towards capacitive charge injection around 10 Hz. The main difference was on the phase plot, which showed that PEDOT electrodeposition made the electrode behaviour more resistive over most of the spectrum, including at 1 kHz. R_A decreased by 31 Ω (≈ 10%), while the 1 kHz impedance decreased by 117 Ω (≈ 26 %) and the phase increased from -26.6° to -0.7° on average

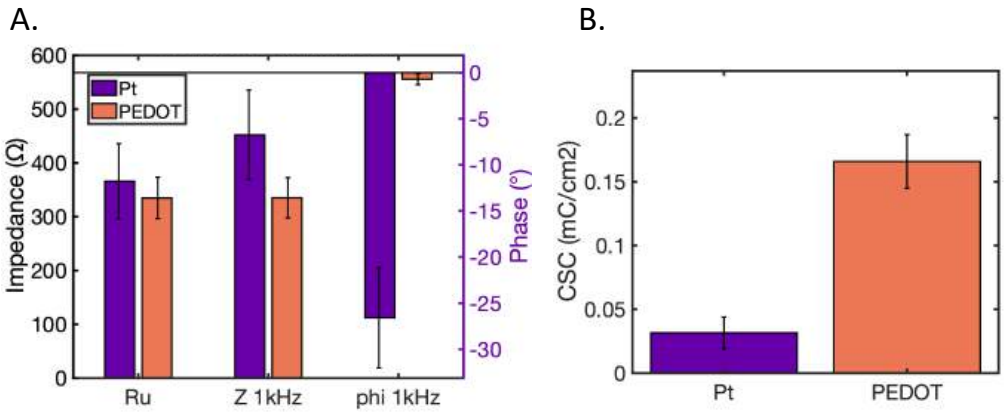

Figure 2.3: *A. Comparison of access resistance (R_A), impedance at 1 kHz, and phase at 1 kHz of Pt and PEDOT-coated electrodes. B. Comparison of charge storage capacity of Pt and PEDOT-coated electrodes.*

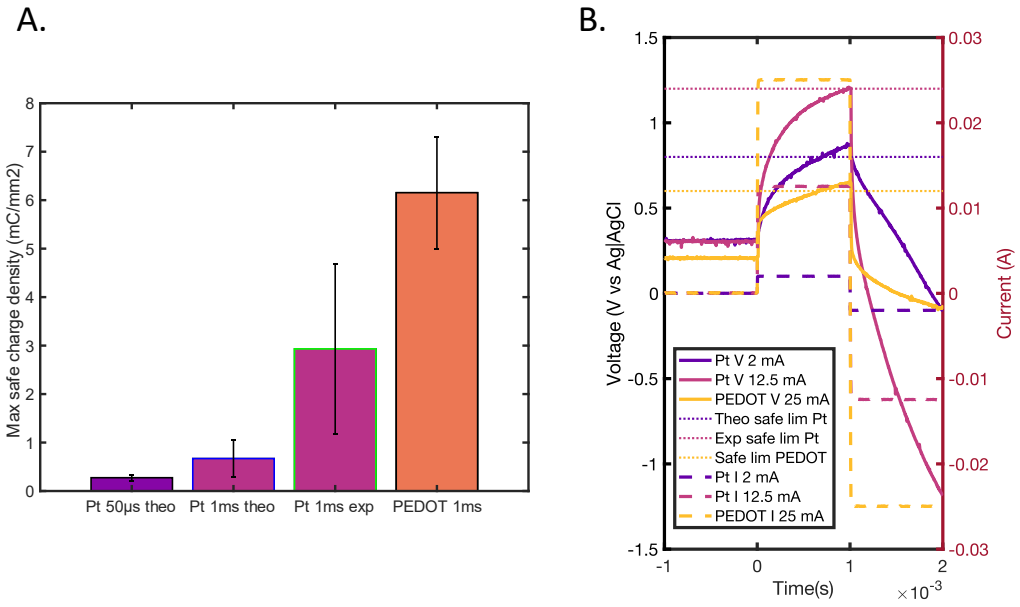

Figure 2.4: *A. Comparison of charge injection limits of Pt and PEDOT-coated electrodes at various pulse widths. B. Example CP polarisation curve showing the current waveform (dashed line), the polarisation (plain line), and the safe limits (dotted line). The selected current values correspond to maximal safe currents (reaching safe limits).*

(Fig. 2.3 A). The CV of PEDOT electrodes was much wider than Pt electrode with broadly defined peaks (Fig. 2.2 B) and as a result, the CSC was multiplied by 5.5 from 0.03 $mC.cm^{-2}$ for Pt to 0.166 $mC.cm^{-2}$ PEDOT (Fig. 2.3 B).

Figure 2.4 A reports theoretical and experimental CIL for two pulse widths for Pt and PEDOT. For 50 μs, the CIL could not be calculated for the experimental safe limit nor for PEDOT-coated electrodes as the potentiostat saturated before the polarisation reached limit values. Therefore, it can only be concluded that the safe charge injection limit was superior to 0.5 $mC.mm^{-2}$ in both cases. For 1 ms pulses, the CIL of Pt electrodes was 4.5 times larger with the experimental safe limit (2.9 $mC.mm^{-2}$ vs 0.66 for theoretical limits). PEDOT electrodeposition multiplied the CIL by 10.1 on the theoretical safe limit and by 2.3 on the experimental safe limit, which was attributed to a higher capacitance yielding a less steep polarisation curve, as can be observed in figure 2.4 A. The CIL was lower for 50 μs pulses although the maximum safe current was significantly higher for Pt because of the pulse width difference. The CIL for PEDOT at that pulse width was not reported as the potentiostat saturated at around 30 mA, which was reached regularly without exceeding the safe potentials, therefore, it can only be concluded that the safe charge injection limit was superior to 0.5 $mC.mm^{-2}$.

2.4 Discussion

The choice of characterisation parameters has two aims, which are giving the best possible insight into the electrode behaviour to understand its performance capability, and comparing the performance to other work. However, as suggested by the literature review, the commonly reported performance indicators are not necessarily a true representation of the electrode behaviour, therefore, these indicators, including the impedance at 1 kHz and CSC should still be reported for the sake of comparison to other work, however, authors are encouraged to adopt a universal standard for their electrode design and application [Boehler et al., 2020b]. Furthermore, a meta-analysis of data exhibited

common parameter choices and identified knowledge gaps and new studies to conduct to understand better the role of a few methods parameters on PEDOT coating performance such as the EDOT/co-ion ratio and the effect of co-ions for instance [Niederhoffer et al., 2023b]. My own characterisation of a PEDOT-coated electrode represents the importance of characterisation parameters and the necessity to report traditional and complete characterisation data. EIS, CV and CP results were reported in two ways: the key parameters usually provided in electrode characterisation, Z at 1 kHz, CSC and CIL, and a typical experimental curve to show the full spectrum. CP was designed to test the CIL in all stimulation regimes and showed how testing parameters and limits may influence characterisation results as well. The CIL measurements illustrated how the choice of water window affected the results with a 450% increase of CIL when changing the safe potential boundaries as suggested by other experimental data (CV). Indeed, a few studies have demonstrated that damaging electrochemical reactions may occur within the water window [Merrill et al., 2005, Cogan et al., 2016, Kumsa et al., 2016b], implying that the safe potential boundaries may not be accurate for all electrodes and stimulation types. The typical stimulation current (1 to 2 mA) used with 1 ms pulses exceeded Shannon's safe stimulation limit $k = 1.75$ (Eq. 1.19), and may therefore cause neural damage and/or degrade the electrode material [Shannon, 1992, Kumsa et al., 2016b]. For a current of 1 mA, the pulse width used for bare Pt electrodes should not exceed 700 μs to remain below Shannon's limit. The safe stimulation limit is not known for PEDOT.

Concerning the results of the cuff electrode characterisation themselves, two key learnings from the review were confirmed by the experimental results: the reduction of impedance magnitude through PEDOT electrodeposition is limited (dependence on electrode dimensions) and the CIL increased independent of Z. Indeed, the EIS Bode plot showed that the access resistance and the 1 kHz impedance were only slightly lower after PEDOT deposition and that the 1 kHz impedance was equal to R_A. The impedance phase however exhib-

ited a more substantial change. The safe injectable charge was multiplied by 10, which suggests that the better CIL for the PEDOT-coated electrode was attributable to the resistive behaviour over a wider frequency range, rather than to a decrease of impedance. The EIS results show a resistive phase shift over the frequency spectrum, suggesting the electrode had a more resistive behaviour over a wide range of frequencies (100 Hz to 100 kHz). The CV however displayed a larger area and a square shape which is characteristic of capacitive behaviour [Wilks et al., 2009], suggesting the charge injection was more capacitive. Nevertheless, both results are not contradictory. First, CV can be considered as a DC signal with a null frequency, locating it further left on the Bode plot, where the phase may be more capacitive. Second, the CV shows that the electrode's double-layer capacitance increased (wider CV), which reduces the electrode-electrolyte interface impedance. As the total impedance measured in EIS can be described as the sum of the interface impedance and the access resistance, the total impedance becomes almost equal to the access resistance as the interface impedance decreases, which was observed as Z at 1 kHz was almost equal to R_A. Therefore, the electrode charge injection behaviour is capacitive, with a larger capacitance, and a large fraction of the electrode impedance is due to access resistance (solution resistance), which appears as a resistive behaviour.

Interestingly, R_A was similar for the uncoated Pt electrode and for the PEDOT-coated electrode. For the planar disc uncoated Pt electrode $R_A = \frac{\rho}{4r}$ following Newman's formula 4.9, showing dependence only on solution resistivity and electrode radius. The PEDOT coating is thought to increase the electrode's ESA as more reactive surface area becomes available inside the PEDOT structure, with authors suggesting that the change of ESA may explain the better performance of PEDOT-coated electrodes [Cui and Martin, 2003, Wilks et al., 2009, Alba et al., 2015, Aqrawe et al., 2019]. However, in this experiment, R_A did not change, suggesting that the change in ESA should not be taken into account when estimating R_A, as the PEDOT layer

may not change the electric field line distribution. PEDOT deposition modes exhibited different coating structures and shapes, which should reflect the current distribution. The PEDOT coating may subsequently change the current distribution as for instance PS deposition was wider than the electrode, and GS was more concentrated at the electrode center. Therefore, different deposition modes may affect R_A among other charge injection parameters, by redistributing the electric field at the electrode surface. In this experiment, only GS deposition was tested, which was the most used as shown in the literature review [Niederhoffer et al., 2023b], however, another deposition method could have yielded a different EIS result, and potentially a different R_A. The CSC and CIL were inferior to typical values reported in the literature, although the deposition charge density was relatively high compared to other studies [Niederhoffer et al., 2023b]. However, there is a close match in CSC with one study by Chapman et al. [2018], which used the same design and deposition methods as the present study, which gives a compelling argument for the role of methods on the electrode performance. A visual inspection of active sites was performed at the end of the electrode characterisation to provide an explanation for the failure of a few active sites. The optical microscopy images (Fig. 2.5) showed contamination of a few active sites with a yellow powder-like material, which created a bubble in the PEDOT coating. When scratching the bubble with a scalpel, the whole PEDOT bubble would come off, revealing the bare gold surface, and indicating improper adhesion. The contamination did not necessarily correlate with failure, however, lower performance was recorded for the majority of them, which may explain some of the variability. The nature of the contamination is unknown. Some active sites failed or had low performance indicators for both Pt and PEDOT electrodes, possibly indicating a failed connection, which caused improper coating and charge injection overall, however, no visual failure signs were observed.

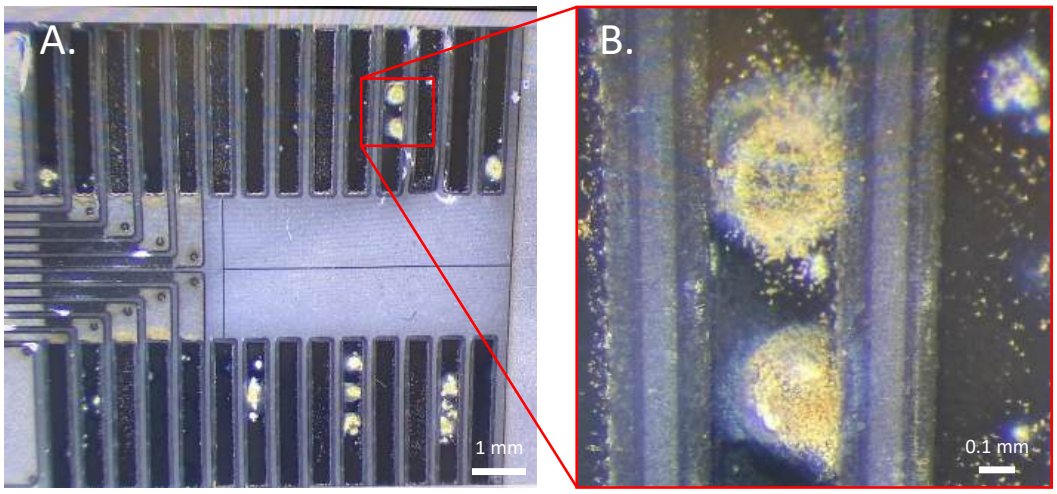

Figure 2.5: *Optical microscopy images of the contamination of the PEDOT-coated cuff contacts with A. 6.4x zoom and B. 40x zoom.*

Chapter 3

Design of a robust experimental setup

Bench-top studies of electrochemical damage mechanisms are challenging, because they involve indirect observation of neural damage through electrochemical processes, since neurons are usually not present in the test solution. As biological components (neurons, immune cells and proteins) are not included, damage needs to be inferred according to a "damage reference" that was empirically determined based on *in vivo* experiments: Shannon's parameter k. Precise control of the electrode's state throughout the experimental process is pivotal to accurately interpreting the electrochemical processes at play, and to produce repeatable results. Therefore, a controlled and robust experimental setup is required to conduct this work. The experimental setup design and testing were described in a publication [Niederhoffer et al., 2024].

3.1 Stimulator circuit design

The experimental framework to study charge-injection behaviour during pulsatile stimulation was based on monitoring the electrode potential during biphasic charge-balanced pulse trains, similar to the protocol used by Kumsa et al. [2016b]. Trains of 1000 biphasic current-controlled cathodic-first asymmetric charge-balanced pulses with capacitive discharge anodic balancing phase (Fig. 3.2) were applied with a custom stimulator inspired from Hudak

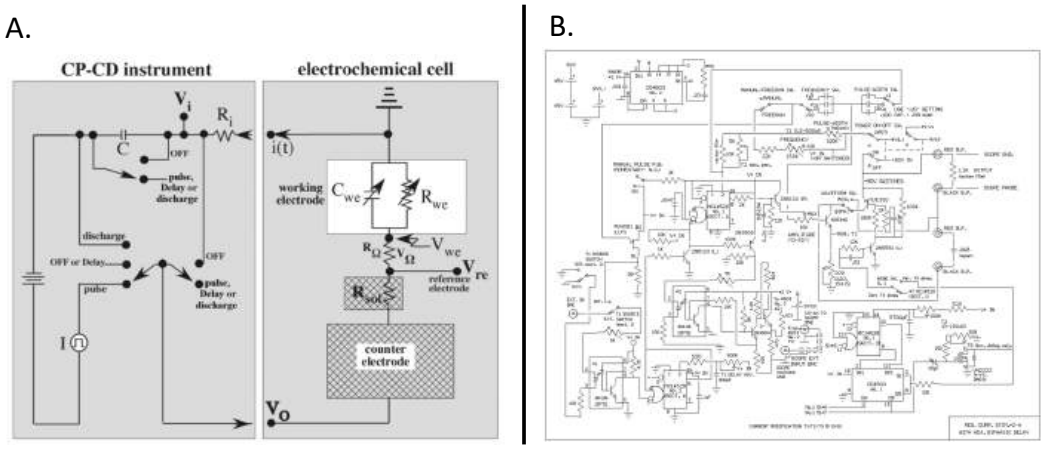

Figure 3.1: *A. Circuit schematic in Kumsa et al. [2016b] (CC BY 4.0) B. Circuit diagram in Hudak [2011].*

[2011] and Kumsa et al. [2016b], see diagrams figure 3.1. The following section details the rationale behind the chosen waveform and presents the stimulator circuit I designed to deliver the biphasic current waveform.

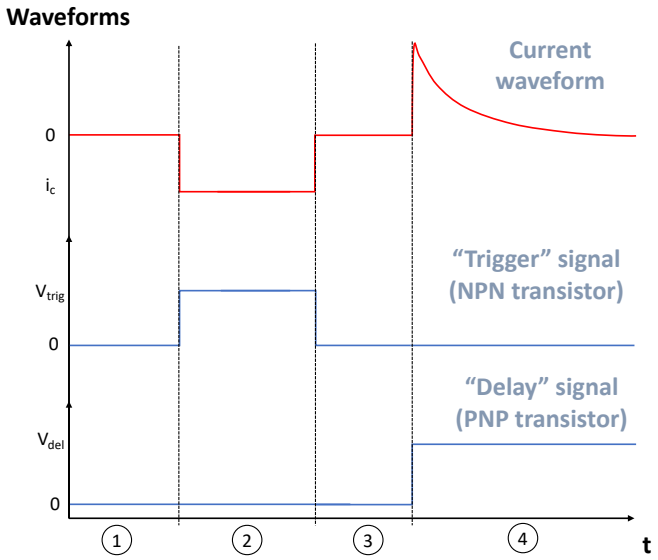

Figure 3.2: *Current waveform (red line) and control signals delivered by an Arduino microcontroller to regulate transistors conductance.*

The capacitive discharge anodic phase effectively ensures electrical charge balancing with a capacitor connected in series with the electrodes, which charges in the cathodic phase and discharges in the anodic phase [Merrill et al., 2005, Kumsa et al., 2016b], where no capacitor leakage occurs. The capacitive dis-

charge shape was chosen to deliver most of the reversal charge as quickly as possible to prevent reactants from diffusing too far away from the electrode surface, therefore enhancing the chances of returning the interface to its initial state. The pulse width was set to 100 μs, and cathodic and anodic phases were separated by a 100 μs interphase delay, used in stimulation protocols to lower excitation thresholds and enhance nerve fiber recruitment [van den Honert and Mortimer, 1979, Gorman and Mortimer, 1983]. The anodic discharge was designed to last for 15 ms to ensure full discharge of the capacitor, followed by a 4.8 ms open-circuit stand-by phase before the next pulse to avoid phase switch artefacts. The total duration of a single pulse was 20 ms, resulting in a 50 Hz pulse frequency. The cathodic current, which was directly calculated from k, was controlled by changing the gate voltage of a transistor acting as voltage-controlled current source [Hudak, 2011]. Charge densities and current values can be found in table 3.1.

Table 3.1: *Table of charges, current, and ohmic drop through the circuit corresponding to various k-values for two electrode sizes.*

	5 mm diameter (S = 19.635 mm^2)				**1 mm diameter (S = 0.785 mm^2)**			
k	**Q** (μC)	**D** ($\mu C/mm^2$)	i_c (mA)	V_{ohmic} (V)	**Q** (μC)	**D** ($\mu C/mm^2$)	i_c (mA)	V_{ohmic} (V)
0.566	0.85	4.33	8.50	2.55	0.17	21.65	1.70	0.51
1.24	1.85	9.41	18.47	5.54	0.37	47.04	3.69	1.11
1.55	2.64	13.44	26.39	7.92	0.53	67.21	5.28	1.28
1.66	3.00	15.26	29.96	8.99	0.60	76.29	5.99	1.80
1.75	3.32	16.92	33.23	9.97	0.66	84.62	6.65	1.99
1.85	3.73	18.99	37.28	11.99	0.75	94.94	7.46	2.24
2	4.43	22.57	44.31	13.29	0.89	112.84	8.86	2.66

The current waveform was achieved by controlling the opening of two BJT[1] transistors, one NPN (MJE340, ON semiconductor) and the corresponding PNP (MJE350, ON semiconductor), circuit architecture shown in figure 3.3. The gate of the NPN transistor regulating the cathodic phase (called "trigger transistor" from now on) was connected to the wiper of a 5 kΩ potentiometer to control the conductance of the transistor, therefore controlling the cathodic current. The PNP transistor controlling the discharge (called "discharge tran-

[1]Bipolar junction transistors

sistor") acts more like a switch, hence the saturation regime. A set of resistors and a capacitor regulate its gate voltage and the signal comes through another NPN BJT transistor (2N5550, ON semiconductor), which opening causes the PNP gate voltage to drop, opening the transistor. The transistor control signals are shown in figure 3.2: both transistors are non-conducting in the zero current phases (1 and 3), NPN is conducting (ohmic regime) and PNP non-conducting in the cathodic phase (2), where the current flows through the electrodes to the ground ("Square" current path in Fig. 3.3), charging the series capacitor ("discharge capacitor" in Fig. 3.3), and NPN is non-conducting and PNP conducting (saturation regime) in the anodic phase (4), where the current flows as the capacitor discharges in a loop only containing the capacitor, the electrodes, and a current measurement resistor ("Discharge" current path in Fig. 3.3). The current measurement resistor, in series with the electrodes and capacitor, was chosen as 100 Ω similarly as Hudak [2011].

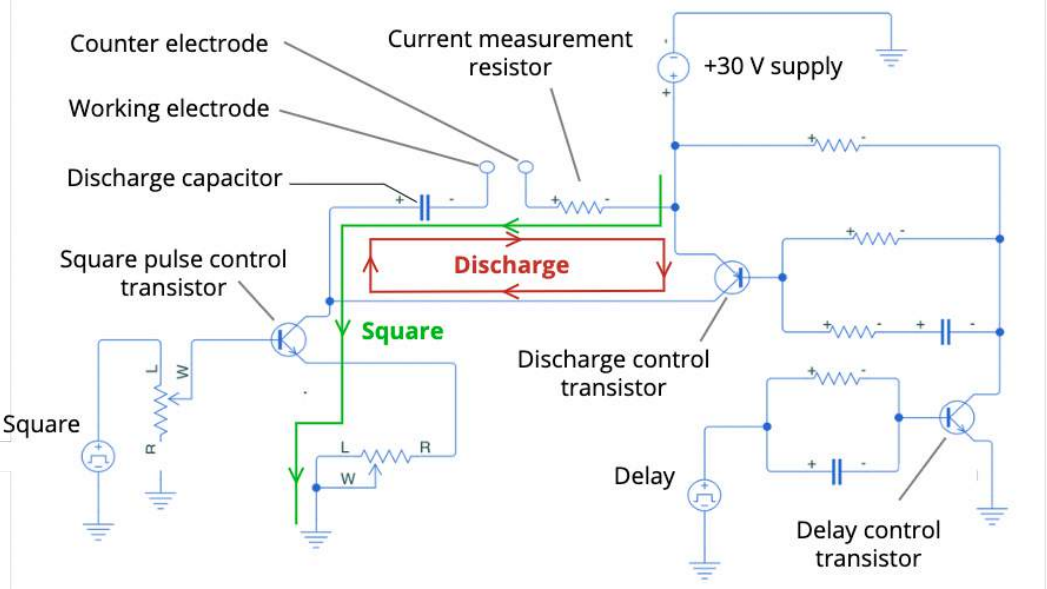

Figure 3.3: *Schematic of the output stage of the stimulator circuit. The current paths are specified for both phases: cathodic in green ("Square") and anodic in red ("Discharge").*

While Hudak [2011] used +90 V as voltage supply, requiring high-voltage graded components and increasing the risk of user and equipment damage, I chose to work with +30 V, which was sufficient to achieve the required ca-

thodic currents for a large electrode (5 mm diameter), see table 3.1. For the 1 mm diameter electrode, the compliance limit was never reached in practice, however, for electrode diameters smaller than 1 mm, the resulting larger impedance would eventually require an increased supply voltage for high k-values. The second main difference with Hudak [2011] circuit is the system controlling the pulse timings: whereas Hudak [2011] used clocks and buffers to set the timings, I used a microcontroller (Arduino Uno Rev 3) to set the pulse timings, followed by an optocoupler and a CMOS level-shifter for power isolation and voltage level control.

After prototype validation, I designed a printed circuit board (PCB) on Autodesk Eagle. The PCB was designed on two layers and manufactured by PCBWAY, see figure 3.4. Further adjustments were made on the PCB: first, resonant ripples in the cathodic square wave (Appendix A, Figure 1.1 B) were corrected by adding capacitors between Arduino outputs and ground. Second, uncontrolled signal triggering was corrected by adding 470 Ω pull-down resistors on the Arduino outputs, effectively putting the Arduino output in a "low" state during the high-impedance "stand-by" phase, without affecting the "high" state. More details are provided in the appendix A.

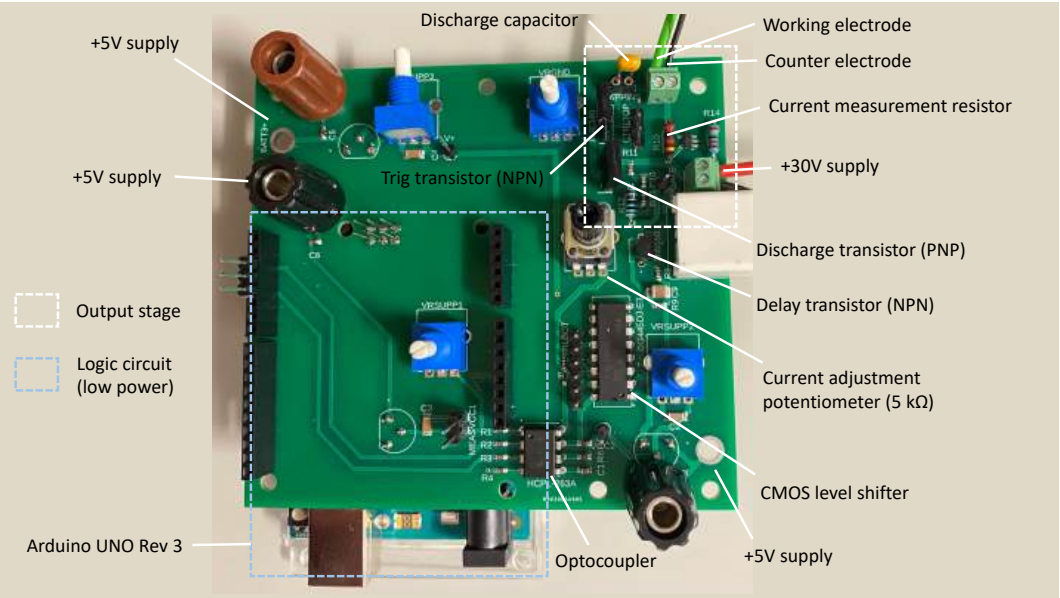

Figure 3.4: *Printed Circuit Board (PCB) with all components and connections.*

3.2 Construction of a repeatable protocol

3.2.1 Pulsing test

Seven k-values were used in experiments: five values from Kumsa et al. [2016b] covering a sufficient range and exceeding Shannon's safe limit: 0.566, 1.25, 1.66, 1.75 (Shannon's limit for Pt), 2, and two complementary values to add data points around $k = 1.75$ for better trend interpretation 1.55 and 1.85 (corresponding charge and current is given in table 3.1). The current magnitude was adjusted by changing the value of a 5 kΩ potentiometer on the NPN transistor gate; however, all current values needed to be set before the experiment as electrodes were only connected to the stimulator during pulses and current flow could alter the electrode's state. Therefore, a current setting step preceded the whole experiment where the setting of the 5 kΩ potentiometer was noted for each current and reproduced when required. The potentiometer settings were measured in the absence of current flow, as the current setting step during experiments was also conducted in the absence of cell current. The current magnitude was measured at a 100 Ω resistor; 100 Ω represents an impedance of comparable magnitude to the 5 mm diameter electrodes' impedance (from 20 Ω to 100 Ω for most electrolytes), which was much smaller than the probes impedances ($\geq$ 10 MΩ), representing a 10^{-5} voltage measurement error factor on the current measurement resistor voltage drop. Smaller resistor values may have induced errors in voltage readings due to the small magnitude of the voltage drop, for instance with 10 Ω, $V_{100\Omega} = 200mV$ at 20 mA over a 30 V signal (1/150 factor).

An oscilloscope (Tektronix DPO 3014) was used to record all the signals to accommodate for the voltage level around +30 V, which greatly exceeds the chosen potentiostat's range of ±12 V. As mentioned earlier, two channels were connected at the current measurement resistor to determine the current waveform from their difference $i_c = \frac{(V_2 - V_1)}{100\Omega}$. A differential probe (Pico TA 041, 25 MHz bandwidth, 4 MΩ input impedance) was used to measure the potential difference between the working electrode and the reference electrode. A trigger

lead was connected to the trigger control signal and the "Single" and "Normal" trigger modes of the oscilloscope were used to record the first and last pulse of the pulse train. The oscilloscope's accuracy was tested to eliminate uncertainty in the measurement by measuring the voltage drop difference across a resistor with no current flow and with 15 V applied, comparing the measurement with a voltmeter. The measurement error on the oscilloscope was 2.6 mV rms at 0 V and 4.4 mV rms at 15 V.

Pulse accuracy was evaluated in a test series of five experiments with seven k-values evaluating pulse timings, current accuracy and charge balance; the results are presented in table 3.2. Cathodic pulse timings were very accurate and consistent with 1μs standard deviation, and cathodic and anodic rise/fall times were also consistent at ≈ 6 μs each, which suggests that rise times may be an intrinsic limitation of the Arduino, or the circuit's ICs[2], including the optocoupler and the CMOS level-shifter. The anodic phase was systematically completed within 1 ms, with durations varying slightly with k, proving the 19.8 ms delay was sufficient to let the capacitor discharge completely. The current accuracy in the cathodic phase was determined by comparing the average measured current with the theoretical value (see table 3.1). Considering that the current was set based on a prerecorded variable resistor value, which was set with error margins (within 10 Ω), the current accuracy was acceptable with a discrepancy of 1.1 mA on average, representing 4.5% of the theoretical current value, without the error ever being larger than 3.5 mA (3.38 mA once, otherwise always lower than 2.3 mA). The peak-to-peak noise was also consistent and relatively low at 1.2 $\pm$ 0.94 mA, although some experiments could yield more noise, without a clear explanation.

Charge balance was a key concept to relate to the *in vivo* studies on which Shannon [1992] based the safe stimulation limit. A few techniques were used to quantify charge balance, only the last, more methodical approach is described in this section, other techniques being detailed in appendix A. A trapezoidal

[2]integrated circuit

estimation function was used ("trapz" function, MATLAB) to quantify separately the cathodic and anodic charge and calculate the net imbalance presented in table 3.2. The imbalance was cathodic on average, with the cathodic charge matching the expected value calculated from k and the anodic charge being inferior. On average, the systematic test concluded to a 5.75% imbalance. Therefore, the results presented in this thesis should be considered as slightly cathodically imbalanced, however, the trends and conclusions are still valid and would only be exacerbated if proper charge balance was achieved by the system: as developed further in the results in chapter 6.1, a positive ratcheting was observed, indicating an anodic charge imbalance, which would only be greater if more anodic charge was injected. Furthermore, on a few occasions ($\approx$ 30 % of tests), an anodic imbalance was measured, meaning that the capacitor reversed more charge than injected during the cathodic phase, which may represent a measurement artefact. In the hypothesis that the imbalance was due to leakage during the cathodic phase, the leakage and therefore the imbalance would be expected to become larger with a larger current, however, the results do not suggest that, with uniform imbalances with k. The imbalance could also be due to different impedance paths faced during both phases, however, more consistent results in the imbalance would be expected. Therefore, although charge balance cannot be proved and will not be assumed for the interpretation of results, the observed charge imbalance may be attributed to a measurement inaccuracy, potentially on anodic rise time, where the initial current may be larger than the measured value and yield a substantial additional anodic charge amount which may have been missed by the recording setup.

The possibility of leakage during the interphase was also explored by monitoring the capacitor voltage during pulses. In the interphase, the voltage at the capacitor exhibited a slight decrease after the initial ohmic drop, however, the result remained inconclusive as the differential probe time constant was of the same order of magnitude as the interphase delay.

Table 3.2: *Table of pulse timings, cathodic current accuracy, and charge balance quantification for 7 k-values across 5 experiments (n = 35)*

		Rise and fall times		
	Cathodic pulse width (μs)	**Cat start** (μs)	**Cat end** (μs)	**Ano start** (μs)
Mean ± std	101.91 ± 1.07	6.14 ± 0.65	5.99 ± 0.21	6.64 ± 2.09

	Current accuracy	
	Relative current error (%)	**Cathodic noise** (μA P-P)
Mean ± std	4.49 ± 4.65	1.20 ± 0.94

	Charge imbalance	
	Absolute (μC)	**Relative** (%)
Mean ± std	0.13 ± 0.24	5.75 ± 9.89

3.2.2 Electrochemical characterisation

Alongside pulsing tests, electrochemical characterisation tests were needed to evaluate the electrode state before and after pulses. First, cyclic voltammetry (CV) provides information about the available electrochemical reactions along a potential range and the properties of these reactions, see 1.2.2.2. In this case, CV was used to locate the potential measured during the pulsing test and identify possible electrochemical reactions. The whole voltammogram was also compared to a reference voltammogram measured before stimulation was applied to the electrode, which gives information about the electrode's state. For instance, if the electrode surface was oxidised during stimulation, there are fewer reactants present for oxidation and more for reduction, therefore, reduction peaks will be favoured and appear larger during initial post-pulse CV cycles, whereas oxidation peaks may appear smaller or see their onset potential shifted towards subsequent oxidation reactions. CV had another pivotal role: as several k-values were tested consecutively in the same setup, it was necessary to make sure that the electrode could be returned to its initial state to have comparable results. Repeating CV cycles through the water window range provides full oxidation and reduction cycles of the surface, which acts as a surface cleaning protocol, resetting the electrode potential to a stable value. After some variation in the first voltammograms, the curve stabilises, indicating a stable interface (see Fig. 3.13 B.). The water window

was determined experimentally for every electrolyte by identifying the oxygen and hydrogen gas formation asymptotes and reading the potential for which the current reached 200 μA (0.01 $mA.cm^{-2}$) for the 5-mm diameter electrode. With the smaller electrode (1-mm diameter), asymptotes were observed as the current reached 100 μA, which is equivalent to 0.025 $mA.cm^{-2}$. A scan rate of 100 $mV.s^{-1}$ was chosen as a compromise between characterisation of slow electron transfer processes and protocol efficiency. A typical number of 30 CV cycles was applied, by which the curve was very stable, starting from OCP in the anodic (oxidation) direction.

Electrochemical impedance spectroscopy (EIS) was the second electrochemical characterisation test used to provide information on the electrode state and its behaviour during stimulation, see 1.2.2.1. At high frequency (f > 10 kHz typically in this case), the electrode's behaviour is resistive, dominated by the access resistance, which is related to solution resistivity and electrode dimensions. At lower frequencies (1 Hz < f < 100 Hz), EIS provides information about the capacitive behaviour of the electrode. A change in the EIS response, either in the high or low frequency region would indicate an alteration of the interface, which would complement the analysis of CV and pulse response. Access resistance is also useful to correct the voltammograms, as there is a small discrepancy between the potential given by the potentiostat and the true potential at the electrode surface, due to an ohmic drop through the access resistance. The EIS frequency range was between 1 Hz and 100 kHz to provide information on both capacitive and reactive electrode behaviour (a few more advanced tests used smaller frequencies), and a 5 mV input sine wave amplitude required to have a reliable linear approximation of the impedance. To make sure the interface was at a rest state between tests, the potential was left to stabilise during long (typically > 600 s) OCP measurements. The duration required for the electrode potential to stabilise between the tests was determined empirically.

3.2.3 Full experimental protocol

The complete experimental protocol repeated for all the studies in this work consists in a combination of pulsing tests and electrochemical characterisation tests. A three-electrode setup was used with a 5 mm diameter Pt disc working electrode (WE) (Pine Research Wavevortex E6R1PK), a silver-silver chloride reference electrode (RE) and a carbon rod (3 mm diameter) counter electrode (CE). Where alternative WEs were used this is specified. RE and CE were rinsed with deionized water (DIW) before and after experiments, while WE was wiped clean with acetone, then with isopropyl alcohol to enhance surface wetting before being placed in solution in a Pine Research cell (AKCELL3). The connections to the electrodes are represented in appendix A figure 1.3: the electrodes were connected to the PCB delivering the pulse trains and to the potentiostat (Gamry Reference 600+) for electrochemical characterisation. The connections were swapped between the PCB and the potentiostat (PS) using a custom-made switchboard, which allowed the electrodes to be connected to either device, or to both at the same time (see 3.4.1).

A test sequence was defined and coded on the potentiostat to ensure repeatability and interface stability. The following whole sequence was applied before and after pulsing trains: OCP for 30 minutes, EIS, OCP for 2 minutes, CV (30 cycles), OCP for 15 minutes, EIS, OCP for 2 minutes. At the end of the sequence, data files were saved, and the electrode connections were swapped to the PCB to apply the pulse train. At the end of the pulsing test, the electrode connections were swapped back to the potentiostat and the electrochemical test sequence was repeated.

3.2.4 Data analysis

Two data streams were collected during experiments: oscilloscope data for the pulse trains and potentiostat data for the electrochemical characterisation. All data were analysed using custom Matlab scripts (MathWorks, versions R2020a through R2023b). Oscilloscope data consisted of the first pulse and the 1000^{th} pulse, which consisted of the voltage at both ends of the current

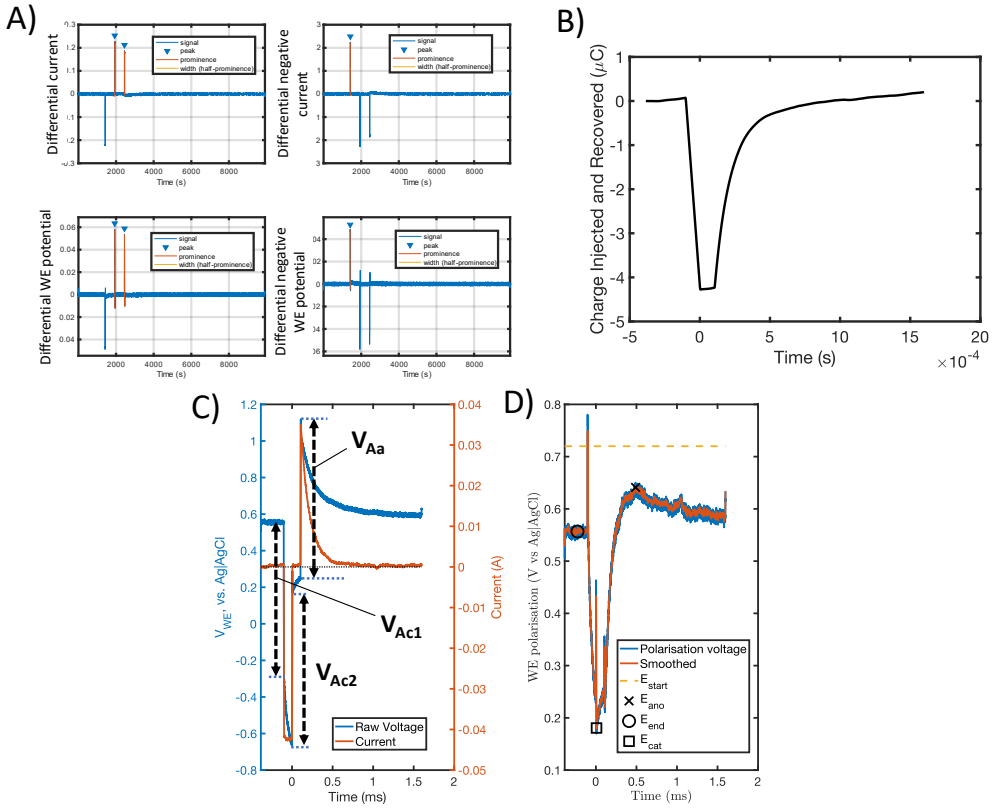

Figure 3.5: *A. Peak detection algorithm, peaks are indicated with blue arrows. B. Cumulative injected charge plot over both phases. C. Raw potential and current waveforms with access voltages indicated at the cathodic phase start (V_{Ac1}), cathodic phase end (V_{Ac2}), and anodic phase start (V_{Aa}). D. Polarisation trace after ohmic correction with key potentials indicated: E_{start}, E_{ano}, E_{end}, E_{cat}.*

measurement resistor and the WE voltage vs RE through the differential probe. A MATLAB script was used to extract the first and last pulse waveforms and calculate the starting potential (E_{start}), the end potential (E_{end}) and the polarisation potentials (E_{ano} and E_{cat}). The waveforms (current and voltage) were directly extracted and plotted after a smoothing (20 pts moving average in a 10000-point oscilloscope trace) for visual assessment, and E_{start} and E_{end} were automatically calculated as the average potentials in the first points of the first and last pulses, see E_{end} in figure 3.5 D). The polarisations refer to the electrode potential from which the ohmic drop generated by current flow is removed, to access the "true" electrode potential. A peak finding algorithm was used to automatically detect phase switches (Fig. 3.5 A), where the ohmic

drops would be calculated (Fig. 3.5 C) to obtain the polarisations. E_{cat} was recorded as the first potential value during the interphase period (Fig. 3.5 D): as the polarisation is a continuous function of time, the extreme polarisation value (last value) during the cathodic phase is equal to the first interphase value, and because there is no current flow in the interphase, no ohmic correction is necessary, avoiding a hypothetical measurement error introduction. The anodic polarisation was obtained by subtracting $R_A.I$ from the raw voltage measurement, as the current during the anodic phase is not constant, therefore, neither is the ohmic drop. The maximal anodic polarisation occurred away from the anodic phase onset (Fig. 3.5 D), so there was minimal impact of artefacts; however, the accuracy of the ohmic correction depends upon noise level in the current waveform: 1 mA P-P noise multiplied by $\approx$ 50 Ω access resistance would yield a variability of 50 mV, which is significant compared to the range of potentials that were measured. However, the variability of results proved to be well under that value, at an acceptable range (see 3.3.2). Figure 3.5 B shows the cumulative charge plot used to assess charge balance at the 1000^{th} pulse by cumulatively integrating current with time.

The second data stream consisted of the electrochemical characterisation files from the potentiostat (Fig. 3.6). EIS and CV (10^{th} cycle) were compared before and after pulse trains to determine whether pulse trains induced an unrecovered change in the interface. OCP plots were produced and a few selected values were compared throughout the experiment to evaluate interface stability: the first value of the OCP immediately after pulsing (Fig. 3.6 A), gauging the interface state immediately after pulsing, the last value of the OCP immediately after pulsing (Fig. 3.6 A), showing the stabilised OCP, and the last OCP before pulsing (Fig. 3.6 G), gauging the stability of the interface after the conditioning process.

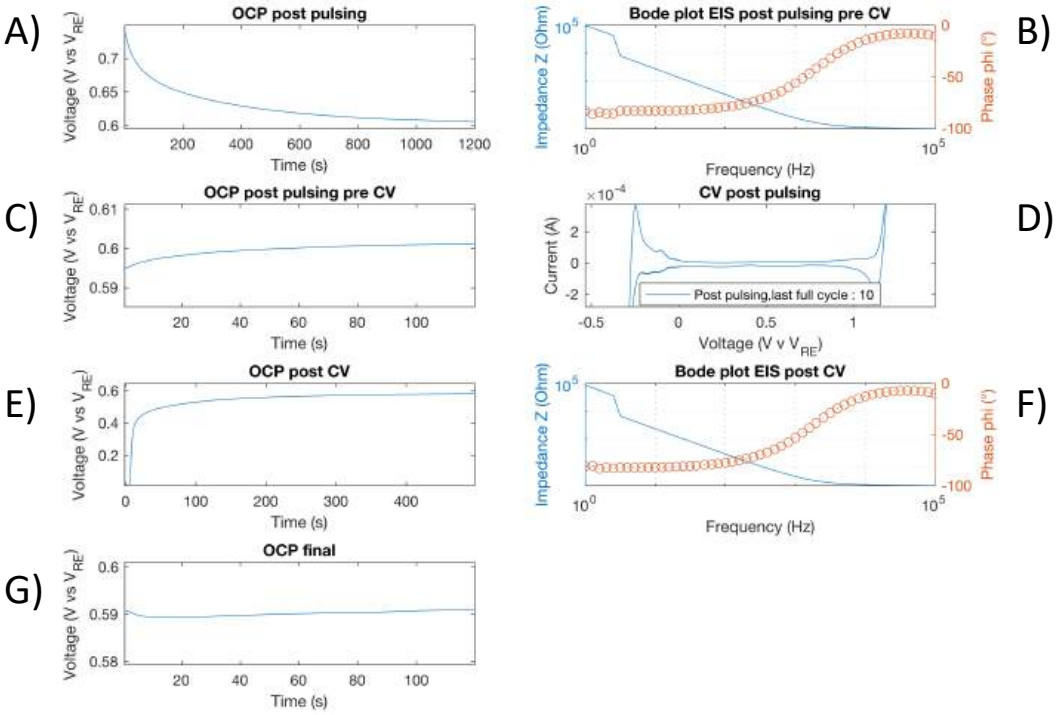

Figure 3.6: *Example of all generated plots from the potentiostat data: A. OCP post pulsing B. First EIS scan C. Short stabilisation OCP before CV D. CV E. Stabilisation OCP after CV F. Second EIS scan G. Short stabilisation OCP before CV.*

3.3 Experimental setup characterisation

Before engaging in experiments, the accuracy of the whole system was assessed to account for possible offsets, drifts and error margins. The electrochemical setup was characterised with two tests: RE potential stability over time (passive) and RE measurement accuracy on a well-known redox couple. Then, the repeatability of electrode potential measurements during pulses was assessed by repeating measurements in two electrolytes, see section 3.3.2.

3.3.1 Characterisation of the electrochemical setup

RE stability

RE potential stability over time was assessed against a master Ag|AgCl reference electrode by measuring the OCP evolution over ten minutes in PBS (Fig. 3.7 A.). The absolute potential difference was minimal (1.5 mV) and there was a slight drift over time of 0.1 μV/s which is acceptable.

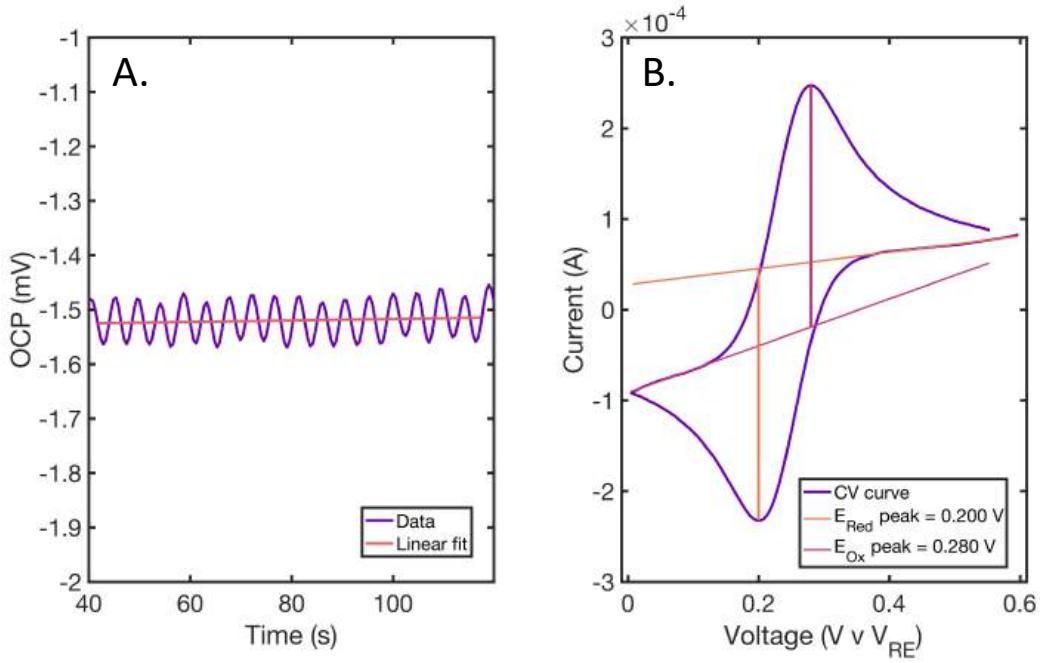

Figure 3.7: *A. OCP of the silver-silver chloride (Ag|AgCl) reference electrode against a master (Ag|AgCl) electrode. B. Cyclic voltammogram of the ferrocyanide/ferricyanide redox couple at 100 $mV.s^{-1}$. Peak potentials are indicated with the baseline current corrections (true peak currents are not relevant here).*

Ferrocyanide CV

Second, cyclic voltammetry was performed on a redox couple with a well-known fully reversible reaction to check whether potentials were accurately recorded. The ferrocyanide-ferricyanide meets all these requirements and has the advantage of being a single electron transfer reaction according to equation 3.1. A solution of ferrocyanide (10 mM $K_3Fe(CN)_6$, 20 mM $K_4Fe(CN)_6$, 0.1 M Na_2SO_4) was used and CV was conducted at a scan rate of 100 mV/s, scan rate to be used in future experiments (Fig. 3.7 B.).

$$[Fe(CN)_6]^{4-} \Leftrightarrow [Fe(CN)_6]^{3-} + e^- \tag{3.1}$$

In the literature, the half-cell potential of the ferrocyanide couple was reported at 0.403 V vs NHE at 25°C [O'Reilly, 1973], which translates to 0.204 mV vs Ag|AgCl in the present system (saturated, room temperature). The peak potentials were calculated using a peak finding algorithm on Matlab,

giving the values of 0.2 V and 0.28 V vs Ag|AgCl, hence a half-cell potential of 0.24 V. Correcting for the RE imprecision of 1.5 mV, the half-cell potential is estimated at 0.238 V vs Ag|AgCl, which is 36 mV away from the literature value. The discrepancy may be due to some electrode surface oxidation or to the fact that the solution was not equimolar between both species. A peak separation of 59 mV is expected in theory for this fully reversible system, however, in practice it behaves as a quasi-reversible system, hence more separation. Here, I report a peak separation of 80 mV, which may be due to some surface oxidation as well or non-ideal potentiostat properties, as potential step may affect peak potential readings. The scan rate may also affect the peak potentials slightly.

3.3.2 Characterisation of the stimulator and full protocol

The characterisation of the stimulation setup could only be completed after determining the stability of the electrochemical characterisation protocol as the reading of potential traces depends equally on the interface's stability [Doering et al., 2023]. A repeatability testing protocol was designed and performed in two electrolytes: PBS and isotonic saline (0.9%w NaCl). The repeatability was assessed for two k-values, 1.25 and 1.75, in the same solution (consecutive tests separated by a reconditioning but electrodes not removed) and between different pours from the same solution batch. Therefore, solutions 2, 3, and 4 in figures 3.8 and 3.9 are not different from solution 1, but the electrodes have been taken out, rinsed, and a new solution was poured from the same stock. The efficiency of the reconditioning protocol was also assessed by comparing a full reconditioning protocol versus a simple OCP stabilisation test: after electrode conditioning, three pulse trains were applied consecutively, separated by a 600 s OCP measurement to stabilise the interface. Therefore, between conditioning steps, each "run" comprised three tests separated by OCP measurements. Figures 3.8 to 3.10 represent the results obtained in PBS, results in NaCl are not shown.

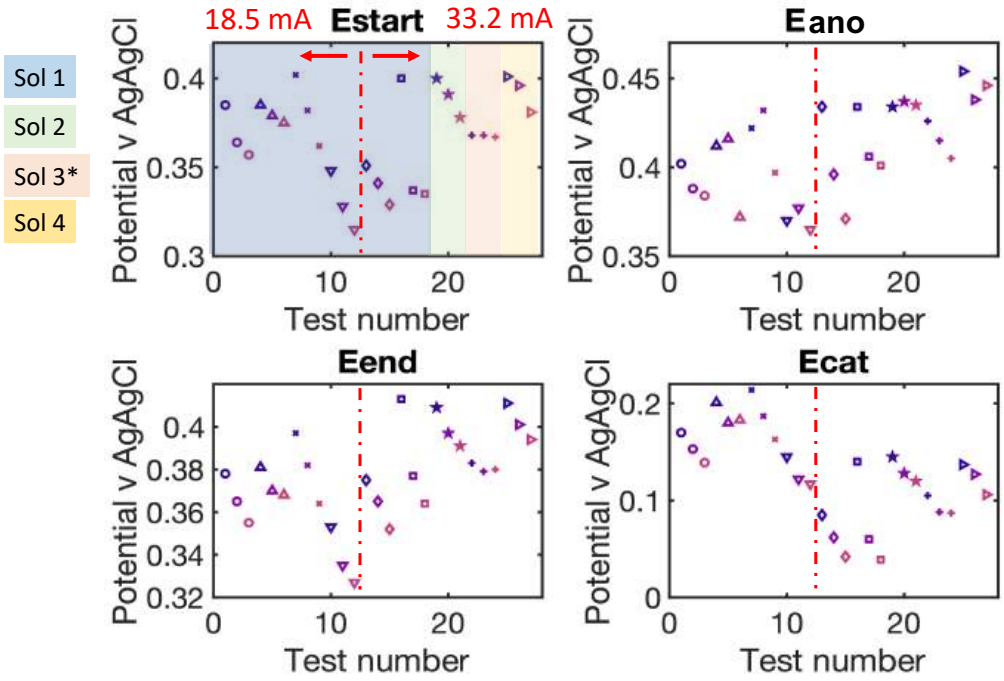

Figure 3.8: *Raw potential measurements in PBS for E_{start}, E_{ano}, E_{end}, and E_{cat} separated in eight runs of three tests each. Runs are distinguished by the markers and tests by the colours of the markers. Different solution pours are indicated by a background colour on the E_{start} plot, and the change in k-value is indicated by a red dotted line. * Solution 3 had two unsuccessful tests prior to the three tests shown on the plot.*

Within each run, the measured potentials decreased at each test, showing that OCP stabilisation alone does not allow for repeatable measurements. The first measurement of each run was consistent, suggesting the conditioning protocol achieved a reproducible interface state. Three runs had unusual values (runs 4, 5 and 8) due to experimental inconsistencies (soaking overnight or improper conditioning), therefore these runs were considered as outliers. Overall, all potentials showed a similar pattern to E_{start}, indicating that the observed variability depends majoritarily on E_{start}, which was tested in figure 3.9 by subtracting E_{start}.

The values were more compact after the subtraction of E_{start}, especially within runs; the three tests did not present the typical decrease observed in raw potentials, suggesting that the discrepancy was due to a general shift of the base potential but the excursions remained similar. The reduction of the discrep-

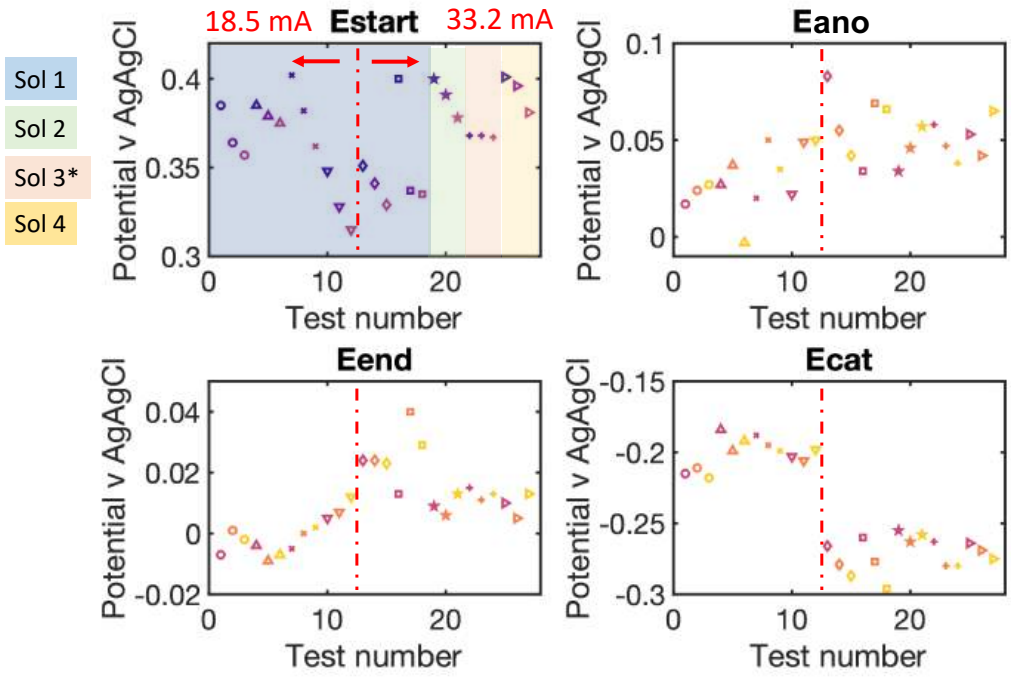

Figure 3.9: *Potential measurements in PBS for E_{ano}, E_{end}, and E_{cat} corrected for E_{start}. Runs are distinguished by the markers and tests by the colours of the markers. Different solution pours are indicated by a background colour on the E_{start} plot, and the change in k-value is indicated by a red dotted line. * Solution 3 had two unsuccessful tests prior to the three tests shown on the plot.*

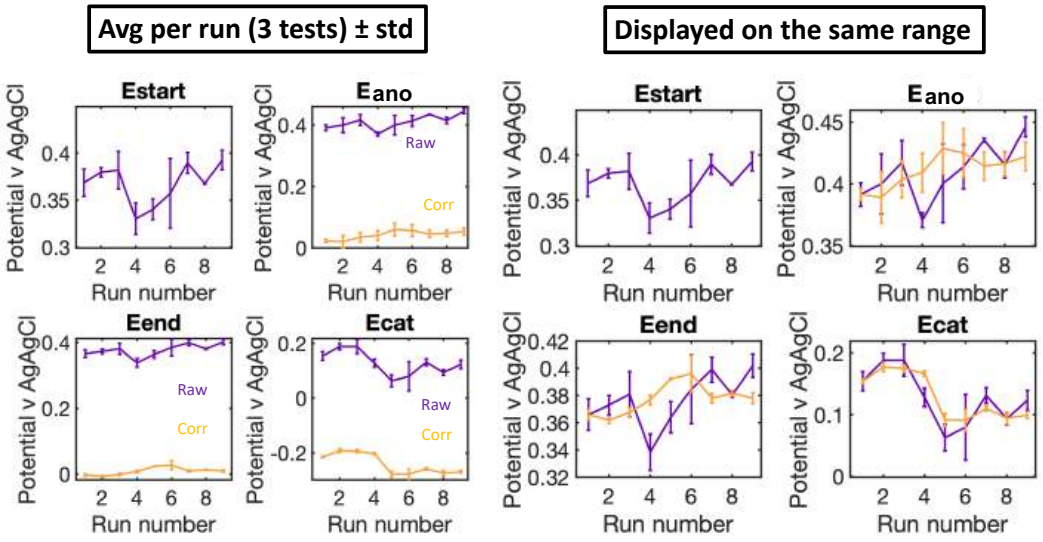

Figure 3.10: *Comparison of the average ± std per run (3 tests) for raw versus corrected potentials in PBS(E_{start} subtraction). Potentials were reported on the same scale on the four figures on the right for better comparison.*

ancy within runs and between runs is shown more emphatically in figure 3.10, where the error bars indicating standard deviation within runs decreased after correction for E_{start}. Although the variability did not vary for E_{ano}, reductions of variability were observed for E_{end} and E_{cat} (Table 3.3). Furthermore, a clear difference emerged between the two k-values as E_{ano} and E_{end} were larger for the larger k and E_{cat} was significantly lower ($\approx$ 80 mV difference). A statistical similarity test (two-sample Kolmogorov-Smirnov test) was performed between the $k = 1.25$ and $k = 1.75$ samples before and after correction for E_{start}, and E_{ano} and E_{end} became statistically different after correction while E_{cat} was significantly different in both instances. In experiments, the measurement that will be analysed is the first test of each run, therefore, the variability between first tests was also assessed before and after correction for E_{start}, and the same conclusions prevailed: the variability in E_{ano} remained the same (17.1 mV after correction vs 11.5 before, for which two values were identical, constituting a statistical anomaly), and E_{end} and E_{cat} variability decreased, respectively from 19.7 mV to 5.3 mV and from 29.4 mV to 7.5 mV.

In isotonic saline, the repeatability results were similar: the three tests of each run showed a potential decrease, which was mainly due to a decrease in E_{start}, and values were more compact after subtraction of E_{start}, identifying trends more clearly, although the potentials measured for the two k-values were statistically different already before correction. The variability was reduced by subtracting E_{start} in a similar way to PBS data (Table 3.3). Variability on the first test of each run decreased for all potentials: from 15.7 mV to 9.6 mV for E_{ano}, from 13.9 mV to 6.9 mV for E_{end}, and from 12.5 mV to 4.9 mV for E_{cat}.

Therefore, the measured potential excursions demonstrated to be reasonably repeatable, with most of the variability stemming from variability in E_{start} attributed to the interface state variability following conditioning. The calculated polarisations proved to be accurate, especially for E_{cat}. The constant variability in E_{ano} can be attributed to the calculation method, using an RI subtraction to account for the access voltage, which was prone to noise, how-

Table 3.3: *Standard deviation of the four potentials of interest in PBS and NaCl before and after subtraction of E_{start}.*

	PBS		
	E_{ano}	E_{end}	E_{cat}
Before correction (mV)	14.2	11.7	20.1
After correction (mV)	14.5	4.2	7.6
	First test		
Before correction (mV)	11.5	19.7	29.4
After correction (mV)	17.9	5.3	7.5
	NaCl		
Before correction (mV)	14.2	12.9	22.5
After correction (mV)	10.6	4.3	8.0
	First test		
Before correction (mV)	15.7	13.9	12.5
After correction (mV)	9.6	6.9	4.9

ever, the variability levels were below half of the theoretical variability due to noise levels calculated earlier ($\approx$ 50 mV theoretically vs 17 mV experimentally). Therefore, the analysis protocol and measuring instrumentation were validated through these tests. The conditioning protocol was also validated as the variability in E_{start} was reduced from 20.5 mV on all tests to 8.2 mV on the first test of each run (Runs 4, 5 and 8 excluded for previously mentioned reasons) for PBS and marginally for NaCl from 19.4 mV to 15.6 mV. The present results also established that the variability from different pours of the same stock solution was equivalent to the variability when using the same solution, demonstrating that inter-experiment repeatability was equivalent to intra-experiment (different k-values) repeatability.

3.4 Adjustments to improve robustness and accuracy

3.4.1 Measurement of OCP during connection swaps

During experiments, the last recorded OCP on the potentiostat at the end of the conditioning sequence and the OCP recorded on the oscilloscope before the pulses differed, although no current is expected to flow during the connection switch as both circuits are open. To assess which potential measurement

to use for further analysis, the potential was monitored while connecting the electrodes to the PCB and disconnecting the electrodes from the potentiostat. Initially, the connections were swapped manually by unplugging the electrode leads from the potentiostat connections and plugging the PCB and differential probe on; however, this protocol was not reproducible enough, took a few seconds during which the potential could change, and was prone to bad connections. To allow a quick and safe connection switch, I introduced two double-throw toggle switches between electrode leads and potentiostat on one switch (second throw open circuit) and PCB on the other switch (second throw open circuit) as shown in appendix A figure 1.3. This way, I was able to have either side connected separately but also both connected or disconnected from the electrodes.

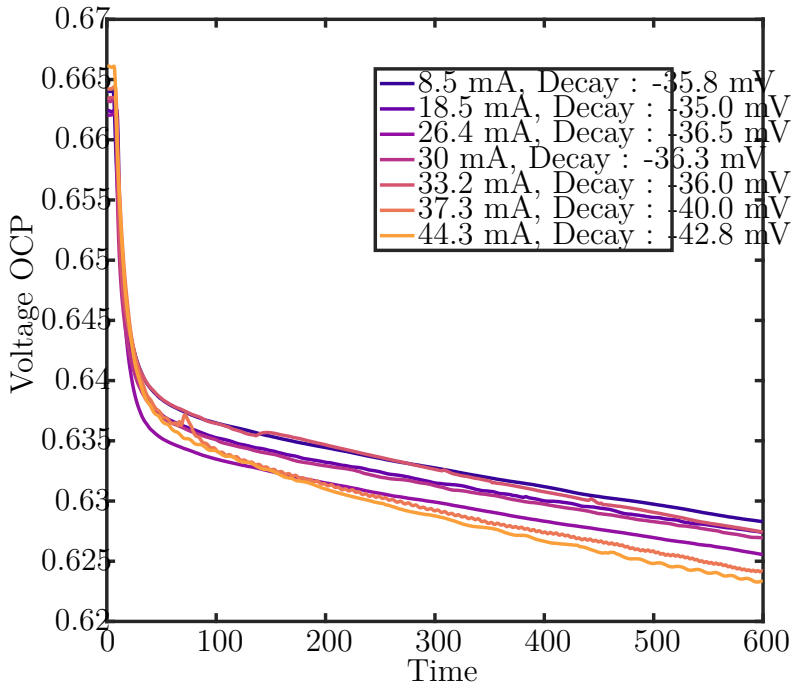

Figure 3.11: *Example of connection OCPs for each k-values in pH 1 sulfuric acid.*

To record the change in potential during the connection swap, the electrodes would remain connected to the potentiostat after a conditioning sequence, and an OCP measurement was performed. After a few seconds (typically 5 s), the

second switch was flipped to connect the electrodes to the PCB. The potential decayed upon connecting the electrodes to the PCB and stabilised after typically less than 5 minutes, however, the OCP measurement was performed for 10 minutes systematically, see figure 3.11. The magnitude of the decay varied between electrolytes but tended to be consistent within experiments, with an initial rapid decay (30 mV in $\approx$ 15 s, 2 mV/s in figure 3.11) followed by a slow linear decay ($<$ 0.02 mV/s in figure 3.11). Disconnecting the potentiostat did not change the potential measured on the oscilloscope. To unify potential measurements, the end value of this connection OCP was considered as the starting potential for the pulsing train. The connection OCP is a different quantity from E_{start}, which was measured at the beginning of the first pulse. The reason for the discrepancy is explained below.

3.4.2 Measurement of passive decay during pulses

Assuming a stable potential or potential ratcheting in either direction, E_{ano}, E_{end} and E_{cat} were expected to be slightly higher or lower than E_{start}, and the discrepancy was expected to increase with increasing k, however, E_{ano}, E_{end} and E_{cat} were substantially lower than E_{start} systematically, outside of the expected reactions regions. Moreover, E_{start} was substantially different than the connection OCP, hinting that the measured potential changed between the disconnection of the potentiostat and the first pulse. However, the evolution of E_{ano}, E_{end} and E_{cat} after E_{start} was subtracted was as expected with some potential ratcheting and E_{ano} and E_{cat} generally increasing with k. Therefore, only E_{start} needed to be understood and corrected for.

The evolution of potential during a pulsing test was recorded over a large timescale (s range instead of 100 μs) on the oscilloscope (Fig.3.12). An instantaneous drop in potential upon +30 V supply switching was observed, followed by a constant rate decay until switched off. The ohmic drop would be recovered quickly and the potential would return to its original value. Both potential drop and potential decay were measured after all k-value pulse trains in a separate measurement, which was performed after the final conditioning

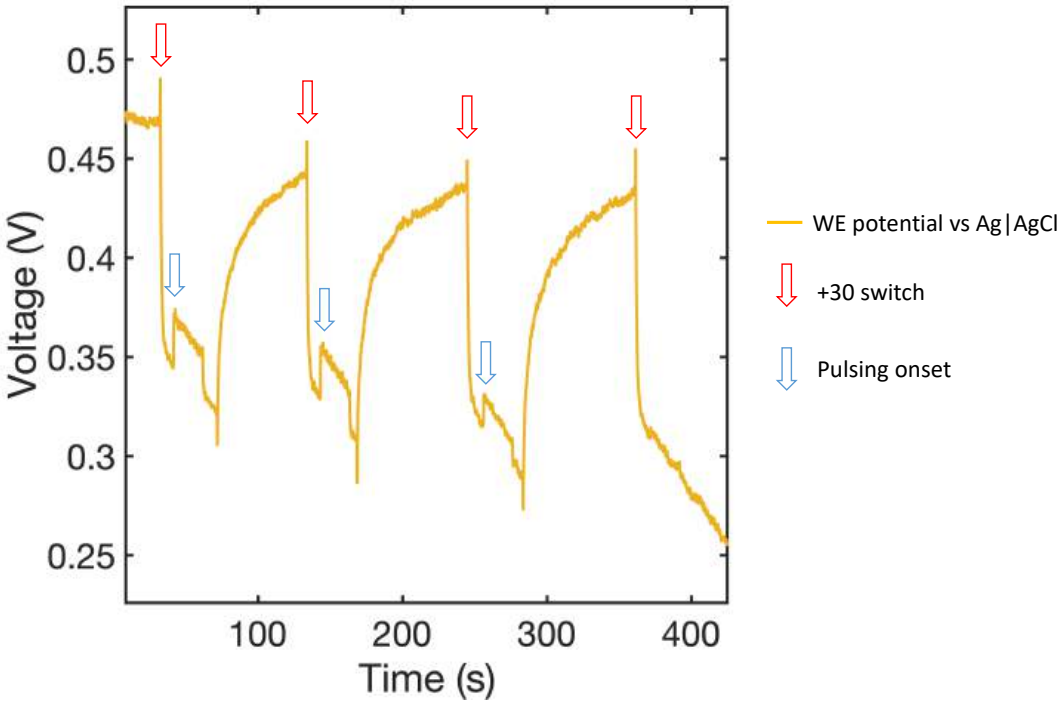

Figure 3.12: *Example of the observed decay of the working electrode potential when switching the +30 V supply on (red arrows). Pulse trains were applied as well (blue arrows), which showed a smaller ohmic drop (positive) than the +30 V switching.*

sequence. During the pulsing tests, the time between switching the +30 V supply on and the first pulse, and the potential variation at these time points were measured for correction. As shown in figure 3.12, the ohmic drop and the decay showed to be repeatable (apparent discrepancy attributed to the discrepancy in potential before +30 V switching) and the potential proved to recover from the decay over time. It was established that in the time frame of the pulsing tests, the decay was linear; the linear rate was determined and added to the last pulse potentials for correction. The ohmic drop was not factored in as it does not represent electrode polarisation and E_{start} was measured

after the drop. The final potentials of interest were calculated as such:

$$E_{start,corr} = E_{OCP-connect} \tag{3.2}$$

$$E_{peak,corr} = E_{peak} - E_{start} + \Delta E_{decay} + E_{start,corr} \tag{3.3}$$

$$E_{end,corr} = E_{end} - E_{start} + \Delta E_{decay} + E_{start,corr} \tag{3.4}$$

$$E_{cat,corr} = E_{cat} - E_{start} + \Delta E_{decay} + E_{start,corr} \tag{3.5}$$

The stimulator circuit was modified to suppress the potential decay, however, the new architecture created a few additional problems, therefore, it was not kept. The investigation and adjustments are detailed in appendix A.

3.4.3 Shorter optimised protocols

To have a more efficient and concentrated protocol, redundant steps among the electrochemical tests were discarded. First, EIS before CV and the following OCP were removed, as it was observed that both EIS were consistent (Fig. 3.13 A.). Second, the number of CV cycles was reduced to 10, as the voltammograms consistently stabilised within the first 3 cycles (Fig. 3.13 B.). The total time of the electrochemical protocol was reduced by a third, without losing any information.

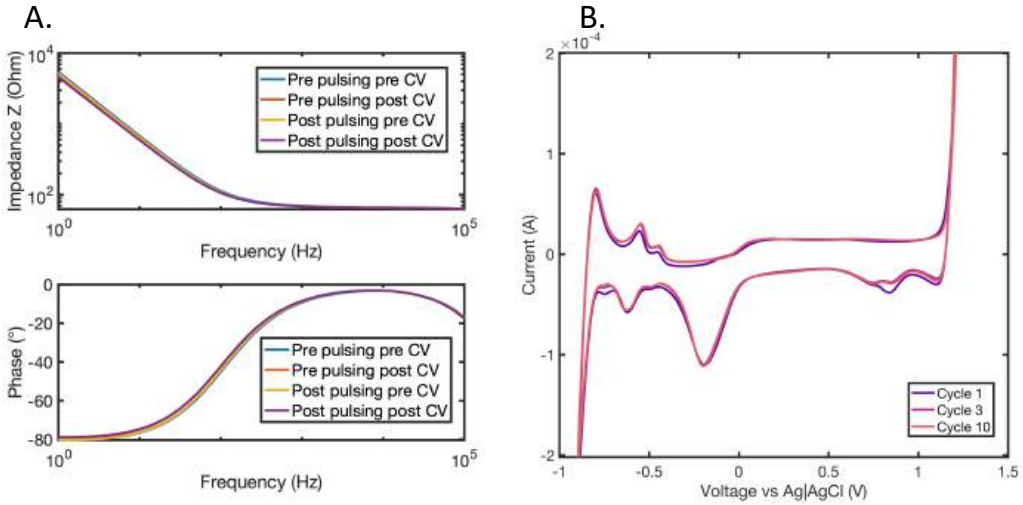

Figure 3.13: *A. Comparison of EIS scans before and after CV, before and after 1000 pulses and a full conditioning sequence. B. Comparison of the first, third and tenth CV cycles in PBS.*

3.5 Summary

This chapter describes the design process of a reliable experimental setup and repeatable protocol to achieve a controlled electrode state before pulses and accurate potential measurement during biphasic pulses. The custom stimulator was shown to deliver the required waveform with adjustable current magnitude, although an inherent charge imbalance was detected. A potential decay, which is attributed to a small current leakage, was also detected, however, a reliable correction method was found. The cleaning and conditioning protocol was shown to achieve a repeatable interface, as indicated by the repeatable potential measurements.

Chapter 4

Effects of electrode design

The distribution of charge transfer at an electrode is dependent on electrode design. The current density at the electrode surface was shown to be higher at the high-curvature areas of the electrode, e.g. the perimeter for circular electrodes or the tip of needle electrodes [Swiontek et al., 1980, McIntyre and Grill, 2001]. Richardot and McAdams [2002] established that the non-uniformities were mainly due to the non-linear charge-transfer resistance. Non-uniform current density and charge-transfer resistance result in non-uniform charge transfer leading to local polarisation gradients. Therefore, potential gradients arise at the high-curvature areas, which may further change the charge-injection regime, favouring charge-injection mechanisms that may be harmful, for example by inducing large pH swings [Ballestrasse et al., 1985]. The non-uniform current distribution occurs at lower potential thresholds for larger electrodes and increases with potential and frequency [Cantrell et al., 2007, Ghazavi and Cogan, 2018], making macro-electrodes more likely to present non-uniform current density distributions. Non-uniformities alter reaction rates and may modify the charge injection behaviour by entering diffusion-limited regimes faster [Fan et al., 2021, Green et al., 2012b]. Electrode degradation profiles have been found to correspond with current distribution non-uniformity [Nagashima et al., 2019], and dissolved Pt was shown to possibly occasion damage *in vivo* with necrosis and increase FBR [Cogan et al., 2016, Nadol Jr et al., 2014, Shepherd et al., 2019] (see 1.3.3.2).

Some electrodes have been designed to deliberately create non-uniform current density profiles for more efficient stimulation: electrodes with large perimeters or sharp-edges designs activate neurons at lower stimulation thresholds due to the higher current density at high-curvature areas [Ghazavi et al., 2013, Wei and Grill, 2009]. In particular, a larger perimeter to surface area ratio increases stimulation efficiency [Ghazavi et al., 2015, Park et al., 2018]. Alternatively, one can reduce charge distribution non-uniformities to have a more controlled charge injection. Recessed electrodes present a more uniform current density and lower peak currents at the electrode surface, increasing the safe charge-injection capacity [Rubinstein et al., 1987, Ksienski, 1992, Suesserman et al., 1991].

This chapter investigates the effects of electrode design on the charge injection behaviour of Pt electrodes. First, the effect of a recessed electrode is investigated: a recess represents an electrode which is not co-planar with an insulating surface but is present at the base of a concave recess, see figure 4.1. This study of recessed electrodes was motivated by prospective custom electrode designs comprising recesses, to anticipate charge injection discrepancies and allow comparisons with planar non-recessed electrodes. The effects of an insulating recess on the current density distribution around the electrode were studied in a computational study, comparing different recess shapes and dimensions.

Second, the role of electrode size is investigated to characterise the transition in damage limit from Shannon's limit for macroelectrodes (cm range) to a maximal charge density of 4 $mC.cm^{-2}$ for microelectrodes [McCreery et al., 2010]. A custom small-diameter electrode was fabricated and the charge injection behaviour during biphasic pulses was assessed in various electrolytes and compared to a 5-mm diameter electrode.

Third, the role of electrode shape, namely the ratio of electrode perimeter to electrode surface area, was investigated to separate the contribution of edge effect and electrode bulk in charge transfer. A custom large aspect ratio (AR)

electrode was fabricated and compared to the 5-mm diameter disc electrode in various electrolytes. The large AR electrode was further used in the investigation of electrolyte composition effects on charge injection, which results are presented in the corresponding chapter 6.

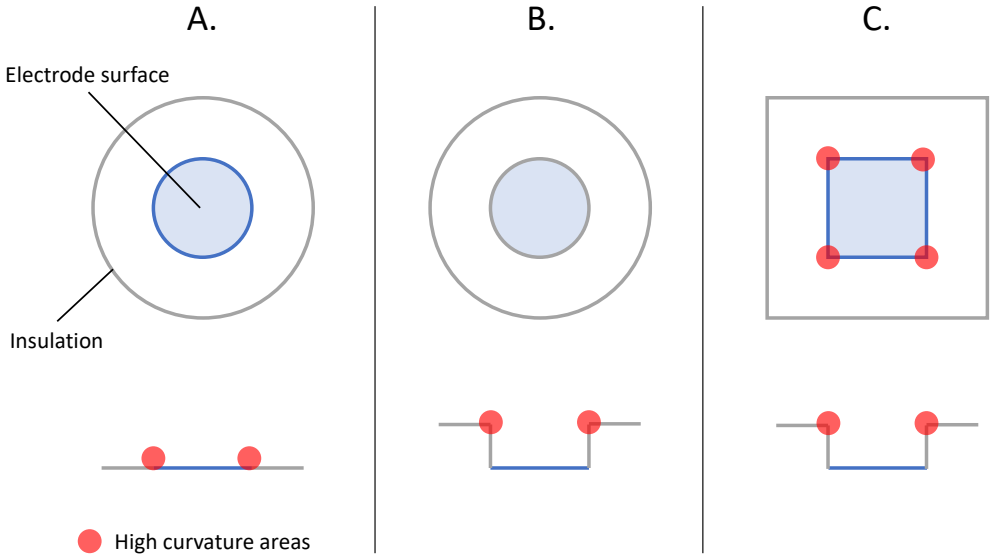

Figure 4.1: *Schematic of various electrode designs studied in this chapter, with areas of high electric field line curvature. A. Co-planar disc electrode (5-mm diameter disc electrode), B. recessed disc electrode (1-mm diameter disc electrode), C. recessed square electrode (similar to large AR electrode).*

4.1 Effect of an insulating recess on current density distribution

The results presented in this section were presented in a poster at the International Society of Electrochemistry (ISE) 71st Annual Meeting (Sept. 2020).

4.1.1 Rationale for studying recessed electrodes

The investigation of the effect of recessed electrodes on charge injection was a preliminary study to prepare for the investigation of electrode size and electrode shape: the study of electrode size and shape required the manufacture of a custom electrode design, which would involve a recess, as co-planar electrodes require high-precision machinery to manufacture. The designs involved

a layer of ceramic (insulation, up to 500 μm thickness) positioned on top of the electrode surface, which would disturb the current density at different strengths depending on the electrode dimensions. Therefore, a preliminary computational study was conducted to quantify the non-uniformities and the influence of the recess. Several recess geometries were considered, including cylindrical (tubular) well, conical recess, and exponential recess, as Suesserman et al. [1991] suggested each configuration had its own advantages, with the tubular well yielding the most uniform current density at the electrode surface, the conical recess yielding the most uniform current density at the recess opening, and the exponential recess having a "directed" current density distribution with higher current density at the electrode centre. The quantification of the current density magnitude discrepancies enabled me to choose the most appropriate recess type, and to predict the changes in charge injection behaviour due to the recess. As the electrode dimensions varied, the current density distributions of three recess aspect ratios were studied as well as the influence of varying dimensions (electrode diameter and recess depth).

4.1.2 Methods

To evaluate the effect of a recess on the charge-injection behaviour of Pt disc electrodes, a preliminary stimulation study was conducted on COMSOL Multiphysics 5.4 (2019). Three types of recess were modelled: tubular, conical, and exponential (Fig. 4.2), with various depths (0.1 mm to 5 mm) and several electrode diameters (0.1 mm to 5 mm). The conical recess had a default angle of 45°, equivalent to the standard achievable chamfer in a machining process, and the effect of recess angle was studied independently. The exponential recess was designed to end at the same width as the conical recess following the formula presented in Eq. 4.1, where r represents the radial coordinate and z the height. The main parameter of interest was the aspect ratio (AR) of the recess, defined as the ratio of recess depth (d) to electrode diameter: $AR = \frac{d}{2R_e}$, with R_e the electrode radius. The individual effects of varying the radius and

depth were also studied at constant AR.

$$r = R_e\, e^{\frac{z}{d} ln(\frac{R_e+d}{R_e})} \tag{4.1}$$

Modelling was performed using the COMSOL Electrochemistry module studying the primary and secondary current distributions in the electrolyte, and the tertiary current distribution was briefly investigated. The primary current distribution considers the distribution at equilibrium with infinite reaction kinetics (electrode potential = electrolyte potential) based on Ohm's law and charge balance, the secondary current distribution addresses the changes with finite electrode reaction kinetics, introducing activation overpotentials governed by Butler-Volmer (1.2) or Tafel (1.5 and 1.4) models, and the tertiary current distribution encompasses chemical reactions and concentration-dependent (Nernst-Planck equation 4.5) electrode polarisation. In order to simplify the computations, a two-dimensional axisymmetric geometry was considered: the electrode was considered rotationally symmetric around its centre with solutions given for a radial section from the electrode centre. Pt was the material used for the electrode surface, Teflon for the electrode body (recess) and a custom material representing saline (conductivity $\sigma = 0.555\ S.m^{-1}$) for the electrolyte. The equations used to solve the problem were defined as follows, with the index x indicating either the electrode (s) or the electrolyte (l), i is the electrical current density, Q is the charge transfer, σ is the electrical conductivity, ϕ_x is the electrochemical potential, E_{eq} is the equilibrium potential, c_i is the concentration of one ion "i", J_i is the molar flux relative to convective transport, u is the velocity vector, F is the Faraday constant (96495 C/mol), z_i is the ion's valence, D_i is the diffusion coefficient, $u_{m,i}$ is the ion's mobility, E_Ω is the potential on the boundary, and n is the normal

vector perpendicular to a boundary:

$$\text{Charge balance: } \nabla i_x = Q_x \tag{4.2}$$

$$\text{Ohm's law: } i_x = -\sigma_x \nabla \phi_x \tag{4.3}$$

$$\text{Secondary distribution: } \eta = \phi_s + \phi_l + E_{eq} \tag{4.4}$$

$$\text{Nernst-Planck equation: } i_l = F \sum_{i=1}^{n} (z_i - D_i \nabla c_i + z_i u_{m,i} F c_i \nabla \phi_l) \tag{4.5}$$

Boundary conditions:

$$\text{Dirichlet condition (Primary): } E_\Omega = E_{bnd} \tag{4.6}$$

$$\text{von Neumann condition (Secondary): } \int_{\partial\Omega} i_x.n\,dl = i_{average,x} \int_{\partial\Omega} dl \tag{4.7}$$

$$\text{Insulation: } -n.i_x = 0 \tag{4.8}$$

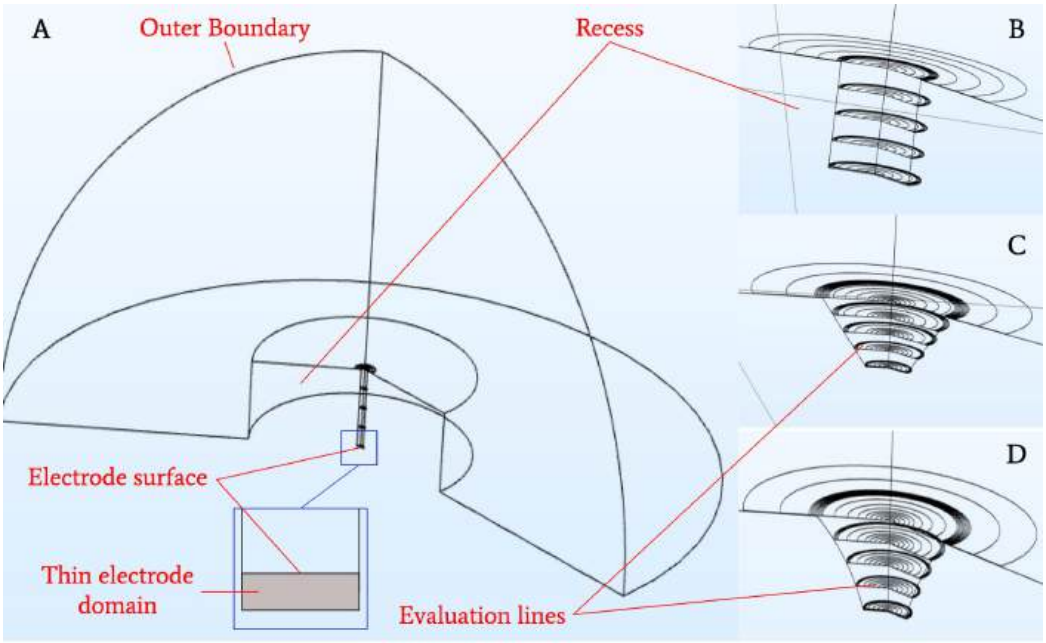

Figure 4.2: *Schematic of recess types studied in COMSOL Multiphysics. A (AR 10) and B (AR 1) represent the tubular recess, C shows the conical recess (AR 1) and D displays the exponential recess (AR 1).*

The Teflon surface (recess) was considered an insulator, meaning no current flow was allowed through the Teflon surface. Two control modes were used: current control and voltage control. In voltage control, the electrode potential

was set at a non-zero potential (boundary condition n°1) and the electrolyte potential at the spherical outer boundaries was set to 0 V (boundary condition n°2, Dirichlet condition), the outer boundary was considered to be sufficiently far away from the electrode surface to be considered as equipotential to a large surface area counter electrode. In current control, the electrode was represented by a thin domain (thickness 1% of electrode diameter, see fig 4.2). The first boundary condition was applied to the "bottom" of the thin electrode domain, set as a current density uniformly distributed across the boundary, while the electrode surface (in contact with the electrolyte) remained free of constraints. The current density was conserved through the electrode domain, yielding an average electrode-electrolyte current density equal to the boundary electrode current density, due to the high conductivity of Pt and the absence of leakage (perfect insulation). The second boundary condition (von Neumann, 4.7) was applied to the outer boundary, constraining the total current as the opposite polarity of what is emitted by the electrode, uniformly distributed across the boundary to satisfy von Neumann's equation (closed system without leakage and without current sources). A third boundary condition was applied to the outer boundary, setting it to 0 V, which was necessary to constrain the potential field. For the tertiary current distribution, the stoichiometric coefficients, the number of electrons exchanged in the reaction, and the initial concentrations were entered for each reaction.

The finite element mesh was composed of tetrahedral elements (triangles for 2-dimensional radial sections, see figure 4.3) with the element size automatically calculated in an adaptive setting, to have a finer calculation near the electrode surface, where the largest gradients were located. Most studies were stationary, i.e. at equilibrium, considering all quantities were independent of time, without transient regime. For time-dependent studies, a stimulation waveform (current or voltage) was created as a function of time and applied as boundary condition. The time step was chosen much smaller than the current step duration (100-fold) and arranged to be delayed from ascending and

falling current steps, which were prone to calculation errors. When several electrode dimensions (electrode diameter and recess depth) were compared, a parameter sweep was used, thereby calculating the current distribution for each parameter value sequentially.

Most results presented show the current density in response to a voltage input (voltage control), however, the current density profiles were similar in current control. The current density magnitude in the electrolyte was compared for each recess type at the electrode surface and at set points along the height of the recess, up to the open end of the recess (Fig. 4.4). The current density was normalised to the mean average current density along a cross-section of the recess, parallel to the electrode surface.

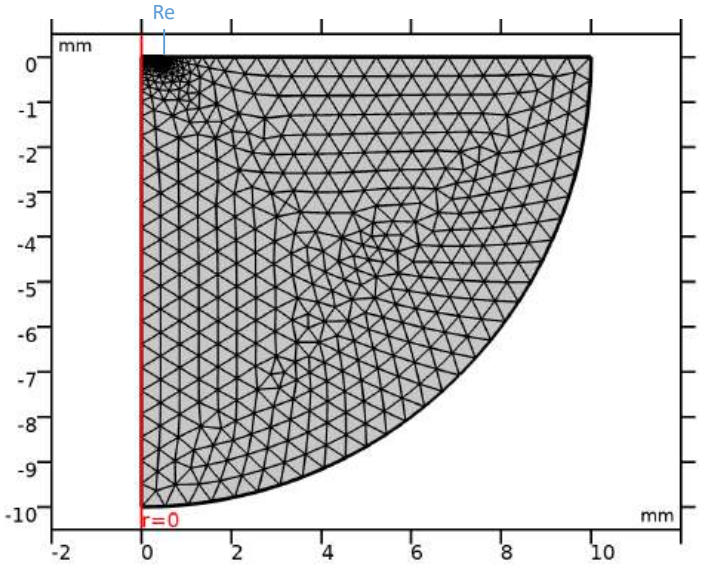

Figure 4.3: *Example adaptive tetrahedral mesh concentrating nodes close to the region of interest.*

4.1.3 Results

A non-recessed electrode presented a uniform current density near the centre, with a peak in current density at the electrode edge, because of a concentration of electric field lines of high curvature (Fig. 4.5). The current density at the edge was up to 16 times the current density at the electrode centre (Fig. 4.4 A), and the discrepancy between edge and centre increased with electrode diam-

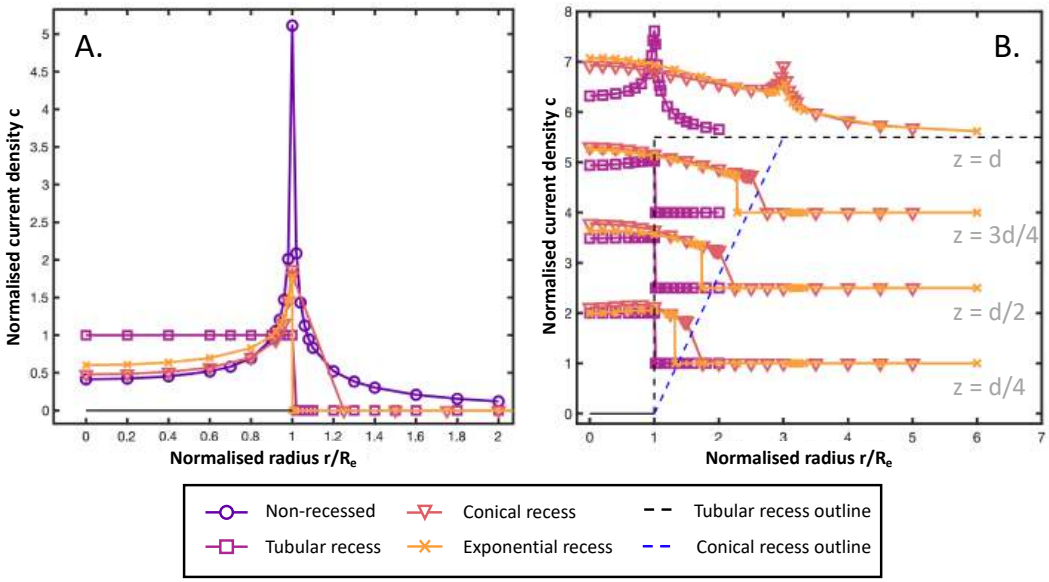

Figure 4.4: *A. Radial normalised current density profile at the electrode surface for all recess types at AR = 1. B. Evolution of the radial normalised current density profile along the recess for all recess types.*

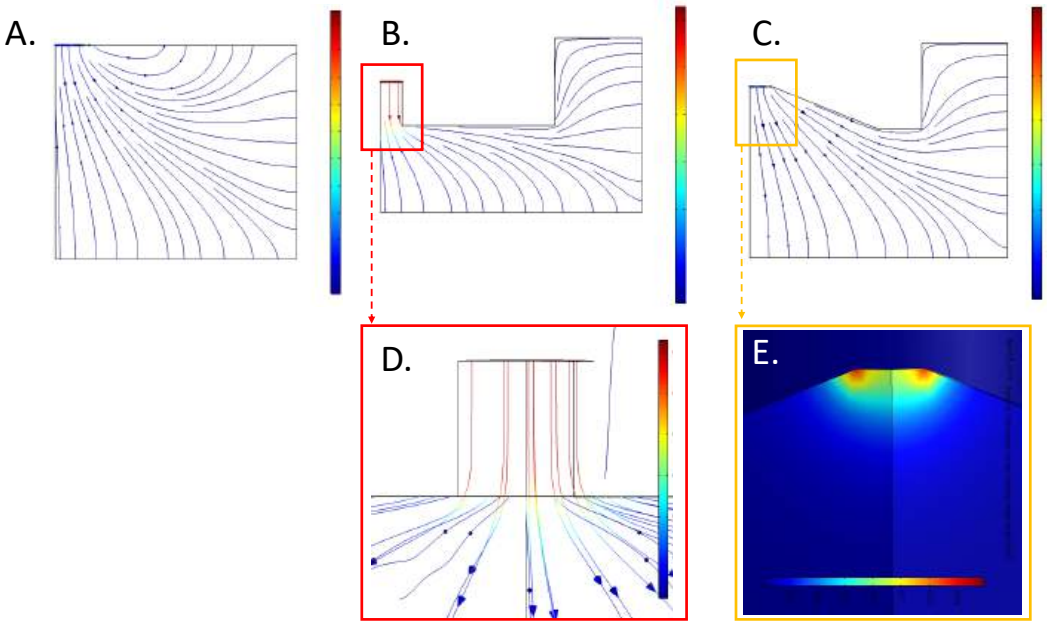

Figure 4.5: *Electric field lines at 1-mm diameter electrodes for A. non-recessed electrodes, B. tubular recess, and C. conical recess. D. represents a magnification of the field lines in the tubular recess and E. a magnification of the conical recess, represented as a heatmap.*

eter (not shown), showing that larger electrodes have larger non-uniformities. Recessed electrodes presented more uniform profiles at the electrode surface, especially the tubular recess, which showed a uniform electrode surface current density for an AR of 1. The conical and exponential recesses had a similar profile to the non-recessed electrodes, which can be explained by the similar curvature of field lines (Fig. 4.5 C), however, the peak current density was lower ($\approx$ 4 times the centre current density for conical and $\approx$ 3 times for exponential). Figure 4.4 B shows the evolution of the radial current density profile for each recess type along the height of the recess, with the profiles shifted vertically to show the geometrical evolution. The recess shapes are also displayed to locate non-uniformities geometrically. The current density profile remained uniform along the tubular recess, which was expected as the electric field lines remain parallel inside the recess (Fig. 4.5). Conical and exponential recesses had similar rounded profiles with a higher current density near the electrode centre. The transition from a higher current density at the edge to the centre is visible at a height of a fourth of the recess ($z = d/4$), where the largest current density was measured at $\approx 2/3$ of the radius. At the open end of the recess ($z = d$), all three recesses exhibited more non-uniformities: a peak in current density was measured above the recess edge, and the current density decreased rapidly away from the electrode. The tubular recess end had a similar profile to a non-recessed electrode, however, the peak current density was only 2.5 times larger than at the centre, showing a three times lower non-uniformity compared with a non-recessed electrode surface. The peak for the conical recess was about the same magnitude as the current density at the electrode centre, showing enhanced uniformity; the exponential recess showed a similar profile, with the peak being smaller than the current density at the electrode centre.

In absolute values, the current density remained constant along the tubular recess, then decreased slightly at the electrode centre at the recess end ($\approx$ 20% decrease) while the peak at the edge was 2 times larger than the current

density at the electrode surface. Therefore, the tubular recess showed uniform current density at the electrode surface and behaved as a non-recessed electrode at the end of the recess, with a reduced peak current density. On the conical and exponential recesses, the current density magnitude decreased along the recess. The central (r = 0) current density at the recess end was 3.6 times lower than the central current density at the electrode surface for the conical recess and 3.5 times lower for the exponential recess. Compared to the peak current at the electrode surface, the central current density was 13.4 times lower for the conical recess, which had a more uniform end-of-recess distribution, and 10 times lower for the exponential recess, which had a parabolic end-of-recess current density.

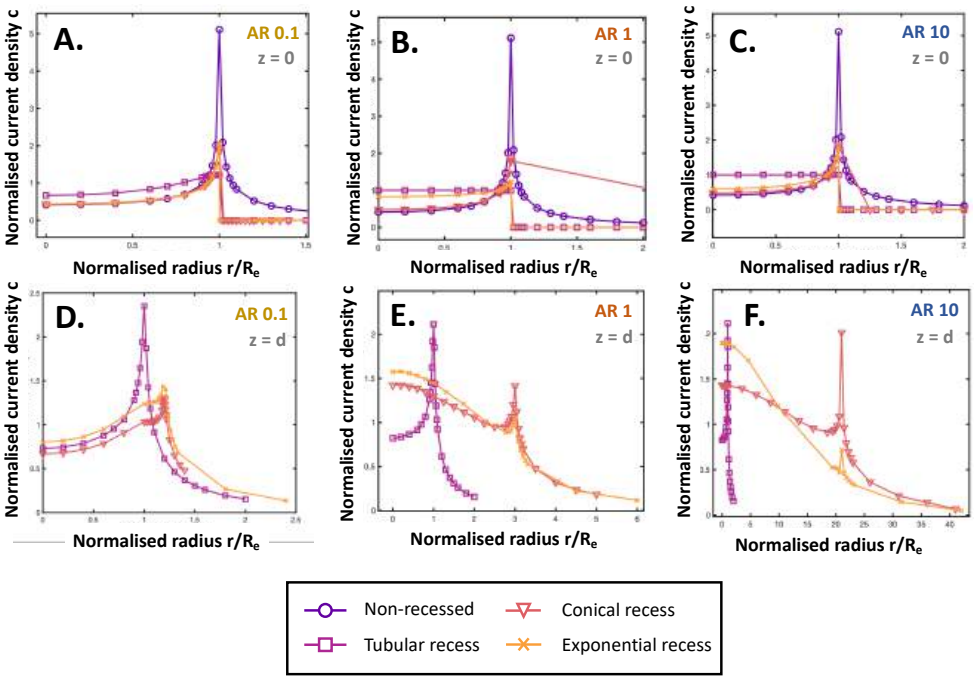

Figure 4.6: *Comparison of the radial normalised current density profile for all recesses at the electrode surface for A. AR 0.1, B. AR 1, and C. AR 10, and at the recess end for D. AR 0.1, E. AR 1, and F. AR 10.*

The AR of the recess changed the current distribution for each recess (Fig. 4.6). Smaller (shallow) AR showed similar profiles as non-recessed electrodes as expected, as shallow recesses had a negligible effect on field lines. At AR 0.1, all recesses exhibited similar current density profiles, with higher current

density at the edge, especially the conical and exponential recess, because the exponential curve could be assimilated as a straight line for such small dimensions. Increasing the AR made the current density profile more uniform for the tubular recess, however, it did not change the conical and exponential recesses, as a deeper recess did not change the curvature of field lines. At the recess end at AR 0.1, the peak current density was two times larger for the tubular recess and slightly larger for the exponential recess compared to the conical recess. Larger ARs did not affect the current density profile of the tubular recess (slight decrease of peak current density between AR 0.1 and 1), however, conical and exponential recesses showed more discrepancy. The recess opening became wider with increasing AR, yielding a peak current further away from the electrode centre and a more rounded current density profile. The peak current density remained in a similar range for the conical recess (the peak value for AR 10 is considered to be a slight artefact), whereas the exponential recess showed a decreasing peak magnitude with AR. The exponential recess became more rounded at a larger AR, which decreased the angle at the end of the recess, which explains the smaller peak current density, caused by less field line curvature.

While AR had a significant effect on the current density profile of recessed electrodes, changes in recess dimensions at fixed AR also changed the current density. Figure 4.7 shows the evolution of the mean average current density at the electrode surface and at the end of the recess for tubular and conical recesses of AR 1, with increasing dimensions (at AR 1, the electrode diameter is equal to the recess depth). The average current density decreased exponentially with recess dimensions for both recess types. At the electrode surface, the average current density was systematically higher for the conical recess, and the decrease was larger. At the recess end, the same trends were observed but the recess types were inverted: the mean current density for a tubular recess was systematically larger and showed a more substantial exponential decrease.

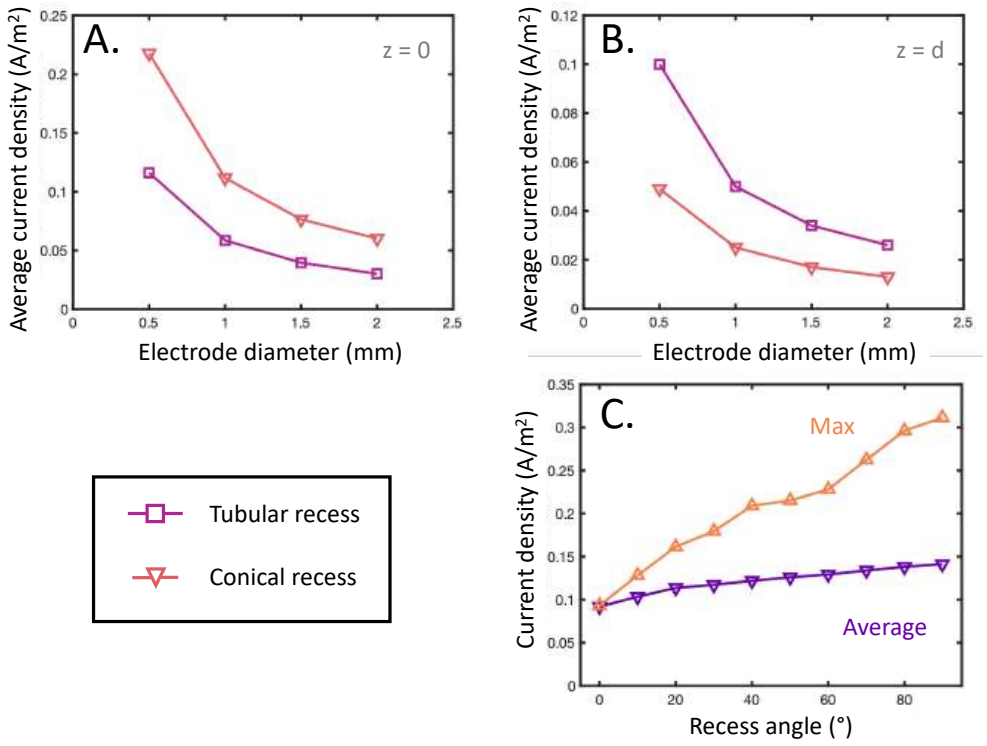

Figure 4.7: *Evolution of the mean average current density with electrode size for tubular and conical recesses for an AR of 1 at the electrode surface (A.) and at the end of the recess (B.). C. Evolution of the mean average and maximum current density at the electrode surface with the angle of the conical recess.*

The effect of changing the angle of the conical recess was assessed in figure 4.7 C, where the average and maximum current density are reported against the recess angle. The angle was defined as the recess angle reported to the vertical, i.e. a 0° angle corresponds to a tubular recess and a 90° recess to a non-recessed electrode.

The effect of a recess on the access resistance R_A was assessed for a tubular recess by deriving the theoretical equations from Newman [1966]: the open end of the recess behaves like a disc electrode, for which the equation for $R_{A,d}$ is described by Eq. 4.9 and inside the recess, the electric field lines being parallel, $R_{A,r}$ can be calculated as in Eq. 4.10, yielding a total $R_{A,tot} = R_{A,d} + R_{A,r}$

(Eq. 4.11).

$$R_{A,d} = \frac{\rho}{4r} \tag{4.9}$$

$$R_{A,r} = \frac{\rho d}{\pi r^2} \tag{4.10}$$

$$R_{A,tot} = R_{A,d} + R_{A,r} = \rho[\frac{1}{4r} + \frac{d}{\pi r^2}] \tag{4.11}$$

As a result, R_A was increased by the presence of a tubular recess independent of electrode dimension. The increase in R_A was larger at larger AR, as an AR of 0.1 multiplied R_A by 1.13, AR 1 by 2.27, and AR 10 by 13.73.

The transient changes in the current density distribution were modelled using the tertiary current distribution, which accounts for time-dependent chemical reactions by solving the concentration-corrected Butler-Volmer equation (Eq. 1.3). One hydrogen evolution reaction (Eq. 1.17) and one oxygen reduction reaction (Eq. 1.16) were modelled at the surface of a non-recessed electrode in response to a voltage step (E_H = -0.5 V and E_O = 0.3 V), see figure 4.8. For both reactions, the current density was higher near the electrode edge initially and after 100 ms, with an increase of the current density in the whole region after 100 ms, especially towards the electrode centre. The oxygen reduction reaction was more localised, close to the electrode surface, than the hydrogen evolution, which showed a pocket of high current density forming slightly above the electrode surface and towards the electrode centre, while at the outermost point of the electrode surface, the current density becomes the lowest. A lower current density at the electrode surface than in the layer above, especially at the electrode edge may indicate local exhaustion of reactants and diffusion of reactive species.

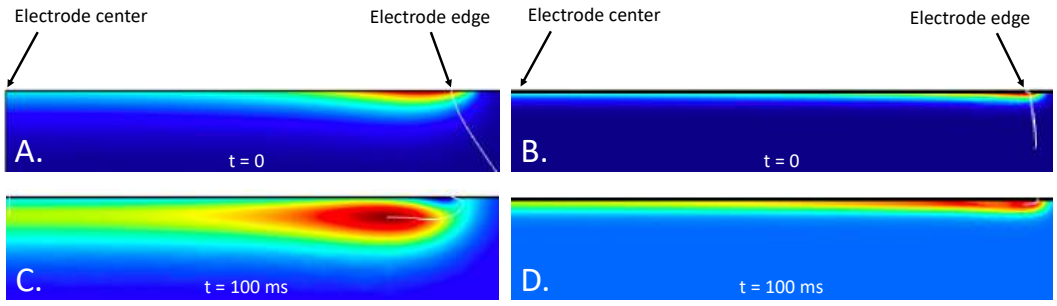

Figure 4.8: *Evolution of the current density over 100 ms for hydrogen (A, C) and oxygen reduction (B, D). The red area represents the highest current density and dark blue the lowest.*

4.1.4 Discussion

Recessed electrodes presented more uniform current density distributions than non-recessed electrodes due to different field line curvatures. The tubular recess displayed a perfectly uniform profile at the electrode surface, and a non-uniform profile similar to a non-recessed electrode at the recess end, although with a lower peak current magnitude. Conical and exponential recesses had similar current density distributions: at the electrode surface, the distribution resembled the non-recessed electrode profile with lower peak currents and the end-of-recess profile was more uniform with a higher central current density and a small current peak over the recess corner. The current density distribution at co-planar and recessed disc electrodes was derived from mathematical expressions in previous studies, showing similar profiles as the results presented here [Newman, 1966, Rubinstein et al., 1987, Suesserman et al., 1991]. At non-recessed electrodes, the primary current density was shown to be half of the average current density at the electrode centre and four times the average at the electrode edge, which is close to the ratio found here of 0.4 at the electrode centre and 5 at the electrode edge [Newman, 1966]. At tubular-recessed electrodes, the edge current density was compared for AR ranging from 0.01 to 1, with AR = 0.1 showing a similar profile at an edge value of 1.5 the average current, which was larger than in the present study [West and Newman, 1991]. At AR = 1, the peak current density was shown to be less than 10% larger than

the average current density, which agrees with my simulation results [West and Newman, 1991, Dinan et al., 1991]. For all recess types presented here, an AR of 0.1 yielded a similar current density profile to a non-recessed electrode with lower peak currents and an AR of 10 decreased the current density magnitude while showing similar profiles to AR = 1. West and Newman [1991] show that the current density profile at AR = 1 is already close to the asymptotic case of infinite AR, which displays a fully uniform distribution, which agrees with my results showing a similarity at AR $\geq$ 1.

Therefore, the introduction of a recess decreases the non-uniformity of the current density distribution, thus the electrode polarisation becomes more uniform. The computational model used in this work was relatively simple, as it considered mostly the primary and secondary current distributions, which do not account for electrochemical reactions and concentration gradients. Hypothesising that the difference in current density leads to changes in electrolyte potential at the electrode edges (the electrode potential is assumed to remain uniform), the reaction rates may differ, causing concentration gradients and possible local reactant exhaustion depending on diffusion rates. Dinan et al. [1991] showed that the mass-transfer-limited electroplated copper thickness was lower towards the electrode edge, and that the non-uniformity progressed towards the edge as the recess AR decreased. The diffusion-limited current increased with the square root of the rotation speed only up to AR = 1, and the absolute current decreased with increasing AR, showing the role of AR on diffusion and reaction rates. In the case of local reactant exhaustion, it can hypothesised that different charge transfer mechanisms may be involved simultaneously at the interface, in regions of different current densities. The results obtained for the large AR electrode (which was a 2-D AR defined as the electrode width and length ratio, see section 4.3) seem to confirm this hypothesis, as the electrode behaviour was different from the disc electrodes, however, such an electrode shape was not modelled, so the results obtained here can only be extrapolated on disc electrodes.

Adding the tertiary current distribution to the model may have given further insight into the effects of recess on the spatial and time distribution of the main electrochemical reactions and help explain some of the observed experimental behaviour, however, only basic information on some reactions could be obtained, yielding a still coarse model of the reactions. A few options that could have been added to make the model more realistic included either a "Water-based with electroneutrality" electrolyte (electroneutral electrolyte with the self-ionisation of water built-in) or a "Supporting electrolyte" (considering small concentration gradients, therefore using the bulk conductivity to approximate the electrolyte voltage drop), a Nernst-Einstein migration law, a null velocity field, and a set of electrode reactions (governed by the concentration-dependent Butler-Volmer equation) and electrolyte reactions (including equilibrium reactions) independent of electrode potential [Guide].

Most of the results presented here used voltage-controlled inputs, whereas the stimulation protocols used in experiments were current-controlled. Current-controlled inputs were used subsequently and the distributions were comparable with voltage control, however, a few discrepancies and errors arose. First, the models did not always converge to a solution, which was attributed to improper grounding. A virtual ground electrode was added, sinking the current and being held to a 0 V potential, however, the electric field lines showed that most of the current flow was occurring between the ground electrode and the outer boundary, with only a small fraction flowing to and from the actual electrode. The grounding problem may have been due to the difference between virtual and true ground, which was misconceptualised in the model. Lastly, the electrode needed to be designed as a domain, as opposed to a boundary, for the current control, and as a result the potential was allowed to vary within a small region of bulk electrode metal. However, since the electrode conductivity is very high, the potential is expected to be uniform in the electrode. On non-recessed electrodes, a potential gradient was observed within the bulk metal of the electrode with a lower potential at

the electrode edge at the electrode-electrolyte interface. The tubular recess restored the uniformity across the electrode surface, however, the gradient was still present at low AR. Although the electrode potential was hypothesised to be uniform, the conical recess presented a higher potential at the electrode edge in current control, which may explain why in some cases, the current density at the electrode surface edge was higher than other recesses. Furthermore, at a threshold input current density, the potential gradient would become significantly non-uniform inside the electrode with a localised drop at r $\approx 4/5\ R_e$, which remains unexplained. The potential discrepancy within the electrode was negligible (0.1 mV), however, the threshold was consistent for AR ≥ 1 at 0.5 A/m^2, and 0.1 A/m^2 for AR 0.1 as shown in figure 4.9. The superposition of these non-uniformities and grounding errors may explain some of the inconsistent results obtained in current control shown in figure 4.9 B and C. The current density was compared at the electrode surface (B, z = 0 μm) and 1 μm above the surface (C), showing substantially different current density distributions. While the distribution above the surface met expectations, with a larger current density at the electrode edge, the distribution at the electrode surface was composed of concentric circles in an irregular wave-like distribution with the highest current density observed around r $\approx$ $3/10\ R_e$. For these reasons, the current-controlled results were considered with caution and the models need to be refined for future analysis.

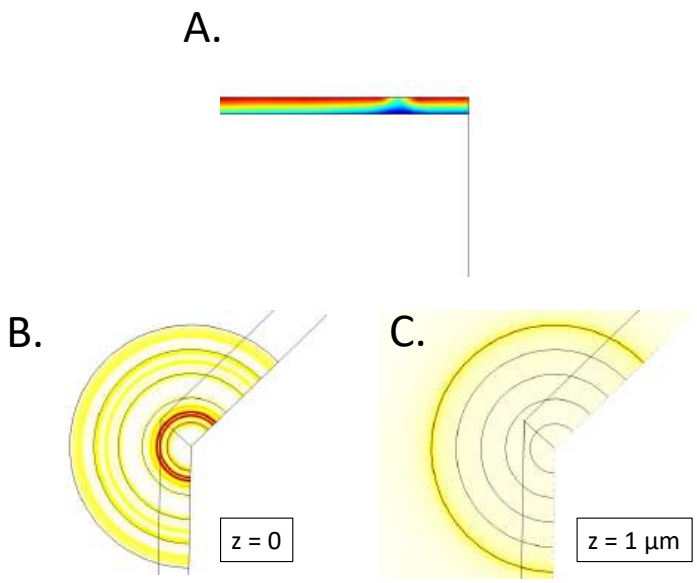

Figure 4.9: *Heatmap of electrode potential for a tubular recess of AR 0.1 in response to a uniform current density of 0.1 A/m^2.*

4.2 Effect of smaller electrode diameter

4.2.1 Rationale for studying smaller electrodes

Shannon's limit was developed on macro-electrodes (cm to mm range), and knowing that smaller dimensions affect the current distribution and charge density [Newman, 1966, Green et al., 2012b, Fan et al., 2021], the recent miniaturisation of electrodes puts the validity of Shannon's limit in question. Reports suggest that Shannon's limit does not translate to microelectrodes [McCreery et al., 2010], since the charge density exceeds the charge per phase in Shannon's equation, making k exceed limits for even small stimulation currents. Smaller electrodes have a larger current density, smaller capacitance, higher access resistance, and increased circumference/surface ratio, all of which may change the electrochemical response occurring during neural stimulation. Therefore, studying the effect of reducing the electrode dimension is needed. The transition from macro- to microelectrode remains a grey area, and the dimension at which the switch in behaviour between Shannon's limit and the microelectrode maximal safe charge density of 4 nC/ph occurs has not been

identified [Cogan et al., 2016]. Therefore, the idea of the following study was to manufacture a set of electrodes of decreasing diameter to study how the transition occurs when the electrode size approaches the microelectrode range ($< 100\ \mu m$). However, due to experimental and manufacturing challenges, only one other electrode diameter was fabricated and tested (1 mm diameter), which still allows some comparisons with a larger commercial electrode.

4.2.2 Fabrication of 1-mm diameter electrodes

The custom smaller diameter electrode consists of three layers, with a Pt foil sheet (12.5 μm held between two ceramic plates (alumina 550 μm and 125 μm), which were laminated using epoxy. All pieces were cut and hatched using a laser cutter. The Pt foil was cut larger than the desired diameter to avoid heat-affected zones near the electrode surface and to have extra surface for adhesion between the ceramic plates. The thin ceramic was used to cover the electrode surface side, thereby presenting a smaller recess (AR 0.125). A 1-mm diameter hole was hatched in the middle, which constituted the electrode opening. A dimension check with a light microscope (Bruker) confirmed that the hole matched the desired dimension. The thick ceramic had a hole hatched through to solder a wire to the Pt foil to connect to the electrode. The ceramic plates were glued together using epoxy making sure to leave the electrode surface and soldering surface clean. The plates were pressed together and left to cure overnight. The electrode surface was then checked visually under the light microscope and little epoxy overflow was present, suggesting that the electrode surface dimensions followed the design. Then, a connecting wire was soldered to the Pt foil: soldering was prepared by heating the Pt foil up using a hot plate (60° C) and etching the surface using phosphoric acid, before soldering a breadboard wire in place. The wire connection and the sides of the ceramic case were encapsulated with epoxy to make sure no unwanted portion of the foil, solder, or wire metal, was exposed to the electrolyte. Electrode characterisation was carried out as described in section 3.2.2.

4.2.3 Results

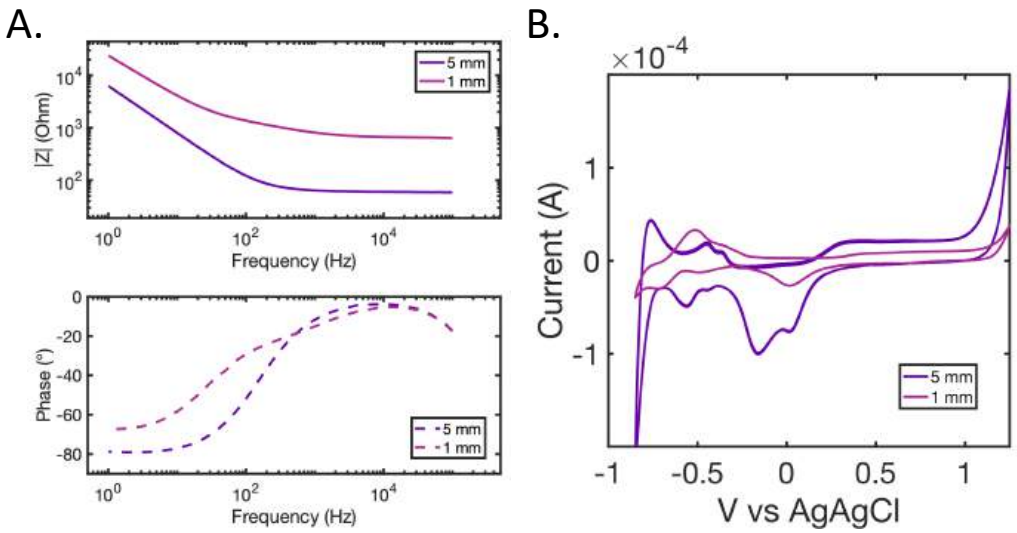

Figure 4.10: *A. Comparison of EIS scans of the 1-mm diameter custom-made Pt electrode with the 5-mm diameter commercial Pt electrode. B. Comparison of CV for both diameters.*

The impedance of the 1 mm diameter electrode was higher at all frequencies compared with the 5 mm diameter electrode (Fig. 4.10 A.). The high-frequency impedance, which is associated with R_A, was approximately ten times larger than the larger electrode, whereas a 5-fold difference was expected, as R_A is inversely proportional to the radius (Eq 4.9). However, as it was shown earlier 4.1, a further doubling of the high-frequency impedance can be attributed to the recess at the 1 mm electrode (aspect ratio of 1/2). The phase shows a two-step transition for the 1 mm electrode with a linear decrease of the phase from 10^4 Hz to 10^2 Hz before reaching a constant phase of -65° at 1 Hz. The double transition was less clear on the impedance magnitude plot, however, it seems that the low-frequency slope is less steep than for the 5 mm diameter electrode suggesting a difference in the double-layer capacitance.

Typical CVs were compared in figure 4.10 B. The CV area was smaller for the 1 mm electrode as expected, as a smaller surface area decreases the double-layer capacitance, reducing the current available from double-layer charging, and decreases the area available for faradaic reaction, hence smaller peaks.

The peak potentials corresponded well for both electrodes, which suggests that both materials were highly similar and could be compared, but only one PtO reduction peak was observed on the 1 mm electrode, which will be addressed in the discussion 7. The H-region exhibited a large oxidation peak (E ≈ -0.55 V), which was associated with the reduction peak at E ≈ -0.7 V marking a step in the CV, which may correspond to phosphate evolution [Hudak et al., 2010]. Overall, the peaks were less defined at the 1-mm electrode, which may be attributed to the recess affecting diffusion.

The electrode area needed to be activated before conducting further measurements, which was done by performing CV in sulfuric acid (H_2SO_4 0.1 M). Figure 4.11 shows the progressive development of faradaic peaks during H_2SO_4 CV, which indicates the increasing availability of reaction sites at the electrode surface.

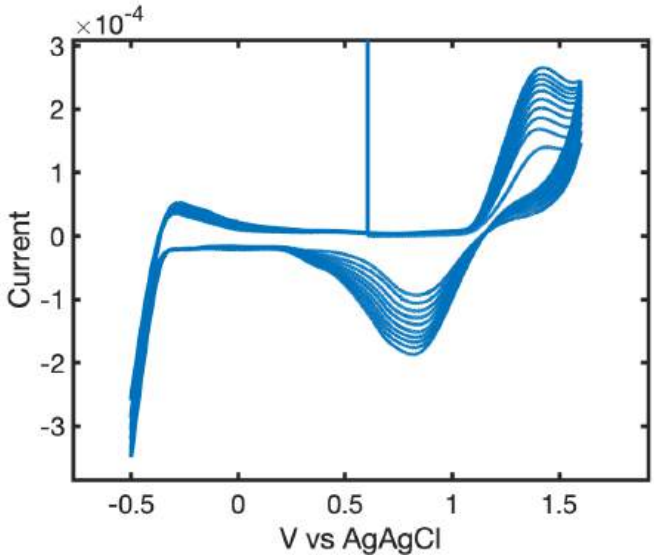

Figure 4.11: *10 CV cycles in H_2SO_4 on a 1-mm diameter custom-made Pt electrode.*

The currents used for the 1-mm electrode are listed in table 3.1. Given the precision of the current waveform (1.2 mA average noise and 4.5 ± 4.65% accuracy on higher currents), the accuracy was more difficult to guarantee on the smaller electrode. As the currents corresponding to k-values were closer to one another, manually setting the variable resistor value did not provide

a safe enough margin to positively discriminate between k-values. Kumsa et al. [2016b] used 1 mm diameter disc electrodes, however, the stimulator was designed with a +90 V voltage source [Hudak, 2011] and a different current adjustment mechanism, which may have allowed more precision. Furthermore, the noise represented a larger proportion of the current, as can be seen in figure 4.12, especially in the anodic phase, which presented a very small anodic peak. The electrode potential and polarisation are shown in figure 4.13. Panels C and D represent the same data as panels A and B, only corrected for the base value, in order to have a better comparison of the ranges. The 1-mm diameter electrode showed a more than twice larger ohmic drop in the cathodic phase and a slightly smaller anodic ohmic drop despite the anodic current being significantly smaller. The shape of the anodic discharge was also significantly different, with a less sharp discharge at the 1-mm electrode, which demonstrates the larger RC constant in the circuit with the smaller electrode, due to higher resistance. In the raw potential trace (4.13 A), one can also see that the end potential of the 1-mm electrode was negative, indicating a large potential decay during pulsing, which was consistent. Nevertheless, the cathodic polarisation was unaffected by the decay as can be seen in figure 4.13 C, where both electrodes showed similar interphase potentials. In 4.13 B and D, the polarisation proved to be very noisy in the anodic phase with 600 mV P-P oscillations, making it not possible to calculate the anodic polarisation. The cathodic phase was also substantially overcorrected (by $\approx$ 400 mV), which may be attributed to the seemingly longer rise and fall times (Fig. 4.12) and to the magnitude of the ohmic drop. The effect of noise was much exacerbated on the 1-mm electrode as the current noise represented a larger proportion of the applied current, but also as the access resistance was higher, multiplying the correction applied by ten. Therefore, despite several trials in different electrolytes, no usable current pulse data were obtained with the 1-mm diameter electrode and the present experimental setup.

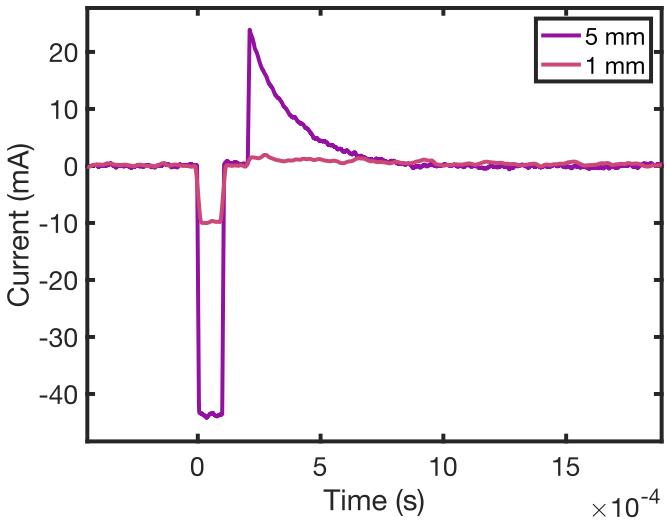

Figure 4.12: *Comparison of current waveforms for k = 2 for 1-mm diameter and 5-mm diameter electrodes.*

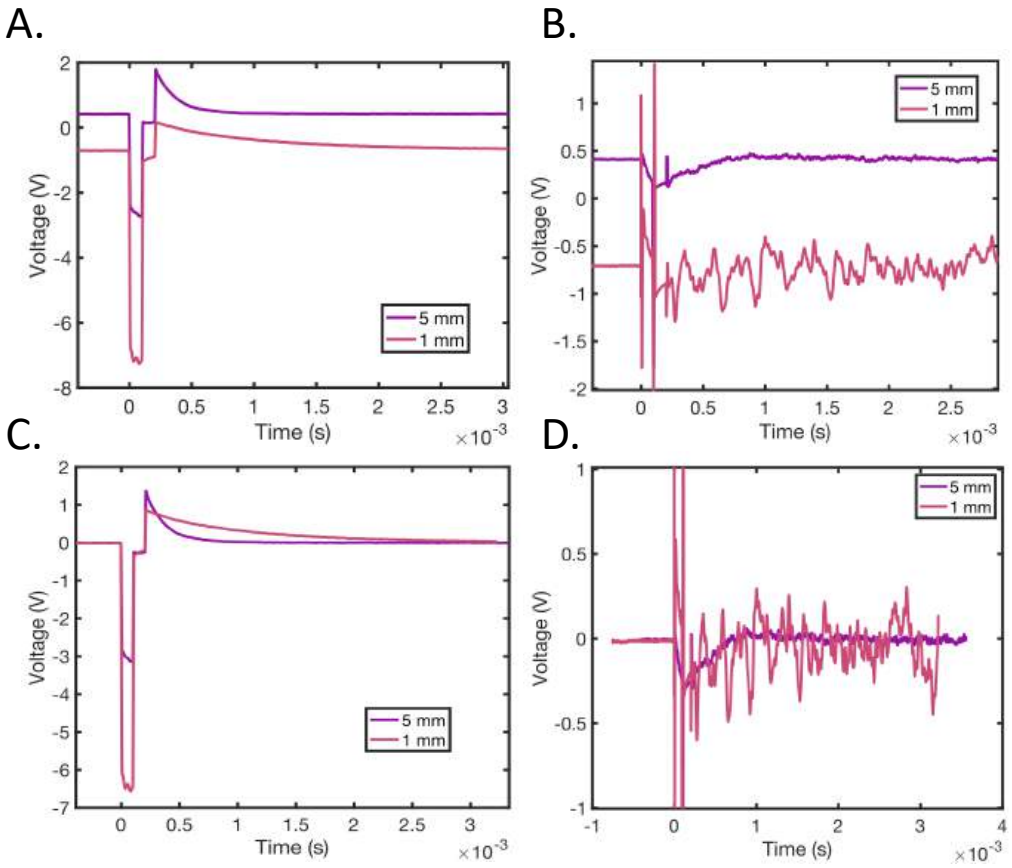

Figure 4.13: *A. Raw potential traces of the last pulse for 1 mm and 5 mm diameter electrodes. B. Polarisation of the last pulse for both electrode diameters. C. Potential traces with base potential subtracted. D. Polarisation with base potential subtracted.*

4.2.4 Discussion

The custom 1 mm disc electrode was made to study the influence of electrode size on electrode behaviour. Smaller electrodes have a higher current density, a higher edge aspect ratio (the electrode edge represents a larger proportion of the surface), and a higher access resistance. The electrochemical behaviour of the 1 mm electrode met expectations for EIS, with an increase in R_A and a decrease in C_{dl}. However, while the absolute values of impedance increased and injected charge in CV or CP decreased with decreasing dimensions, the normalised values by area followed opposite trends: on Pt electrodes, the high-frequency impedance per area decreased with electrode diameter below 500 μm, the CSC increased twofold, and the CIL 3.4 fold [Green et al., 2012b]. On SIROF electrodes, the CSC was stable for area $\geq$ 200 μm^2 and increased at lower dimensions, while CIL increased steadily with decreasing electrode dimension [Ghazavi et al., 2020]. The impedance Bode plots exhibited a steady increase of impedance at all frequencies, which seems proportional to the reduction in area, hinting at a constant or slightly decreasing impedance per area [Ghazavi et al., 2020]. The change in performance of 250 μm diameter electrodes compared to 500 μm measured by Green et al. [2012b] correlates with the area condition hypothesised by Ghazavi et al. [2020]. For the custom electrode, the high-frequency impedance remained higher after normalisation by area, contrary to Green et al. [2012b] and Ghazavi et al. [2020] suggesting additional resistive elements, which may be the recess and surface contamination. C_{dl} per surface area increased with decreasing diameter, which made the low-frequency impedance closer to the larger electrode, entering the boundaries of scaling with area as shown by Ghazavi et al. [2020]. A similar bump in phase shift at f $\approx$ 100 Hz was also reported by Green et al. [2012b], explained by an increased capacitance per area. The CSC increased 2.7-fold when dividing the diameter by 5, which is consistent with the twofold increase for a 4-fold diameter decrease reported by Green et al. [2012b].

In the CPE modelling, alpha decreased from 0.9 to 0.7 when decreas-

ing electrode area, indicating that the interface changed towards a non-perfect capacitance translating surface non-uniformities, which may be due to contamination with epoxy or to the higher edge/surface ratio. The CV also met expectations with similar features to the 5-mm electrode, however, with broader peaks and a smaller area, pointing at the smaller surface area and at the recess. The change in electrode size is thought to modify the diffusion profile by reshaping the electric field [Green et al., 2012b]: on a large electrode, the diffusion is dominated by linear diffusion whereas the electric field becomes hemispherical as the electrode size decreases (for co-planar electrodes), which increases the charge accessibility as suggested by Cogan et al. [2014]. However, these changes in behaviour may occur at lower diameters than 1 mm (Green et al. [2012b] mention their 1-mm diameter electrode to behave like a large electrode), therefore, we may not be able to fully observe these effects. Further considerations on edge effect are presented in section 4.3.

The custom electrode design may have presented a few flaws: the electrode was made by glueing discs of ceramic on a Pt foil using epoxy, therefore, a recess was created at the electrode surface, which may affect the current density as shown in 4.1, and epoxy may have leaked onto the surface, changing the electrode surface area and contour. The contact between the ceramics may not be perfect and some solution may have infiltrated in the gap, coming into contact with the Pt foil further than the required diameter, however, the apertures between both materials are expected to be small, yielding very high access resistance and a long diffusion path and therefore unlikely to participate in the charge injection. The electrode performance may also have been hampered by the use of a laser as Green et al. [2012b] report surface oxidation, which decreased the electrode performance. Ultimately, no satisfactory data could be obtained from pulse trains with the 1-mm diameter electrode for various reasons. First, smaller electrodes imply larger impedances, therefore, more compliance voltage is needed to inject current, and measurement noise sources need to be reduced. Thus the setup and especially the stimulator need to be

adapted for smaller electrode sizes in future experiments, as a larger compliance voltage is needed along with a more precise resolution on the control of the current levels. Indeed, the current values were closely grouped together, allowing less room for error when setting the current levels, and the noise proportion was too large to precisely calculate the anodic polarisation. Furthermore, a 1-mm diameter electrode remains quite large compared to other implants, e.g. Utah array, and smaller electrode diameters need to be studied to understand the response of microelectrodes better, and identify if Pt dissolution processes or large local polarisation may induce more neural damage. Another main problem with the 1-mm diameter electrode was the large decay during pulses due to current leakage through the circuit. The large decay created a too large artefact to be efficiently corrected for, leading to a distribution of values which did not reflect the electrode behaviour. The large decay was not a direct consequence of the reduction in size, since it was observed in other experiments, including the introduction of gels 6.3 and dissolved gases 6.5.

4.3 Influence of electrode shape maximising edge effect

4.3.1 Rationale large perimeter to surface ratio electrode

On planar electrodes, the current density was shown to be higher at the edge [Newman, 1966, Rubinstein et al., 1987], as illustrated in the recess modelling study (4.1). In a zone of high current density, reaction rates increase, accelerating the consumption of reactants, which may change the local environment. The potential may change locally, enabling different electrochemical behaviours, which may be harmful, for instance with the electrolysis of water. In the vast majority of electrode characterisations, the reference electrode is placed at some distance from the electrode, therefore, the recorded working electrode potential is an average of the potential over the whole electrode

surface. For macroelectrodes, the edge with high current density is much smaller than the centre, therefore, the behaviour that is picked up by the RE corresponds majoritarily to the electrode centre [Green et al., 2012b]. As a consequence, edge effect is often neglected and although the average WE potential appears to be within the safe potential limits, local harmful reactions may occur at the edge, possibly including electrode dissolution [Park et al., 2019] or water electrolysis. Indeed, although a higher edge effect ratio provides better electrochemical performance and lower activation thresholds, high perimeter-to-area ratio electrodes showed to have significantly higher and faster dissolution rates well within Shannon's safe stimulation boundaries (k = 0.93) [Park et al., 2019]. Moreover, a theory suggested in a personal correspondence to explain the phenomena behind Shannon's limit is that $k = 1.75$ is the charge threshold at which water electrolysis starts occurring at the electrode edge, damaging the electrode and neighbouring neurons. To study this hypothesis, and more generally whether the behaviour at the electrode edge is substantially different than at the electrode centre, I designed an electrode shaped such that the edge effect becomes predominant. The electrode was designed as a thin and long rectangular strip (44 mm x 0.445 mm, AR $\approx$ 10) with a surface area equal to the 5-mm diameter disc electrode (19.635 mm^2) but with a three times larger perimeter (88.89 mm vs 31.41 mm), thus a larger edge effect.

The large AR electrode was used to corroborate hypotheses when analysing results about the solution composition effect (chapter 6) and results are presented in the relevant sections, while this section addresses the changes in traditional electrolytes only.

4.3.2 Fabrication of the large AR electrode

The large AR electrode was fabricated using platinum foil (12.5 μ m thickness) and a ceramic housing in a similar "sandwich" assembly as the 1-mm diameter electrode. A strip of Pt foil was cut using a laser cutter (LaserVall Violino 2); the dimensions were larger than the desired electrode dimensions (52 x 5

mm) so the foil could be glued to the ceramic housing. Two ceramic plates (alumina 550 μm thickness) were cut larger than the Pt strip (55 x 10 mm) using the laser cutter by hatching a narrow outline of the desired shape. One plate (bottom) was also hatched in the centre to yield an opening at the desired electrode dimensions, while the other had a hole hatched through which a wire would be soldered onto the Pt foil to make the electrode connection. The Pt foil was visually checked under light microscopy (Bruker) to ensure there was no burnt area where the electrode surface would be (Fig. 4.14, the burnt area was marginal), and the ceramic bottom plate opening was checked to control the size of the electrode. The edges of the opening were relatively irregular, possibly due to ceramic burning, making the measurement less accurate, however, the width of the rectangular opening was consistently larger than the desired electrode width. The assembly of the different parts and the soldering were realised similarly to the 1-mm diameter electrode (4.2.2).

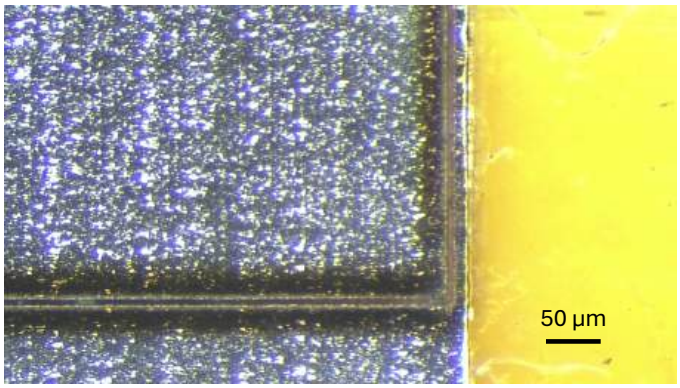

Figure 4.14: *Optical microscope image of the laser cut to visually check the burnt area around the cut.*

4.3.3 Results

The large AR electrode had a similar but slightly lower R_A as the RDE in all electrolytes despite having a different shape (Fig 4.15 A). The shape of the Bode plot was different otherwise, exhibiting a sort of two-step transition identified on the phase plot with a first semi-circular shape at high frequency (f > 200 Hz), followed by a linear decrease of phase for f > 3 Hz, before

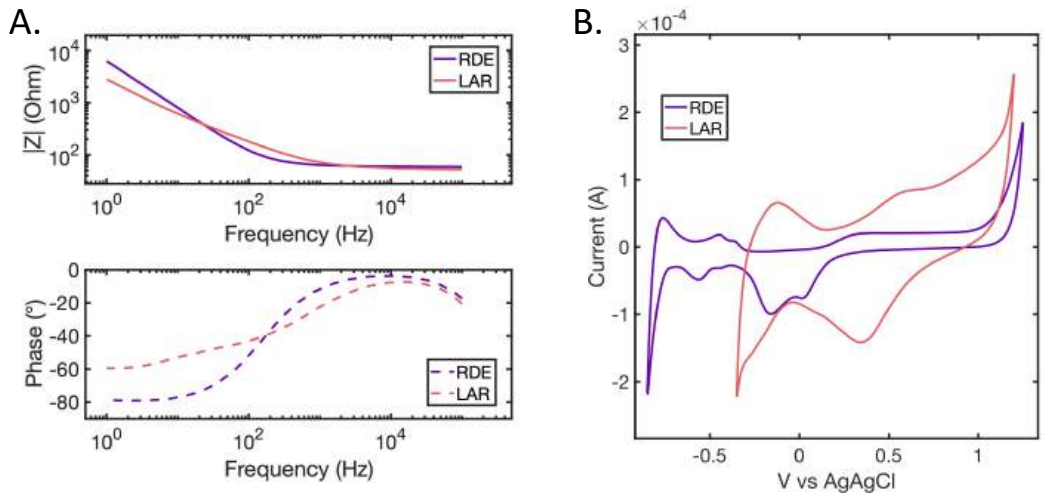

Figure 4.15: *A. Comparison of EIS scans in PBS of the large AR rectangular electrode (LAR) with the 5-mm diameter disc Pt electrode (RDE). B. Comparison of CV in PBS for both electrode shapes.*

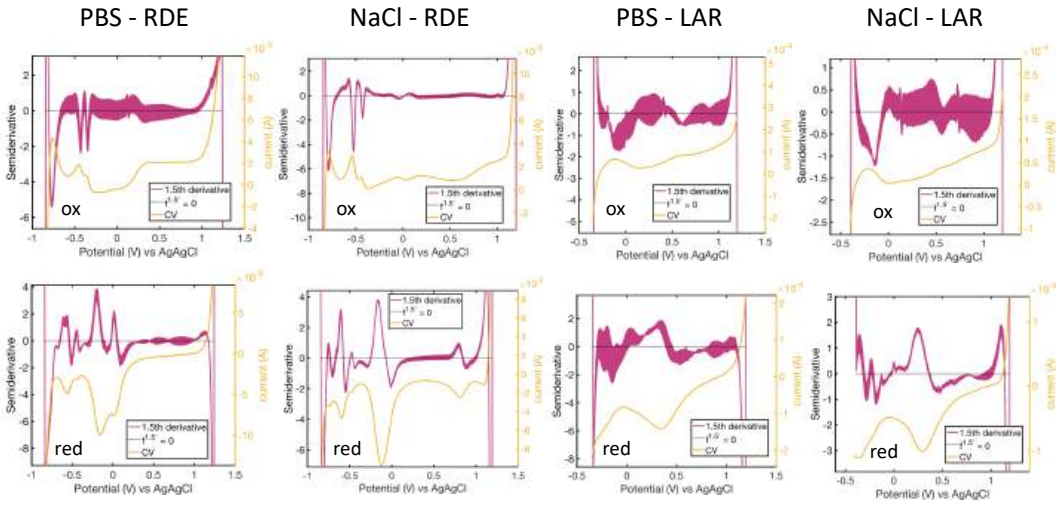

Figure 4.16: *Comparison of semiderivative of CVs of the 5 mm diameter electrode (RDE) and the large AR electrode (LAR) in PBS and NaCl. The CVs were separated in the oxidation ("ox") and reduction ("red") scans.*

stabilising around -60°. A -60° phase suggests that the interface behaviour may be better described by a CPE than a capacitance, demonstrating surface non-uniformity due to a high proportion of edge effect. Indeed, EIS fitted data showed a decrease in alpha with a CPE model from 0.9 for the 5-mm diameter electrode and 0.7 for the large AR, similar to the value found for the 1-mm diameter electrode. The CPE model also had a better agreement with the data than Randle's model. Q_{dl} increase to 60 μF, larger than the 1-mm diameter electrode. The three phase regions can be distinguished on the impedance module plot with different slopes, with the large AR starting transitioning at a higher frequency and ending up with a lower impedance at low frequencies than the disc electrode.

The CV of the large AR electrode was substantially different from the disc electrode (Fig. 4.15 B). The water window was shorter for the large AR electrode ([-0.4 V ; 1.1 V]), demonstrating that lower overpotentials were required for water electrolysis, especially for hydrogen evolution. The voltammogram displayed larger currents overall for the large AR electrode with larger, broader peaks, which were less defined than the 5-mm diameter electrode. Similarly to the 1-mm diameter electrode, a recess was present on the large AR electrode, which may interfere with diffusion processes, resulting in less defined peaks. Subsequent tests showed an extension of the water window in the H-evolution region by 200 mV (Fig. 4.18), reaching a water window ([-0.6 V ; 1.1 V]) more in agreement with the literature [Daubinger et al., 2014]. A slower sweep rate CV was performed in PBS, which decreased the overall current magnitude as expected, and exacerbated two peaks on the reduction scan (E $\approx$ +0.05 V and E $\approx$ +0.3 V), which appeared as a single broad peak on the faster CV. The semiderivative comparison of the large AR electrode and the 5 mm disc electrode in PBS and NaCl is shown in figure 4.16. PBS and NaCl had similar features, with very similar oxidation scans and H-reduction. PBS showed a double PtO reduction peak on the RDE, which almost disappeared on the large AR electrode, and did not appear on either electrode in NaCl. Though, an

additional reduction peak was clearly observable in NaCl with the 5 mm electrode, which almost disappeared with the large AR. Both peaks may represent a similar mechanism, which does not occur on the larger AR electrode.

OCP recovery was similar between the 5-mm disc electrode and the large AR, which had a similar surface area, although the OCP recovered more quickly for the LAR. The 1-mm disc electrode had a large decay causing a longer recovery time, starting from negative potentials whereas the two other electrode types started at the same potential, and did not have time to fully recover over 20 minutes.

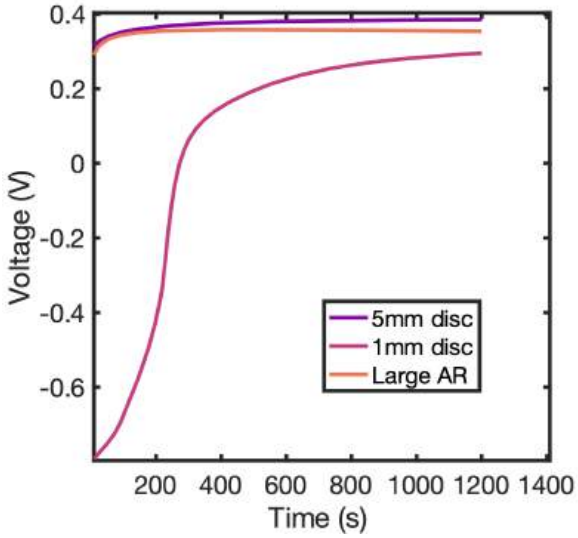

Figure 4.17: *Comparison of post-pulsing OCP traces of different electrode shapes and sizes.*

As the large AR electrode was designed to maximise edge effect, especially at the ends of the rectangle, EIS and CV were performed with the RE placed at three different locations along the electrode longitude: at both ends and in the middle, with RE as close as possible to the electrode, effectively in contact with the ceramic recess, 550 μm away from the electrode surface (Fig. 4.19). While the CV did not exhibit any major changes, the impedance modulus was slightly lower in the middle of the electrode, indicating a lower R_A, and the phase was also uniformly lower over the frequency range, suggesting a slightly

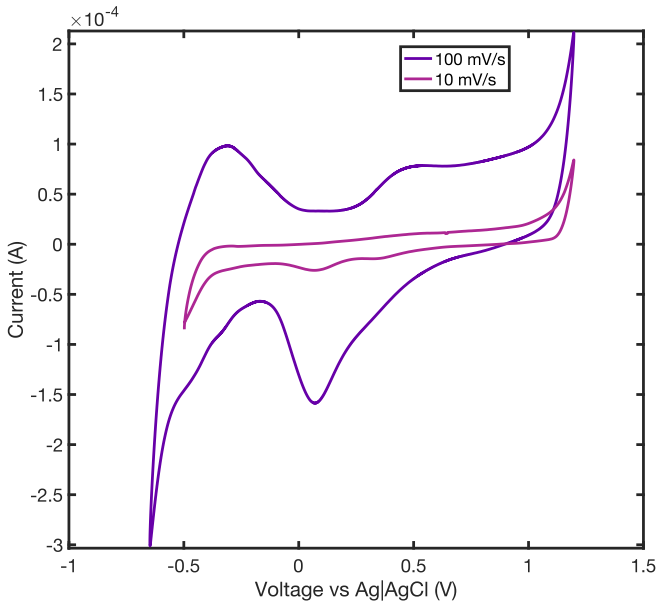

Figure 4.18: *Comparison of CV in PBS for two different sweep rates: 100 mV/s and 10 mV/s for the large AR electrode.*

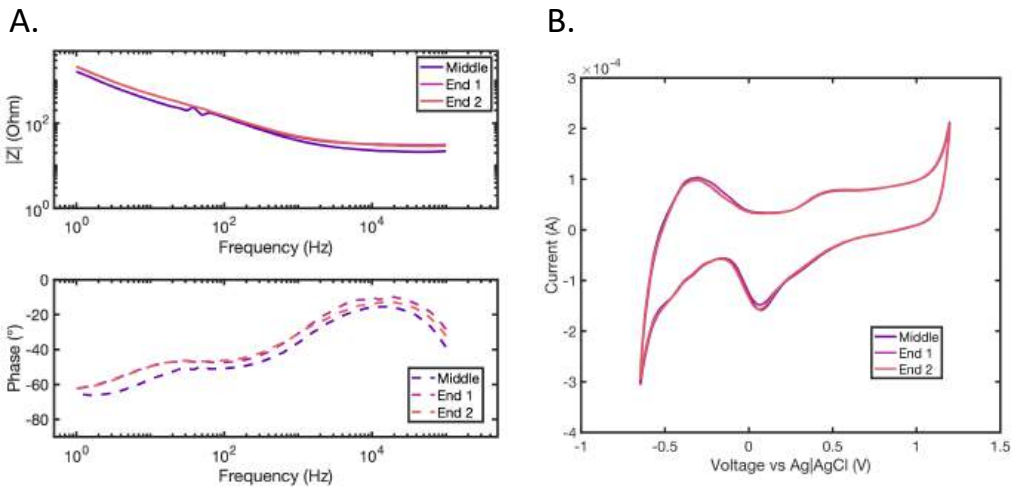

Figure 4.19: *A. Comparison of EIS when varying the longitudinal position of RE: placed in the middle, and at the edges, of the large AR electrode (PBS) B. Comparison of the CV in PBS with RE placed in the middle, and at the edges, of the large AR electrode.*

more capacitive behaviour. Although these changes were expected from the theory, as the denser current distribution at the electrode edges would result in higher R_A and slightly more dominant resistive behaviour, it was unexpected to experimentally measure such a difference with an aspect ratio of 100.

Low-frequency noise with a unique was quite frequently observed with the large AR electrode as shown in figure 4.20. Unlike previously observed noise involving the module and phase jumping between different values, the module showed a continuous semi-circular shape after an initial jump at f $<$ 20 Hz of more than one order of magnitude. While the impedance change was abrupt and decreased with decreasing frequency, the phase experienced only a minor change of around -10 to -15°.

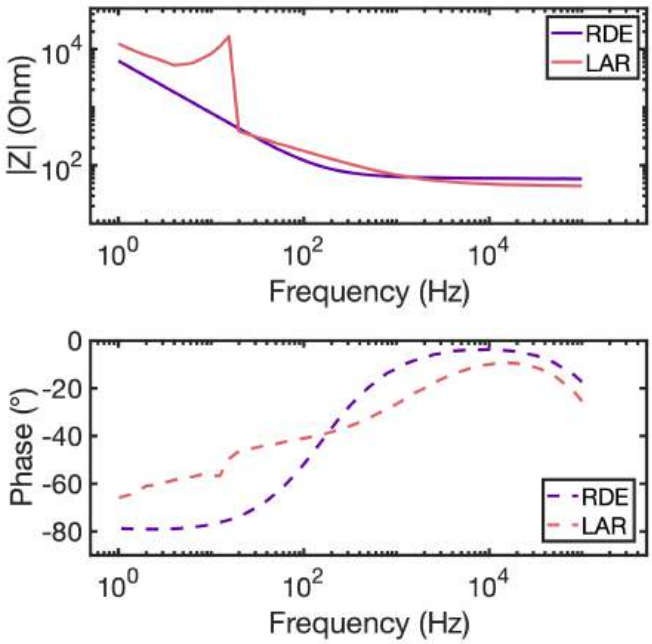

Figure 4.20: *Example of low-frequency noise observed for the large AR electrode (LAR) in PBS compared with EIS on the 5-mm diameter RDE.*

In pulsing tests, the large AR electrode behaved differently from the 5-mm disc electrode. First, the cathodic polarisation was larger on the large AR electrode as it reached a similar value of ≈ 280 mV for $k = 1.25$ as did the disc electrode for $k = 2$, and a twice larger polarisation (≈ 500 mV) for $k = 2$ (Fig. 4.21). The shape of the anodic polarisation was also substantially differ-

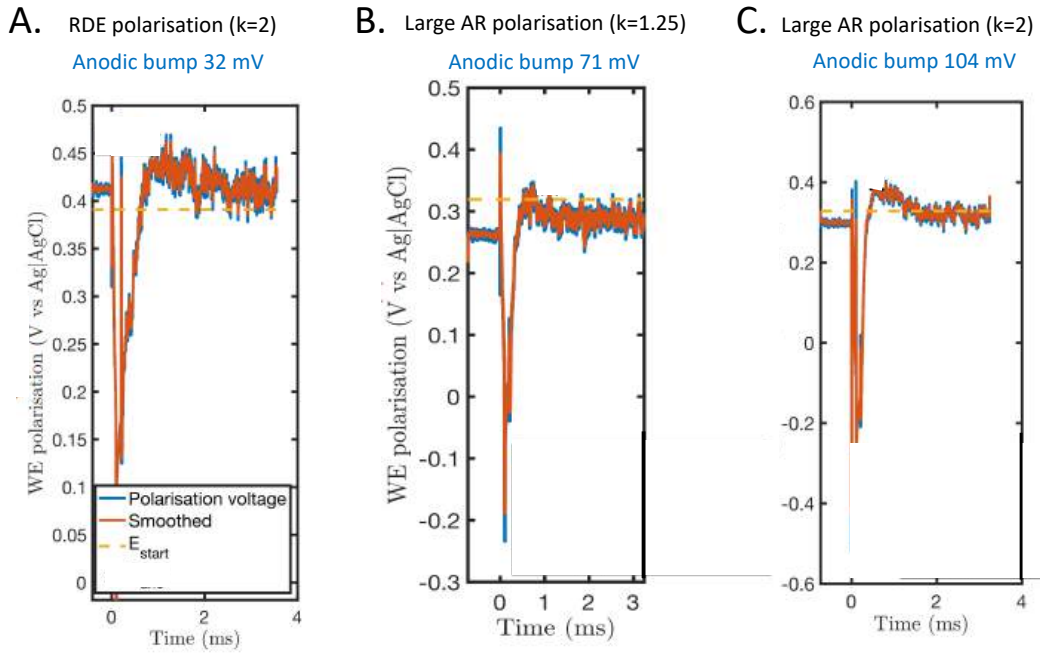

Figure 4.21: *A. Polarisation at the largest k for the disc electrode. B. Polarisation at the smallest k for the large AR electrode. C. Polarisation at the largest k for the large AR electrode.*

ent, yielding a larger anodic potential, as the anodic bump at the beginning of the anodic phase was much larger for the large AR electrode: the bump (measured relatively to the end potential) was already more than twice as large on the large AR electrode for the smallest k-value as the largest k-value on the disc electrode and more than three times as large for the largest k-value. The larger anodic bump may be related to a larger anodic current peak (7 mA larger for $k = 2$). The end potential was systematically lower than the starting potential, indicating some decay which also occurred occasionally with the 5-mm disc electrode. Therefore, although the polarisation was larger in both directions on the large AR electrode, suggesting a larger part of cathodic irreversibility (larger anodic bump), less ratcheting was observed, potentially due to consistent potential decay and faster diffusion, which would reduce the irreversibility due to reactant diffusion.

The location of the pulse potentials on the CV was substantially different with the large AR electrode compared to the 5-mm diameter disc electrode

(Fig. 4.22). E_{ano} was located in the shoulder of the presumed PtO formation peak, at a similar potential to the 5-mm electrode, which may be due to how the electrode shape and recess affect mass transport to the electrode, rendering peaks broader. E_{cat} however was more negative by 200 mV and located at the beginning of the H-evolution region, far beyond the oxide reduction peak. This observation suggests that on the large AR electrode, which favours edge effect, a different mechanism is at play during biphasic stimulation, which consists in PtO formation in the anodic phase and H-desorption in the cathodic phase.

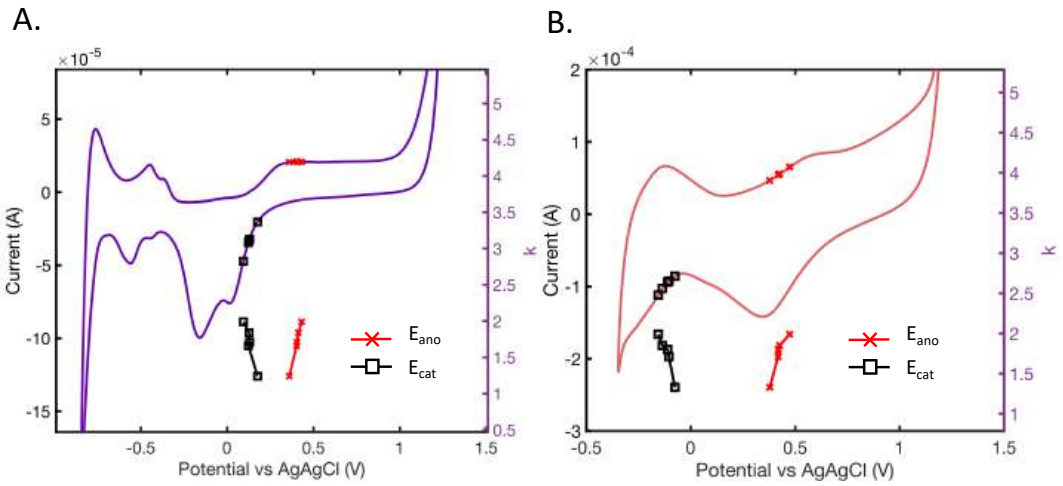

Figure 4.22: *Evolution of E_{ano} and E_{cat} with k and location on the CV in PBS for A. 5-mm disc electrode, B. large AR electrode.*

4.3.4 Discussion

The large AR electrode introduced a large edge-to-surface proportion to the electrode but also added a recess, like the small diameter electrode. As the perimeter-to-area ratio (P/A) increases, edge effects become a larger contribution to electrode performance [Green et al., 2012b], therefore, the large AR electrode provides insight into charge injection at the electrode edge. The change in EIS and CV was more obvious than in the comparison of electrode diameters, with larger currents in the CV and wide, poorly defined peaks, hinting at a different electrode behaviour. Large AR electrodes or electrodes with large P/A ratio have been widely studied as they may offer several advantages over disc electrodes: whether in a rectangular shape [Cogan et al., 2014], frac-

tal shape [Golestanirad et al., 2013, Watterson et al., 2017, Park et al., 2018, 2019], or serpentine shape [Park et al., 2018], high P/A electrodes have higher CSC and CIL, higher C_{dl} and lower R_A [Green et al., 2012b, Cogan et al., 2014, Park et al., 2018] which reduce the power consumption [Golestanirad et al., 2013, Park et al., 2018] and higher current density and total current which decrease the activation threshold on neurons [Park et al., 2018, Jensen et al., 2005]. I observed the same changes on the large AR electrode with higher C_{dl}, lower R_A, and larger CV currents yielding a higher CSC, and these effects scaled with P/A ratio, as was reported by Park et al. [2018]. The double "bump" observed on the EIS phase of the 1 mm electrode and the large AR electrode is a consequence of the larger P/A ratio, as it was reported for fractal electrodes and small diameter disc electrodes and is attributed to the larger C_{dl} [Green et al., 2012b, Park et al., 2019].

Nevertheless, large P/A electrodes may not be a sustainable shape for neural stimulation as larger cathodic polarisation and enhanced dissolution were reported [Cogan et al., 2014, Park et al., 2019]. In this experiment, larger cathodic polarisations were also recorded, as the cathodic potential was located in the hydrogen evolution region instead of the PtO reduction peak as observed in previous experiments (cf 6.1). The results imply that the electrode undergoes PtO formation in the anodic phase and H-reduction in the cathodic phase, possibly after reducing PtO. Park et al. [2019] report significantly faster dissolution rates for fractal Pt electrodes at $k = 0.93$, which is lower than the k-values used in this study, suggesting the damage threshold may have been lower than $k = 1.25$, explaining the cathodic polarisation potentials beyond the oxide reduction peak. Platinum dissolution was shown to begin at the electrode edge [Doering et al., 2022, Nagashima et al., 2019], which correlates with the high current density area. As the total current was shown to scale with electrode perimeter [Park et al., 2018], Shannon's plot, which relates charge/phase and charge density, may be understood as a relationship between electrode perimeter and electrode area. Therefore, I postulate

that large P/A electrodes reach Pt dissolution thresholds faster because of the larger edge charge density and enhanced diffusion profile. Because of the larger reaction rate at the edge, concentration overpotentials arise, increasing the electrode cathodic polarisation, which reaches potentials favourable for hydrogen adsorption. Charge density may even exceed the safe potential limits in high charge density areas, as Weiland et al. [2002] report charge densities exceeding the water electrolysis threshold at the corners of a square electrode. From this extrapolation, the hypothesis may be formulated that during neural stimulation, the safe stimulation limit of $k = 1.75$ corresponds to the onset of platinum dissolution through repeated cycles of oxidation and reduction of platinum oxide on the bulk of the electrode, and in parallel, hydrogen adsorption or water reduction at the electrode edge. Hydrogen reduction at the electrode edge may occasion local pH shifts and concentration gradients which may influence electrochemical reactions (see 6.1). Furthermore, Schulte et al. [2024] demonstrated the correlation of mechanical micromotion following electrical stimulation and Pt dissolution, which was again mainly located at the edge of circular electrodes (444 μm diameter). The mechanical micromotion was attributed to cyclic expansion-contraction cycles induced by electrochemical reactions, which are hypothesised to be Pt oxide formation and hydrogen storage (hydrogen adsorption), which are the two pending reactions observed as the extreme polarisation during charge-balanced biphasic pulsing.

Similar features for recessed electrodes were also observed on the EIS measurements: the introduction of a recess decreased the CPE α coefficient describing the double-layer capacitance perfection, which means that the electrode surface had a less uniform behaviour with the presence of a recess, possibly indicating a predominance of diffusion effects (Warburg element). Indeed, a large P/A ratio was shown to also influence faradaic reactions by reducing the Warburg coefficient and the non-linear resistance [Park et al., 2018]. The non-uniformity of the C_{dl} correlating to the presence of recess may also be attributable to a manufacturing flaw, namely the contamination of the sur-

face with epoxy, which may harm the double-layer arrangements. Future work should aim to improve the accuracy of the experimental results by manufacturing large AR strip electrodes without a recess and compare the performance under the same conditions, to disentangle the effects of electrode shape and recess. In the discussion of the advantages of large P/A electrodes, Cogan et al. [2014] suggest that such electrodes may be more beneficial in limited diffusion environments because of the enhanced diffusion profile at the edge. In this case, the large AR electrode was not tested in agar or gelatin gels (see 6.3) because of the difficulty introduced by a recess, therefore, a non-recessed large AR electrode would allow to further this investigation. The shape of the electrode may also be modified as the long strip electrode showed discrepancies in EIS measurements (lower R_A and lower phase) between the middle and the edges, which are attributed to the average distance between RE and WE. A ring electrode may offer this advantage of increasing the perimeter while reducing the average distance between RE and WE, however, studies have shown that the outer perimeter dominates the electrode behaviour [Watterson et al., 2017, Park et al., 2018], which may call for a more complex design.

Chapter 5

Effects of stimulation parameters

The stimulation waveform is crucial for successful electrical therapy outcomes, and strategies to design safe and efficient stimulation protocols were detailed in 1.3.2. In this chapter, the effect of varying the pulse width was investigated, however, there are a few other parameters that may influence charge injection and that were not investigated in this thesis, which are discussed briefly in the following paragraph.

Biphasic pulses are the clinical and bench-top standard as the charge reversal phase allows the electrode to return to a neutral state, which improves long-term performance [Merrill et al., 2005], although recent studies showed higher dissolution rates were measured for biphasic pulses versus monophasic pulses [Kumsa et al., 2016a]. Most biphasic pulses are symmetric square, as they offer a straightforward option to ensure charge balance, however, I worked here with an asymmetric waveform with an anodic capacitor discharge to allow quick charge reversal to maximise electrochemical reversibility [Merrill et al., 2005, Kumsa et al., 2016b, Gorman and Mortimer, 1983], see also 3.1. However, sharp edges in the current waveforms were shown to induce current density non-uniformity, increasing edge effect and therefore, participating to charge imbalance [Behrend et al., 2008]. Therefore, the extent to which the pulse asymmetry helps with electrochemical charge balance has not been quantified

in this work, as it was not compared to other waveforms, which should be the case in future work. The interphase period delays the charge reversal phase to ensure that the stimulation phase could elicit the desired effect, however, the interphase delay may also induce more corrosion by keeping the electrode in a favourable state [Merrill et al., 2005, Kumsa et al., 2016a, Mortimer and Bhadra, 2018]. The interphase was kept constant in all experiments, however, future work could investigate the influence of interphase delay on potential ratcheting. Cathodic-first pulses are predominantly used in neural stimulation [Niederhoffer et al., 2023b], offering a more efficient, direct stimulation and less destabilisation of the interface than anodic-first pulses [Doering et al., 2023]. AF pulses also correlated with larger dissolution [Black and Hannaker, 1979, Kumsa et al., 2016a]. Last, frequency may cause neural damage by overstimulating neurons or by polarising the interface if the interface is not left to stabilise. Frequency was set at 50 Hz to let the capacitor discharge in the anodic phase and increasing frequency may have been possible to an extent, as the capacitor discharge proved to be complete in a few μs.

5.1 Effect of varying the pulse width

5.1.1 Rationale for varying k with pulse width

During neural stimulation shorter pulse widths (PW) tend to have a higher efficiency [Crago et al., 1974, Butterwick et al., 2007], as shorter PWs are located closer to chronaxie, stemming from the Weiss-Lapicque equation (Fig. 1.2). Shorter pulses are also favoured for safety concerns [Merrill et al., 2005]), as kinetics and mass-transport phenomena are more likely to influence reactions at the interface with longer pulses, for instance by having new reactions available, which could not happen on shorter PWs because of their sluggishness, or by prolonging some reactions where reactants would become exhausted in short pulses by allowing diffusion to supply reactant to the interface. Mortimer et al. [1980] reported an increased rate of electrode failure due to electrode degradation when using larger PWs. Regarding Shannon's limit, varying the current

and the PW should have a similar influence on neural damage as k is based on injected charge, which is the product of intensity and PW. Kumsa et al. [2016b] varied k by changing the current, with a set PW of 100 μs. k can be varied in a similar way by changing only the PW, keeping the current constant. However, varying current and PW may have different effects on the electrode behaviour and electrochemical mechanisms. The electrode polarisation was shown to be larger for shorter PWs at equal charge/phase, even after ohmic drop correction on iridium oxide coated electrodes [Cogan, 2008]. *In vivo*, different PWs were found to recruit slightly different nerve fiber diameters, although only up to 200 μs [Szlavik and de Bruin, 1999]. The CIL was shown to scale almost linearly with PW on activated iridium oxide films (AIROF) and sputtered iridium oxide films (SIROF) [Cogan et al., 2005, 2009]. PEDOT electrodes with various coatings and surface treatments had a similar trend, however, the slope was different depending on the interface state (coating, roughening) and on the presence of serum, which showed a smaller slope than in simple PBS [Green et al., 2011, 2012a, 2013]. Therefore, although theoretically pulse width should not have a different effect on the safe stimulation limit than stimulation intensity (regarding Shannon's limit), experimentally, longer pulses are still associated with more corrosion [Black and Hannaker, 1979]. As the Pt dissolution is a millisecond-timescale process [Cho et al., 2023], pulse widths approaching 1 ms may induce dissolution before the charge reversal phase. As Pt corrosion is a leading hypothesis to explain Shannon's limit, corrosive behaviour may be observed at a lower threshold when changing k by changing the pulse width rather than the current.

5.1.2 Specific methods for pulse width experiments

For PW experiments, I used a 5-mm diameter Pt electrode in the same three-electrode setup as other experiments, however, the execution of the protocol was slightly different. Each set of measurements (n = 5) was performed at a single current value, so the current was set at the desired value before the first conditioning sequence and not changed afterwards. To change k, the PW

was varied by changing the pulse timings in the Arduino coding sequence (see Table 5.1). Therefore, a new code needed to be uploaded to the microcontroller before every pulse train, which was done at the start of the pulses, whereas usual pulses were started using the "Reset" button on the Arduino board. These two manoeuvres had different timings (almost instantaneous start for the reset button, $\approx$ 5 s to 10 s loading otherwise) but the protocol was kept consistent to have comparable results.

Studying the effect of varying k through PW only requires one current value, however, various currents correspond to substantially different PWs (as shown in Table 5.1), hence the need to test at different current values. Therefore, three current values were used, which corresponded to the range of currents that was used in set PW experiments: 5 mA, 20 mA, and 40 mA. Pws are inversely proportional to current, therefore, cathodic pulses were eight times longer at 5 mA than 40 mA at equal k-values. This posed the question of interphase delay, which was kept at 100 μs (equal to the initially used PW), as there is no rationale to have the interphase delay equal to the cathodic PW, the intrinsic values have more meaning as it should delay the anodic pulse enough to illicit neural stimulation while avoiding net DC current, which may lead to harmful reactions including Pt dissolution (see 1.3).

Two electrolytes were tested in these conditions: one buffered, PBS, and one unbuffered, pH 6 saline.

Table 5.1: *Table of pulse widths to achieve k-values for various cathodic currents with a 5 mm diameter Pt disc electrode.*

k	Δt_{5mA} (μs)	Δt_{20mA} (μs)	Δt_{40mA} (μs)
0.566	170	43	21
1.24	369	92	46
1.55	528	132	66
1.66	599	150	75
1.75	665	166	83
1.85	746	186	93
2	886	222	111

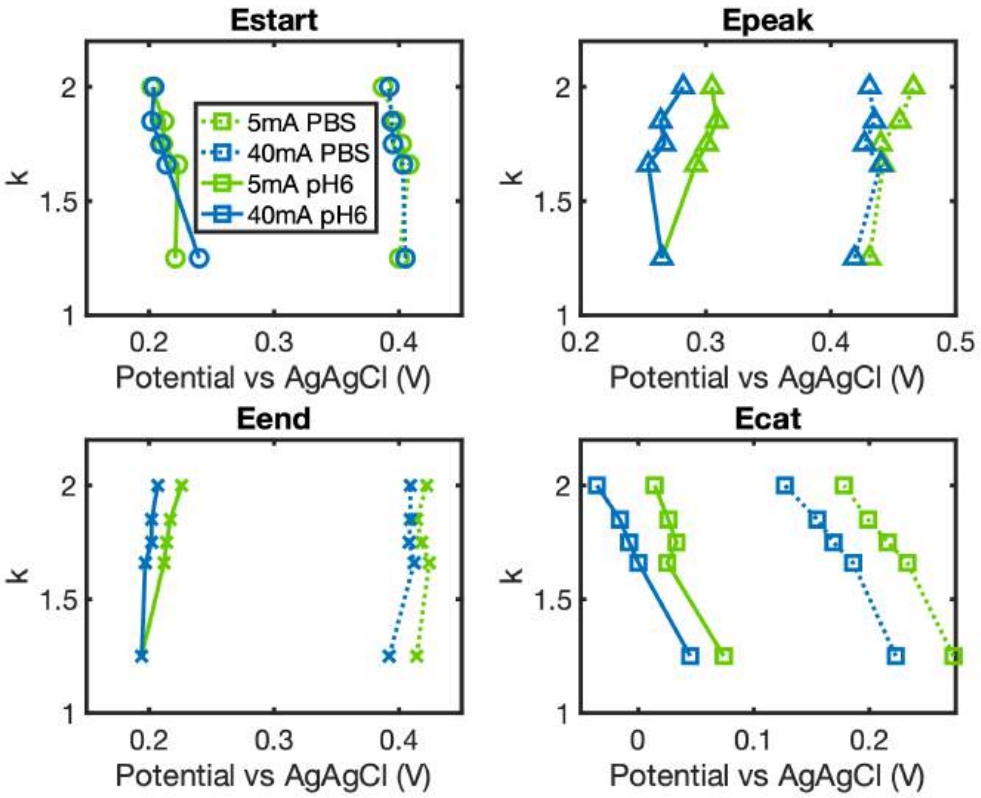

Figure 5.1: *Comparison of raw potentials in PBS and pH 6 saline while varying the pulse widths for cathodic currents of 5 mA and 40 mA. Current values are distinguished by colours and electrolytes by line styles.*

5.1.3 Results

The effect of PW was assessed in buffered and unbuffered electrolytes to determine whether buffer exhaustion influenced the polarisation. The results are compared between the longest and the shortest PW, which are identified by the cathodic current values as PW was varying with k. Raw potential traces (Fig. 5.1) showed that the PBS traces were grouped by electrolyte, with highly similar trends for E_{start}, E_{ano}, and E_{end} and a little more discrepancy between the PW for E_{cat}. E_{cat} was lower at 40 mA than 5 mA for both PBS and NaCl, while E_{ano} and E_{end} were larger for 5 mA, with larger discrepancies in unbuffered saline. The discrepancies due to electrolyte differences were removed by subtracting E_{start} in figure 5.2. Variations in E_{ano} were very similar for all

PW, for both electrolytes. The trends in E_{end} were similar for both electrolytes with similar spans ($\approx$ 30 mV), although E_{end} remained higher in PBS for both PW. E_{cat} polarisations show two interesting points: first, both 40 mA polarisations were more negative (larger polarisation) than the 5 polarisations, and second, the spans were shorter for pH 6 NaCl than for PBS, although this could be due to increased noise. Polarisation potentials were corrected by adding the starting OCP measured by the potentiostat as the starting potential (Fig. 5.3). The correction of polarisations with the OCP showed less obvious trends, which suggests that the differences between PWs and between electrolytes were limited. E_{cat} still showed that larger PW resulted in larger cathodic excursions in PBS than in pH 6 saline, and that within electrolytes, the excursions were larger for 40 mA pulses than 5 mA pulses. With NaCl, it seems clearer that 5 mA excursions are smaller both in terms of span and in terms of absolute potential. While E_{end} and E_{ano} seemed similar in figure 5.2, the OCP correction introduced a positive offset for the 40 mA NaCl traces, which may be an artefact in this case.

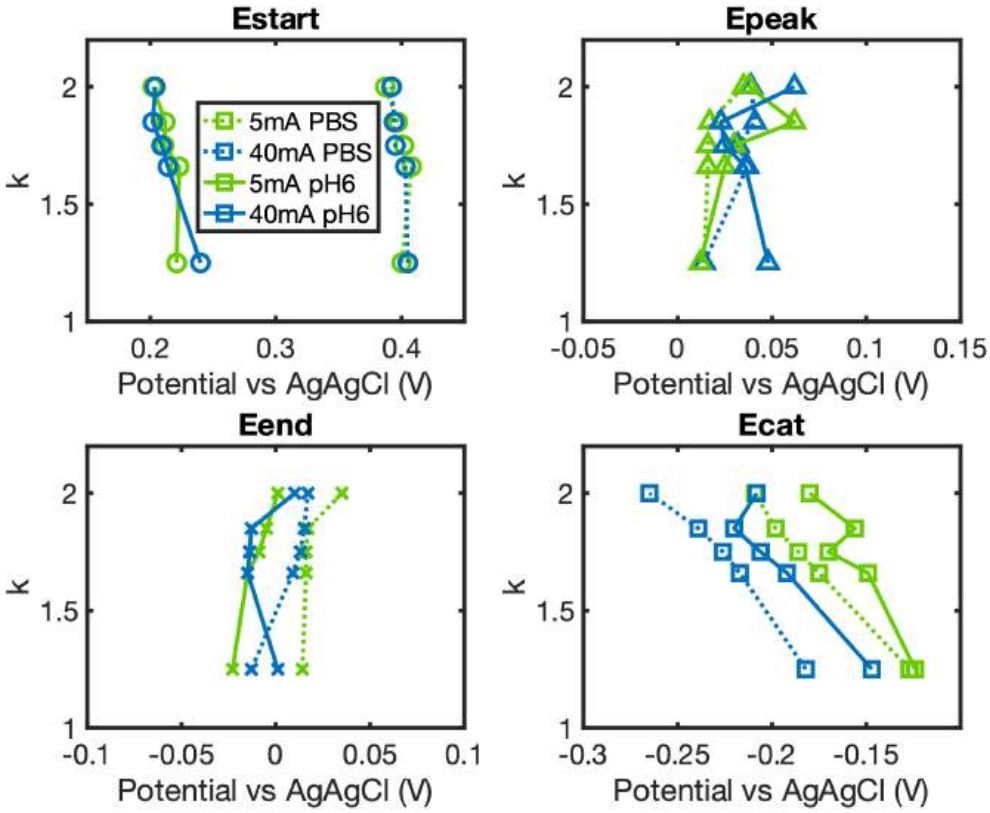

Figure 5.2: *Comparison of polarisations in PBS and pH 6 saline while varying the pulse widths for cathodic currents of 5 mA and 40 mA. Current values are distinguished by colours and electrolytes by line styles.*

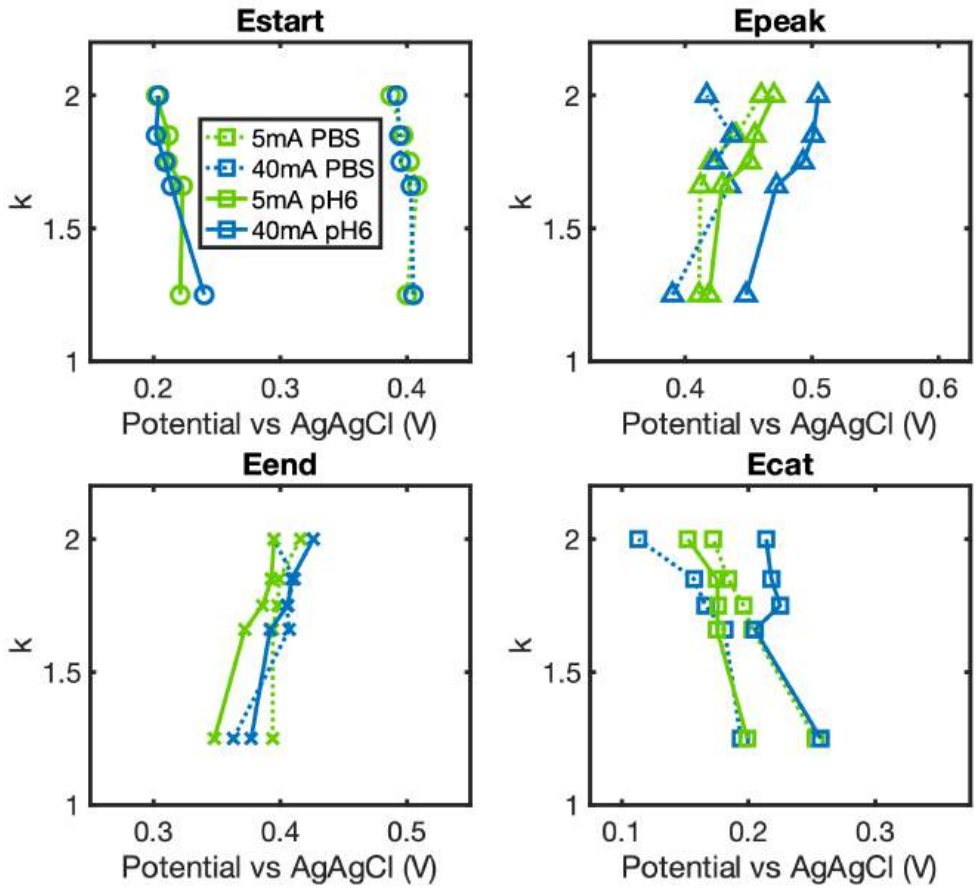

Figure 5.3: *Comparison of real potentials in PBS and pH 6 saline while varying the pulse widths for cathodic currents of 5 mA and 40 mA. Current values are distinguished by colors and electrolytes by line styles.*

5.1.4 Discussion

The effect of PW on charge injection during biphasic charge-balanced pulses was investigated to compare with the effect of varying current intensity. k was increased by increasing the PW up to fivefold at three different currents: from 21 μs to 111 μs for 40 mA, 43 μs to 222 μs for 20 mA, and 170 μs to 886 μs for 5 mA. At equal charge/phase, longer PWs (around 1 ms and higher) favour diffusion and slower kinetics mechanism, possibly leaving the electrode in a dissolution-favourable state for longer periods, while shorter PWs induce larger polarisation due to non-uniform current density, which may trigger un-

safe mechanisms [Mortimer and Bhadra, 2018, Cogan, 2008]. The potential-dependent chemical dissolution of Pt occurs on a millisecond timescale [Cho et al., 2023], meaning that upon reaching favourable potentials Pt will start dissolving after a few ms. This dissolution mechanism may occur during long interphase delays, keeping the electrode within corrosion-favourable potentials. However, the dissolution mechanism during biphasic pulses is likely to be different, relying on repetitive oxidation and reduction of Pt, with oxygen atoms migrating within the first layers of Pt, releasing pockets of Pt upon reduction [Shah et al., 2024, Cherevko et al., 2014]. Therefore, on one hand, longer PWs may increase oxygen atom diffusion inside Pt, but on the other hand, shorter PWs present larger polarisations which increase the Pt oxidation and reduction proportions, which may induce more dissolution. These two competing factors may explain why the polarisation traces with k were not substantially different for different PWs. The lowest current value of 5 mA was chosen as the lowest achievable current presenting a sufficient ohmic drop to allow precise current measurements. This value was of specific interest as it represented the low current-large PW situation, which was likely to exacerbate irreversible mechanisms and may favour mechanisms with slow kinetics. The trends of polarisation with k were independent of PW for both electrolytes and the differences in polarisation remained small (few tens of mV), which revealed an important influence of voltage correction. The following analysis is based on the raw voltage measurements (Fig. 5.1) as all potential measurements were consistent. E_{cat} was larger for 5 mA, meaning a smaller polarisation, and exhibited a slightly less rounded shape for the 5 mA, suggesting that at long pulse widths, less polarisation was required to inject the same amount of charge, confirming that longer PWs induce smaller cathodic polarisation as observed by Cogan [2008], Cogan et al. [2014] on AIROF and Pt electrodes. The CIL was not measured in this work, however, CIL correlates directly with the cathodic polarisation (CIL corresponds to E_{cat} exceeding the water window), therefore, the measurements also suggest that CIL is positively correlated with PW as suggested

by Green et al. 2011, 2012a, 2013. It is worth noting that the safe limits used to calculate CIL are different than the limits considered in this study, as usual CIL limits are based on exceeding water electrolysis potentials, whereas this experiment considers a charge density to charge/phase ratio, which may trigger noxious reactions within the water window. Therefore, trends on k may differ from trends on CIL. For instance, the CIL does not offer information on the anodic polarisation, which was shown to be larger for the shorter PW. E_{end} was also larger for the shorter PW, showing a greater increase with k in NaCl than longer PW, which suggests more potential ratcheting during pulses. Therefore, these experiments suggest that although the cathodic polarisation and CIL are lower for larger PW, more Pt dissolution may be induced by larger potential ratcheting. Reduction of molecular oxygen is a diffusion-limited cathodic reaction, which is a source of irreversible charge injection and may induce potential ratcheting [Merrill et al., 2005, Kumsa et al., 2016b]. As longer pulse widths favour timely processes such as diffusion, the hypothesis can be made that the extra polarisation observed for larger currents (smaller PW) occurs to overcome diffusion overpotentials, whereas at large pulse widths natural diffusion is able to supply reactants to the electrode surface. Lower polarisation may be due to a slower passage of current through the interface, which causes "true" interface polarisation with well-established diffusion paths, whereas high current transfer during quick pulses causes larger current distribution non-uniformity, depleting the electrolyte locally and inducing concentration overpotentials in a diffusion-limited regime. Therefore, the favoured diffusion for larger PWs enable more molecular O_2 reduction, creating more charge imbalance, which translates into larger anodic polarisation after 1000 biphasic pulses. With larger E_{ano}, more Pt oxide is formed, which was shown to be proportional to the dissolution rate [Topalov et al., 2014a], although the subsequent reduction of Pt oxide leading to dissolution is not guaranteed as E_{cat} was smaller for larger PW. The effect of PW was shown to depend on electrode dimensions and perimeter-to-area (P/A) ratio [Cogan et al., 2014],

which suggests a particular importance of edge effect and current distribution uniformity. E_{cat} was shown to decrease with P/A and CIL to increase with P/A with an exacerbated increase with PW: E_{cat} decreased more with P/A at small PW and the increase in CIL with PW was slightly larger at larger P/A for smaller electrode, with no significant difference with P/A for larger electrodes [Cogan et al., 2014]. Both results point to a threshold related to the P/A ratio (electrode dimensions also influence P/A) and small PW which indicate an influence of the current density distribution and diffusion. Increasing P/A increases the diffusion availability [Green et al., 2012b, Cogan et al., 2014], which has a greater influence at short PW to mitigate higher non-uniformities in the current distribution. The greater influence of P/A on the increase in CIL with PW for small electrodes can also be explained by the diffusion profile, which is closer to a hemisphere for smaller electrodes than a linear profile. This combination of effects suggests that enhanced diffusion plays a more important role in the safe stimulation limits than the non-uniformity of charge injection creating local overpotentials. Due to the large dimensions of the range of electrodes used in this work, the observations by Cogan et al. [2014] suggest no significant effect of P/A would have been observed. Further experiments may be conducted to validate the hypotheses raised in this chapter, including removing dissolved oxygen from the solution and enhancing/hindering diffusion to measure the consequential changes. To conclude, my results suggest that longer PW may increase Pt dissolution during biphasic pulses although longer PW pulses exhibit a smaller cathodic polarisation, which unifies previous contradictory results showing that longer PW increase the CIL but also Pt dissolution.

A concern arose when designing the PW experiments: how reliable was the capacitor to retain the cathodic charge over nearly 1 ms pulses. Some degree of leakage was already measured over short pulses (see 3.2), and more leakage would cause further imbalance, which would yield less potential ratcheting and overall change the electrode's state [Merrill et al., 2005, Kumsa et al.,

2019]. The capacitor's leakage was tested first by integrating the area under the current waveform in the cathodic phase and anodic phase separately. Five k-values were tested for the three current values and compared to k-values for 100 μs pulses and varying intensities. The imbalance average and standard deviation are reported for all pulse types along with the cathodic and anodic charge accuracies ($\frac{(Q_{meas}-Q_{theo})}{Q_{theo}}$) are reported in table 5.2. The imbalance was consistent for all pulse types, between 4 % and 9 %, with the highest average imbalance recorded for the set 100 μs PW. Although 5 mA pulses had the largest variability in imbalance, it did not present a substantially larger imbalance than other currents, therefore, larger leakage for longer pulses can be ruled out. 5 mA pulses also presented a cathodic charge that was lower than the theoretically injected charge on average, whereas other pulse types had consistently larger Q_{cat}, which further shows that 5 mA was more prone to imprecision. Q_{ano} was consistently lower than the theoretically injected charge for all pulse types.

Table 5.2: *Table of measured charge imbalance and charge accuracy in both phases for various pulse widths*

Pulse type	**Average imbalance ± std**	Q_{cat} **accuracy**	Q_{ano} **accuracy**
100 μs	8.28 ± 3.26 %	3.47 %	-5.10 %
5 mA	4.22 ± 8.85 % *	-0.92 %	-5.48 %
20 mA	4.42 ± 2.29 %	2.34 %	-2.18 %
40 mA	6.13 ± 3.13 %	1.29 %	-4.92 %

* Without the negative imbalance for $k = 1.25$, the imbalance was 7.73 ± 6.31 %.

Chapter 6

Effects of solution composition

While electrode design determines the physics of electrical charge injection by shaping the charge density distribution and electric field, the electrolyte has an influence on the actual charge injection mechanisms, the thermodynamics and kinetics of (electro)chemical reactions, thus complementing the previous chapters on electrode design (4) and stimulation protocol (5). The electrolyte composition affects the double-layer capacitance (influence of adsorbed species, pH, solvent), thus the capacitive charge injection, and the faradaic reactions (ions in presence, concentration, affinity with the electrode). Tissue can be modelled in bench-top studies by saline solutions [Boehler et al., 2020a], however, the *in vivo* environment is very complex, including various ions, dissolved gases, proteins, and cells, which may all contribute in different situations, in various proportions to charge injection. This chapter aims at studying the individual effects of a variety of electrolyte parameters on the charge injection behaviour during biphasic charge-balanced pulses, including pH (6.1), ionic strength (6.2), gel structure (6.3), buffer type (6.4), and dissolved gases (6.5). Parameters were combined in a few situations to uncover co-dependent effects, including using the large AR electrode to study changes on the edge effects.

6.1 Influence of electrolyte pH in unbuffered saline

The results presented in this section were presented at a conference (IEEE Biosensors 2023) as a 4-page paper published in the conference proceedings [Niederhoffer et al., 2023a] and featured in a journal paper in Journal of Neural Engineering [Niederhoffer et al., 2024].

6.1.1 Rationale for studying electrolytes of different pH

Shannon's damage threshold has been associated with platinum oxide formation in studies performed in sulfuric acid [Kumsa et al., 2016b] and subcutaneously in rats [Kumsa et al., 2017], which showed that above a charge injection threshold, platinum oxide is likely formed, which would eventually result in platinum dissolution [Kumsa et al., 2016b], which may cause subsequent neural damage [Agnew et al., 1977]. In this thesis, I reproduced the same approach in alternative electrolytes to understand how electrolyte characteristics affect charge injection mechanisms near Shannon's limit, thereby deepening the understanding of electrode behaviour near Shannon's limit. Sulfuric acid (H_2SO_4) is an electrolyte that is substantially different than tissue, especially because of the pH shift (pH 1 in H_2SO_4 and pH 7.4 in the body), although the authors argue that all charge injection mechanisms are unchanged [Kumsa et al., 2016b]. Some faradaic reactions may induce pH variations [Merrill et al., 2005], for example molecular oxygen reduction (see 1.16), however, pH shift is usually not considered as a major source of neural damage, as pH is regulated by the body's buffers. In benchtop tests, buffered electrolytes, such as PBS, are usually used to reproduce the buffering system in the body and mitigate pH changes. However, the buffering capacity in the body was shown to be overestimated by PBS [Harris et al., 2019a] and may be temporarily exhausted locally during neural stimulation [Weltin and Kieninger, 2021], which may explain the different electrode behaviour measured *in vitro* and *in vivo*. Since the body buffer may be exhausted at the electrode surface, pH changes may

arise, which may change the electrode behaviour. In a mathematical modelling study, the pH showed to steer away from 7.4 only in the first few μm away from the electrode [Ballestrasse et al., 1985, Huang et al., 2001], however, the pH shift at the electrode surface may be significant (> 3) [Ballestrasse et al., 1985]. Huang et al. [2001] compared the pH shifts at Pt electrodes during biphasic stimulation in PBS, unbuffered saline and *in vivo*, and demonstrated that pH shifted by 1 pH unit at 0.2 mm from the electrode surface both in saline and *in vivo*. These results were achieved at a stimulation equivalent to $k \approx 1.36$, at 1000 pulses per second, with the pH shift shown to depend on stimulation intensity, pulse frequency, and distance of the pH sensor to the electrode. Thus, regarding the expected larger stimulation intensity (up to 10 times) and 20 times fewer pulses, the magnitude of pH shifts close to the electrode was expected to be larger than measured by Huang et al. [2001], as suggested by Huang et al. [2001] and Ballestrasse et al. [1985]. Therefore, to study the extreme case of buffer exhaustion and how different pH values affect electrode behaviour, I chose to use unbuffered saline, which allowed me to voluntarily steer the pH across a wide range. Huang et al. [2001] also showed that buffering the electrolyte cancelled the pH shift, as did a series capacitor. Thus in this study, the applied stimulus was expected to cause a pH shift at the electrode surface; however, the addition of a series capacitor for anodic discharge may have cancelled the effective pH shifts I wanted to study. Therefore, to study the effect of a pH shift on the charge injection mechanisms in this pulsing regime, unbuffered saline was used, manually adjusted the pH across a wide range, and measured the potential excursions in these conditions.

6.1.2 Specific methods for pH experiments

Unbuffered saline solutions were prepared by mixing a sodium chloride (NaCl) saline solution with hydrochloric acid (HCl) or sodium hydroxide (NaOH) to adjust pH to the desired value. Medical grade NaCl (MW: 58.45 $g.mol^{-1}$, Promega) was diluted in deionized water (DW, 15.6 $M\Omega$, Millipure system) at a concentration of 18 $g.L^{-1}$ or twice the isotonic concentration (0.9%w/v,

equivalent to 9 $g.L^{-1}$). HCl (1 M, Sigma-Aldrich) and NaOH (crystals, BDH) were diluted at twice the desired concentration in DW and mixed in a 1:1 ratio with 18 $g.L^{-1}$ NaCl to have an isotonic 9 $g.L^{-1}$ solution of desired pH. Solutions were not degassed before experiments and were carried out in equilibrium with the ambient oxygen concentration (21%). Solution pH was measured before and immediately after every set of measurements (5 or 7 k-values) to detect possible chemical changes in the unbuffered electrolyte.

A three-electrode setup was used, a 5 mm-diameter platinum disk WE (geometric surface area = 19.635 mm^2, Roughness factor 1.29), an Ag|AgCl RE and a carbon rod counter electrode (CE), were placed in a 150 mL chamber (Pine Research RRPG310). The WE roughness was determined using the charge of hydrogen adsorption in sulfuric acid and dividing by the theoretical value of $Q_H = 210\,\mu C/cm^2$ [Topalov et al., 2014a, Weltin et al., 2019], which yielded a roughness factor of 1.29, hence a real surface area of 25.3 mm^2. Before being placed in solution, the WE surface was cleaned with acetone and isopropyl alcohol.

6.1.3 Results

For reliable comparisons between results the electrode-electrolyte interface needed to return to a consistent state between pulsing experiments. The conditioning sequence was developed with that intention, with CV reestablishing the surface state through repetitive oxidation and reduction, and EIS and OCP used to monitor for interface changes. It was not assumed that stable EIS and OCP implied that no surface dissolution occurs, instead that the surface was returned to a similar starting condition between current-controlled pulse trains to allow for comparison between sequential experimental steps.

The first conditioning CV, performed before the first pulse train, decreased the high-frequency impedance of electrodes (not shown). After a change following the first conditioning CV, the EIS response remained consistent, neither CV nor pulse trains affected the EIS values, showing that the interface conditioning protocol was suitable. Fig. 6.1 shows the relationship between

measured OCP and pH and compares the trend to the Nernstian response for a single electron transfer. Each data point corresponds to the average of stabilised OCP values after pulsing trains (n = 7, OCP taken at the end of the first step of the testing sequence). Mean and variability of OCP within experiments (OCP after each pulsing test, n = 7) are given in appendix B figure 2.1. OCP remained stable throughout experiments, with a maximum standard deviation of ±11.75 mV within a single pulsing test series (typically conducted in a single day of experimentation). For each pulsing test series, the mean OCP was plotted against pH (Fig. 6.1) to verify that OCP varied with pH following Nernst's relation. A linear fit yielded a gradient of -48.1 $mV.pH^{-1}$ such that the expected Nernstian response, –59 $mV.pH^{-1}$, was not within the 95% confidence interval (CI) [-53 $mV.pH^{-1}$; -43 $mV.pH^{-1}$] due to large residuals observed at low pH. A fit excluding pH < 4 showed a gradient of -56.2 $mV.pH^{-1}$ with a 95% CI of [-62 $mV.pH^{-1}$; -50 $mV.pH^{-1}$], hence a single electron Nernstian response. The deviation from a -59mV/pH slope at low pH shows that the acid-base equilibrium reaction does not follow a single-electron transfer regime. A shallower slope indicates a shift towards a multi-electron transfer (-29.5 mV/pH for a two-electron transfer), therefore, I suggest that a multi-electron transfer regime occurs at pH ≤ 4.

Saline solutions from pH 4 to pH 12 showed similar impedance Bode plots (Fig. 6.2 A.), with only a slightly lower impedance at high frequencies (f $>$ 1 kHz) for pH 12. pH 1 was substantially different, showing a three to four times lower impedance at high frequencies and transitioning to capacitive behaviour at higher frequencies than other pH values, by about one order of magnitude. EIS data were fitted using the Simplex method of the Gamry Echem analyst software, using the autofit function to determine the coefficients. A Randle's model and a CPE model (CPE in parallel in faradaic impedance, in series with solution resistance) were compared. The CPE model was generally a slightly better fit, especially in the phase transition region, however, the values for R_A and C_{dl} (or Q_{dl} for the CPE) were similar (2% discrepancy on R_A and 18% on

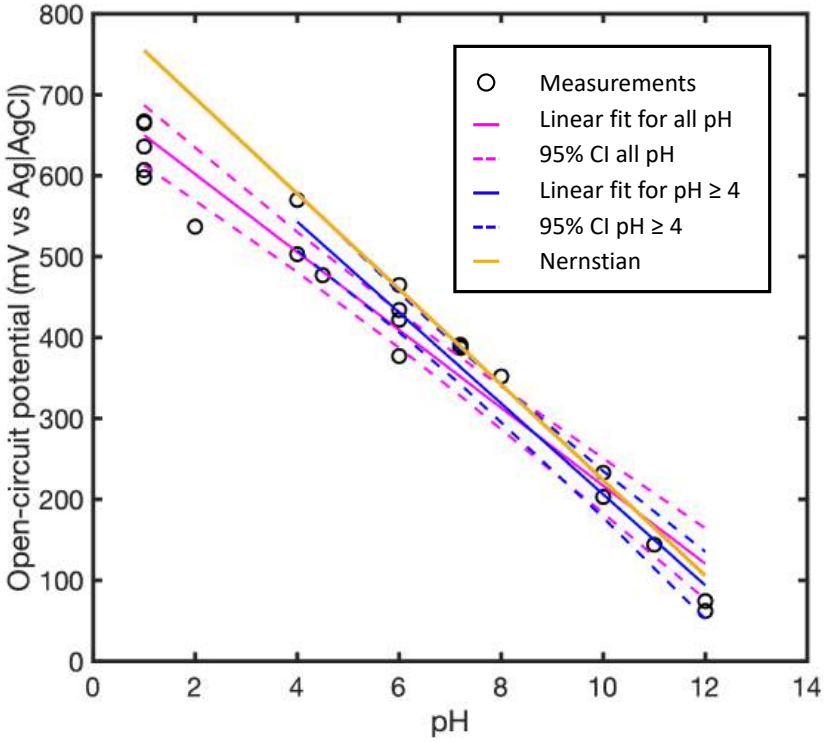

Figure 6.1: *Experimental open-circuit potential values plotted against pH and compared with Nernst's equation. Linear fits are represented with their respective 95% confidence intervals.*

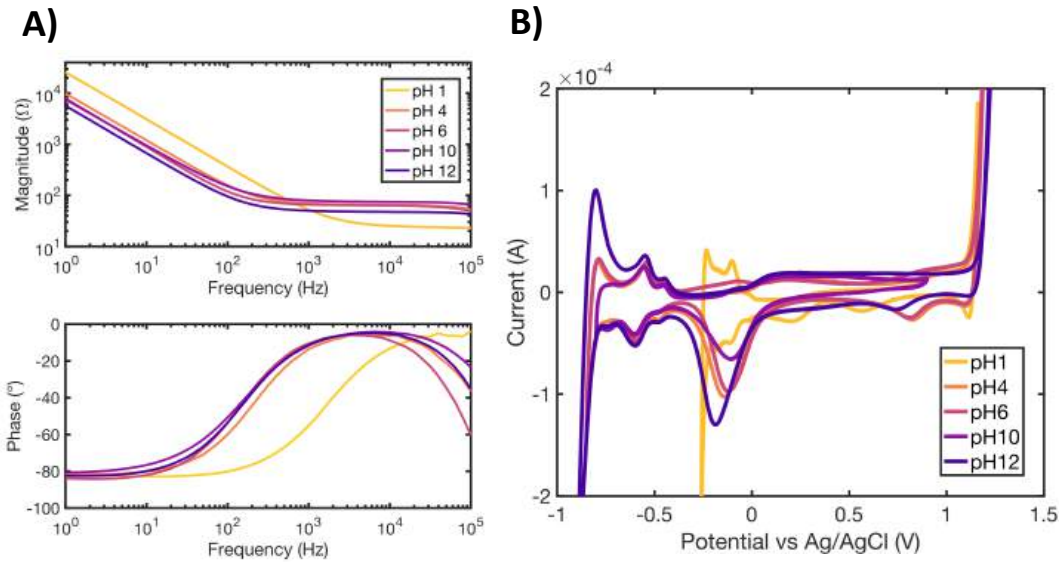

Figure 6.2: *A. Bode plot of the impedance spectrum for isotonic saline solutions of pH from 1 to 12 with impedance magnitude at the top and phase at the bottom. B. Cyclic voltammograms for solution electrolytes of pH from 1 to 12.*

C_{dl}). The fitted values for R_A corresponded to the observations on the Bode plot, with pH 1 R_A being half of pH 12, a third of pH 4 and 6, and a quarter of pH 10. C_{dl} increased with pH with pH 1 and 4 exhibiting similar values ($\approx$ 7 μF), which were three times smaller than pH 6 and 10 ($\approx$ 20 μF) and eight times smaller than pH 12 ($\approx$ 50 μF).

CVs were stable throughout pulsing experiments. CVs were expected to exhibit similar peaks, only shifted along the potential axis according to Nernst's relation (Fig. 6.2 B.). pH 1 H-evolution and pH 12 O-evolution were expected to differ from other pH values. pH 1 and 12 had narrower water windows than pH 4, 6 and 10, which exhibited similar voltammograms. pH 1 was shifted towards higher potential as expected, and the pH 1 voltammogram showed differences in the H-evolution region (E $<$ 0 V vs Ag|AgCl), exhibiting a wider voltammogram in that region and peaks closer to one another, and an oxide reduction peak split into two distinct peaks (E $\approx$ 0.2 V and E $\approx$ 0.55 V). For pH 12, and slightly less for pH 10, 6 and 4, H-peaks were more spaced due to a scarcer presence of H^+ ions, with higher overpotentials for H^+ ion interactions with the electrode surface [Ledezma-Yanez et al., 2017].

The WE potential at the last (1000^{th}) pulse was higher than at the first pulse, which indicates positive potential ratcheting (Fig. 6.3). Potential ratcheting is characteristic of asymmetrical charge injection mechanisms between the cathodic and anodic phase, leading to more irreversible charge injection in one phase, causing changes in the electrode-electrolyte interface potential. Positive ratcheting was observed for every experiment, although in various capacities. The current and potential waveforms were highly similar for all pH (not shown). The cathodic polarisation was slightly larger at pH 1, 4 and 10, and slightly lower for pH 12, compared to pH 6; the anodic recovery was similar at pH 4, 6, and 10, and had a rounder shape for pH 1 and 12. The anodic peak current was slightly larger for acidic pHs.

The maximum anodic potential (E_{ano}) was positively correlated with k. E_{ano} increased gradually with k, at a steeper rate for higher k-values (Fig. 6.4).

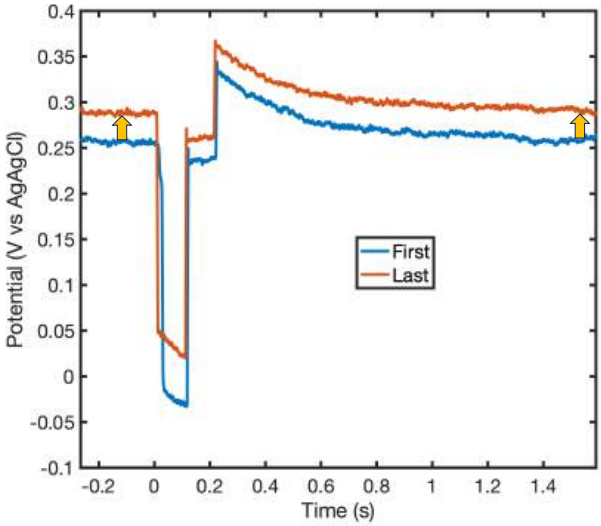

Figure 6.3: *Working electrode potential in PBS (pH = 7.4) during the first and last (1000^{th}) pulses of the pulse train, uncorrected for ohmic drop. The gradual increase in potential, or potential ratcheting, is shown by arrows.*

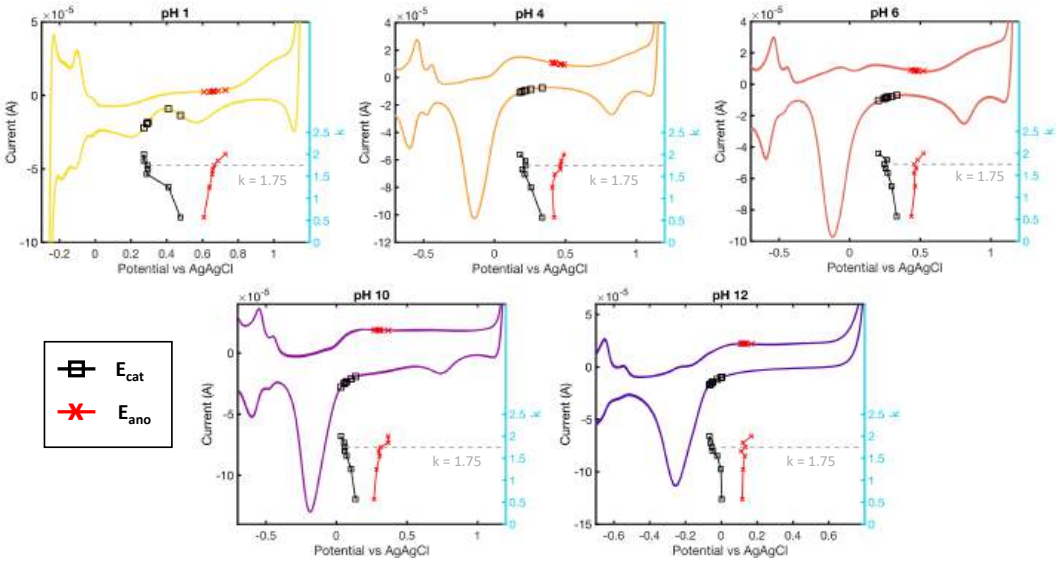

Figure 6.4: *Evolution of peak anodic potential (red) and peak cathodic potential (black) with k in saline solutions of pH from 1 to 12 and location on the respective cyclic voltammogram (100 $mV.s^{-1}$). Shannon's limit k = 1.75 is indicated by a dashed grey line.*

The trends are similar for all pH values, especially for pH 1, 6, and 12. In comparison, pH 4 transitions to a steeper increase at a lower k-value ($k \approx 1.3$ vs. $k \approx 1.7$ for other pH values), and pH 10 shows a step increase around $k \approx 1.75$ between two linear evolution regions. For every pH, E_{ano} was located in the oxide formation region independently of k, which suggests that even though E_{ano} increased with k and showed some steeper variations around Shannon's damage limit, the same electrochemical mechanism was available for charge injection.

The minimum cathodic potential (E_{cat}) was negatively correlated with k (Fig. 6.4). A decrease of E_{cat} with k was expected as increasing k equates to increasing i (k increases with increasing charge, which increases with increasing current), thus driving the potential more negative. At all pH except pH 1, the trend was similar with a steady decrease of E_{cat} with k, pH 6 and 12 showing a slightly steeper decrease from $k \approx 1.5$. At pH 1, E_{cat} decreased steeply at $k \leq 1.5$, then decreased at a much slower rate, almost plateauing. The location of E_{cat} on the voltammogram is interesting: while E_{cat} for pH 4 and 6 was between two peaks independent of k, pH 1, 10 and 12 E_{cat} entered an oxide reduction peak around Shannon's damage limit $k = 1.75$. The mechanism is apparent for pH 1 where E_{cat} transitions from one peak to the other, showing that there is a change of electrochemical mechanism when a certain amount of charge is injected.

The recovery OCP after pulses was different for various pH, showing that the re-equilibration of the interface involved different mechanisms or the same mechanisms at different kinetics (Fig 6.5). pH 1 and 12 showed a decrease in OCP, which was larger for pH 1, and pH 4, 6, and 10 an increase of OCP. pH 10 recovered its stable OCP more rapidly (within 200 s), while pH 4 and 6 showed a longer stabilisation period (double for pH 4 and triple for pH 6). pH 4 and 6 also showed several inflexions, similar to shoulders observed in CV, while other pHs exhibited a single arc to the stable value, which may explain the quicker recovery.

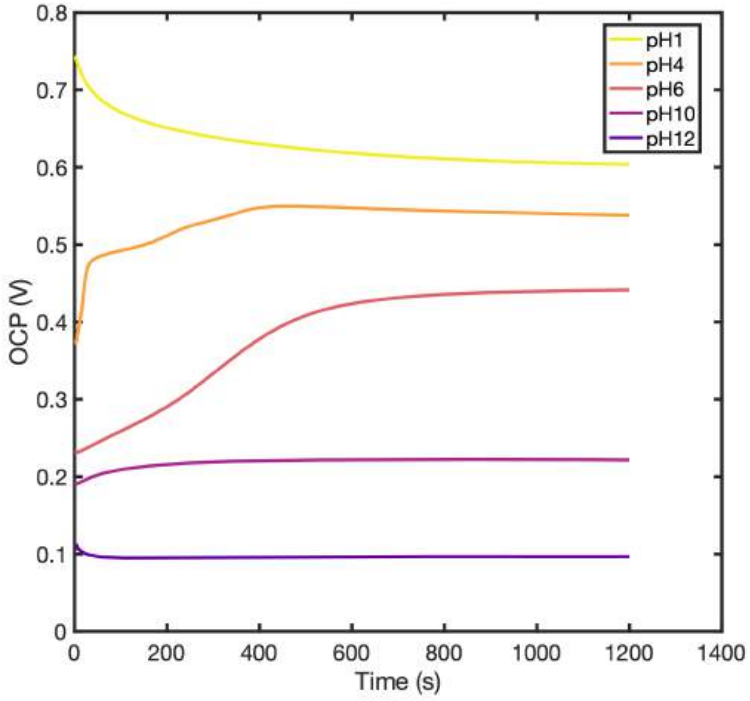

Figure 6.5: *OCP measured immediately after the end of pulse trains for saline solutions of pH ranging from 1 to 12 (average of three measurements).*

6.1.4 Discussion

6.1.4.1 Electrochemical impedance spectroscopy

The high-frequency impedance decrease observed after the first CV cycles is hypothesised to be due to electrochemical surface cleaning and surface activation following repeated oxidations and reductions. CV caused a conditioning of the surface, achieving a reproducible state, which explains why the EIS did not change through further stimulation. The lower high-frequency impedance and high-frequency transition to capacitive behaviour observed for pH 1 are attributed to the greater H^+ ion concentration, which have a high affinity with the electrode surface since H^+ ions participate in pseudocapacitive charge injection through H-plating [Puglia and Bowen, 2022]. The evolution of calculated double-layer capacitance values with pH was counter-intuitive, as one would expect a higher capacitance in acidic pH, due to the increased presence

of H^+ ions, which act as a pseudo-capacitance on platinum.

6.1.4.2 Cyclic voltammetry

The voltammograms present some differences from typical CVs reported in literature. Often, the baseline current in the H-evolution region is noticeably negative due to oxygen reduction [Musa et al., 2011, Hudak et al., 2010]. Here, the baseline current was effectively more negative in that region, but the shift was not very sharp, due to the large electrode size [Weltin and Kieninger, 2021]. The water window for isotonic saline [-0.9 V;+1.2 V] was wider than the usually reported [-0.6 V;+0.9 V] window in PBS, however, wider windows have been reported in the literature [Boehler et al., 2020a] and may be due to crystallographic structures and electrode surface states [Weltin and Kieninger, 2021]. The water window is also known to be wider in NaCl [Hudak et al., 2017a]. Daubinger et al. [2014] demonstrated the influence of pH on the width of the water window as acidic or basic electrolytes shared a similar width ($\approx$ 1.4 V) whereas neutral pH electrolytes, whether buffered or not, had a wider water window $\approx$ 2 V, which is similar to the width measured in this work. At a sufficient concentration of base or acid, the window shrunk around similar values as Daubinger et al. [2014] for pH 1 saline and slightly wider for pH 12 saline, which was less concentrated. The change in water window width was attributed to local pH changes and local buffer exhaustion, which demonstrates that such effects may occur, including during stimulation.

The absence of pH shift for pH 4, 6 and 10 is counter-intuitive but has been observed in fundamental electrochemistry: Strbac [2011] swept the potential on a Pt rotating disk electrode and found that diffusion-limited currents were different for pH < 3.5 and pH > 10 but no difference was observed in between. In low buffer concentrations, outside of extreme solution pH (pH < 3.5 and pH > 10), the local pH at the electrode surface changes, converging to a value that is independent of bulk pH and without changing the global solution pH. Therefore, even if the solution pH is measured at various values, the local pH will converge to the stable value, different from the solution pH and the

electrode behaviour will remain unchanged [Strbac, 2011, Liao et al., 2013, Briega-Martos et al., 2020]. The local pH change may not occur in buffered electrolytes due to efficient pH buffering, therefore, the results obtained in unbuffered saline may differ from results in buffered electrolytes.

The cleaning protocol was designed to leave the electrode surface with a natural partial oxide coverage, which may influence the charge injection mechanisms during pulsing, as electrode conditioning and experimental protocols may influence the ratio of oxidation and reduction charge injection capacity [Musa et al., 2011, Harris et al., 2018a] and electrode behaviour, demonstrating more influence than the presence of dissolved oxygen for instance [Doering et al., 2023]. The technique used in this work to let the OCP return to a stable value after stopping the CV at 0 V yielded OCPs sufficiently stable for comparison; however, OCP variability may have been reduced by carefully controlling the electrode potential with a potentiostatic step following CV, as implemented by Doering et al. [2023]. The protocol was slightly modified for experiments comparing gel and solution electrolytes, with a 20-minute step (i) instead of 30 minutes (the potential could still stabilise in that time), 10 instead of 20 CV cycles (voltammograms were stable after 6-7 cycles), and suppression of steps (ii) and (iii) as EIS did not change after the first CV. Thus, it is possible that the results observed for pH 1 and pH 11 saline in the gel vs solution experiment were slightly different than the pH experiment because of the modified protocol; such discrepancy is expected to be minor, since CVs and OCP traces were similar before and after the protocol modification.

6.1.4.3 Evolution of peak potentials

pH was shown to have a substantial effect on several electrochemical reactions in voltammetric studies including hydrogen evolution reactions [Auinger et al., 2011, Liao et al., 2013, Ledezma-Yanez et al., 2017, Briega-Martos et al., 2020, Obata et al., 2019], oxygen evolution reactions [Hsueh et al., 1983, Li et al., 2013, Strbac, 2011, Briega-Martos et al., 2017], and platinum dissolution [Xing et al., 2014, Furuya et al., 2015, Deng et al., 2019]. In this work, the

influence of pH on charge injection mechanisms during biphasic pulses is investigated with a similar analysis strategy as Kumsa et al. [2016b], using CVs and electrode polarisations during pulsing to identify possible electrochemical reactions. There are three main anodic reactions for Pt electrodes in chloride (Cl^-) containing electrolytes: hydrogen (H) desorption, platinum oxide (PtO) formation, and adsorbed Cl^- oxidation through chloride complexation, which is outside of traditional water window ($E^0 \approx 0.95V$ vs Ag|AgCl [Geiger et al., 2015]) for Pt but may be reached in acidic media. The anodic polarisation was recorded in the PtO formation peak for all pH and all k-values, which shows that PtO formation is the main faradaic reaction supplying anodic current. The cathodic reaction path is more complex to determine, as there are several competing processes that may occur, including mainly PtO reduction, reduction of molecular oxygen (O_2) and Cl^- adsorption. It is likely that both reactions occur during pulsing, and Cogan et al. [2010] and Musa et al. [2011] evaluate contribution of molecular O_2 reduction respectively at 7% in O_2-saturated saline on 25 μmm diameter electrodes and 19-34% in ambient O_2 concentration on 50 μm diameter electrodes. Dissolved O_2 was present in the electrolytes at ambient conditions (21%), therefore it may contribute to charge injection during pulsing. Positive potential ratcheting was observed, indicating a cathodically-biased imbalanced irreversible charge injection, meaning more irreversible charge was injected during the cathodic phase. The imbalance is observed in the polarisation curve (Fig. 6.3 B)) in the form of a potential overshoot in the anodic phase, which would not be present with a completely reversible charge injection, and is most likely due to molecular oxygen reaction.

Nonetheless, the cathodic polarisation was located in the potential region where molecular oxygen reduction and PtO reduction contributions are superimposed on a CV (-0.6 V $< E_{O_2} <$ +0.05 V, vs $E_{PtO} \approx$ 0.1 V). I hypothesise molecular oxygen reduction to be a source of cathodic irreversible charge injection; however, the change of behaviour observed around Shannon's damage limit is related to the onset potential of PtO reduction, whereas O_2 reduction

is present for all k-values. Indeed, for pH 1, 10, and 12, the cathodic polarisation enters the PtO reduction peak for the highest values of k, suggesting a correlation between Shannon's damage limit and the onset of PtO reduction. Topalov et al. [2014a] studied Pt dissolution mechanisms by varying anodic and cathodic potential extremes separately during cyclic voltammetry. Topalov et al. [2014a] showed that increasing the upper limit of the CV did not affect anodic dissolution greatly but had a significant effect on cathodic dissolution, which was explained by a larger PtO coverage created, so a larger amount of PtO for reduction: the amount of Pt dissolution was proportional to oxide coverage. Therefore, I hypothesise the following compound mechanism: molecular O_2 reduction causes irreversible cathodic charge injection, which drives the potential more positive through potential ratcheting. As a consequence, the anodic potential is driven further into the PtO formation region, leading to larger oxide coverage, and at k-values approaching Shannon's limit, PtO reduction occurs at a substantial rate, which yields toxic levels of platinum dissolution [Brummer and Turner, 1975]. These findings support the hypothesis about the importance of the cathodic potential in dissolution mechanisms. This interpretation supplements the findings by Kumsa et al. [2016b], which suggested that the tipping point for Shannon's damage limit was the onset of PtO formation during the anodic phase. In this work, substantial changes were not observed in the available anodic reactions when k exceeded the damage limit, as E_{ano} was consistently found inside the oxide formation peak, independent of k. The PtO formation region is a broad peak (0.1 V$\leq$ E $\leq$ 0.9 V), which is able to supply substantial anodic charge, and may explain the relatively small variation in E_{ano}. The combination of E_{cat} entering oxide reduction and E_{ano} reaching oxide formation creates cycles of oxidation-reduction of platinum to platinum oxide, which eventually leads to platinum dissolution [Doering et al., 2022, Lopes et al., 2018, Inzelt et al., 2010]. Pt dissolution through repetitive oxidation and reduction is a well-known mechanism as a combination of electrochemical and chemical reactions [Lopes et al.,

2018, Myers et al., 2018], which has been established mainly through potentiostatic and potentiodynamic (CV) techniques [Myers et al., 2018, Doering et al., 2022, Topalov et al., 2014a]. In neural engineering, a recent review explored the different possible mechanisms for Pt dissolution during stimulation, suggesting the oxidation/reduction mechanism as a main candidate [Shah et al., 2024], and the present work investigated the incidence of this mechanism during current-controlled biphasic pulses. Therefore, I suggest that the tipping point explaining neural damage as observed by McCreery et al. [1990] is the combination of a sufficient PtO coverage formed during the anodic phase and the electrode potential entering the PtO reduction region during the cathodic phase as described by Inzelt et al. [2010] and Topalov et al. [2014a].

The electrochemical reactions corresponding to Shannon's limit did not change with pH, which corroborates observations by Cherevko et al. [2014], that Pt dissolution rate was equal in acidic and alkaline electrolytes. However, in the same study, the authors show that the transient dissolution of Pt (rapid alternation of phases) was higher by a factor of two in base. While pH electrolyte did not visibly change the potential excursions, it was hypothesised that the local pH at the electrode surface drifted to a common value for pH between 4 and 10, value estimated around 9 [Liao et al., 2013, Strbac, 2011]. Therefore, although the mechanism did not change with pH, the dissolution rate may have been faster for pH 12 compared to pH 4, 6 and 10. The different dissolution rate may be correlated with the slightly different current waveforms for various pH: the anodic discharge had a larger peak current and a sharper profile for pH 1 and 12, which suggest a faster charge injection than lower ionic strength electrolytes (not shown). In a similar mechanism as for the discrepancy in water window width in CV, the low ionic strength saline may have exhibited more surface changes and local buffer exhaustion, which make the charge injection slower, hence the rounder anodic phase profile.

In pH 1, the cathodic behaviour was substantially different to other pH, with the cathodic polarisation clearly transitioning from one reduction peak

to another, more negative, peak. Cl^- is known to adsorb onto platinum and compete particularly with Pt oxidation, and this phenomenon is enhanced by electrolyte acidity [Black and Hannaker, 1979, Hudak et al., 2017a, Geiger et al., 2015, Shrestha et al., 2014, Doering et al., 2022]. It is possible that in pH 1 saline, another Pt dissolution path was observed, as Cl^- adsorbed on the Pt surface, competing with Pt oxide, and dissolved the surface when the $Pt-Cl_{ads}$ was oxidised. While Pt dissolution still occurs predominantly during oxidation/reduction cycles [Geiger et al., 2015], Cl^--mediated dissolution adds another mechanism taking place in both phases: the strongest influence is observed during the anodic phase as Cl^- adsorbs onto the Pt surface, competing with Pt oxide formation and blocking Pt redeposition [Shrestha et al., 2014, Geiger et al., 2015, Hudak et al., 2017a], while in the cathodic phase, Pt-chloro complexes are formed, stabilising Pt ions and possibly influencing both dissolution and redeposition as well [Shrestha et al., 2014, Geiger et al., 2015]. *In vivo*, this phenomenon is less likely to take place, as proteins such as albumin adsorb onto Cl^- preferential adsorption sites [Hudak et al., 2017a, Robblee et al., 1983].

The evolution of E_{ano} and E_{cat} with respect to pH was analysed separately for each k-value in Fig. 6.6. E_{ano} followed Nernst's equation closely with a mean average gradient of -42.1 ± 1.59 $mV.pH^{-1}$ (see appendix B table 2.1), and Nernst's gradient inside the 95% C.I. for 6 out of 7 k-values (except $k = 0.566$). E_{cat} presented a less steep mean gradient of -31.7 ± 4.52 $mV.pH^{-1}$, with Nernst's gradient outside the 95% C.I. for all k-values. pH 4 and 6 showed similar E_{ano} and E_{cat}, which marked a plateau in the E vs pH plots.

6.2 Effect of electrolyte concentration

6.2.1 Rationale for varying the electrolyte salinity

Electrolytes used to characterise stimulation electrodes may have different conductivities, for instance in the pH experiment, unbuffered NaCl had a different conductivity for different pH values and was different to PBS and H_2SO_4. Fur-

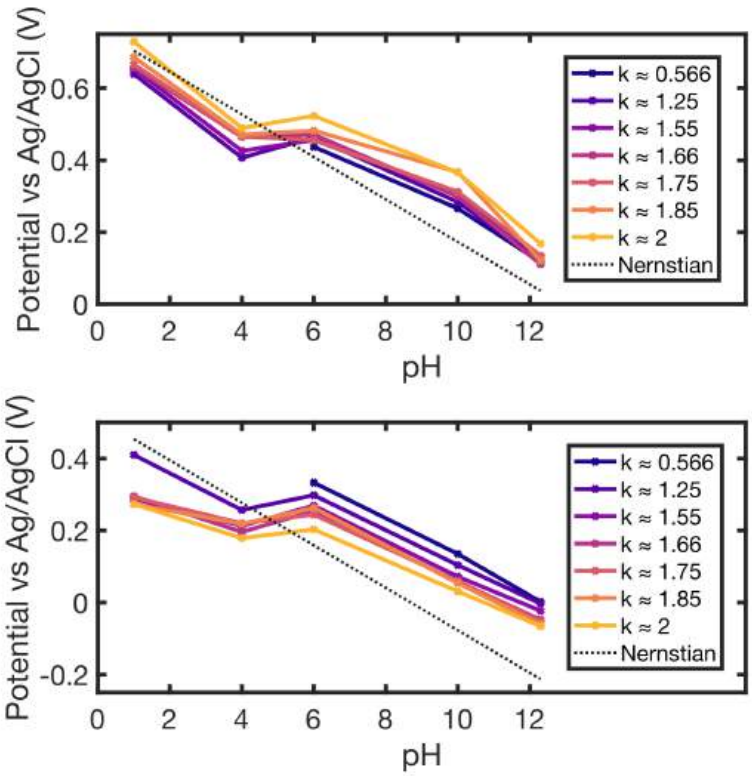

Figure 6.6: *Evolution of peak anodic potential (top) and peak cathodic potential (bottom) with pH (solution electrolytes) for all values of k and comparison with Nernst's equation.*

thermore, the conductivity inside the body may vary [McCann et al., 2019], and recorded values of conductivity of CSF (1.71 ± 0.3 S/m [McCann et al., 2019] with a commonly used value of 1.79 S/m at 37° [Baumann et al., 1997, Latikka and Eskola, 2019]; 1.45 S/m at room temperature [Baumann et al., 1997]) and ISF (measured as 1.33 ± 0.08 S/m [Schaupp et al., 2014], however, same values as ISF are also used in some cases [Hladky and Barrand, 2014]) are different than usual characterisation fluids. Therefore, there is an interest in studying the effect of electrolyte conductivity through the variation of salinity (supporting ions ionic strength in saline). Decreasing the conductivity increases the access resistance (cf. 4.9 [Newman, 1966]), thus it may affect electrode polarisation during pulses. If the conductivity is too low, high voltage drops arise and the accuracy of potential readings may be affected [Harris, 2024]. The potential measured by RE may appear to exceed

safe limits, which leads to inaccurate conclusions, and may affect potentiostatic/potentiodynamic techniques, which apply a reduced electrode potential range due to uncompensated resistance. Finally, the voltage compliance of the stimulation circuit may be exceeded due to the large ohmic drops, which may lead to saturated waveforms and inaccurate measurements. Therefore, there is a minimum conductivity limit, which depends highly on the experimental setup, that should be observed when designing low conductivity electrolytes.

6.2.2 Specific methods for salinity experiments

The effect of salinity was tested for two electrolytes: saline (NaCl), where the conductivity was decreased (0.45% vs 0.9% NaCl concentrations, and PBS, where the conductivity was increased by using PBS 10×, which is ten times more concentrated than PBS 1×, which is usually used. Conductivity was measured using a conductivity meter (Hanna HI98304), and other electrochemical tests were conducted as presented in chapter 3.

6.2.3 Results

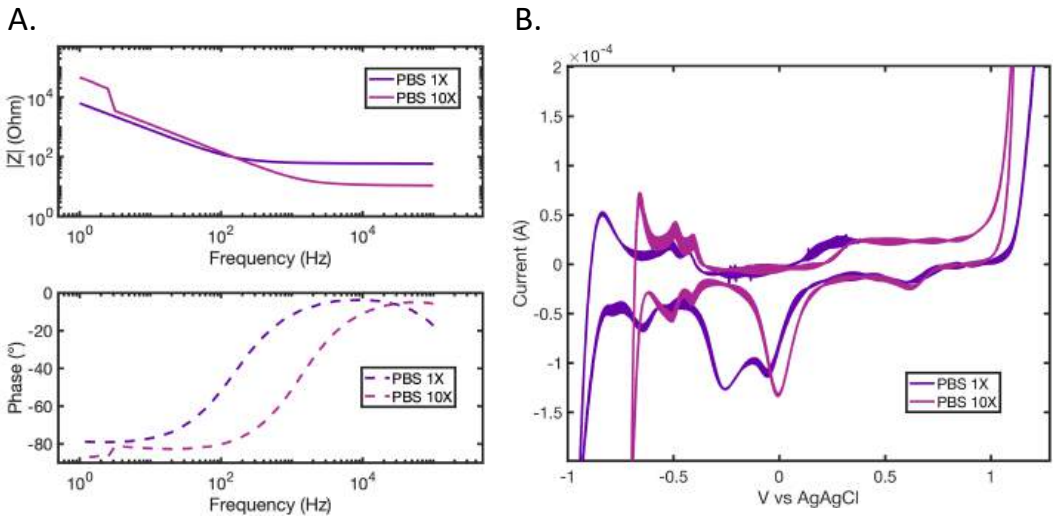

Figure 6.7: *A. Comparison of EIS of PBS 1× and PBS 10×. B. Comparison of CVs of PBS 1× and PBS 10×.*

PBS 10× exhibited a six times lower high frequency impedance than PBS 1× (≈ 10 Ω vs 60 Ω) and similar low frequency impedance (ignoring the noise at f

$<$ 3 Hz), which drove the cut-off frequency towards higher frequencies by one order of magnitude (Fig. 6.7 A). The fitted EIS data also showed that C_{dl} was divided by two in PBS 10× (25 μF for PBS 1× vs 13 μF for PBS 10×) and that the electrode behaviour was effectively more capacitive in PBS 10× as the CPE model value α, which gives information on the closeness to a capacitive behaviour of the CPE (see 1.2.2), increased from 0.9 to 0.95. The increase in cut-off frequency confirms the fitted values as dividing R_A by six and C_{dl} by two yields an increase in f_c by twelve, which corresponds to one order of magnitude, as observed.

CVs showed similar features with a few key differences (Fig. 6.7 B): the water window was shorter for the more concentrated PBS especially in the H-evolution region (≈ 200 mV), and especially the spacing between the first and second H-oxidation (desorption) peaks was shorter in PBS 10×. Both PtO formation and reduction peaks were shifted towards more positive potentials by ≈ 50 mV, and more interestingly only one PtO reduction peak was observed in PBS 10×, suggesting the double PtO reduction peak pertains to lower conducitivity 1× PBS.

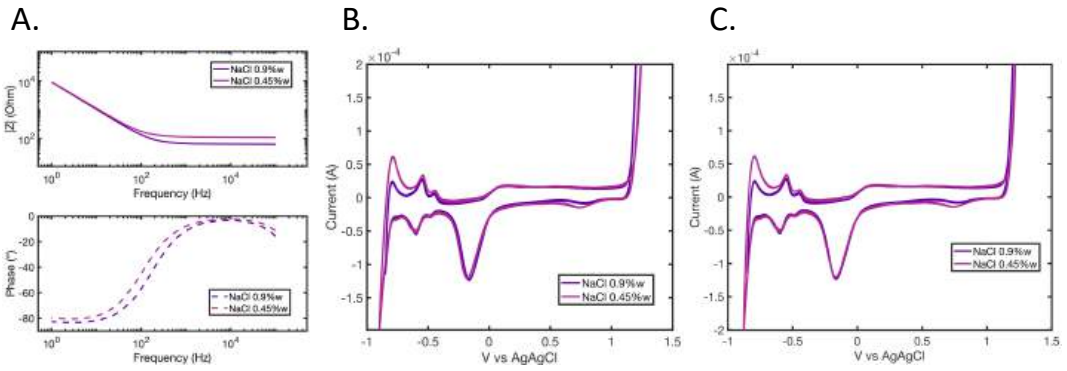

Figure 6.8: *A. Comparison of EIS of 0.9%w saline and 0.45%w saline. B. Comparison of CVs of 0.9%w saline and 0.45%w saline without RI correction. C. Comparison of CVs with RI correction.*

Unbuffered saline of isotonic concentration (0.9%w) and half isotonic concentration (0.45 %w) were compared following the same protocol (Fig. 6.8). The less concentrated saline exhibited a twice higher high frequency impedance

(110 Ω vs 55 Ω), similar low frequency impedance suggesting that C_{dl} was equal for both electrolytes, and a phase transition at a slightly lower frequency conisistent with an increased series solution resistance. The EIS fitted data yielded a similar but slightly lower C_{dl} value for lower salinity (15 μF vs 18 μF). The CPE parameters were similar to a capacitor in both cases, with a consistent α (0.94 for 0.9%w and 0.93 0.45%w), which shows that unbuffered saline had a more capacitive behaviour than PBS 1×, similar to PBS 10× regardless of salinity. The CV was almost identical for both solutions except for larger peaks at +0.7 V on the reduction scan and -0.8 V on the oxidation scan for lower conductivity solution, which were the consequence of further venture in the O- and H-evolution regions for the half-concentrated saline, and slightly more pronounced slopes in the O- and H-evolution regions for the half-concentrated saline (Fig. 6.8 B). The slopes were due to the slight R_A increase, which is demonstrated on the RI-corrected CV (Fig. 6.8 C), where the H- and O-evolution slopes were similar.

The change in salinity, whether increasing or decreasing the conductivity, did not have much effect on the location of polarisation potentials on the CV (Fig. 6.9). In PBS (panels A and C), E_{ano} was located in the PtO formation region, after the shoulder at E ≈ 0.35 V. E_{cat} was located at the beginning of the PtO reduction peak, slightly further along for PBS 1×, however, the current amplitude was similar for both, indicating similar polarisation levels. For NaCl too, E_{ano} was found in the PtO formation region and E_{cat} at the beginning of the PtO reduction peak. The evolution of E_{ano} with k was different in the less concentrated saline, exhibiting a plateau for $k \geq 1.66$. The current waveform during biphasic pulses showed a smaller anodic peak current in less concentrated saline, suggesting current injection may have been slower in the anodic phase, which could explain the E_{ano} plateau. Both the more concentrated PBS and the less concentrated saline showed similar cathodic polarisations (slightly more positive and larger value span with k) compared to their respective references, whereas opposite effects were expected in both

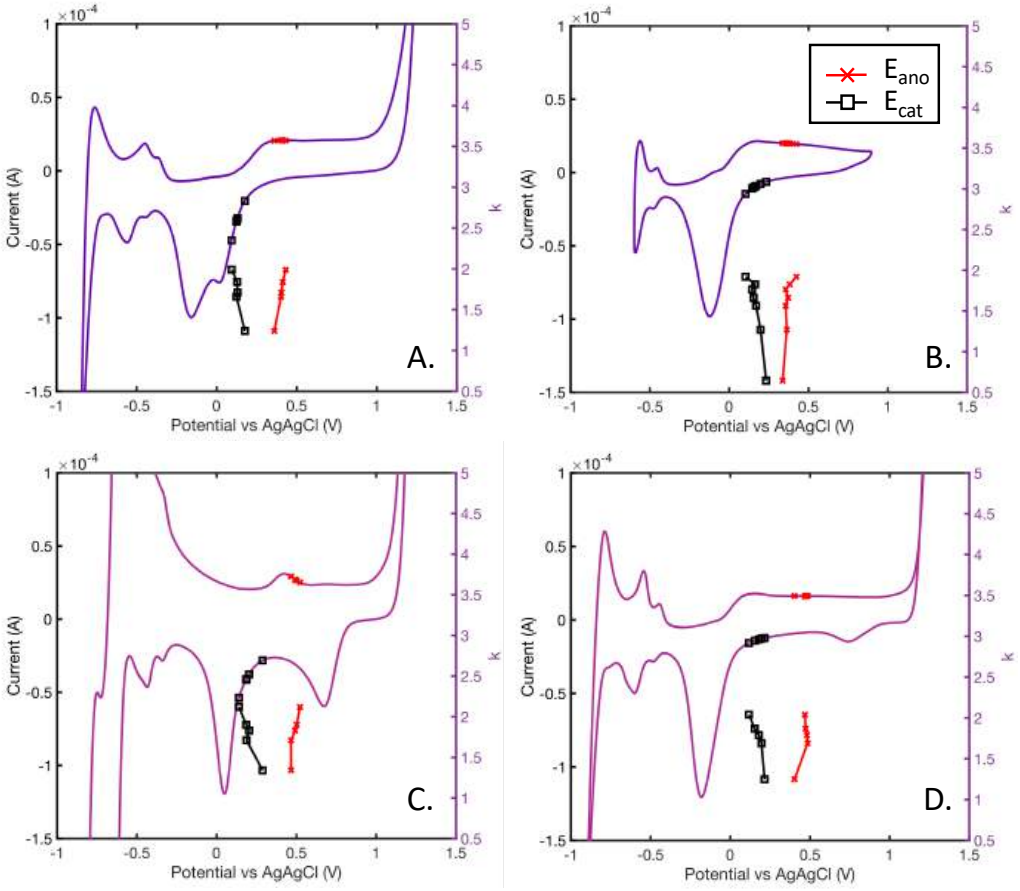

Figure 6.9: *Evolution of anodic and cathodic corrected potentials with k and comparison with associated CV for A. PBS 1×, B. 0.9%w saline, C. PBS 10×, and D. 0.45%w saline.*

cases. CVs in figure 6.9 were recorded during the pulsing tests yielding the corresponding polarisations, though the CV shapes in panels B and C were different from CVs reported in figure 6.8 and 6.7 respectively: figures 6.8 and 6.7 represent a "correct" CV, while in figure 6.9, the water window was not accurate, being too narrow for NaCl 0.9%w and too wide for PBS 10X, yielding large phosphate evolution peaks and H-evolution at E < -0.4 V.

A brief discussion of the salinity results is included in the section reporting experiments on electrolyte gelation (6.3.4) as the results and relevant discussion points are complementary.

6.3 Effect of electrolyte gelation

6.3.1 Rationale for using gel electrolytes

Penetrating neural electrodes are implanted in body tissues, more specifically in the extracellular matrix (ECM), which is a three-dimensional network of collagen fibers and other proteins supporting cells [Bosman and Stamenkovic, 2003]. The ECM has a structure comparable to a gel, and thus it is often substituted in cell culture experiments by other similar gelating agents such as agar (a vegetal protein) [Boehler et al., 2017b, Thakur et al., 2021] and gelatin (an animal protein) [Furlani et al., 2022]. After implantation, stimulation electrodes experience an increased polarisation, which is hypothesised to be correlated with tortuous diffusion paths induced by the ECM structure [Cogan, 2008]. The tortuous diffusion paths also affect conductivity, as ions ensuring current flow diffuse slower; therefore, the access resistance will be higher in a gel, however, further effects may be observed. The gel and salinity chapters are therefore complementary, as varying salinity was used to study the effect of conductivity and R_A changes alone, and the differences observed in gels may be attributed to the gel structure.

6.3.2 Specific methods for gel electrolytes

Agar gel electrolytes were prepared with three base solution electrolytes: phosphate-buffered saline (PBS); sulfuric acid (H_2SO_4); and saline (NaCl) at two pHs, pH 11 saline (NaOH in isotonic 0.9 wt% saline), and pH 1 saline (HCl in isotonic saline). Agar powder was added (0.5 wt% and 2.5%w) to the base electrolytes, and gelation was achieved by heating to boiling point followed by cooling to room temperature. pH was measured following gelation. A gelatin gel was also made to compare the difference between an animal protein and a plant protein ECM model at a gelatin concentration of 10%w. Two gelation methods were tested for gelatin, by diluting gelatin in DIW before adding it to a concentrated version of the electrolyte, or by adding gelatin directly to the electrolyte, both methods produced a gel with similar properties.

Electrodes were introduced carefully in the gel electrolytes, making sure to avoid pulling electrodes up when setting them in place to avoid the formation of bubbles. Electrochemical tests were conducted as presented in chapter 3.

6.3.3 Results

Gel electrolytes showed different characteristics depending on gel concentrations and electrolytes. First, acidic electrolytes including pH 1 saline and H_2SO_4 did not gelify, leaving some of the agar visible in solution, which may be due to protein denaturation in acids, therefore, high gel concentrations were not tested on these electrolytes. pH 11 gels had a slightly yellow tint regardless of gel concentration and gelating agent used, suggesting some chemical change in a basic environment, which was not characterised. Agar concentrations above 2.5% w yielded a too rigid structure which did not allow for seamless electrode introduction and yielded cracks and air bubbles which did not allow for usable and reproducible measurements. Agar gels at 2.5% w were fully gelated and quite stiff but demonstrated sufficient flexibility to allow for electrode insertion without breaking apart, and Agar gels at 0.5% w were less stiff, yielding some residual liquid in holes left by electrodes. The 10% gelatin gel was firm like the 2.5% w but had a greater elasticity, which also allowed for electrode insertion without breaking apart.

The gelation of the electrolyte increased the high-frequency impedance slightly for PBS (80 Ω vs 60 Ω in solution) and for pH 11 saline (70 Ω vs 60 Ω in solution), however, increasing the agar concentration did not further increase R_A despite making the gel stiffer. From EIS fitted values, 0.5% w agar did not change C_{dl}, however, 2.5% w agar decreased C_{dl} by a factor three (7.5 μF vs 25 μF) and α increased in the CPE model respectively from 0.89 to 0.93 in PBS and from 0.88 to 0.9 in pH 11 saline. The lower C_{dl} is consistent with the higher cut-off frequency for 2.5% w gels. The gelatin gel (data not shown) showed similar features to agar gels on the CV and on the Bode plot with $R_A \approx 80$ Ω and 5 μF C_{dl}, with $\alpha = 0.939$. This shows that gelatin at 10% concentration had a similar behaviour to 2.5% w agar, exacerbating the drift

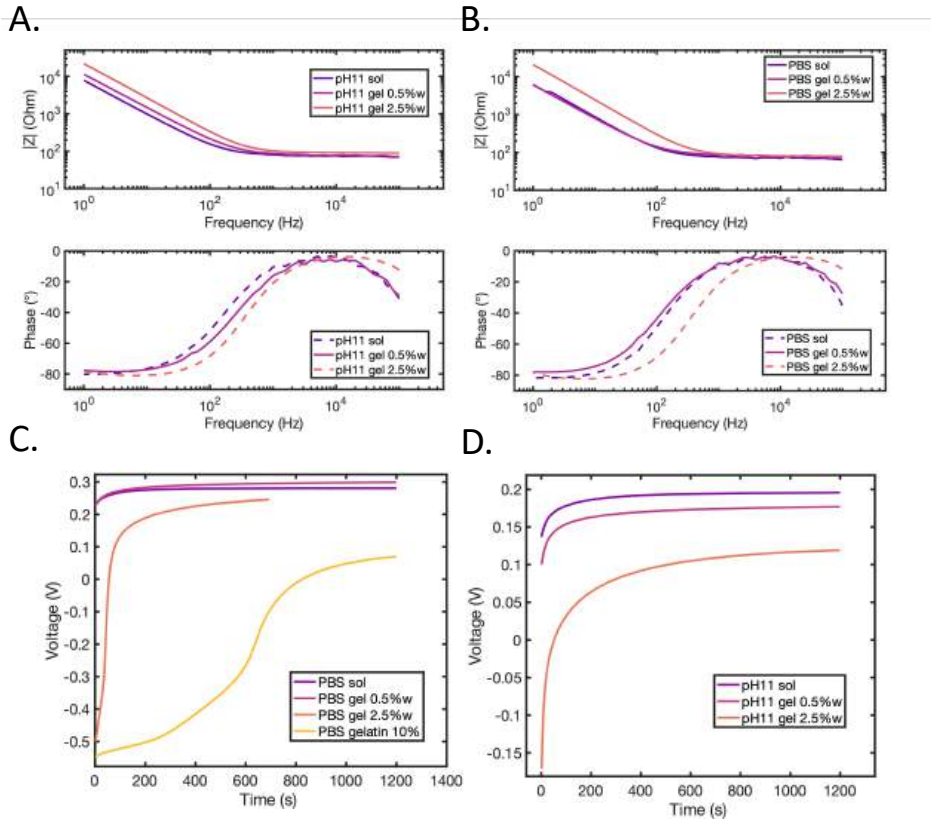

Figure 6.10: *EIS of three gel concentrations in A. PBS and B. pH 11 saline, and OCP post pulsing of the three gel concentrations in C. PBS and D. pH 11 saline.*

from solution a little further.

Gelation of the electrolyte with agar generally yielded a lower mean OCP except for PBS by 22.5 mV on average (average of mean(E_{sol}) - mean(E_{gel})), see Table 6.1, although the stabilised OCP in figure 6.10 was slightly higher for gelated PBS. The gel concentration had an effect on the potential decay during pulses and, as a consequence, on the recovery OCP after the pulse trains, see figure 6.10. While in PBS, the low agar concentration did not change the OCP by a large amount, the high concentration agar and similar gelatin gel showed a negative initial potential (750 mV to 800 mV lower than the solution OCP) immediately after pulses and a longer recovery period ($\approx$ 600 s for agar and $>$ 1200 s for gelatin), which did not finish within 20 minutes for gelatin. In pH 11 saline at a low concentration, the OCP was shifted negatively but with a

similar span and for a higher agar concentration, the potential started in the negative range and recovered over 1000 s, at a lower value than other pH 11 electrolytes.

Table 6.1: *Mean average OCP and standard deviation (std) within experiments for each electrolyte in solution and gel form.*

Electrolyte	PBS		H_2SO_4	
pH	7.4		1	
Gel or **S**olution	S	G	S	G
OCP (mV)	284.1±7.69	281.9±29.43	607.3±9.21	584.9±8.61
Electrolyte	NaCl			
pH	11		1	
Gel or **S**olution	S	G	S	G
OCP (mV)	196.5 ± 1.87	175.3±2.36	568.6±10.31	524.2±1.10

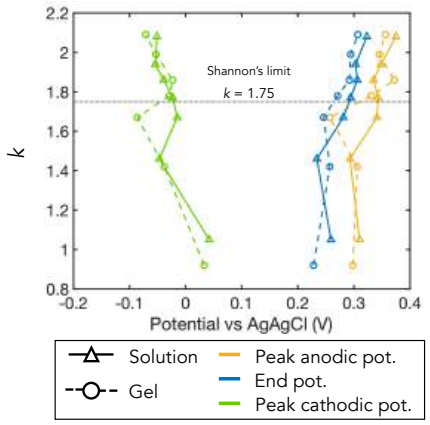

Figure 6.11: *Evolution of peak anodic potential (yellow), peak cathodic potential (green), and end potential (blue) with k in gelated vs solution PBS (pH = 7.4). Shannon's limit k = 1.75 is indicated by a dotted line.*

E_{ano} and E_{cat} showed similar evolutions with k for gel and solution in four different electrolytes, for example in PBS in Fig. 6.11. E_{ano} and E_{cat} were not significantly different with 95% confidence by two-sample Kolmogorov-Smirnov test (data not shown). Plotting potential excursions (E_{ano} or E_{cat}) in gel electrolytes against solution electrolytes showed a substantial discrepancy in E_{cat} (Fig. 6.12). While the linear fit was almost superimposed with the identity line ($E_{gel} = E_{sol}$) for E_{ano} ($E_{gel} = 0.959\,E_{sol}$, 95% C.I. [0.856; 1.061]), the E_{cat} linear fit showed a steeper gradient ($E_{gel} = 1.294\,E_{sol}$, 95% C.I. [1.094;

1.493]), which left the identity line outside the 95% CI. The four electrolytes figure as separate groups, with pH 11 saline at the bottom (gel E_{cat} < sol E_{cat}) and H_2SO_4 and pH 1 saline at the top (gel E_{cat} > sol E_{cat}), which indicates a cumulative effect of electrolyte gelation and pH.

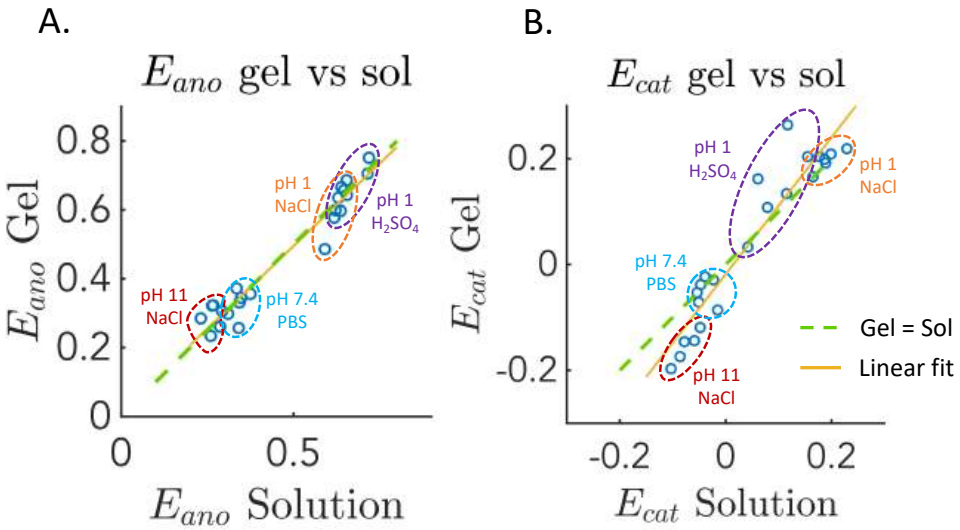

Figure 6.12: *Direct comparison of A) anodic and B) cathodic polarisation potentials in gel electrolytes vs solutions. Each data point is a pair (E_{gel};E_{sol}) for the same k-value. A linear fit of all data points is shown (yellow line) and compared $E_{gel} = E_{sol}$ (green dotted line).*

E_{ano} and E_{cat} were placed on cyclic voltammograms for gel electrolytes, similarly to the analysis of pH solutions (Fig. 6.14). CVs of gel electrolytes showed similar peaks to solution electrolytes but less defined, suggesting an alteration of reaction kinetics. A semiderivative analysis of CVs of gels and solutions (Fig. 6.13) confirms this trend, with similar traces, although noisier for gels. A few clear features are observable in all semiderivatives, including the H-evolution region with three to four clearly identified peaks in both directions, PtO reduction with at least one clear arch, and two arches for H_2SO_4, pH 1 NaCl, and PBS gel. pH 1 H_2SO_4 and pH 1 NaCl showed similar features, except in the PtO reduction region, with two more spaced out shoulders (less defined peaks) for NaCl. A clear consistent reduction peak was observed for all electrolytes except H_2SO_4 at E $\approx$ 1, which can therefore be attributed to

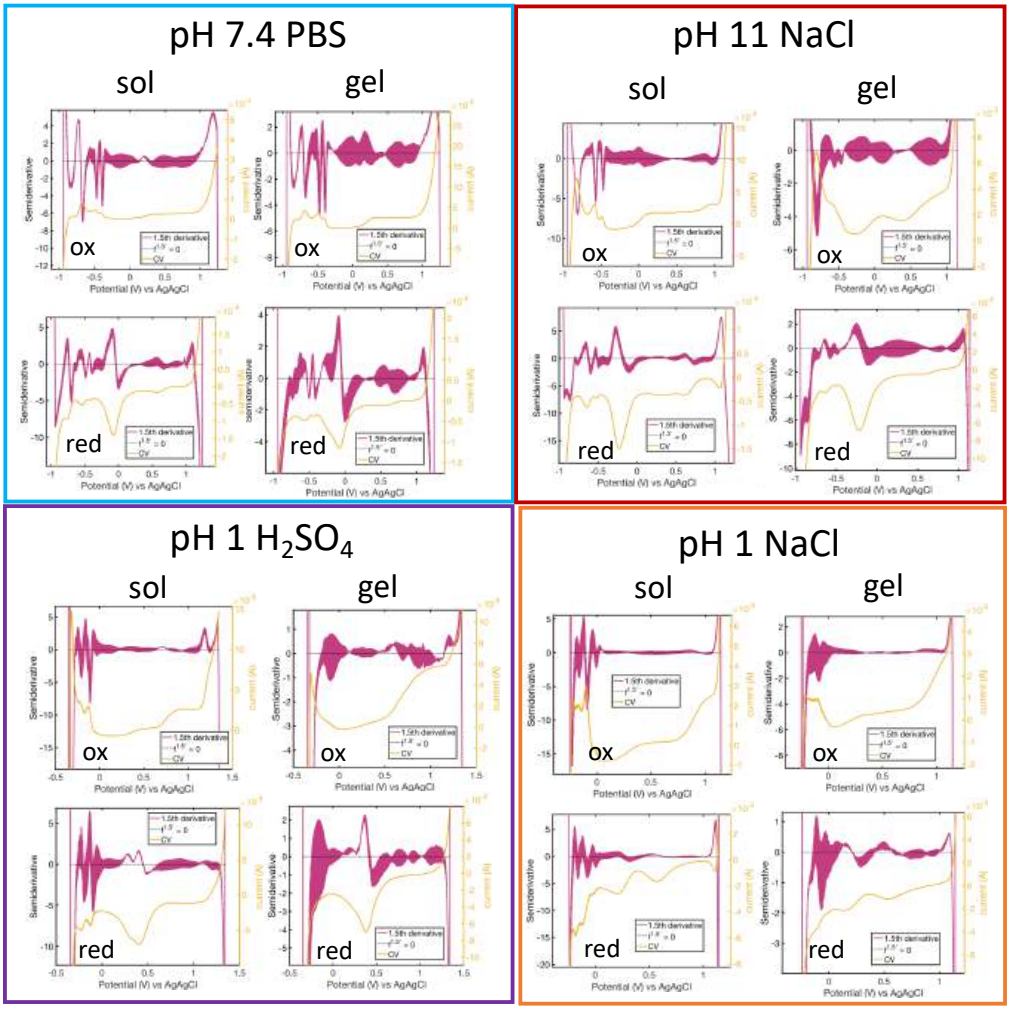

Figure 6.13: *Comparison of 1.5th order derivative of CVs of gels and solutions for four electrolytes. The CV scans were separated in oxidation ("ox") and reduction ("red") scans.*

Cl^- reduction, whereas an oxidation peak only present in H_2SO_4 can be attributed to SO_4^{2-} oxidation. For all electrolytes, E_{ano} was consistently located in the oxide formation region and E_{cat} was consistently located in the oxide reduction region. Despite a noticeable oxidation peak starting at E $\approx$ 0.6 V, E_{ano} of H_2SO_4 gel and pH 1 saline gel and solution varied almost linearly with k, as did the E_{cat}, and H_2SO_4 solution showed a linear increase in E_{cat} and a step increase in E_{ano} around $k = 1.75$, entering an oxidation peak. H_2SO_4 solution behaviour is similar to the observations of Kumsa et al. [2016b] and different to for example pH 1 saline, showing that electrodes in H_2SO_4 may

have a different charge injection behaviour than in saline electrolytes.

High-concentration gels (2.5% agar, five times usual concentration) were tested for two electrolytes (PBS, pH 11 saline) with Agar and compared with PBS gelatin gel to understand how gel concentration, which determines the gel's stiffness, affected the polarisation during pulses. For pH 11 saline and PBS gelatin, the potential decay was too large, yielding unstable potential readings, with both E_{ano} and E_{cat} decreasing with k. The discrepancy between E_{ano} and E_{cat} was between 50 mV and 100 mV in gelatin, which was smaller than for other agar gels and solutions, generally larger than 200 mV. PBS high-concentration agar gels were more stable and consistent, yielding similar trends as lower concentrations of agar, however, the potentials were shifted negatively, with E_{ano} being located in the double-layer charging region before the PtO formation peak, and E_{cat} in the H-evolution region.

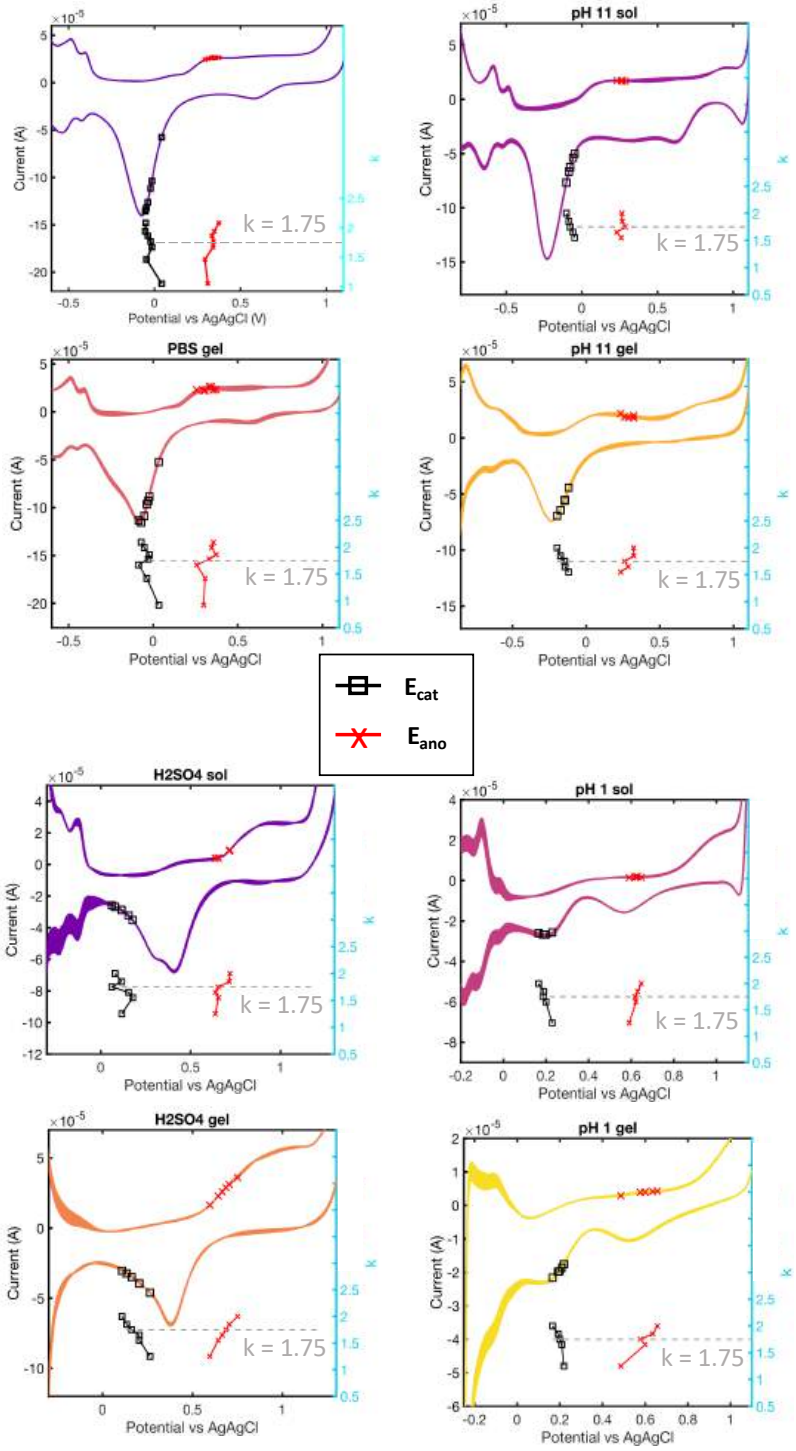

Figure 6.14: *Evolution of peak anodic potential (red) and peak cathodic potential (black) with k in gelated vs solution electrolytes and location on the respective cyclic voltammogram (100 mV.s^{-1}). Shannon's limit k = 1.75 is indicated by a dashed grey line.*

6.3.4 Discussion

The gel electrolyte experiment was designed to be complementary to the two previous experiments on pH (6.1) and salinity (6.2), therefore, co-dependent effects were investigated in both cases. The effect of changing the electrolyte salinity was studied to determine whether gels have an additional effect on charge injection beyond that of changing the conductivity. Changing the salinity changed R_A as expected (a lower salinity yielded a proportionally higher R_A); however, a change in C_{dl} was also observed for PBS, with a more capacitive CPE behaviour and a lower capacitance value (halved) for more concentrated PBS. Jones and Scott [2014] confirmed a proportional increase of R_A and decrease of cut-off frequency with decreasing electrolyte concentration, however, an increase of the CPE magnitude is reported with increasing concentration (proportional to the log of concentration) and no change in α, although the authors state the CPE does not mainly rely on salt ions and must arise from another phenomenon. Therefore, the change in α for PBS may have another explanation: the electrode surface may have been contaminated for a period, which could explain the more imperfect capacitive behaviour as well as the second oxide reduction peak in the CV. A slight capacitance change was observed in saline, which may have been larger with a larger salinity discrepancy between electrolytes. During biphasic pulses, the anodic and cathodic potentials were located in the same regions on the CVs despite the variation in salinity, suggesting the increase in R_A and lower conductivity do not affect charge injection at the electrode surface, which also confirms the conclusion of Jones and Scott [2014], stating that the onset of faradaic charge injection and the safe charge injection limit do not scale with electrolyte concentration. The slightly larger cathodic polarisation span observed for PBS 10× may be attributed to the more capacitive behaviour observed in EIS measurement and the lower C_{dl}. Counter-intuitively, high-concentration gels (2.5%w agar) had a lower C_{dl} similarly to high-concentration PBS, which yielded larger anodic and cathodic polarisations. PBS 0.5%w agar gels showed no significant changes in

E_{ano} and E_{cat}, which suggests that gels did not have additional effects other than slightly changing the electrolyte conductivity, with similar results as in the salinity experiment. It is worth noting that the range of salinity used in this work exceeds the variations of conductivity observed in the body [McCann et al., 2019], although it may provide a good approximation for the behaviour of implanted electrodes. Indeed, Jones and Scott [2014] compared the impedance traces of Pt electrodes in various PBS concentrations with implanted electrodes in sheep spines and showed that the high-frequency and low-frequency behaviour of implanted electrodes were better represented by different concentrations of saline: 0.25× PBS for HF and 0.025× PBS for LF. Therefore, less concentrated electrolytes may offer more insight into implanted electrode reactance and capacitive behaviour. Moreover, organic species affect various components of the interface impedance: cells were shown to increase R_A without modifying C_{dl} [Newbold et al., 2004], whereas proteins increase the polarisation [Newbold et al., 2010], likely decreasing the capacitance by adsorbing on the electrode surface [Robblee et al., 1980, Donaldson and Donaldson, 1986b, Hibbert et al., 2000]. Decreasing the electrolyte conductivity, by decreasing the salt concentration or by gelating the electrolyte, increases R_A without increasing the polarisation despite introducing proteins to the environment because the structural proteins do not adsorb onto the electrode surface, contrary to body proteins [Donaldson and Donaldson, 1986b, Carnicer-Lombarte et al., 2017, Harris et al., 2021].

Coupling the gelation experiment with changes in pH revealed that gels have an additional discriminant effect on pH, as E_{cat} showed a different behaviour depending on pH. There is a similarity between the pH experiment and the gel versus solution experiment: E_{ano} followed the expected trend, respectively Nernst's relation for the pH study and gel = solution for the gelation study, but E_{cat} exhibited a different slope, indicating that E_{cat} is more influenced by electrolyte properties. Except for hydrogen evolution reactions, Pt anodic and cathodic reaction paths are asymmetrical, therefore

different behaviours of cathodic and anodic polarisation can be expected. The gel structure may limit mass transport, which may affect molecular O_2 reduction, which is the only mass-transport limited cathodic reaction [Merrill et al., 2005]. Gels also induce larger polarisations, which may affect Faradaic reactions in presence, without substantially changing CVs. While PBS and pH 1 saline had similar cathodic behaviour between gels and solutions, pH 11 saline gels showed consistently lower E_{cat} than solutions and pH 1 sulfuric acid gels consistently higher E_{cat} than solutions. Thus, in basic gel electrolytes, a larger polarisation was needed to deliver the same charge, and a lower polarisation in acidic gel electrolytes. Basic electrolytes have lower concentrations of H^+, which is consumed in both cathodic reactions (molecular oxygen reduction and PtO reduction), which may explain the overpotential discrepancy. Indeed, protons were identified as the limiting factor for surface reactions at Pt electrodes [Daubinger et al., 2014], therefore, variations in H^+ availability affect the cathodic reactions. The amount of O_2 reduction did not vary significantly as E_{ano}, which characterises the degree of irreversibility, remained highly similar, however, the increase in polarisation in basic electrolytes may have increased the dissolution. Local pH is hypothesised to change in the vicinity of the electrode during pulses and CV [Liao et al., 2013, Strbac, 2011, Daubinger et al., 2014] and gels may exacerbate the concentration gradients as diffusion is reduced, introducing a positive feedback loop at the electrode interface, reducing polarisation in acidic electrolytes and increasing polarisation in basic electrolytes. It was also observed that a smaller overpotential was present for gel H_2SO_4 compared to H_2SO_4 solution and not for similar pH 1 NaCl gel vs solution, which suggests that gel electrolytes may indeed affect Pt dissolution processes. pH 1 H_2SO_4 and pH 1 NaCl showed similar features in the P174: semiderivative CV analysis, however, E_{cat} appeared to scale differently, which may be attributed to the different PtO reduction region, which was one of the only significantly different features. The polarisation may not have decreased significantly in pH 1 saline because of the larger gap between the PtO reduc-

tion peaks, which was incompressible. Pt dissolution was shown to be affected by pH, being more prominent in acidic media [Topalov et al., 2014a, Doering et al., 2022] and occurring at higher rates in sulfuric acid than hydrochloric acid [Topalov et al., 2014a]. These results may indicate that gels exacerbate the influence of pH and influence Pt dissolution mechanisms, decreasing the necessary polarisation in favourable acidic conditions (for sulfuric acid) and increasing the necessary polarisation in unfavourable basic conditions. The effect observed in this work should be dissociated from proteins affecting Pt dissolution: several studies concluded that the presence of proteins decreased or annihilated Pt dissolution [Robblee et al., 1980, Donaldson and Donaldson, 1986b, Hibbert et al., 2000] because Pt traces decreased in solution, however, recent evidence suggests that Pt is captured by the adsorbed protein layer at the electrode surface [Shepherd et al., 2021], decreasing the measured Pt traces but actually not hindering the dissolution process itself. The gel structural proteins in this experiment behave somewhat differently as they do not adsorb on the electrode surface, however, the gel structure may affect diffusion and create local gradients which strengthen the dissolution pattern.

High-concentration gels increased the gels' stiffness, which hypothetically further affected the diffusion paths. The shape of post-pulsing OCP showed that high-concentration gels affected the recovery time at the interface, which confirms an effect on diffusion paths. PBS agar gels showed some variation in the recorded potentials during pulsing, however, the results were unstable, especially for pH 11 saline and PBS gelatin gels, which remained inconclusive due to equipment limitations. The comparison of gelating agents was difficult, as no objective measurement of gel stiffness was made. Therefore, it cannot be concluded that gelatin impacts polarisation more, as the gel may have been more concentrated. Nevertheless, PBS and pH 11 saline behaved differently with the same gelating agent, which may be correlated to the buffering capacity of both electrolytes: as the diffusion paths become more tortuous, the stronger buffer retains some capacity to mitigate the electrode polarisation,

while the polarisation in unbuffered electrolytes increases drastically. These preliminary results suggest higher gel concentration may have exacerbated effects on polarisation and diffusion, however, more data needs to be collected to confirm and quantify this trend.

6.4 Influence of buffering: the carbonate buffer system

6.4.1 Rationale for testing the carbonate buffer systems

PBS is a commonly used buffered saline solution in *in vitro* neural engineering. PBS presents the advantages of having a similar equilibrium pH to interstitial fluid ($\approx$ 7.4) and a subset of the main ions present in interstitial fluid (ISF)/cerebrospinal fluid (CSF), including sodium Na^+, chloride Cl^- and phosphate PO_4^{3-}. The pH buffering in PBS is ensured by the phosphate buffer system ($H_2PO_4^-/HPO_4^{2-}$), which, although present in the body (see 1.1.3), has less importance in the buffering capacity than the carbonate buffer system (CBS) [Chesler, 1990, Theparambil et al., 2020]. Indeed, the ions participating in the CBS are present in significantly larger quantities in the extracellular fluids (65 times, see table 6.2), making them more likely to bear a larger part of the buffering activity. The standard pH of the HCO_3^-/CO_3^{2-} pair is around pH = 9 and injection of carbon dioxide is necessary to reduce the pH to the homeostatic value of 7.4, and provide a heterogeneous phase, which enhances the buffering capacity of CBS [Al-Gousous et al., 2018]. However, CO_2 injection makes CBS more demanding experimentally, hence the tendency to use PBS more frequently in neural engineering, while CBS is used more often in cell culture, where climate and CO_2 control are already used. As CBS and PBS exhibit different buffering capacities, and CBS was shown to offer a better prediction of *in vivo* behaviour than PBS in a range of applications [Deitmer, 1992, Fadda et al., 2009, Chesler, 1990], there is a legitimate interest in testing the influence of CBS compared with PBS on charge injection during charge-balanced pulse trains.

Moreover, carbonate species, and especially carbon dioxide have shown electrochemical activity within the typical water window of platinum electrodes, especially CO_2 may reduce to carboxylic acid $COOH^-$ ($E^0 = -0.811$ vs Ag|AgCl), interacting with the CBS buffer [Sobkowski and Czerwiński, 1974, Jitaru, 2007]. CO_2 is also reduced in contact with adsorbed hydrogen on Pt and dissociates into adsorbed carbon monoxide (CO) and water ($E^0 = -0.731$ vs Ag|AgCl) [Bellows et al., 1996]. Cathodic CO_2 reduction is accompanied by H evolution by reacting with the underpotentially-deposited hydrogen (H_{upd}), and formed CO is known to interact with adsorbed H-atoms, however, it does not react with absorbed hydrogen [Jitaru, 2007]. CO is a known "poison" for H_2 oxidation as it bonds strongly with Pt, blocking Pt and Pt-H sites for H_2 dissociation and reacting with H_{ads} [Jitaru, 2007, Bellows et al., 1996]. Furthermore, CO is oxidised within the water window, and may therefore participate in charge injection. Bellows et al. [1996] report a CO oxidation peak at 0.9 V vs RHE in sulfuric acid, which translates to 0.701 V vs Ag|AgCl and a pH-corrected potential of 0.437 V at pH 5 (PBS + CO_2) and 0.319 V at pH 7 (CBS + CO_2). Adsorbed CO reacts with oxidised Pt as a heterogeneous chemical reaction taking place at the edge of oxidised PtO islands and steady-state oxidation of CO occurs on a complete monolayer of oxidised Pt [McCallum and Pletcher, 1976]. As a result, CO was shown to hinder anodic dissolution of Pt by restructuring the Pt surface, reducing the number of low-coordinated sites, however, adsorbed CO was also associated with larger cathodic Pt dissolution as CO is thought to block Pt redeposition sites [Topalov et al., 2014b], in a similar manner as chloride ions. Therefore, introducing CO_2 may have a large impact on Pt dissolution pathways.

6.4.2 Specific methods for carbonate buffer tests

CBS buffer solutions were prepared following Cold Spring Harbor Protocols [CSPH]. First, stock solutions were prepared by mixing respectively 22 g of anhydrous sodium carbonate ($NaHCO_3$) in 1 L of DIW and 16.8 g of sodium bicarbonate (Na_2CO_3) in 1 L of DIW to obtain equal concentrations of 0.2

Table 6.2: *Buffer - Ionic concentrations in vivo vs common electrolytes.*

Ions	**Extracellular fluid**[1] (mM)	**PBS**[2] (mM)	**Model ISF**[3] (mM)
Na^+	147	153	142.5
Cl^-	113	140	112
HCO_3^-	23.3	-	35.5
K^+	2.9	4.2	7.5
Ca^{2+}	1.14	-	0.5
Mg^{2+}	1.1	-	1
PO_4^{3-}	0.358	9.57	2.5
SO_4^{2-}	-	-	0.5

[1] from [Hladky and Barrand, 2014]
[2] from [Boehler et al., 2020a]
[3] calculated from [Cogan, 2008]

M for both stocks. To make 100 mL of CBS electrolyte, 2 mL of 0.2 M $NaHCO_3$ was mixed with 23 mL of 0.2 M Na_2CO_3, 75 mL DIW, and 2.4 g KCl. While KCl is not usually included in CBS solutions, the conductivity of the pure CBS buffer was too low to measure potential traces due to high impedance, therefore, KCl was added as a supporting electrolyte to match the conductivity of PBS. A conductivity measurement was performed, attributing a higher conductivity to CBS, which reached the appliance measurement limit of 20 mS.cm, whereas PBS was usually measured between 13 mS.cm and 16 mS.cm. Moreover, KCl was chosen instead of NaCl because the conditioning of both the carbonate and the bicarbonate ions involved Na^+ ions, adding NaCl would create an even larger imbalance between Na^+ and Cl^-.

As prepared, the CBS buffer presented a pH measured between 8.6 and 8.8, which is one order of magnitude away from PBS. Therefore, to work at similar pH values, and to represent the *in vivo* CBS behaviour more accurately, gaseous CO_2 was added to decrease the pH. While measuring the solution's pH with a pH-meter (Jenway, 3510 pH-meter), CO_2 was bubbled into the solution. After an initial delay, the pH started decreasing and within 5 minutes, a limit value of pH = 5.6 was reached, after which the pH did not decrease with additional CO_2. The system proved to have some inertia, and stopping the gas flow when reading the desired pH value on the pH-meter would yield a significantly inferior value due to delays in pH meter response and gas dissolution and

diffusion; therefore, it was established that the gas flow needed stopping ≈ 0.5 pH units above the desired value. Subsequently, the usual protocol was applied without further gas injection, and solution pH was checked again at the end of the experiment series of 5 k-values; the question of replenishing the electrolyte's CO_2 to maintain a stable pH and concentration will be addressed in the discussion.

6.4.3 Results

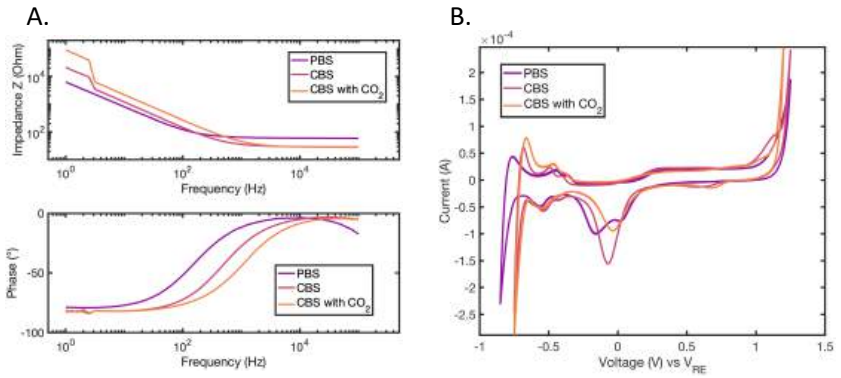

Figure 6.15: *A. Comparison of EIS Bode plots of PBS, CBS and CBS with CO_2. B. Comparison of CVs of PBS, CBS and CBS with CO_2*

Figure 6.15 shows a comparison of typical EIS and CV scans of CBS with and without CO_2 and PBS. Both CBS solutions exhibited lower high frequency impedance (≈ 30 Ω vs 70 Ω for PBS), indicating lower R_A. As mentioned earlier, the conductivity of CBS electrolytes was higher than PBS, which explains the lower R_A value as $R_A = \frac{\rho}{4r} = \frac{1}{\sigma 4r}$, where σ is the electrolyte's conductivity. Therefore, for a 2.33 times lower R_A, the conductivity of CBS electrolytes can be estimated to be 2.33 times higher than PBS, around 37.3 $mS.cm$. The gradient in impedance magnitude in the capacitive region (f $< 10^2$ Hz) was slightly higher for CBS electrolytes, suggesting a smaller double-layer capacitance, which was confirmed by the EIS fitting results. EIS fitted data confirmed a factor two division of R_A in CBS and for C_{dl} (26 μF for PBS vs 15 μF for CBS), along with an increase of α in the CPE fit from 0.9 to 0.93, indicating a more capacitive behaviour. Although the addition of CO_2 changed R_A and C_{dl} (see 6.5), CBS still exhibited a twice lower C_{dl} than PBS, confirming the effect

of CBS. Otherwise, CBS with and without CO_2 had similar EIS profiles with equal high-frequency impedance and similar consistent noise at low frequency (f < 3 Hz), however, the addition of CO_2 to the CBS solution increased the cutoff frequency slightly ($f_{CBS} \approx 7.10^2\,Hz, f_{CBS+CO_2} \approx 2.10^3\,Hz$), which suggest a decrease of the double-layer capacitance ($f_c = \frac{1}{RC_{dl}}$). The low-frequency noise magnitude was also larger after addition of CO_2.

Overall, CVs were similar between PBS and CBS, with similar PtO formation region, H-evolution and similar potentials for PtO reduction peaks, however, a few differences were observed. First, the water window was slightly larger for PBS in the H-evolution region, but similar to CBS without CO_2 in the O-evolution region, while the addition of CO_2 further shortened the water window in the O-evolution region only. The double peak on the cathodic scan for PBS ($E_1 \approx 0$ V and $E_2 \approx$ -0.2 V) was not observed for the CBS electrolytes, which exhibited a single peak at E ≈ -0.1 V for CBS and E ≈ -0.05 V for CBS with CO_2. Both CBS electrolytes also had two additional peaks: in the reduction scan at E ≈ 0.6 V and in the oxidation scan at E = 1 V, which was also observed in PBS with CO_2 (Fig 6.22). Finally, the slightly larger peaks in the H-evolution (oxidation) region are attributed to more H adsorption during the reduction phase for CBS with CO_2.

The evolution of OCP throughout experiments is shown in figure 6.16 B. First, CBS electrolytes had a consistently lower OCP than PBS by ≈ 80 mV, which was not due to a pH difference as CBS with CO_2 had a similar pH to PBS. While PBS, exhibited more variability (within 20 mV), CBS was very stable and CBS with CO_2 showed a slight increase of OCP with increasing k, which corresponds to chronologically successive experiments, which may indicate a slight acidic drift over time. On the other hand, E_{start} (Fig 6.16 A.) remained stable throughout experiments for CBS with CO_2, while CBs without CO_2 showed an overall decrease with time. The increased stability of E_{start} could suggest better buffering stability in repeated experiments. The discrepancy between OCP and E_{start}, which is attributed to the background decay that

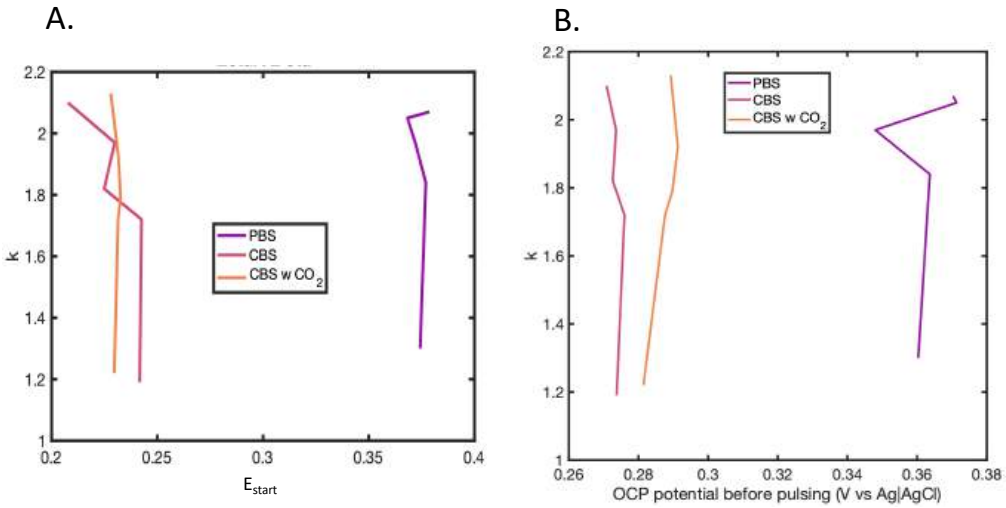

Figure 6.16: *A. Starting potentials (E_{start}) recorded on the oscilloscope for PBS and CBS with and without CO_2 mean for each k-values. B. OCP values recorded on the potentiostat before pulse trains for PBS and CBS with and without CO_2 mean for each k-values.*

was characterised in section 3.4.2, was larger for CBS (between 20 mV and 70 mV) than for PBS ($<$ 20 mV except for one outlier value at $k = 2$), which may indicate that PBS mitigates the small current flow better than CBS.

The profile of the OCP step following pulse trains was compared for different electrolytes of various buffering capacities in figure 6.17. While H_2SO_4 is not strictly considered as a buffered solution, the high concentration in H^+ yields a stable pH against moderate perturbations. Indeed, the rapidity of recovery of OCP post pulsing was similar in H_2SO_4 and well-known buffers PBS and CBS, while the unbuffered saline solution showed a recovery time at least five times superior. Therefore, there is a correlation between OCP recovery time and buffering capacity, which may suggest different behaviours at the interface during pulses. The higher buffering capacity of CBS seems to be confirmed as CBS showed a quicker recovery time than PBS.

The corrected anodic and cathodic polarisations, and the evolution of corrected end potential with k are shown in figure 6.18. First, the repeatability of the results stood out for CBS without CO_2 and CBS with CO_2 to a slightly

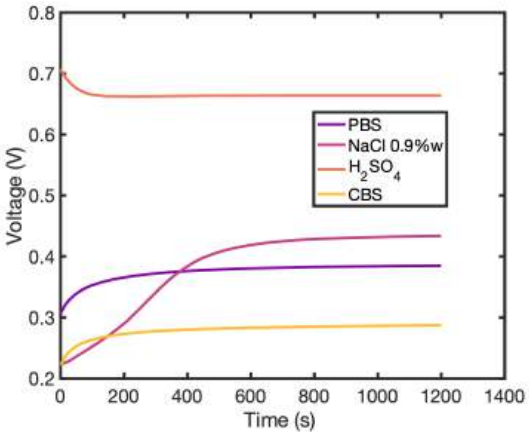

Figure 6.17: *OCP post pulsing for four different electrolytes with various buffering capacities*

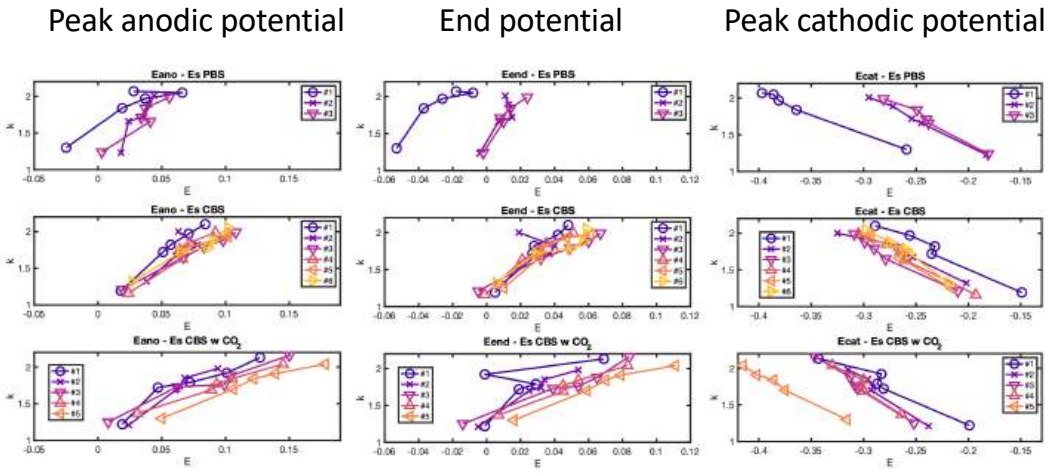

Figure 6.18: *Evolution of corrected potentials ($E - E_{start}$), E_{ano}, E_{end}, and E_{cat}, with k for PBS, CBS without CO_2 and CBS with CO_2.*

lesser extent (except for E_{cat} in the fifth dataset), while the second and third datasets in PBS were very consistent, indicating the first dataset may have been an outlier. The cathodic potential excursion was similar for all three electrolytes, exhibiting similar ranges (106 ± 9 mV for PBS, 108 ± 22 mV for CBS and 91 ± 29 mV for CBS with CO_2), and similar inflexions around $k \approx 1.75$, as it was already observed on other experiments (pH, gels). The actual cathodic excursions were slightly more negative for CBS compared to PBS (20 mV to 40 mV difference) and more negative after CO_2 addition by an extra 50 mV, yielding a more negative cathodic polarisation between ≈ 70 mV and 110 mV. The anodic polarisation and end potential exhibited the same trends and discrepancies between solutions. The potentials were similar for the lowest k-value (around 20 mV for E_{ano} and 0 V for E_{end}), however, larger k-values yielded larger excursions in CBS, especially after the addition of CO_2. On average for E_{ano}, the potential values spans were 40 ± 19 mV in PBS, 73 ± 10 mV for CBS, and 113 ± 24 mV for CBS with CO_2, meaning a twice as large anodic polarisation in CBS without CO_2 and three times as large with CO_2 compared to PBS. The discrepancy was similar for E_{end} with 21 ± 8 mV in PBS, 54 ± 11 mV in CBS, and 79 ± 16 mV in CBS with CO_2, indicating more anodic ratcheting in CBS, enhanced by the presence of dissolved CO_2. The shape of the excursions was also different, with PBS traces exhibiting an inflexion around $k \approx 1.75$, while in CBS with and without CO_2, E_{ano} and E_{end} were increasing almost linearly with k.

The average anodic and cathodic potentials were compared with cyclic voltammograms to identify electrochemical reaction mechanisms (Fig 6.19). As in previous experiments, E_{ano} was positively correlated with k and E_{cat} negatively correlated with k. E_{ano} was consistently located inside the PtO formation peak for all three electrolytes and all k values, despite the significantly larger excursion spans observed in CBS. The larger anodic excursion in CBS with CO_2 may be explained by the less pronounced PtO formation peak compared to PBS and CBS. The onset of PtO formation is less sharp CBS with

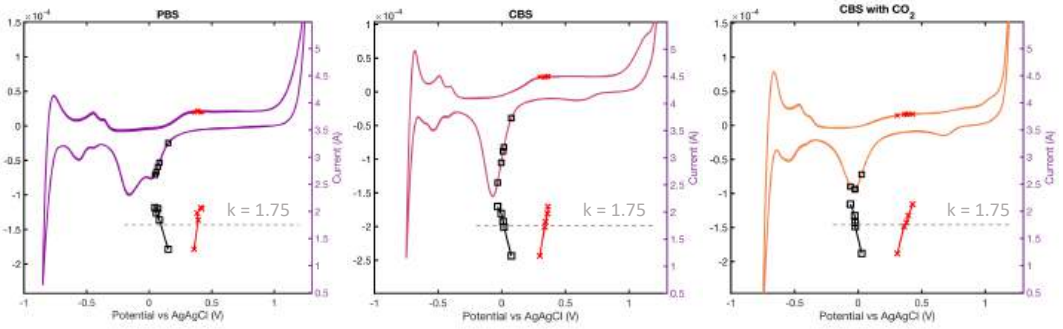

Figure 6.19: *Evolution of average anodic (red) and cathodic (black) potentials with k (right axis) and location on the respective cyclic voltammograms for PBS, CBS without CO_2 and CBS with CO_2.*

CO_2; therefore, further polarisation is needed to inject equal amounts of anodic charge. PtO formation may be hindered by competing reactions or a blockage of preferential reaction sites, which could be due to dissolved CO_2.

Cathodic potentials were all located in the PtO reduction peak, the first of two peaks in PBS. In comparison with other experiments such as the pH experiment (6.1), high k-values were not associated with cathodic potentials entering the PtO reduction region anymore, as all k-values were located in that peak, with high k corresponding to larger currents supplied by the same reaction. For CBS, the decrease of E_{cat} with k was almost linear, with potentials located along the peak from its base at low k to the peak at high k. PBS showed an initial increase with k before plateauing as potentials reached the actual peak, and CBS with CO_2 showed a similar behaviour, plateauing around the peak for k around 1.75, and $k = 2$ falling beyond the peak. The similarity between PBS and CBS with CO_2 suggests that the single peak reduction in CBS with CO_2 corresponds to the first peak in PBS (E $\approx$ 0 V), while the second peak (E $\approx$ -0.2 V) may not be present in CBS with CO_2, possibly being related to the presence of molecular oxygen. In a deeper analysis of the CV, the semiderivative of CVs for all three electrolytes were compared to separate peak contributions on the 5 mm disc electrode (Fig. 6.20) and on the large AR electrode (Fig. 6.21). PBS showed two clearly separate peaks of similar magnitude on the semiderivative, and CBS with or without CO_2

exhibited a single well-defined peak, suggesting the reaction constituting the second peak in PBS did not occur in CBS. Therefore, this reaction is not attributable to the injection of CO_2, or the reduced concentration of dissolved oxygen, but may be associated with phosphate evolution (1.13) [Hudak et al., 2010], which is the only species present in PBS and not in CBS. Moreover, the hypothesis that the reduction peak potential shift between CBS without CO_2 and with CO_2 was due to the disappearance of one reduction peak when adding CO_2 can be rejected; the peak shift is attributed to pH change ($\approx$ 50 mV shift for a pH difference of $\approx$ 1, which agrees with Nernst's ratio of -59 mV/pH). The semiderivative curves show almost identical features for H-evolution in all three electrolytes, showing that H-evolution was not disturbed by gas sparging or carbonate species. An additional reduction peak at E $\approx$ 0.75 V was observed for both CBS electrolytes indicating carbonate species evolution, and an additional oxidation peak at E $\approx$ 1.1 V may indicate the pending oxidation reaction. The semiderivative of CBS with CO_2 showed more activity in the oxidation scan than the other electrolytes, which was observed on PBS with CO_2 (see 6.25), indicating an increasing number of faradaic oxidation reactions following CO_2 injection.

6.4.4 Discussion

The charge injection of platinum electrodes was compared in the usual phosphate-buffered saline and in a carbonate-buffered saline with an ionic composition corresponding better to interstitial fluid. CBS was complemented with gaseous CO_2 to decrease the pH from $\approx$ 9 to $\approx$ 7, closer to PBS and the body's pH. CBS had lower R_A, C_{dl}, and OCP than PBS, even after addition of CO_2, which corrected the pH discrepancy. CBS with CO_2 displayed a lower C_{dl} than without CO_2 and a narrower water window on the CV. CBS without CO_2 had a narrower water window than PBS and exhibited a few different peaks, essentially an additional reduction peak at 0.6 V vs Ag|AgCl and a single PtO reduction peak. The single peak observed in the PtO reduction region in CVs of CBS may be the fusion of both peaks observed in ambient PBS as

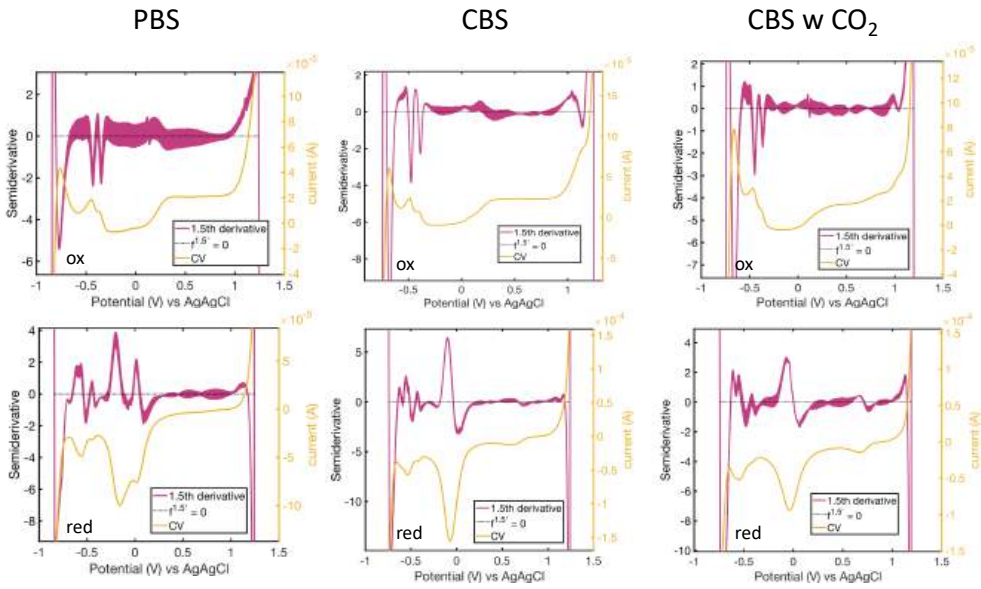

Figure 6.20: *Semiderivative (1.5^{th} order) analysis curves of the CV of PBS, CBS without CO_2, and CBS with CO_2 on the 5 mm disc electrode. The CVs were separative in oxidation ("ox") and reduction ("red") scans.*

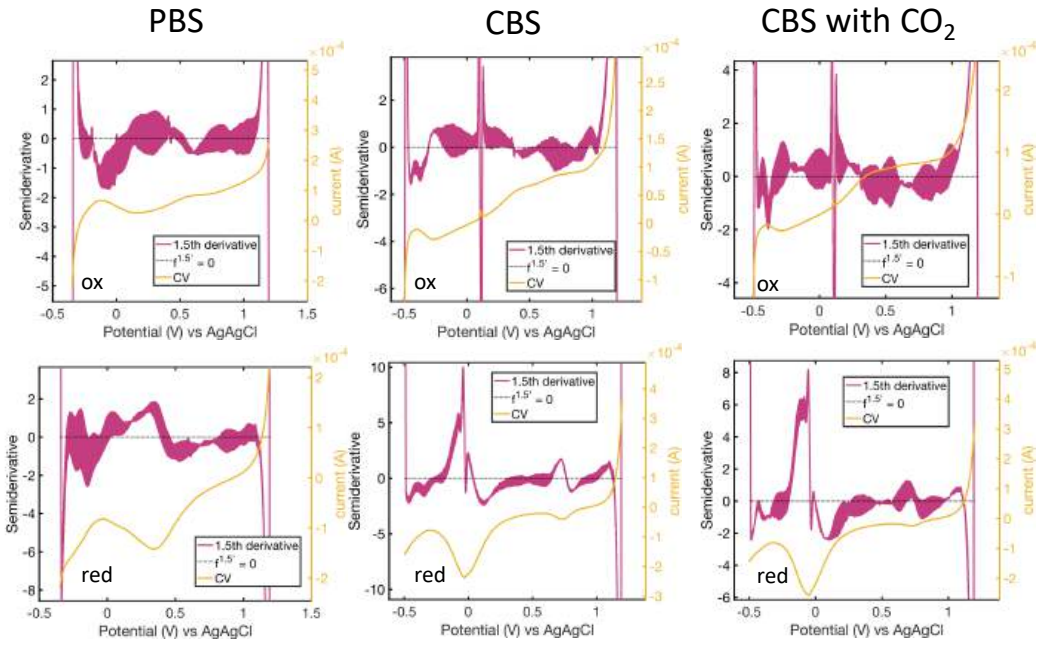

Figure 6.21: *Semiderivative (1.5^{th} order) analysis curve of CV in PBS, CBS, and CBS with CO_2 on the large AR electrode. The CVs were separative in oxidation ("ox") and reduction ("red") scans.*

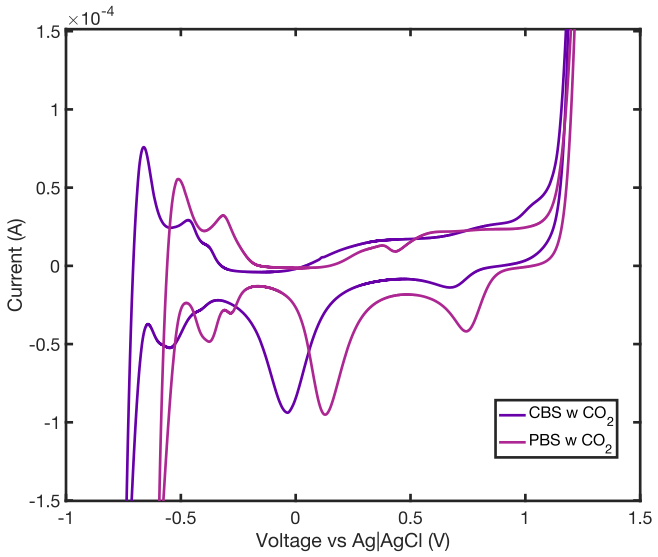

Figure 6.22: *Comparison of CVs of PBS and CBS with CO_2.*

it was located in the middle and has an amplitude equivalent to the sum of both peaks. An additional shoulder was observed in the anodic scan starting at E $\approx$ 1 V, which may be attributed to carbonate activity. The amplitude was smaller in CBS with CO_2, therefore, it may be attributed to the reaction of carbonate species with dissolved oxygen. An additional reduction peak was common to CBS with and without CO_2 and PBS with CO_2, which suggests a relationship with CO_2 or CO_2-derived species such as carbon monoxide (CO), but not specific to CBS.

In CBS, both polarisations (anodic and cathodic) showed an increased span over the same k-values span than PBS, which may be a direct consequence of the lower C_{dl} values for carbonate solutions. The more capacitive behaviour of CBS may be attributed to a better buffering capacity, similar to higher concentration PBS (cf 6.2). CBS buffering capacity may be enhanced by its lower viscosity than PBS [Obata et al., 2019], enhancing diffusion. Since it is hypothesised that the body may be represented more accurately by CBS, this work suggests that the larger polarisation observed *in vivo* may be attributed, at least in part, to the carbonate buffer system. Moreover, this observation suggests that characterisation performed in PBS may underesti-

mate the electrode polarisation as mentioned in previous studies [Cogan, 2008, Harris et al., 2019a, Doering et al., 2023], and thus the safe charge injection levels *in vivo*, and using CBS may help reduce the translation gap to *in vivo* implantation. The anodic polarisation was further increased by CO_2 in CBS, which was counter-intuitive as removing O_2 should decrease the irreversible cathodic charge injection, therefore, reduce the positive potential ratcheting. However, larger ratcheting along with the lower OCP were shown to be consequential of removing O_2 from the electrolyte [Harris et al., 2019a, Hudak et al., 2017b]. The increase in anodic polarisation may be the consequence of other mechanisms involving carbonate species. The onset of PtO formation was less sharp in CBS and further flattened by injection of CO_2; therefore, further polarisation was needed to inject equal amounts of anodic charge, which may explain the larger anodic excursion in CBS with CO_2. The injection of CO_2 also increased the slope of the EIS magnitude at low frequency (Fig. 6.15), suggesting a decrease of the double-layer capacitance. CO_2 may have affected the OH^- coverage participating to pseudo-capacitive charge injection 1.8 by decreasing the dissolved O_2 concentration or directly interacting with the OH coverage. Indeed, CO is known to react with PtO, especially disturbing the PtOH coverage [McCallum and Pletcher, 1976]. Therefore, by combining both observations, it was concluded that CO affected the PtO formation process, which increased the polarisation during biphasic pulses due to higher overpotentials needed for charge injection. The anodic polarisation remained similar in PBS after injection of CO_2, suggesting that the large anodic polarisation corresponds to a specific effect of CBS, as CO_2 interaction with PtO may have been less prominent without a bicarbonate buffer environment. The cathodic polarisation in CBS with CO_2 kept a similar value span, although the recorded potentials were similarly located as in PBS sparged with CO_2 and N_2, suggesting an influence of absence of O_2. Reduction of molecular O_2 is a well-known cathodic reaction at Pt electrodes which supplies between 7% and 30% of the cathodic charge injection, therefore, removing dissolved oxygen may explain

the larger cathodic polarisations. The cathodic polarisation was shown to be correlated with Shannon's limit in section 6.1, and there is evidence that Pt dissolution occurs mostly in the cathodic phase, once a sufficient part of the surface is oxidized and reduced [Kumsa et al., 2016b, Topalov et al., 2014b]. CO, which is a direct product of CO_2 reduction, was shown to hinder anodic dissolution and to enhance cathodic dissolution, possibly by blocking redeposition sites in the PtO formation region [Topalov et al., 2014b]. Therefore, I hypothesise that using CO_2-sparged electrolyte may increase Pt dissolution by increasing the cathodic polarisation through molecular oxygen removal and by blocking dissolved Pt redeposition sites. However, in a realistic electrolyte, similar concentrations of CO_2 and O_2 are expected, therefore, the cathodic polarisation is expected to be less affected.

CBS and PBS were made slightly differently, using different salts (KCl vs NaCl), which resulted in a higher conductivity for CBS. As a 2.3 times more conductive solution, CBS should exhibit similar differences in behaviour as the difference between 0.45% NaCl and 0.9% NaCl used in the salinity experiment (see 6.2). With a higher conductivity and better diffusion properties, CBS faradaic mechanisms are expected to be less diffusion-limited, therefore, the larger polarisations should be attributed to the lower C_{dl} and carbonate species interference. Further differences between both buffers may arise from the salt cations, as potassium ions have been shown to favour oxygen reduction reactions, while sodium ions favour hydrogen evolution [Jin et al., 2010, Ding et al., 2022]. The slightly larger polarisation with CO_2-sparged CBS may be due to the absence of favoured O_2 reduction, however, the difference in cathodic polarisation was minimal between CBS and PBS, and already pertaining to a lower capacitance, therefore, the effect of K^+ ions is hypothesised to be minimal. Overall, the buffer experiment unveiled the great complexity of understanding charge transfer at Pt electrodes as opposing influences, including ionic affinities, competing (electro)chemical reactions, changes in capacitance and access resistance, and changes in diffusion patterns compete and need to

be quantified to understand precisely what effect is more likely to dominate.

Initial experiments were conducted without replenishing the CO_2 stock in the solution and both the OCP (-30 mV) and pH (+1) changed over the course of the experiment, suggesting CO_2 may be irreversibly consumed. The changes were not observed when CO_2 was added to PBS, which suggests that CO_2 irreversible evolution was specific to CBS, with CO_2 participating in the buffering. In the comparison of the electrolytes in figure 6.16, the injection of CO_2 increased the OCP by 10 to 20 mV on average, therefore, an OCP decrease of 30 mV would mean that all of the CO_2 was consumed. The pH at the end of experiments increased to become closer to the pH of ambient CBS, however, it still remained more acidic, which nuances the point that all the CO_2 disappeared by the end of experiments. However, this result showed that constant CO_2 supply was preferable to ensure better comparability between results.

During experiments, gas bubble formation was observed on the counter electrode in CBS without the injection of CO_2, however, no bubbles were observed on the working electrode. Whereas gas bubbles on the WE surface would have disrupted charge injection and electrochemical tests because of a large impedance increase, no change was observed with bubbles on the CE surface. The CE area was chosen to be at least ten times larger than the WE so that the charge injection could be supplied solely by capacitive mechanisms, avoiding faradaic changes at the CE. Therefore, it is unlikely that the gas bubbles originated from a faradaic process at the CE, especially because it would have occurred at the WE beforehand, thus the reaction must be a spontaneous chemical reaction or a physical reaction, for example bubble formation resulting from the merging of smaller gas bubbles. The absence of bubbles of the WE further suggests that the chemical reaction may be catalyzed by the carbon CE, and that it would not occur on a different material.

6.5 Discrimination of the effect of dissolved gases

6.5.1 Rationale for isolating the effect of dissolved gases

Hydrogen and oxygen are well-known reactants in aqueous electrolytes as they are produced in the electrolysis of water; production of gas (H_2 at the inferior boundary and O_2 at the superior boundary) are the usual potential limits of the water window. However, dissolved gases and derived species may also interact with the electrode within those boundaries: for instance, reduction of molecular oxygen is a well-known faradaic reaction contributing to cathodic charge injection, which manifests itself in CVs as a change in baseline currents at low potentials (E $\leq$ 0 V vs Ag|AgCl) [Cogan et al., 2010, Hudak et al., 2010, Musa et al., 2011]. Cogan et al. [2010] evaluated the contribution of molecular oxygen reduction to charge injection *in vitro*, concluding that 88% of cathodic charge in slow-sweep CV was attributable to O_2 reduction versus 7% during current pulsing in O_2-saturated saline. The authors extrapolated their data for *in vivo* charge injection, reaching a 0.5% estimate considering the lower oxygen concentration *in vivo*. Musa et al. [2011] used a coulometric method to estimate that O_2 reduction was responsible for 19 to 34% of charge injection in ambient O_2 concentration on electrodes twice as large (50 μm diameter vs 25 μm for Cogan et al. [2010]). The absence of oxygen may affect reaction pathways, as cathodic charge injection needs to resort to larger overpotentials to supply charge [Kumsa et al., 2016b, Doering et al., 2022].

The activity of carbon dioxide, which is present in tissue at a concentration which is thought to be equivalent or slightly larger to O_2 [Cogan, 2008], was presented in the preceding section 6.4). Nitrogen (N_2) and argon are considered inert, and are often used to degas solutions, assuming they do not induce new electrochemical reactions. In this experiment, N_2 was used as a control to remove the dissolved oxygen from the solution without inducing new reactions, thereby separating the contributions of other gases and of the

absence of oxygen.

6.5.2 Specific methods for dissolved gases

To achieve a controlled atmosphere in the cell and limit the gas emission in the room, a custom cell lid was designed and 3D-printed (Fig. 6.23). The external diameter of the cell lid was slightly smaller than the cell and used a silicone O-ring to ensure gas-tight sealing. Four holes were pierced in the middle of the piece to let the three electrodes in and the gas dispenser. From the original design shown in figure 6.23, the electrode holes were filed at a larger angle to let all the electrode bodies fit together, which made the system permeable, however, still useful to keep a gas-saturated atmosphere in the air layer topping the solution. Nevertheless, due to gas leakage through the cell lid, gas replenishment was performed throughout the experiments, to have comparable gas concentrations for each k-value.

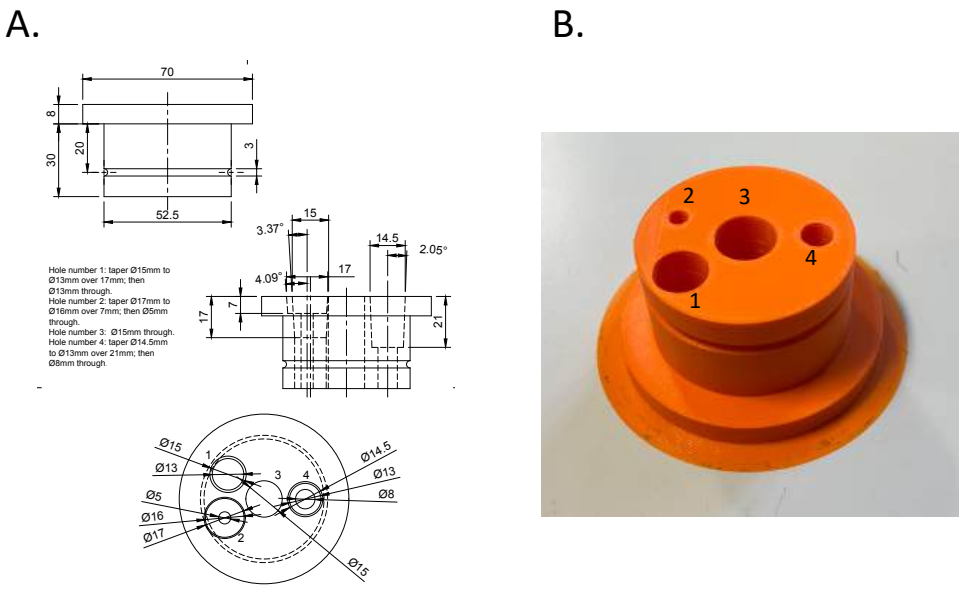

Figure 6.23: *A. Engineering drawing of the cell lid with dimensions. B. Picture of the 3D-printed lid, numbers correspond to the holes numbered as in A.*

Constant gas injection generated a problem of gas bubbles being trapped on the WE surface as it was placed upside-down, which affected the electrode

impedance and charge transfer. The first solution to keep the bubbles from the WE surface was to use a permeable cloth-type material such as a tea bag, which was placed around the WE to deflect gas bubbles away. The drawback of this method was due to the opacity of the teabag, which made visual inspection of the electrode surface for gas bubbles difficult, especially upon immersion, which was the most critical moment for bubble trapping. Despite keeping most bubbles away from the WE, the teabag was not impermeable to small bubbles which were travelling to the electrode surface and merging into larger bubbles, which would end up disrupting the measurements and need manual handling of the electrode. The final solution was to manually arrange for the gas dispenser to be as far away from the WE as possible and use a low gas flow rate to keep bubbles in the vicinity of the dispenser, unable to get trapped under the electrode. This solution prevented repeated measurement disruption due to bubbles.

The ultimate goal of this experiment was to test a realistic gas mixture for the dissolved gas concentration in the body. Model fluids [Cogan, 2008] use 6% CO_2 and 5% O_2, which is the concentration that was aimed for, the balance 89% being N_2. A three-channel gas mixing system was designed to obtain the desired mix based on gas flow proportion. Indeed, making the assumption of the perfect gas law at room temperature, the partial pressures of the various gases were equivalent to the proportion of volume, which is set by the gas flow. Therefore, with three adjustable gas flow meters, the flow rate of three gases was adjusted so the common outlet contained a gas mixture with set proportions. Ball valves were added to enable/disable channels when necessary. Gas cylinders used included pure nitrogen (100% N_2), pure carbon dioxide (100% CO_2), and air (approx 80% N_2 20% O_2); therefore, the realistic gas mix entailed drawing 6% CO_2, 25% air and 69% N_2 to complete the gas mix.

Prior to testing the gas mix, individual contributions of gases were evaluated: N_2-sparged, air-sparged and CO_2 sparged PBS were tested three times each, following the same protocol that would be used when using the realistic

gas mix. Gas was bubbled for 20 minutes before starting the electrochemical characterisation and conditioning and a constant low gas flow was kept throughout the whole experiment. Initial experiments did not include constant gas flow, which showed a progressive reoxygenation of the electrolyte, which was not desired. Solution pH was measured at the end of the initial gas sparging and at the end of the experiment.

6.5.3 Results

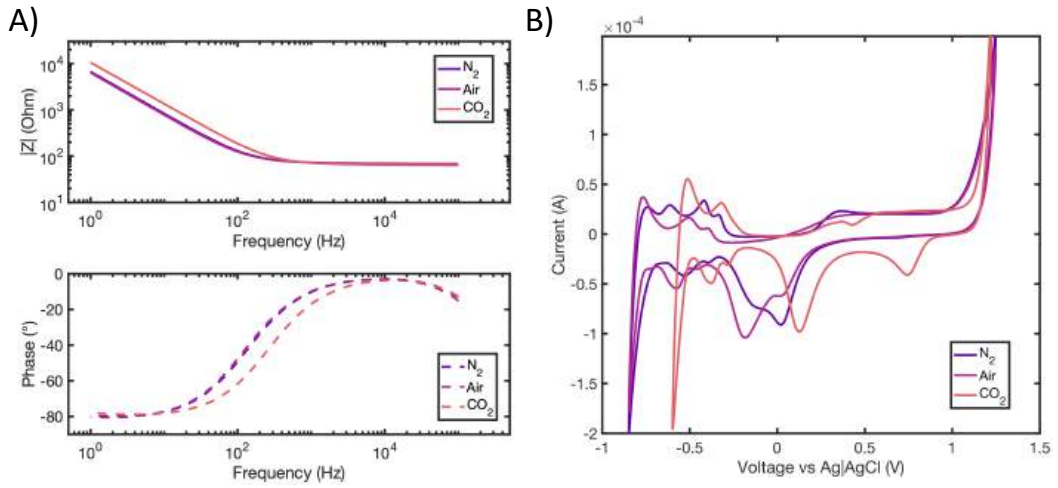

Figure 6.24: *A) Comparison of EIS Bode plots of three dissolved gases in PBS. B) Comparison of CVs of three dissolved gases in PBS.*

N_2-saturated and air-saturated PBS had identical EIS Bode plots, similar to ambient PBS (no gas sparging) with a slightly higher R_A (70 Ω vs 60 Ω). CO_2-saturated PBS had a similar Bode plot, with a similar R_A (70 Ω) and a phase transition at a slightly larger frequency (350 Hz vs 150 Hz), suggesting a smaller C_{dl} ($f_c = \frac{1}{RC}$), which was similar to CBS with CO_2. Indeed, C_{dl} was decreased by the addition of CO_2 by a factor two (14 μF vs 25 μF). N_2 exhibited a slightly lower C_{dl} than ambient PBS, however, α in the CPE fit was slightly larger (0.92 vs 0.9 for ambient PBS and 0.91 for PBS CO_2). CVs showed some differences. First, the water window was shorter for CO_2 by 200 mV; the addition of CO_2 made the solution more acidic (pH 5.8), which would suggest a positive shift of the curve, however, the CV shifted only at the H-evolution region, which was

similar to CBS. The H-evolution region was similar for air-sparged and CO_2-sparged PBS, with three oxidation peaks, while N_2-sparged PBS exhibited a fourth peak and smaller peaks on the reduction scan. The H-reduction peaks showed similar profiles for all gases on the semiderivative curves (Fig. 6.25), and the H-oxidation confirmed the different number of peaks with three peaks for ambient PBS, four clear peaks and an additional small peak for N_2, and two clear peaks and two small peaks for CO_2. The PtO reduction peak was different in all electrolytes: a single peak was observed in CO_2 and two peaks in N_2 and air, however, the predominant peak was different (E = 0 V for N_2 and E = -0.2 V for air). As the only difference between N_2 and air is the presence of dissolved oxygen, the second reduction peak may be attributed to the presence of O_2, however, it was not clear why the first peak was smaller. An additional peak was observed in the reduction scan for CO_2-sparged PBS (E = +0.75 V), which was similar to peaks observed in CBS (with and without CO_2), which can therefore be associated with carbonate species evolution (see Fig. 6.20). As a similar peak was present in CBS without CO_2 and PBS with CO_2, we can infer that a common species stems from dissolved CO_2 and CBS. The PtO formation region exhibited two peaks for CO_2, and the single PtO formation shoulder was sharper in N_2 than air. The semiderivative curves show that PBS with CO_2 exhibited a different peak shape (Fig. 6.25): for ambient PBS and PBS with N_2, the derivative is positive, then negative, while for CO_2, the derivative does the opposite. This indicates a relative negative peak, which may be attributed to CO adsorption competing with PtO formation.

CV features evolved throughout experiments for N_2 and CO_2, contrary to air, which was documented in figure 6.26. In N_2, the second PtO reduction peak grew with increasing k and time, while the second H-oxidation peak decreased. Since the second PtO reduction peak was associated with O_2 presence, this may indicate the progressive reintroduction of dissolved oxygen at the electrode surface, which may in turn change the affinity of hydrogen with platinum, explaining the changes in the H-evolution region. CO_2 showed only

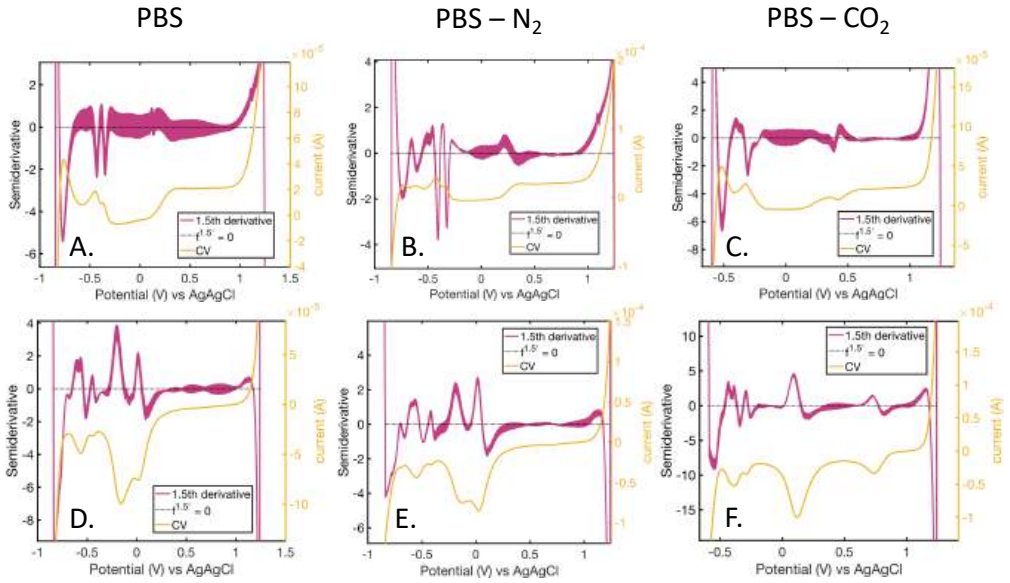

Figure 6.25: *Semiderivative analysis curves (1.5^{th} order) of CV in PBS sparged with various gases. The CVs were separated in oxidation ("ox") and reduction ("red") scans.*

a slight increase in PtO reduction, which may also indicate a slight increase in O_2 concentration. Therefore, combining the evolution of CVs in N_2-sparged and CO_2-sparged PBS with the absence of changes for the air-sparged and ambient PBS, the CV evolution was attributed to a progressive reoxygenation of the electrolyte.

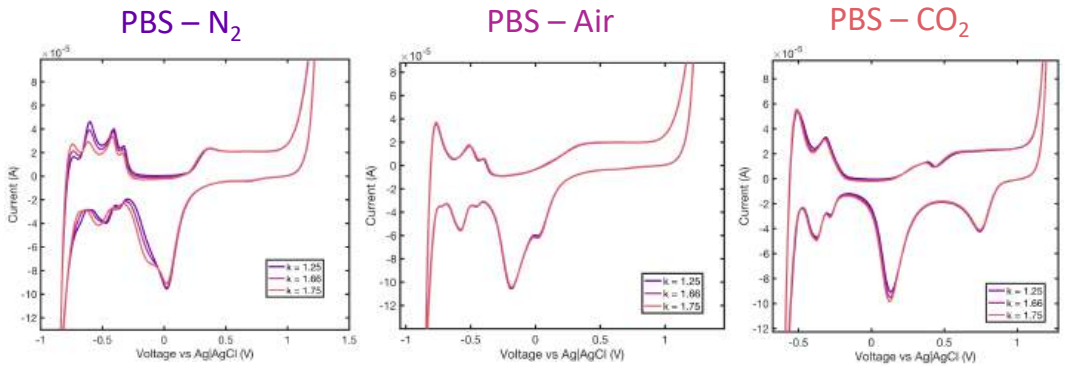

Figure 6.26: *Evolution of CVs of three dissolved gases in PBS with increasing k, which represents consecutive experiments*

The recovery OCPs were similar between ambient and sparged PBS, with PBS CO_2 sitting $\approx$ 100 mV over ambient PBS due to the pH difference of 1.4. PBS N_2 showed a quicker recovery, which may explain the lower OCP, and

CO_2 had a larger recovery time, possibly due to the absence of oxygen.

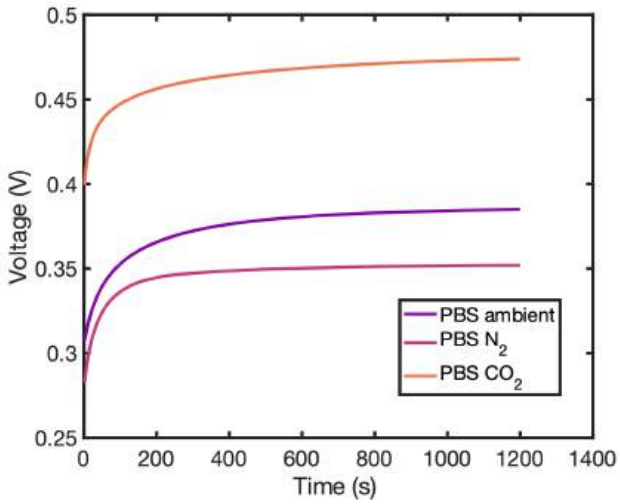

Figure 6.27: *OCP measured after pulse trains in PBS ambient, sparged with N_2 and sparged with CO_2.*

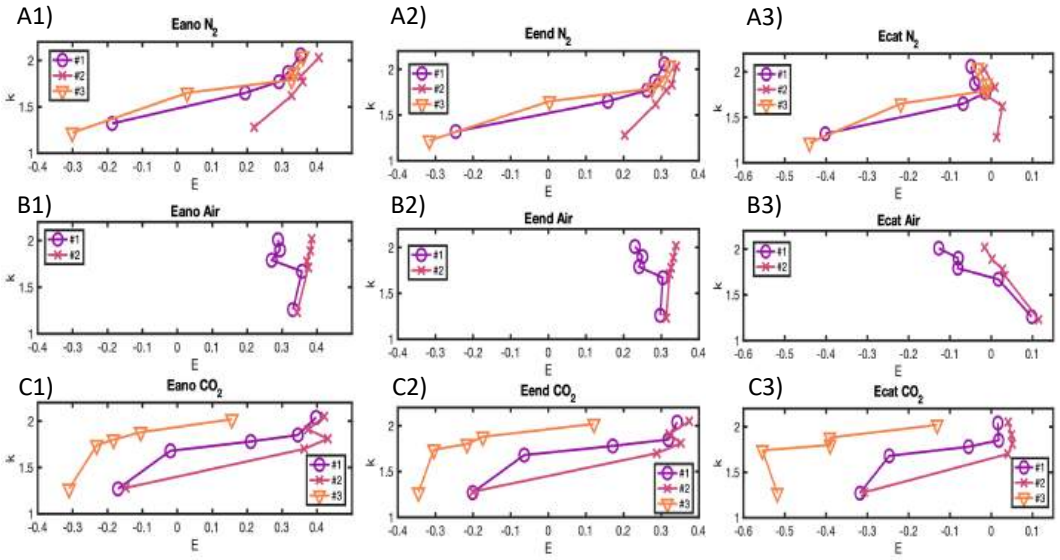

Figure 6.28: *Evolution of raw potentials with k for three dissolved gases in PBS. Grid system with gases assigned to rows (A for N_2, B for air, and C for CO_2) and columns assigned to the potential of interest (1 for anodic, 2 for end, and 3 for cathodic).*

Each gas was tested three times, and the recorded potentials are presented in figure 6.28. While air was quite consistent and corresponded to what was

observed in ambient PBS, N_2 and CO_2 exhibited large discrepancies and behaviours unlike any previous experiments, especially for E_{cat}, which suggested these measurements were artefacts. Indeed, large potential decays were observed for both gases, and the amplitude of the decays decreased with increasing k or with time. Since the decays were not observed in air-sparged PBS, and decreased over time during experiments, it may suggest that the absence of oxygen destabilised the interface, causing larger decays during current leakage. The progressive reoxygenation of the electrolyte could also explain the progressive decrease of the decay and increase in potential. A few supplementary tests were performed, where the potential decay was monitored for each k-value to be subtracted, however, the measured decays were inconsistent with the recorded potentials, therefore inconclusive. The decays were measured 30 s after the pulse train was applied to let the potential recover, therefore, it is possible that the interface did not fully recover or that the behaviour changed from the pulse train to the decay measurement, as was seen in the repeatability tests (3.4.3).

Test n° 2 was more consistent than others for N_2, with trends and spans in the range of previous experiments, which suggested that the introduction of N_2 increased the E_{ano} and E_{end} spans while E_{cat} remained in the same range, which was similar to CBS with CO_2. The drop in potential observed on the first test with air came along with a sudden change in CV, which cause remains unknown, therefore, the second test served as reference.

The behaviour of Pt electrodes with different dissolved gases and buffer systems was further assessed on the large AR electrode (Fig 6.30). In PBS, sparging with N_2 increased the span of values for E_{ano} and E_{cat}, however, the potentials were located in the same regions, respectively the oxide formation peak for E_{ano} and the H-evolution region for E_{cat}. CO_2 increased the spans similarly to N_2 for E_{cat}, but E_{ano} remained almost constant, even slightly decreasing with k. For both gases, E_{cat} was located slightly more towards the oxide reduction region, in the transition between oxide reduction and gas

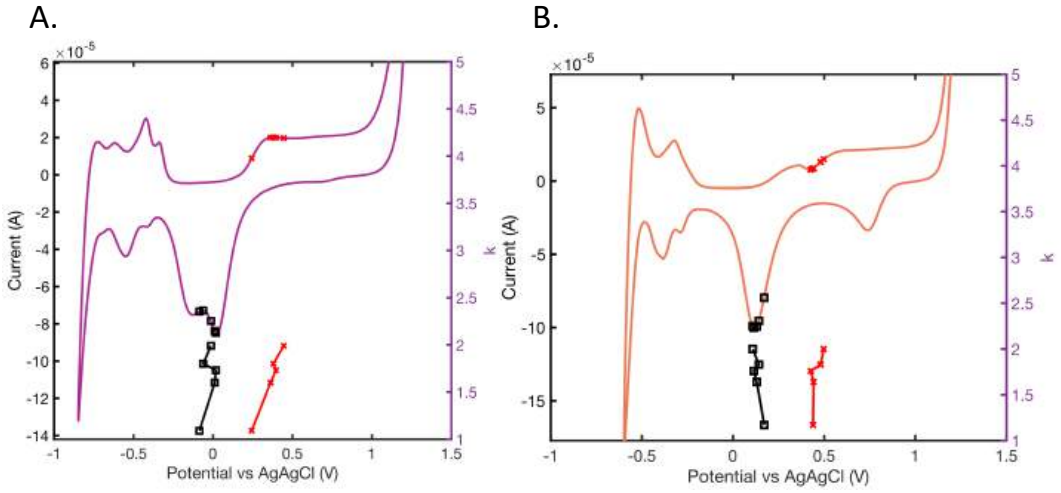

Figure 6.29: *Evolution of real potentials with k, and projections on CV for A. PBS sparged with N_2 and B. PBS sparged with CO_2.*

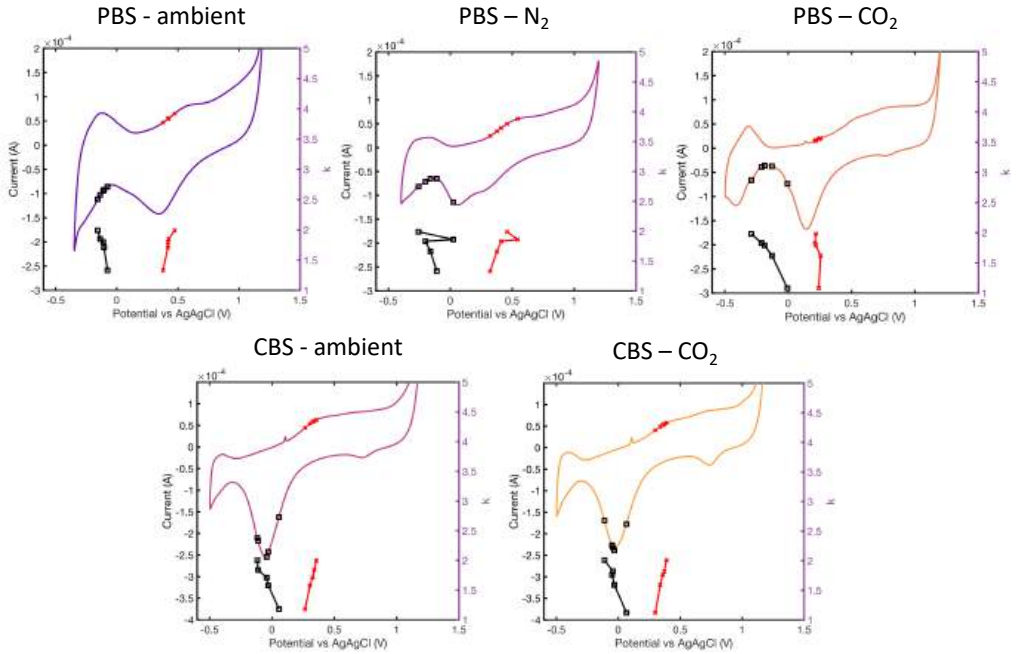

Figure 6.30: *Evolution of real potentials with k, and projections on CV for PBS and CBS with and without dissolved gases.*

evolution, while for ambient PBS, E_{cat} was in the gas evolution region for all k.

E_{ano} was located in a similar range of values in CBS (with and without CO_2) as in PBS, and the span was not changed by the addition of CO_2. E_{cat} showed a similar trend and span in CBS with and without CO_2. Unlike in PBS, E_{cat} was located in the PtO reduction peak for all k-values. Thus, the large AR electrode revealed a noticeable difference in behaviour between CBS and PBS.

6.5.4 Discussion

Sparging the solution with gases had a double effect: removing the dissolved oxygen and adding a new dissolved gas. Observations that were common to N_2 and CO_2 sparging suggest a behaviour consequential of the absence of oxygen, while individual effects suggest a gas-specific influence. Removing the dissolved oxygen slightly increased R_A and decreased C_{dl} suggesting that O_2 participates in charge transfer in several ways, for instance through favoring OH-plating, which may contribute to capacitance. CVs without oxygen had different features, including a sharper PtO formation region and a predominant PtO reduction peak, whereas CVs with oxygen (air-sparged or ambient) showed two almost equal PtO reduction peaks, the second one favoured in air-sparged PBS, which highly suggest that dissolved O_2 contributes to that reaction heavily. This was further confirmed by the gradual increase of that second peak over time for CVs in sparged electrolytes as it was hypothesised that O_2 content increased gradually throughout the experiment. Therefore, the peak observed at E $\approx$ -0.2 V vs Ag|AgCl relates to a form of reduction of molecular oxygen. The sharper PtO formation shoulder may be due to oxygen presence facilitating PtO formation, while the addition of CO_2 delayed the onset of PtO formation, which can be explained by adsorbed CO activity. The first peak in the oxidation region (E = 0.4 V) may indeed correspond to CO adsorption.

The charge injection attributable to dissolved gases (oxygen) was shown

to be less prominent during pulses than in cyclic voltammetry [Cogan et al., 2010]. In the original comparison (Fig. 6.28), the oxygen-stripped electrolytes (N_2 and CO_2) exhibited negative potential excursions in a similar potential range at low k (600 mV lower than air-sparged), which gradually increased with k until reaching more common values and trends at $k \geq 1.75$. The excursions were larger than observed in all previous experiments, and were attributed to the potential decay when the +30 V supply was switched on (see section 3.4.2), yielding unrealistic values and trends, especially for E_{cat} which should decrease with increasing k. Thus, the larger decay and excursions were correlated with the absence of oxygen and decreased over time as the oxygen content in the solution increased, as was observed in the CVs (Fig. 6.26). Therefore, the original hypothesis was that dissolved oxygen provided better stability to the interface by being able to absorb the low current flow through the circuit without causing a large potential decay, whereas in the absence of oxygen, the WE became more polarised to supply charge through capacitive and further faradaic mechanisms. The influence of dissolved oxygen is double-sided as it offers a major cathodic charge injection mechanism while creating an imbalance in charge injection which favours Pt dissolution [Musa et al., 2011, Cogan et al., 2010, Kumsa et al., 2016b]. The direct influence of dissolved O_2 on Pt dissolution is also controversial as Matsumoto et al. [2011] reported a significant enhancement of dissolution with O_2, while Topalov et al. [2014b] report no observable differences between O_2-sparged and N_2-sparged saline. The discrepancy may be due to the potential boundaries and electrolytes used in these voltammetric studies, with Topalov et al. [2014b] using a larger window of 0.1 V to 1.65 V vs RHE in $HClO_4$ compared to windows of 0.6 V to 0.95 V or 1.25 V vs RHE in H_2SO_4 for Matsumoto et al. [2011]. In these regimes, the dissolution may be dominated by different mechanisms, as Topalov et al. [2014b] use a chlorinated electrolyte with a higher potential limit favourable for chlorine-mediated Pt dissolution, while Matsumoto et al. [2011] may observe oxidation/reduction dissolution of Pt. Therefore, the con-

ditions I observed may relate rather to Matsumoto et al. [2011], suggesting that removing the oxygen from the solution reduced the dissolution. Although sparging PBS with N_2 and CO_2 decreased the OCP as expected [Hudak et al., 2017b, Harris et al., 2019a] and decreased C_{dl} for CO_2, the charge injection mechanism did not substantially change, with alternations of PtO formation and reduction remaining the main candidates. However, discrepancies arose when using the large AR electrode and comparing PBS and CBS sparged with different gases, showing a greater dependence of the behaviour on electrolyte than dissolved gases. While CBS remained almost identical after CO_2 sparging with E_{cat} located in the PtO reduction peak, PBS exhibited E_{cat} located in the hydrogen evolution region for all k-values for ambient PBS and for higher k-values for sparged PBS. Therefore, sparging had a little effect at low k in PBS, however, E_{cat} consistently finished in the hydrogen evolution region while CBS potentials were kept in bound of PtO reduction. The superior diffusion quality of CBS may have enhanced the diffusion of protons to the interface during the cathodic reactions, while in PBS, a greater polarisation occurs at the electrode edge, eventually leading to hydrogen evolution. Therefore, this combination of factors suggests that the electrode behaviour during pulsing is highly dependent on diffusion and that the local environment at the electrode surface is different than the bulk electrolyte and is crucial to understanding charge injection mechanisms.

Further experiments were conducted with continuous gas sparging to limit the reoxygenation of the electrolyte. This was not adopted initially out of concern that the constant bubbling would trouble the electrochemical tests and cause bubbles at the electrode surface, however, this was avoided by using a low flow rate (< 0.1 L/min) and positioning the gas dispenser far away from the WE. Even when continuously sparging the solution, CV peaks associated with dissolved oxygen kept growing over time, at a lesser rate, which was attributed to the imperfect hermeticity of the cell lid or the gas injection being too low and too far from the WE to effectively displace dissolved O_2 com-

pletely. Nonetheless, the electrolyte was considered comparable for all k-values in those conditions, as neither pH nor OCP varied substantially throughout experiments.

Chapter 7

Discussion

7.1 Thesis significance

This thesis investigated the influence of a range of experimental parameters on the charge injection behaviour of platinum electrodes near Shannon's safe stimulation limit with the aim of extending the understanding of the electrochemical mechanisms correlated with neural damage. A particular focus was made on the characterisation methods, as electrode characterisation is crucial to predict electrode behaviour *in vivo*, therefore, understanding the parameters that best discriminate electrode behaviours is key, so efficient characterisation protocols, including testing electrolytes, can be developed and used as a standard in the neural engineering community. This work was organised around several research questions stemming from knowledge gaps identified in a preliminary literature review presented in chapter 1:

- How do the methods influence electrode performance and how to best characterise stimulation electrodes' behaviour?

- How do materials and methods which do not figure in Shannon's equation influence platinum electrodes' behaviour in relationship to Shannon's parameter k?

- How do electrolyte characteristics influence platinum electrodes' behaviour in relationship to Shannon's parameter k, especially model body fluid conditions?

A hypothesis was developed recently to explain the electrochemical mechanisms causing neural damage when Shannon's safe stimulation limit of $k = 1.75$ is exceeded: repeated cycles of oxidation and reduction of platinum ultimately lead to platinum dissolution, which may harm surrounding tissue [Kumsa et al., 2016b, Niederhoffer et al., 2024, Shah et al., 2024]. The present thesis extends the understanding of Shannon's limit by testing the Pt to PtO redox cycles hypothesis across a range of electrolytes and electrode types, which represent possible use cases for implanted electrodes. Most studies on Pt dissolution come from the fuel cell industry and use cyclic voltammetry to determine triggers and catalysing factors [Topalov et al., 2014a, Cherevko et al., 2014, Geiger et al., 2015, Xing et al., 2014, Shah et al., 2024]. While cyclic voltammetry is useful to identify electrochemical reactions and obtain smooth pseudo-steady-state cycles of oxidation/reduction (opposed to potentiostatic control with abrupt voltage steps), CV does not reflect pulsatile charge injection for neural stimulation, which is often current-controlled and at higher frequencies. Therefore, although results of CV studies were used for interpretation, the electrode behaviour needed to be assessed during biphasic pulses. My work uses a similar approach and framework to Kumsa et al. [2016b], which showed that the electrode potential reached PtO formation in the anodic phase and reduction in the cathodic phase during biphasic pulses in aerated H_2SO_4, while PtO formation was not reached in de-aerated H_2SO_4. The authors proposed that the presence of oxygen-induced irreversible charge injection causes potential ratcheting, which makes the electrode potential enter the PtO formation region at sufficient k. The behaviour was then confirmed subcutaneously in rats [Kumsa et al., 2017]. The present work confirms the observations and interpretations from Kumsa et al. [2016b], although the damage threshold at $k = 1.75$ was found to correspond to PtO reduction rather than formation. Although

H_2SO_4 is a good model electrolyte to study Pt electrodes' behaviour [Kumsa et al., 2017, Weltin and Kieninger, 2021], the confirmation of the results in commonly used electrolytes I made with my research is significant. Then, the hypothetical mechanism was tested in electrolytes of different characteristics, which may alter the capacitive charge injection (4.2, 4.3, 6.1, 6.4, 6.5), the faradaic charge injection (4.3, 5.1, 6.1, 6.4, 6.5), and diffusion (4.1, 4.3, 5.1, 6.2, 6.3), showing how these characteristics may affect the electrode behaviour and whether the oxide-mediated Pt dissolution remained a strong candidate to explain neural damage.

The role of electrolyte composition on the behaviour of Pt electrodes has been assessed with a variety of electrochemical characterisation techniques by Harris et al.: CV (2018b) and Fourier Transform AC voltammetry (FTACV) (2019b), chronoamperometry (2018a), and CP (2019a). Valuable insight was provided by these studies on the influence on capacitance, charge injection, and polarisation, however, the direct influence of electrolyte on biphasic current-controlled pulses was only captured with CP and the relationship with Shannon's damage limit or Pt corrosion was not established. Other studies have shown direct characterisation methods of electrochemical reactions during biphasic current-controlled pulses: Doering et al. [2023] assess the role of dissolved oxygen, electrode conditioning, and pulse polarity on the potential trace of current-controlled pulses, however, no correlation to damage limits or electrode corrosion were made and the electrode behaviour was studied only over a few pulses, although I show time-dependent effects may occur over longer times, see 7.1.2. Musa et al. [2011] show a coulometric detection method of electrochemical reactions during biphasic pulsing, and evaluate the role of oxygen and albumin on Pt dissolution, showing the importance of dissolved O_2 on cathodic charge injection and how albumin blocks Pt dissolution. The considered Pt dissolution mechanism is anodic dissolution, which was shown to occur [Topalov et al., 2014a]; however, the onset potential is outside of the traditional water window potential limits, so it should not occur if safe stimu-

lation limits are respected, and represents a smaller contribution than cathodic Pt dissolution, which I hypothesise to observe in my experiments. It should be noted that the local environment at the electrode surface may be different from the bulk electrolyte and there may be some spatial disparities, which may result in some faradaic reactions taking place outside of theoretical limits, see 7.1.2.

Shannon's limit was developed experimentally to provide an explanation of stimulation-induced neural damage, and it has been criticised for leaving stimulation parameters out of the equation and for its lack of scaling with electrode size, roughness, and design [Cogan et al., 2016, Harris, 2024]. Posterior studies have reported low to no neural damage above $k = 1.75$ [McCreery et al., 1994, Shepherd et al., 2019, 2020], and electrode corrosion has been observed below $k = 1.75$ [Park et al., 2019, Doering et al., 2022], which suggests that the onset of Pt dissolution either does not correspond to Shannon's limit, or that other parameters may favour or delay its onset. My research provides an answer to this knowledge gap, as by keeping the electrode type close to the electrodes considered by Shannon, I established a correlation between Shannon's limit and an electrochemical mechanism, which had been suggested as a candidate in previous work [Kumsa et al., 2016b], and subsequently I showed that the threshold varied with experimental conditions, although the mechanism did not.

Therefore, this thesis provides novel insight into the behaviour of Pt electrodes during biphasic pulses at injected charges close to Shannon's limit, supporting previously hypothesised mechanisms explaining Shannon's limit across a range of experimental parameters. Specifically, my work shows that across the variety of experimental parameters, two main parameters most likely determine the onset and degree of Pt dissolution: the double-layer capacitance and the diffusion, discussed in 7.1.1. Furthermore, my research highlighted the complexity and variability of the electrode-electrolyte interface, discussed in 7.1.2, and the necessity of standardised, thorough characterisation processes to

understand charge injection mechanism, discussed in 7.1.3, while my research offers a robust protocol for the *in situ* characterisation of electrode processes during biphasic current-controlled pulses. Future directions to extend this work and take the conclusions further are discussed below in 7.2.

7.1.1 Platinum dissolution during biphasic pulses

In this work, many observations point to a dissolution process through repetitive oxidation and reduction of platinum. The suggested mechanism at Shannon's limit is similar to the mechanism described in fuel cell analysis papers with cyclic voltammetry, showing that upon oxidation of Pt through OH binding to the surface Pt atoms, some oxygen atoms migrate inside of the Pt lattice forming PtO bonds, see figure 7.1. Subsequently in the cathodic scan, PtO is reduced, which removes pockets of Pt atoms which have been isolated from the bulk by a layer of intercalated oxygen atoms. Pt may then redeposit anodically, however, two mechanisms may reduce the redeposition rate: adsorption of other species, such as Cl^{-}, blocking redeposition sites, and stabilisation of Pt^{2+} ions in solutions [Geiger et al., 2015]. The thermodynamics of these electrochemical reactions are governed mainly by the electrochemical potential at the interface, which constitutes a major difference between cyclic voltammetry studies and current-controlled biphasic pulses, as the voltage excursions are not controlled in the latter. Therefore, the experimental methods used in this work provide valuable insight to identify the dissolution mechanism by recording the electrode potential during pulses and identifying the corresponding electrochemical reactions. In the majority of experiments, the anodic polarisation was located in the oxide formation region, and the cathodic polarisation in the oxide reduction region, showing that the electrode undergoes cycles of oxidation/reduction. Increasing k increases both polarisations, increasing the PtO quantity in the anodic direction and increasing the amount of PtO reduction in the cathodic direction. The increase of the end potential following a pulse train with k suggests irreversibility in the charge transfer, which is attributed to the reduction of molecular oxygen during the cathodic pulse. Thus,

during pulses, cathodic charge injection involves capacitive charging, molecular O_2 reduction, and PtO reduction, and anodic charge injection involves double-layer capacitance discharge and PtO formation.

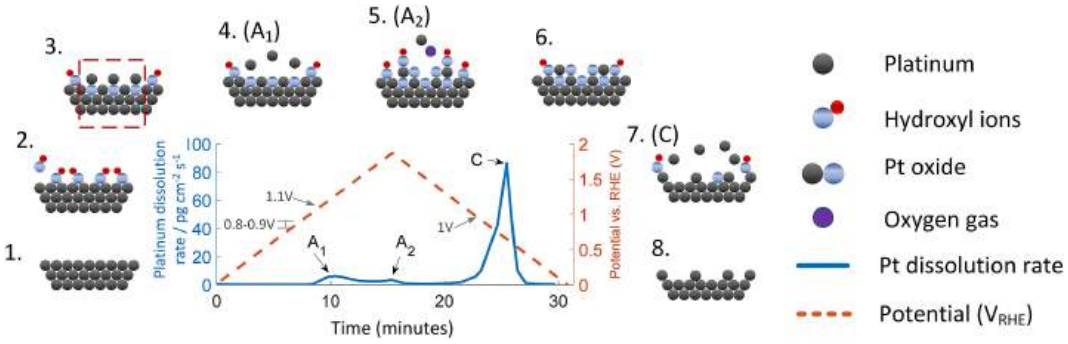

Figure 7.1: *The illustration describes a process where metallic Pt (1). undergoes adsorption of hydroxyl ions when subjected to anodic potentials (≈0.8–0.9 V) (2). At ≈1.1 V, place-exchange mechanisms take place (red dashed square) incorporating the oxygen atom into the metallic lattice, leading to the formation of Pt oxide (3). Oxidised Pt atoms are more exposed and more prone to de-stabilisation compared to their metallic lattice counterparts, allowing for Pt dissolution into the electrolyte (A_1 peak) (4). In anodic excursions above 1.1 V_{RHE}, a competitive process between Pt dissolution and oxide passivation is possible. With sufficiently high anodic potentials, oxygen gas evolution occurs and can dislodge more Pt from the surface (peak A_2) (5). Further anodic excursions result in a Pt surface with exposed sites and further passivation (6). During cathodic excursions below ≈1 V, the reduction of oxides occurs, removing the oxygen atoms from the surface, thus resulting in significant Pt dislodgment (7). Also, at this stage surface reduction could be in competition with Pt re-deposition and dissolution. Reproduced from Shah et al. [2024], CC BY 4.0*

Hence, I found that two factors particularly affect the polarisation during biphasic pulsing: the capacitance of the interface and the diffusion profile.

A lower C_{dl} (or Q_{dl} for CPE models) was associated with larger polarisation (Q = CV, Q being the electric charge) in both anodic and cathodic directions. With a lower capacity, the charge injection more likely relies on faradaic reactions after the maximal capacitance is reached, which may increase the degree of Pt oxidation and/or reduction, therefore favouring dissolution. C_{dl} was mostly affected by changes in the electrolyte, with lower values in low pH (6.1), high salinity (6.2), high gel concentration (6.3), and CBS and CBS with CO_2 (6.4); in all cases, larger polarisation was observed in both directions.

Increasing the perimeter-to-area ratio (P/A) increased the capacitance (per area for the 1 mm diameter electrode), however, the polarisation increased as well, suggesting that another parameter may influence potential excursions and charge injection, which I hypothesise to be diffusion. A larger diffusivity allows ions to travel quicker to supply electrochemical reactions, avoiding additional concentration overpotentials, but it may also enhance reaction rates by lifting the diffusion limitations. In the case of biphasic pulses, the diffusion of O_2 and H^+ ions for the reduction of molecular O_2 controls the irreversibility rate, therefore, in the case of enhanced diffusion, more O_2 may be reduced, inducing more potential ratcheting. With the example of the large AR electrode (4.3), we can see that although C_{dl} was larger, the anodic polarisation increased more with k than the 5 mm disc electrode, suggesting more ratcheting, which was probably due to a larger rate of O_2 reduction. Besides the P/A ratio, the electrolyte viscosity (higher in gels for example) and the ionic composition, including buffer and pH, may affect the diffusion profile. However, the enhancement of diffusion has different implications when it is due to the charge density distribution (P/A ratio) versus the electrolyte characteristics: the P/A ratio improves the diffusion profile as a larger proportion of higher current density at the electrode edge attracts more ionic flux with hemispheric flux lines instead of parallel for lower P/A, and as the edge represents a higher proportion of the electrode surface, the whole electrode charge injection benefits from the flux. Therefore, the diffusion enhancement is local and does not improve the diffusion far away from the electrode, of products from the electrolyte bulk to the electrode surface. P/A may accommodate diffusion-limited processes over a short period, however, after enhanced stimulation as we might see in my experiments, further diffusion limits may be hit, changing the charge injection regime. This hypothesis may explain the increased polarisation at the large AR electrode, which is supposed to have a larger capacitance and enhanced diffusion, however, enhanced diffusion may only enhance O_2 reduction for a few pulses before depleting the electrode vicin-

ity, and with less O_2 available in subsequent pulses, greater polarisation arises. Thus, with a larger diffusion rate, the electrode vicinity may deplete faster than for a disc electrode, which leads to different charge injection mechanisms, including increased PtO reduction and possibly hydrogen adsorption, which may both increase Pt corrosion.

These considerations lead me to a crucial factor in the analysis of the behaviour of stimulation electrodes, and brought complexity to the analysis: spatio-temporal changes at the electrode-electrolyte interface, which may greatly affect charge injection behaviour.

7.1.2 Non-uniform, time-dependent changes at the electrode-electrolyte interface

Spatial and temporal discrepancies were observed in several experiments. First, edge effects, which were specifically studied in section 4.3 and present in section 4.2, change the global behaviour of the electrode. The current density is larger at high curvature areas, at edges and corners, causing high reaction rates, which may exhaust reactants locally. As the P/A ratio increases, the edge effects represent a larger proportion of the electrode behaviour as captured by the RE, therefore, measurements on the large AR electrode hinted at the behaviour at the electrode edge while the 5 mm diameter electrode showed mainly the electrode centre behaviour. From the measurements of the large AR electrode, I hypothesise that during biphasic pulses, local exhaustion of reactants occurs, especially during the cathodic phase, which has diffusion-limited reactions, which lead to different reactions occurring simultaneously at the electrode surface: O_2 and PtO reduction in the centre and H-evolution at the electrode edge after exhausting O_2 and PtO reduction. As large disc electrodes present more non-uniformity of the current density, and the edge represents a smaller effect, at a far distance from the electrode centre, further polarisation yields more Pt dissolution through oxidation/reduction or mechanical oscillations during H-storage [Schulte et al., 2024], explaining the edge-driven dissolution. Local gradients were also observed in the pH and gel

experiments as the surface pH changes during CV and biphasic pulses due to local buffer exhaustion, and the local pH may favour some electrochemical reactions, as shown in the gel experiment, where a combined gel/pH effect was observed. The spatial gradients create additional polarisation and may induce different reactions, for instance for gel where a positive feedback loop was hypothesised with acidic electrolytes lowering the polarisation, favouring dissolution and basic electrolytes doing the opposite. While buffers that are used *in vitro* may mitigate local reactant depletion and pH gradients, the situation *in vivo* may be exacerbated, as diffusivity is reduced [Cogan et al., 2014] and biological elements may add to these effects.

Time-dependent effects may also affect charge injection mechanisms and should be duly considered in the analysis of Pt electrode behaviour during pulses. Pt dissolution is a time-dependent phenomenon, as it was shown to be a ms scale process [Cho et al., 2023] and more importantly as I show further evidence that Pt dissolution occurs through repetitive oxidation and reduction, with the electrode potential reaching unsafe thresholds due to unfavourable potential ratcheting. Therefore, although most of the ratcheting occurs after a few pulses [Merrill et al., 2005], stimulation safety cannot be assumed over short time frames, using only a few pulses, as it is usually the case in chronopotentiometry. Moreover, the results presented here further show the inadequacy of the common safe stimulation criteria used in CP of the cathodic polarisation exceeding 0.6 V vs Ag|AgCl, as electrode damage occurs earlier, possibly causing damage to neurons, and the interface may change over time. Considering spatial discrepancy as well, although the average electrode potential may be within the water window potential limits, unsafe reactions including water electrolysis may occur at the electrode edge. Pt dissolution creates a rougher surface, which increases the electrochemical surface area (ESA), thus decreasing the charge density. As k is based on the geometric surface area (GSA), Shannon's limit may be inaccurate, and techniques have been developed since, which allow to increase the ESA, including laser roughening [Green et al.,

2012a] or Pt black deposition [Arcot Desai et al., 2010]. With such surface treatments, the charge injection mechanisms would be altered for a given geometric current density, especially with increased C_{dl}, which would enable more non-faradaic charge injection. Further, the electrochemically available area of rough electrodes may depend upon PW, a factor not considered in Shannon's relationship [Cogan et al., 2016]. Therefore, an adapted version of Shannon's limit may be appropriate, based on electrochemical surface area, rather than geometric. In the present work, a roughness factor of 1.29 was reported, which yielded inferior real k-values by roughly 0.1 compared to geometric k-values (Table 3.1). As roughness was not reported in the studies on which Shannon's relationship is based, it is not possible to suggest the real charge densities and real k-values. k is correlated with $-log\ R_f$ (R_f being the roughness factor): from Eq. 1.19, $D = \frac{Q}{S} = \frac{Q}{R_f S_{geo}}$, with S_{geo} the geometrical surface area. Thus, doubling the roughness factor would only make k smaller by 0.3. Therefore, there may have been some imprecision in the reported charge densities in the studies characterised by Shannon [1992], which may slightly change the real safe charge injection limit. As my results show a change of charge injection mechanism between $k \approx 1.5$ and $k \approx 1.85$, I suggest that the real safe charge injection limit may be located between those limits, so caution is advised for stimulation protocols with $k \geq 1.5$. As mentioned by Shannon [1992], $k = 1.75$ is an estimation of the safe stimulation limit and therefore it should not be used as a hard limit between damaging and non-damaging stimulation.

The electrode's state changes over time and the history of the electrode may condition the performance, further than just corrosion. Initial CVs in PBS with the 5 mm electrode showed one clear PtO reduction peak, which evolved towards a double peak in the final experiments see figures 6.14 and 6.19. A marked double peak as was reported here is unusual for Pt electrodes in PBS, however, a smaller second peak in the tail of the PtO reduction peak is visible in CVs in literature [Kumsa et al., 2016b, Boehler et al., 2020a]. From CV comparisons, the feature was likely associated with phosphate but dis-

appeared with the presence of CO_2, therefore, a suggested explanation could be the following: the second reduction peak corresponds to an alternative Pt oxide form, which is not present in CBS or in the presence of CO_2 because of the competitive interaction of carbonate species during Pt oxidation. The alternative Pt oxidation may arise after some wear of the surface due to polishing scratches or stimulation-induced corrosion as observed on the electrode (Fig. 7.2) and could be the case in other studies, which have not performed a thorough polishing before recording CVs. The cleaning protocol and the electrode conditioning play a significant role in the charge injection behaviour (see 6.1.4, 3.3.2). Potentiostatic conditioning of the electrode prior to pulses was shown to change the CIL during biphasic pulses by yielding different oxide coverage ratios, which affect the charge injection profile as it may change available reactions, for instance PtO reduction during the cathodic phase if the surface was stripped of oxide [Doering et al., 2023]. Electrode state control is further discussed in 7.1.3. Due to electrode history and protocol design, the electrode may also show reduced charge injection and reduced dissolution if the surface becomes passivated. By oxidising the electrode at high potentials for long periods of time, a shielding layer of adsorbed oxygen atoms may be formed, protecting the electrode from oxide-mediated dissolution, but also reducing the charge injection as fewer Pt atoms are available [Donaldson and Donaldson, 1986b, Topalov et al., 2014a].

In vivo, time-dependent effects also occur, for instance with the foreign body reaction (FBR) after implantation, which yields impedance changes over a few weeks [Newbold et al., 2014]. pH is also known to change, as the inflammation due to implantation was shown to decrease the pH [Kellum et al., 2004]. Alkaline pH was shown to favour Pt dissolution because of the larger OH^- ions concentration [Cherevko et al., 2014], without changing the mechanism (see 6.1.4), while acidic pH favours Cl^--mediated dissolution [Topalov et al., 2014a]. Therefore, while inflammation is present, the electrode may be in a safer situation regarding corrosion, and the corrosion risk may increase as

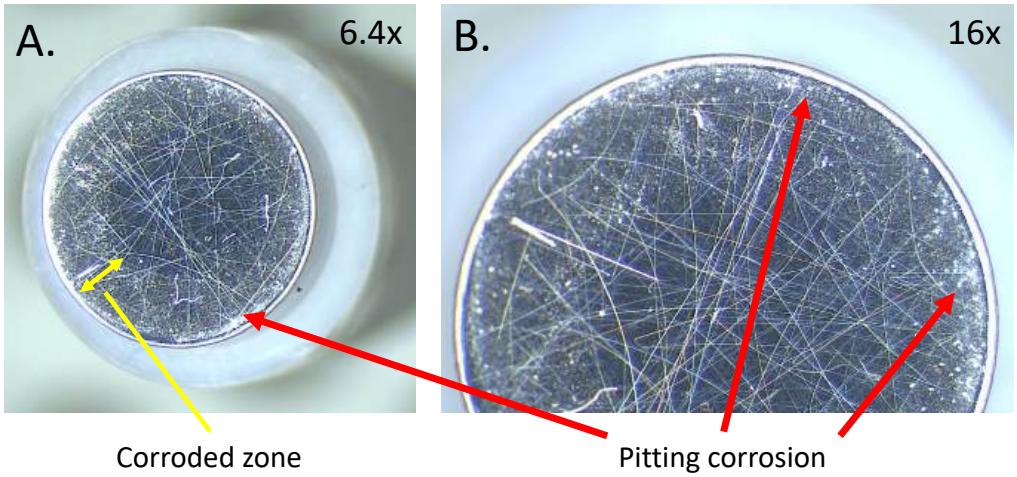

Figure 7.2: *Optical microscopy images of corrosion observed on the 5 mm diameter disc electrode with A. 6.4x zoom and B. 16x zoom.*

the inflammation disappears. Although the body's pH is not expected to take alkaline values, it was shown that the surface pH may change during stimulation, possibly enhancing damage. The discrepancy between acute and chronic experiments may pertain to time-dependent effect modifying the dissolution rate: for the first few hours, the inflammation starts and proteins have not fully adsorbed to the electrode surface, yielding some dissolution, then proteins adsorb and the inflammation sets, decreasing the dissolution drastically, and finally after a few days, when the inflammation decreased, the dissolution may be more likely, given that electrical stimulation removes proteins from the electrode surface [Newbold et al., 2004].

7.1.3 What is more desirable: fully-controlled and repeatable experimental conditions, or real-life use-case conditions?

During the development and analysis of the work produced for this thesis, the question of characterisation accuracy was a central element. In a few instances, I observed a discrepancy between the apparent and the real state of the electrode: the bulk electrolyte pH being different from the electrode surface pH, which may itself not be uniform, the electrode edge behaving differently than

the centre, suggesting that although the average electrode potential is safe, the edges may exceed safe limits, and the PEDOT electrodes, which appear to have a resistive behaviour from EIS measurements but actually exhibit a capacitive behaviour with a large capacitance which decreases the interface impedance making R_A the main impedance component. The systematic review on PEDOT deposition methods (2) showed the importance of characterisation parameters for result comparison and my own PEDOT electrode characterisation confronted me directly with the problem of making an accurate characterisation. A characterisation should both give a maximum of information on the electrode behaviour and offer comparable quantities to previous work. Thus, I reported the 1 kHz impedance to be able to compare to other results although the information on the electrode behaviour is limited with a single frequency and a full EIS spectrum should be provided.

There is another duality when designing a characterisation protocol: should the characterisation only be tailored for a specific application or should it aim at developing a broader knowledge of the general electrode behaviour? For instance, CP could be conducted only at the planned PW and intensity to assess the protocol safety without calculating the CIL necessarily, or EIS could be conducted around the pulsing frequency to only gain information on this specific use case. However, I believe that wider characterisation scopes are desirable and beneficial to the whole community, as they offer a more global understanding of the electrode behaviour, but also, as mentioned previously 7.1.2, spatio-temporal changes at the interface may change the charge injection conditions and behaviour and flexibility may be required to adapt to these changes, therefore, a better knowledge of the electrode behaviour across a range of parameters is desirable.

The extrapolation of results is complex without identical experimental conditions. The literature review on the electrodeposition methods of PEDOT demonstrated how the discrepancy in characterisation methods and the multiplicity of deposition parameters make it nearly impossible to have perfectly

repeatable conditions, therefore, difficult to extrapolate. In this thesis, considerable work was achieved towards results repeatability and interface control, including the modelling of the effect of a recess (4.1) and a detailed protocol to optimise repeatability (3.3.2). However, unknown variables remained in the analysis: the quantification of the recess effect could not be applied for the large AR electrode due to a different shape without rotational symmetry, and variations in OCP and recorded potentials in the pH (6.1), gels(6.3), and gases (6.5) studies suggest some uncontrolled parameters despite the thorough conditioning protocol. Further control on the electrode-electrolyte interface could have been provided with a potentiostatic preconditioning [Doering et al., 2023], by polishing the electrode surface to an identical state before each use [Kumsa et al., 2016b], or by sparging the electrolyte rather than leaving an unknown ambient gas concentration [Harris et al., 2018b, 2019a]. However, these control steps were not adopted in the experimental protocol in an effort to reproduce the electrode conditions used in studies supporting Shannon's parameter k as much as possible, to provide a better understanding of Shannon's limit.

There is a duality in the approach of electrode characterisation: a controlled interface is needed to understand the electrochemical state and produce repeatable results, and at the same time, the characterisation of the electrode behaviour should reproduce the use conditions, where full control of the experimental conditions is impossible. I suggest that both characterisation strategies should be used in parallel as they complement each other: a fully controlled environment should be achieved for a theoretical understanding of electrochemical mechanisms under a broad spectrum of conditions and "real-life" conditions should be studied separately to understand the uncontrolled electrode state. The ultimate goal for neural implant characterisation is to produce a standardised protocol in an electrolyte which could accurately describe the *in vivo* environment [Weltin and Kieninger, 2021]. The present work represented a step in that direction by individually characterising the effects of a few electrode and electrolyte parameters on electrode behaviour

while applying a reasonable amount of control. The evidence presented in this thesis indicates the path that should be adopted for future studies on neural implants: building on the framework used in this work, researchers should seek controlled environments corresponding to a specific use case, including buffer, gas concentration, and electrolyte structure, and monitor the electrode potential as closely as possible over thousands of pulses to determine safe charge injection limits after potential ratcheting. As shown in this work, it is challenging to precisely measure the local electrode potential, therefore, the reference electrode should be placed as close as possible to areas of large current density, and physical modelling tools should be used to understand the current density distribution, which determines the zones most likely to see the onset of unsafe electrochemical reactions. Comprehensive characterisation protocols are pivotal to increasing the knowledge and understanding of complex behaviours. The following section details the next steps from this work towards a comprehensive understanding of Pt electrode behaviour and Shannon's damage limit.

7.2 Future directions

The work presented in this thesis provides a consistent interpretation of the charge injection behaviour and electrode degradation during biphasic charge-balanced pulses, however, a few conclusions may be taken further with a few additional measurements. First, the effect of a recess could be studied more systematically with a recessed 5 mm disc electrode and a co-planar rectangular strip electrode (large AR) to understand the effects on the CPE, CV shape, and polarisations. Then, the characterisation of electrode size can be taken further, decreasing the electrode diameter further, which requires a more robust stimulator. Comparing the asymmetric waveform with a traditional biphasic square could allow a more simple stimulator design if both waveforms proved to be equivalent. For the electrolyte parameters, the effect of gases should be confirmed and compared to a gas mixture of realistic *in vivo* concentrations.

Finally, I believe that a dedicated analysis of the potential decay that was observed could be beneficial to the community, as the decay was seemingly related to the presence of oxygen and to the access resistance of the electrode. As tiny leakage currents or charge imbalances may occur in many experimental setups, a dedicated study of their effect and the implications for the changes at the interface and charge injection would certainly be of interest.

On a wider scope, there are two studies that I would conduct to build upon the evidence shown in this thesis. First, given the importance of diffusion in the corrosion process, I would have a study of the diffusion profile of electrolytes, with the aim of recreating *in vivo* diffusion conditions. Furthering the work on gels, I would add proteins [Palmer et al., 2019], both adsorbing onto the electrode surface and structural proteins which do not, and cells, and assess the Pt dissolution extent. This model for acute implantation could be extended with the inclusion of reactive oxygen species like hydrogen peroxide [Ehlich et al., 2022]. Then, a chronic implantation model could be developed with a dense insulating connective sheath around the electrode. Measurements of Pt contents inside and outside the sheath would be compared to Pt measurements in saline and in the acute model to test the hypothesis of the protein sheath retaining dissolved Pt.

A second study would aim to cement our knowledge of the electrode-electrolyte interface during charge injection by using electrochemical imaging. With fluorescent dyes, one could image the potential distribution, the pH distribution, or the molecular oxygen reduction for instance [Bouffier and Doneux, 2017]. The mechanisms during CV and pulses could be compared and the dynamics of the reactions could be assessed in real time and superimposed to electrochemical characterisation tests. The uncontrolled state of electrodes which have not been cleaned or preconditioned could be evaluated and better understood, which would allow for the development of standardised guidelines of electrode preparation for controlled stimulation. The fluorescent imaging technique could then be used on a wider range of electrode materials, including

PEDOT, iridium oxide, or conductive hydrogels.

Chapter 8

Conclusion

This thesis presents an investigation of the charge injection mechanisms at platinum electrodes during biphasic, cathodic-first, charge-balanced, asymmetric, current-controlled pulse trains at charge densities close to Shannon's safe stimulation limit. By recording the electrode potential during pulses and reporting it on a cyclic voltammogram, I identified repetitive cycles of oxidation and reduction causing platinum dissolution as the main candidate to explain Shannon's limit. Subsequently, the electrode behaviour was tested through variations in the electrode design, including a recess and changes in size and in shape, in the stimulation protocol, changes in pulse width, and in the electrolyte composition, including pH, ionic strength, density, buffer system, and presence of gases. The corrosion mechanism was supported through all experiments, providing compelling arguments to justify the platinum dissolution hypothesis, and two key parameters emerged, which played pivotal roles in the onset and degree of platinum corrosion: the electrode double-layer capacitance and the diffusivity of the electrolyte. Therefore, this thesis extends the understanding of stimulation-induced electrode degradation, which may create neural damage. A particular focus on electrode characterisation and how to paint a true portrait of the electrode state during biphasic stimulation was made, unveiling the complexity and changing nature of the electrode-electrolyte interface. The considerations presented throughout this work provide a robust characterisation protocol for stimulation electrodes and show a new path to-

wards the creation of a standardised bench-top characterisation strategy for neural electrodes.

Bibliography

W. Agnew, T. Yuen, D. McCreery, and L. Bullara. Histopathologic evaluation of prolonged intracortical electrical stimulation. *Experimental Neurology*, 92 (1):162–185, 1986.

W. F. Agnew, T. G. Yuen, R. H. Pudenz, and L. A. Bullara. Neuropathological effects of intracerebral platinum salt injections. *Journal of Neuropathology & Experimental Neurology*, 36(3):533–546, 1977.

W. F. Agnew, D. B. McCreery, T. G. Yuen, and L. A. Bullara. Histologic and physiologic evaluation of electrically stimulated peripheral nerve: considerations for the selection of parameters. *Annals of biomedical engineering*, 17 (1):39–60, 1989.

J. Al-Gousous, K. X. Sun, D. McNamara, B. Hens, N. Salehi, P. Langguth, M. Bermejo, G. Amidon, and G. Amidon. Mass transport analysis of the enhanced buffer capacity of the bicarbonate-co2 buffer in a phase-heterogenous system: Physiological and pharmaceutical significance. *Molecular pharmaceutics*, 15 11:5291–5301, 2018. doi: 10.1021/acs.molpharmaceut.8b00783.

N. A. Alba, Z. J. Du, K. A. Catt, T. D. Kozai, and X. T. Cui. In vivo electrochemical analysis of a PEDOT/MWCNT neural electrode coating. *Biosensors*, 5(4):618–646, 2015.

H. Angerstein-Kozlowska, B. Conway, and W. Sharp. The real condition of electrochemically oxidized platinum surfaces: Part i. resolution of compo-

nent processes. *Journal of Electroanalytical Chemistry and Interfacial Electrochemistry*, 43(1):9–36, 1973.

Z. Aqrawe, B. Wright, N. Patel, Y. Vyas, J. Malmstrom, J. M. Montgomery, D. Williams, J. Travas-Sejdic, and D. Svirskis. The influence of macropores on PEDOT/PSS microelectrode coatings for neuronal recording and stimulation. *Sensors and Actuators B: Chemical*, 281:549–560, 2019.

S. Arcot Desai, J. D. Rolston, L. Guo, and S. M. Potter. Improving impedance of implantable microwire multi-electrode arrays by ultrasonic electroplating of durable platinum black. *Frontiers in neuroengineering*, 3:1303, 2010.

K. Aristovich, M. Donega, C. Fjordbakk, I. Tarotin, C. A. Chapman, J. Viscasillas, T.-R. Stathopoulou, A. Crawford, D. Chew, J. Perkins, et al. Model-based geometrical optimisation and in vivo validation of a spatially selective multielectrode cuff array for vagus nerve neuromodulation. *Journal of neuroscience methods*, 352:109079, 2021.

M. Auinger, I. Katsounaros, J. C. Meier, S. O. Klemm, P. U. Biedermann, A. A. Topalov, M. Rohwerder, and K. J. Mayrhofer. Near-surface ion distribution and buffer effects during electrochemical reactions. *Physical Chemistry Chemical Physics*, 13(36):16384–16394, 2011.

C. L. Ballestrasse, R. T. Ruggeri, and T. R. Beck. Calculations of the ph changes produced in body tissue by a spherical stimulation electrode. *Annals of biomedical engineering*, 13(5):405–424, 1985.

A. J. Bard, L. R. Faulkner, and H. S. White. *Electrochemical methods: fundamentals and applications*. John Wiley & Sons, 2022.

S. B. Baumann, D. R. Wozny, S. K. Kelly, and F. M. Meno. The electrical conductivity of human cerebrospinal fluid at body temperature. *IEEE transactions on biomedical engineering*, 44(3):220–223, 1997.

M. R. Behrend, A. K. Ahuja, and J. D. Weiland. Dynamic current density of the disk electrode double-layer. *IEEE Transactions on Biomedical Engineering*, 55(3):1056–1062, 2008.

R. J. Bellows, E. P. Marucchi-Soos, and D. T. Buckley. Analysis of reaction kinetics for carbon monoxide and carbon dioxide on polycrystalline platinum relative to fuel cell operation. *Industrial & engineering chemistry research*, 35(4):1235–1242, 1996.

D. K. Binder, G. M. Rau, and P. A. Starr. Risk factors for hemorrhage during microelectrode-guided deep brain stimulator implantation for movement disorders. *Neurosurgery*, 56(4):722–732, 2005.

R. Black and P. Hannaker. Dissolution of smooth platinum electrodes in biological fluids. *Stereotactic and Functional Neurosurgery*, 42(6):366–374, 1979.

C. Boehler, F. Oberueber, S. Schlabach, T. Stieglitz, and M. Asplund. Long-term stable adhesion for conducting polymers in biomedical applications: Irox and nanostructured platinum solve the chronic challenge. *ACS applied materials & interfaces*, 9(1):189–197, 2017a.

C. Boehler, F. Oberueber, T. Stieglitz, and M. Asplund. Nanostructured platinum as an electrochemically and mechanically stable electrode coating. In *2017 39th Annual International Conference of the IEEE Engineering in Medicine and Biology Society (EMBC)*, pages 1058–1061. IEEE, 2017b.

C. Boehler, S. Carli, L. Fadiga, T. Stieglitz, and M. Asplund. Tutorial: guidelines for standardized performance tests for electrodes intended for neural interfaces and bioelectronics. *Nature Protocols*, 15(11):3557–3578, 2020a.

C. Boehler, S. Carli, L. Fadiga, T. Stieglitz, and M. Asplund. Tutorial: guidelines for standardized performance tests for electrodes intended for neural interfaces and bioelectronics. *Nature Protocols*, 15(11):3557–3578, 2020b.

T. Boretius, J. Badia, A. Pascual-Font, M. Schuettler, X. Navarro, K. Yoshida, and T. Stieglitz. A transverse intrafascicular multichannel electrode (time) to interface with the peripheral nerve. *Biosensors and Bioelectronics*, 26(1): 62–69, 2010.

F. T. Bosman and I. Stamenkovic. Functional structure and composition of the extracellular matrix. *The Journal of Pathology: A Journal of the Pathological Society of Great Britain and Ireland*, 200(4):423–428, 2003.

L. Bouffier and T. Doneux. Coupling electrochemistry with in situ fluorescence (confocal) microscopy. *Current opinion in electrochemistry*, 6(1):31–37, 2017.

V. Briega-Martos, E. Herrero, and J. M. Feliu. Effect of ph and water structure on the oxygen reduction reaction on platinum electrodes. *Electrochimica Acta*, 241:497–509, 2017.

V. Briega-Martos, A. Ferre-Vilaplana, E. Herrero, and J. M. Feliu. Why the activity of the hydrogen oxidation reaction on platinum decreases as ph increases. *Electrochimica Acta*, 354:136620, 2020.

E. E. Brink and R. G. Mackel. Time course of action potentials recorded from single human afferents. *Brain*, 116(2):415–432, 1993.

W. J. Brown, T. L. Babb, H. V. Soper, J. P. Lieb, C. A. Ottino, and P. H. Crandall. Tissue reactions to long-term electrical stimulation of the cerebellum in monkeys. *Journal of neurosurgery*, 47(3):366–379, 1977.

S. Brummer and M. Turner. Electrical stimulation of the nervous system: the principle of safe charge injection with noble metal electrodes. *Bioelectrochemistry and Bioenergetics*, 2(1):13–25, 1975.

S. Brummer and M. Turner. Electrochemical considerations for safe electrical stimulation of the nervous system with platinum electrodes. *IEEE Transactions on Biomedical Engineering*, (1):59–63, 1977.

A. Butterwick, A. Vankov, P. Huie, Y. Freyvert, and D. Palanker. Tissue damage by pulsed electrical stimulation. *IEEE Transactions on Biomedical Engineering*, 54(12):2261–2267, 2007.

G. Buzsáki, C. A. Anastassiou, and C. Koch. The origin of extracellular fields and currents—eeg, ecog, lfp and spikes. *Nature reviews neuroscience*, 13(6): 407–420, 2012.

A. Campbell and C. Wu. Chronically implanted intracranial electrodes: tissue reaction and electrical changes. *Micromachines*, 9(9):430, 2018.

D. R. Cantrell, S. Inayat, A. Taflove, R. S. Ruoff, and J. B. Troy. Incorporation of the electrode–electrolyte interface into finite-element models of metal microelectrodes. *Journal of neural engineering*, 5(1):54, 2007.

A. Carnicer-Lombarte, H. T. Lancashire, and A. Vanhoestenberghe. In vitro biocompatibility and electrical stability of thick-film platinum/gold alloy electrodes printed on alumina. *Journal of neural engineering*, 14(3):036012, 2017.

V. Castagnola, E. Descamps, A. Lecestre, L. Dahan, J. Remaud, L. G. Nowak, and C. Bergaud. Parylene-based flexible neural probes with PEDOT coated surface for brain stimulation and recording. *Biosensors and Bioelectronics*, 67:450–457, 2015.

C. A. Chapman, K. Aristovich, M. Donega, C. T. Fjordbakk, T.-R. Stathopoulou, J. Viscasillas, J. Avery, J. D. Perkins, and D. Holder. Electrode fabrication and interface optimization for imaging of evoked peripheral nervous system activity with electrical impedance tomography (eit). *Journal of Neural Engineering*, 16(1):016001, 2018.

S. Cherevko, A. R. Zeradjanin, G. P. Keeley, and K. J. Mayrhofer. A comparative study on gold and platinum dissolution in acidic and alkaline media. *Journal of The Electrochemical Society*, 161(12):H822, 2014.

M. Chesler. The regulation and modulation of ph in the nervous system. *Progress in neurobiology*, 34(5):401–427, 1990.

J. Cho, H. Kim, H.-S. Oh, and C. H. Choi. Elucidation of electrochemically induced but chemically driven pt dissolution. *JACS Au*, 3(1):105–112, 2023.

A. Cisnal, J.-C. Fraile, J. Pérez-Turiel, V. Muñoz-Martinez, C. Müller, and F. R Ihmig. A measurement setup and automated calculation method to determine the charge injection capacity of implantable microelectrodes. *Sensors*, 18(12):4152, 2018.

G. M. Clark, J. Clark, T. Cardamone, M. Clarke, P. Nielsen, R. Jones, B. Arhatari, N. Birbilis, R. Curtain, J. Xu, et al. Biomedical studies on temporal bones of the first multi-channel cochlear implant patient at the university of melbourne. *Cochlear implants international*, 15(sup2):S1–S15, 2014.

S. F. Cogan. Neural stimulation and recording electrodes. *Annu. Rev. Biomed. Eng.*, 10:275–309, 2008.

S. F. Cogan, A. A. Guzelian, W. F. Agnew, T. G. Yuen, and D. B. McCreery. Over-pulsing degrades activated iridium oxide films used for intracortical neural stimulation. *Journal of neuroscience methods*, 137(2):141–150, 2004a.

S. F. Cogan, T. Plante, and J. Ehrlich. Sputtered iridium oxide films (sirofs) for low-impedance neural stimulation and recording electrodes. In *The 26th Annual International Conference of the IEEE Engineering in Medicine and Biology Society*, volume 2, pages 4153–4156. IEEE, 2004b.

S. F. Cogan, P. R. Troyk, J. Ehrlich, and T. D. Plante. In vitro comparison of the charge-injection limits of activated iridium oxide (airof) and platinum-iridium microelectrodes. *IEEE Transactions on Biomedical Engineering*, 52 (9):1612–1614, 2005.

S. F. Cogan, J. Ehrlich, T. D. Plante, A. Smirnov, D. B. Shire, M. Gingerich, and J. F. Rizzo. Sputtered iridium oxide films for neural stimulation electrodes. *Journal of Biomedical Materials Research Part B: Applied Biomaterials: An Official Journal of The Society for Biomaterials, The Japanese Society for Biomaterials, and The Australian Society for Biomaterials and the Korean Society for Biomaterials*, 89(2):353–361, 2009.

S. F. Cogan, J. Ehrlich, T. D. Plante, M. D. Gingerich, and D. B. Shire. Contribution of oxygen reduction to charge injection on platinum and sputtered iridium oxide neural stimulation electrodes. *IEEE transactions on biomedical engineering*, 57(9):2313–2321, 2010.

S. F. Cogan, J. Ehrlich, and T. D. Plante. The effect of electrode geometry on electrochemical properties measured in saline. In *2014 36th Annual International Conference of the IEEE Engineering in Medicine and Biology Society*, pages 6850–6853. IEEE, 2014.

S. F. Cogan, K. A. Ludwig, C. G. Welle, and P. Takmakov. Tissue damage thresholds during therapeutic electrical stimulation. *Journal of neural engineering*, 13(2):021001, 2016.

P. E. Crago, P. H. Peckham, J. T. Mortimer, and J. P. Van Der Meulen. The choice of pulse duration for chronic electrical stimulation via surface, nerve, and intramuscular electrodes. *Annals of biomedical engineering*, 2:252–264, 1974.

CSPH. Cold spring harbor protocols. URL https://cshprotocols.cshlp.org/.

J. Cuevas. The action potential. *xPharm: The Comprehensive Pharmacology Reference*, 2007.

X. Cui and D. C. Martin. Electrochemical deposition and characterization of poly (3, 4-ethylenedioxythiophene) on neural microelectrode arrays. *Sensors and Actuators B: Chemical*, 89(1-2):92–102, 2003.

X. T. Cui and D. D. Zhou. Poly (3, 4-ethylenedioxythiophene) for chronic neural stimulation. *IEEE Transactions on Neural Systems and Rehabilitation Engineering*, 15(4):502–508, 2007.

P. Daubinger, J. Kieninger, T. Unmüssig, and G. A. Urban. Electrochemical characteristics of nanostructured platinum electrodes–a cyclic voltammetry study. *Physical Chemistry Chemical Physics*, 16(18):8392–8399, 2014.

P. Davis and J. Gaitanis. Neuromodulation for the treatment of epilepsy: a review of current approaches and future directions. *Clinical therapeutics*, 42 (7):1140–1154, 2020.

J. Deitmer. Evidence for glial control of extracellular ph in the leech central nervous system. *Glia*, 5, 1992. doi: 10.1002/glia.440050107.

X. Deng, F. Galli, and M. T. Koper. In situ afm imaging of platinum electrode surface during oxidation–reduction cycles in alkaline electrolyte. *ACS Applied Energy Materials*, 3(1):597–602, 2019.

T. Denison and M. J. Morrell. Neuromodulation in 2035: the neurology future forecasting series. *Neurology*, 98(2):65–72, 2022.

D. J. DiLorenzo, J. Jankovic, R. K. Simpson, H. Takei, and S. Z. Powell. Neurohistopathological findings at the electrode–tissue interface in long-term deep brain stimulation: systematic literature review, case report, and assessment of stimulation threshold safety. *Neuromodulation: Technology at the Neural Interface*, 17(5):405–418, 2014.

T. Dinan, M. Matlosz, and D. Landolt. Experimental investigation of the current distribution on a recessed rotating disk electrode. *Journal of the Electrochemical Society*, 138(10):2947, 1991.

X. Ding, D. Scieszka, S. Watzele, S. Xue, B. Garlyyev, R. W. Haid, and A. S. Bandarenka. A systematic study of the influence of electrolyte ions on the electrode activity. *ChemElectroChem*, 9(1):e202101088, 2022.

K. Doblhoff-Dier and M. T. Koper. Modeling the gouy–chapman diffuse capacitance with attractive ion–surface interaction. *The Journal of Physical Chemistry C*, 125(30):16664–16673, 2021.

M. Doering, J. Kieninger, G. A. Urban, and A. Weltin. Electrochemical microelectrode degradation monitoring: in situ investigation of platinum corrosion at neutral ph. *Journal of Neural Engineering*, 19(1):016005, 2022.

M. Doering, J. Kieninger, J. Kübler, U. Hofmann, S. J. Rupitsch, G. Urban, and A. Weltin. Advanced electrochemical potential monitoring for improved understanding of electrical neurostimulation protocols. *Journal of Neural Engineering*, 2023.

N. d. N. Donaldson and P. Donaldson. When are actively balanced biphasic ('lilly') stimulating pulses necessary in a neurological prosthesis? i historical background; pt resting potential; q studies. *Medical and Biological Engineering and Computing*, 24:41–49, 1986a.

N. d. N. Donaldson and P. Donaldson. Performance of platinum stimulating electrodes mapped on the limitvoltage plane: Part 2 corrosion in vitro. *Medical and Biological Engineering and Computing*, 24:431–438, 1986b.

J. Ehlich, L. Migliaccio, I. Sahalianov, M. Nikić, J. Brodskỳ, I. Gablech, X. T. Vu, S. Ingebrandt, and E. D. Głowacki. Direct measurement of oxygen reduction reactions at neurostimulation electrodes. *Journal of Neural Engineering*, 19(3):036045, 2022.

M. Elam and B. Conway. State of overpotential-deposited h species at electroplated platinum surfaces in comparison with bright platinum. *Journal of applied electrochemistry*, 17(5):1002–1020, 1987.

J. R. Eles, A. L. Vazquez, T. D. Kozai, and X. T. Cui. In vivo imaging of neuronal calcium during electrode implantation: spatial and temporal mapping of damage and recovery. *Biomaterials*, 174:79–94, 2018.

I. Epelboin and M. Keddam. Faradaic impedances: Diffusion impedance and reaction impedance. *Journal of The Electrochemical Society*, 117(8):1052, 1970. doi: 10.1149/1.2407718.

H. Fadda, H. Merchant, B. Arafat, and A. Basit. Physiological bicarbonate buffers: stabilisation and use as dissolution media for modified release systems. *International journal of pharmaceutics*, 382 1-2:56–60, 2009. doi: 10.1016/j.ijpharm.2009.08.003.

B. Fan, B. Wolfrum, and J. T. Robinson. Impedance scaling for gold and platinum microelectrodes. *Journal of Neural Engineering*, 18(5):056025, 2021.

W. Franks, I. Schenker, P. Schmutz, and A. Hierlemann. Impedance characterization and modeling of electrodes for biomedical applications. *IEEE Transactions on Biomedical Engineering*, 52(7):1295–1302, 2005.

F. Furlani, M. Montanari, N. Sangiorgi, E. Saracino, E. Campodoni, A. Sanson, V. Benfenati, A. Tampieri, S. Panseri, and M. Sandri. Electroconductive and injectable hydrogels based on gelatin and PEDOT:PSS for a minimally invasive approach in nervous tissue regeneration. *Biomaterials Science*, 10 (8):2040–2053, 2022. doi: 10.1039/D2BM00116K.

Y. Furuya, T. Mashio, A. Ohma, M. Tian, F. Kaveh, D. Beauchemin, and G. Jerkiewicz. Influence of electrolyte composition and ph on platinum electrochemical and/or chemical dissolution in aqueous acidic media. *Acs Catalysis*, 5(4):2605–2614, 2015.

S. M. Gateman, O. Gharbi, H. G. de Melo, K. Ngo, M. Turmine, and V. Vivier. On the use of a constant phase element (cpe) in electrochemistry. *Current Opinion in Electrochemistry*, 36:101133, 2022.

L. A. Geddes and J. D. Bourland. The strength-duration curve. *IEEE Transactions on Biomedical Engineering*, BME-32(6):458–459, 1985. doi: 10.1109/tbme.1985.325456.

S. Geiger, S. Cherevko, and K. J. Mayrhofer. Dissolution of platinum in presence of chloride traces. *Electrochimica Acta*, 179:24–31, 2015.

A. Gencoglu and A. Minerick. Chemical and morphological changes on platinum microelectrode surfaces in ac and dc fields with biological buffer solutions. *Lab on a Chip*, 9(13):1866–1873, 2009.

A. Ghazavi and S. F. Cogan. Electrochemical characterization of high frequency stimulation electrodes: Role of electrode material and stimulation parameters on electrode polarization. *Journal of neural engineering*, 15(3): 036023, 2018.

A. Ghazavi, D. T. Westwick, C. Luk, N. I. Syed, and C. Dalton. Improving neuron stimulation efficency by altering electrode geometry. In *BIODEVICES*, pages 51–56, 2013.

A. Ghazavi, D. Westwick, F. Xu, P. Wijdenes, N. Syed, and C. Dalton. Effect of planar microelectrode geometry on neuron stimulation: Finite element modeling and experimental validation of the efficient electrode shape. *Journal of neuroscience methods*, 248:51–58, 2015.

A. Ghazavi, J. Maeng, M. Black, S. Salvi, and S. Cogan. Electrochemical characteristics of ultramicro-dimensioned sirof electrodes for neural stimulation and recording. *Journal of neural engineering*, 17(1):016022, 2020.

L. Golestanirad, B. Elahi, A. Molina, J. R. Mosig, C. Pollo, R. Chen, and S. J. Graham. Analysis of fractal electrodes for efficient neural stimulation. *Frontiers in neuroengineering*, 6:3, 2013.

P. H. Gorman and J. T. Mortimer. The effect of stimulus parameters on the recruitment characteristics of direct nerve stimulation. *IEEE Transactions on Biomedical Engineering*, BME-30(7):407–414, 1983.

R. Green, C. Duan, R. Hassarati, J. Goding, P. Byrnes-Preston, G. J. Suaning, L. Poole-Warren, and N. H. Lovell. Electrochemical stability of poly (ethy-

lene dioxythiophene) electrodes. In *2011 5th International IEEE/EMBS Conference on Neural Engineering*, pages 566–569. IEEE, 2011.

R. Green, P. Matteucci, R. Hassarati, B. Giraud, C. Dodds, S. Chen, P. Byrnes-Preston, G. Suaning, L. Poole-Warren, and N. Lovell. Performance of conducting polymer electrodes for stimulating neuroprosthetics. *Journal of neural engineering*, 10(1):016009, 2013.

R. A. Green, R. T. Hassarati, L. Bouchinet, C. S. Lee, G. L. Cheong, F. Y. Jin, C. W. Dodds, G. J. Suaning, L. A. Poole-Warren, and N. H. Lovell. Substrate dependent stability of conducting polymer coatings on medical electrodes. *Biomaterials*, 33(25):5875–5886, 2012a.

R. A. Green, H. Toor, C. Dodds, and N. H. Lovell. Variation in performance of platinum electrodes with size and surface roughness. *Sensors and Materials*, 24(4):165–180, 2012b.

C. U. Guide. Electrochemistry module users guide. URL https://doc.comsol.com/5.4/doc/com.comsol.help.echem/ElectrochemistryModuleUsersGuide.pdf.

C. Günter, J. Delbeke, and M. Ortiz-Catalan. Safety of long-term electrical peripheral nerve stimulation: review of the state of the art. *Journal of neuroengineering and rehabilitation*, 16(1):13, 2019.

L. Guo. Perspectives on electrical neural recording: a revisit to the fundamental concepts. *Journal of Neural Engineering*, 17(1):013001, 2020.

A. K. Gupta, D. A. Zygun, A. J. Johnston, L. A. Steiner, P. G. Al-Rawi, D. Chatfield, E. Shepherd, P. J. Kirkpatrick, P. J. Hutchinson, and D. K. Menon. Extracellular brain ph and outcome following severe traumatic brain injury. *Journal of neurotrauma*, 21(6):678–684, 2004.

K. Gurney. *An introduction to neural networks*. CRC press, 2014.

J. E. Hall. Access resistance of a small circular pore. *The Journal of general physiology*, 66(4):531–532, 1975.

A. R. Harris. Limitations in the electrochemical analysis of voltage transients. *Journal of Neural Engineering*, 21(1):013003, 2024.

A. R. Harris and G. G. Wallace. Electrochemical methods for analysing and controlling charge transfer at the electrode-tissue interface. *Current Opinion in Electrochemistry*, 2019.

A. R. Harris, C. Newbold, P. Carter, R. Cowan, and G. G. Wallace. Charge injection from chronoamperometry of platinum electrodes for bionic devices. *Journal of The Electrochemical Society*, 165(12):G3033–G3041, 2018a.

A. R. Harris, C. Newbold, P. Carter, R. Cowan, and G. G. Wallace. Measuring the effective area and charge density of platinum electrodes for bionic devices. *Journal of neural engineering*, 15(4):046015, 2018b.

A. R. Harris, C. Newbold, P. Carter, R. Cowan, and G. G. Wallace. Using chronopotentiometry to better characterize the charge injection mechanisms of platinum electrodes used in bionic devices. *Frontiers in Neuroscience*, 13, 2019a.

A. R. Harris, C. Newbold, R. Cowan, and G. G. Wallace. Insights into the electron transfer kinetics, capacitance and resistance effects of implantable electrodes using fourier transform ac voltammetry on platinum. *Journal of The Electrochemical Society*, 166(12):G131, 2019b.

A. R. Harris, P. Carter, R. Cowan, and G. G. Wallace. Impact of protein fouling on the charge injection capacity, impedance, and effective electrode area of platinum electrodes for bionic devices. *ChemElectroChem*, 8(6):1078–1090, 2021.

A. R. Harris, C. Newbold, D. Stathopoulos, P. Carter, R. Cowan, and G. G.

Wallace. Comparison of the in vitro and in vivo electrochemical performance of bionic electrodes. *Micromachines*, 13(1):103, 2022.

D. B. Hibbert, K. Weitzner, B. Tabor, and P. Carter. Mass changes and dissolution of platinum during electrical stimulation in artificial perilymph solution. *Biomaterials*, 21(21):2177–2182, 2000.

P. Hickey and M. Stacy. Deep brain stimulation: a paradigm shifting approach to treat parkinson's disease. *Frontiers in neuroscience*, 10:173, 2016.

S. B. Hladky and M. A. Barrand. Mechanisms of fluid movement into, through and out of the brain: evaluation of the evidence. *Fluids and Barriers of the CNS*, 11:1–32, 2014.

G. Hong, R. D. Viveros, T. J. Zwang, X. Yang, and C. M. Lieber. Tissue-like neural probes for understanding and modulating the brain. *Biochemistry*, 57(27):3995–4004, 2018.

O. D. Howes, M. E. Thase, and T. Pillinger. Treatment resistance in psychiatry: state of the art and new directions. *Molecular psychiatry*, 27(1):58–72, 2022.

K. Hsueh, E. R. Gonzalez, and S. Srinivasan. Electrolyte effects on oxygen reduction kinetics at platinum: a rotating ring-disc electrode analysis. *Electrochimica Acta*, 28(5):691–697, 1983.

Z. Hu, P. R. Troyk, T. P. Brawn, D. Margoliash, and S. F. Cogan. In vitro and in vivo charge capacity of airof microelectrodes. In *2006 International Conference of the IEEE Engineering in Medicine and Biology Society*, pages 886–889. IEEE, 2006.

C. Q. Huang, P. M. Carter, and R. K. Shepherd. Stimulus induced ph changes in cochlear implants: an in vitro and in vivo study. *Annals of biomedical engineering*, 29(9):791–802, 2001.

E. Hudak, J. Mortimer, and H. Martin. Platinum for neural stimulation: voltammetry considerations. *Journal of Neural Engineering*, 7(2):026005, 2010.

E. M. Hudak. *Electrochemical evaluation of platinum and diamond electrodes for neural stimulation*. PhD thesis, Case Western Reserve University, 2011.

E. M. Hudak, D. W. Kumsa, H. B. Martin, and J. T. Mortimer. Electron transfer processes occurring on platinum neural stimulating electrodes: calculated charge-storage capacities are inaccessible during applied stimulation. *Journal of neural engineering*, 14(4):046012, 2017a.

E. M. Hudak, D. W. Kumsa, H. B. Martin, and J. T. Mortimer. Electron transfer processes occurring on platinum neural stimulating electrodes: Calculated charge-storage capacities are inaccessible during applied stimulation. *Journal of Neural Engineering*, 14(4):046012, 2017b. doi: 10.1088/1741-2552/aa6945.

A. S. Idil and N. Donaldson. The use of tungsten as a chronically implanted material. *Journal of neural engineering*, 15(2):021006, 2018.

G. Inzelt, B. Berkes, and Á. Kriston. Temperature dependence of two types of dissolution of platinum in acid media. an electrochemical nanogravimetric study. *Electrochimica Acta*, 55(16):4742–4749, 2010.

R. J. Jensen, O. R. Ziv, and J. F. Rizzo. Thresholds for activation of rabbit retinal ganglion cells with relatively large, extracellular microelectrodes. *Investigative ophthalmology & visual science*, 46(4):1486–1496, 2005.

W. Jin, H. Du, S. Zheng, H. Xu, and Y. Zhang. Comparison of the oxygen reduction reaction between naoh and koh solutions on a pt electrode: the electrolyte-dependent effect. *The Journal of Physical Chemistry B*, 114(19): 6542–6548, 2010.

M. Jitaru. Electrochemical carbon dioxide reduction-fundamental and applied topics. *Journal of the University of chemical Technology and Metallurgy*, 42 (4):333–344, 2007.

M. H. Jones and J. Scott. Scaling of electrode-electrolyte interface model parameters in phosphate buffered saline. *IEEE Transactions on Biomedical Circuits and Systems*, 9(3):441–448, 2014.

S. R. Kane, S. F. Cogan, J. Ehrlich, T. D. Plante, D. B. McCreery, and P. R. Troyk. Electrical performance of penetrating microelectrodes chronically implanted in cat cortex. *IEEE Transactions on Biomedical Engineering*, 60 (8):2153–2160, 2013.

Y. P. Kayinamura, M. Ovadia, D. Zavitz, and J. F. Rubinson. Investigation of near ohmic behavior for poly (3, 4-ethylenedioxythiophene): A model consistent with systematic variations in polymerization conditions. *ACS Applied Materials & Interfaces*, 2(9):2653–2662, 2010.

J. A. Kellum, M. Song, and J. Li. Science review: extracellular acidosis and the immune response: clinical and physiologic implications. *Critical care*, 8: 1–6, 2004.

J. H. Kim, G. H. Lee, S. Kim, H. W. Chung, J. H. Lee, S. M. Lee, C. Y. Kang, and S.-H. Lee. Flexible deep brain neural probe for localized stimulation and detection with metal guide. *Biosensors and Bioelectronics*, 117:436–443, 2018.

K. M. Kovach, D. W. Kumsa, V. Srivastava, E. M. Hudak, D. F. Untereker, S. C. Kelley, H. A. von Recum, and J. R. Capadona. High-throughput in vitro assay to evaluate the cytotoxicity of liberated platinum compounds for stimulating neural electrodes. *Journal of neuroscience methods*, 273:1–9, 2016.

D. A. Ksienski. A minimum profile uniform current density electrode. *IEEE transactions on biomedical engineering*, 39(7):682–692, 1992.

D. Kumsa, E. M. Hudak, F. W. Montague, S. C. Kelley, D. F. Untereker, B. P. Hahn, C. Condit, M. Cholette, H. Lee, D. Bardot, et al. Electrical neurostimulation with imbalanced waveform mitigates dissolution of platinum electrodes. *Journal of neural engineering*, 13(5):054001, 2016a.

D. W. Kumsa, F. W. Montague, E. M. Hudak, and J. T. Mortimer. Electron transfer processes occurring on platinum neural stimulating electrodes: pulsing experiments for cathodic-first/charge-balanced/biphasic pulses for $0.566 \leq \mathrm{k} \leq 2.3$ in oxygenated and deoxygenated sulfuric acid. *Journal of neural engineering*, 13(5):056001, 2016b.

D. W. Kumsa, N. Bhadra, E. M. Hudak, and J. T. Mortimer. Electron transfer processes occurring on platinum neural stimulating electrodes: pulsing experiments for cathodic-first, charge-balanced, biphasic pulses for $0.566leq$ kleq 2.3 in rat subcutaneous tissues. *Journal of neural engineering*, 14(5): 056003, 2017.

D. W. Kumsa, E. M. Hudak, N. Bhadra, and J. T. Mortimer. Electron transfer processes occurring on platinum neural stimulating electrodes: pulsing experiments for cathodic-first, charge-imbalanced, biphasic pulses for $0.566leq$ kleq 2.3 in rat subcutaneous tissues. *Journal of neural engineering*, 16(2): 026018, 2019.

A. M. Kuncel and W. M. Grill. Selection of stimulus parameters for deep brain stimulation. *Clinical neurophysiology*, 115(11):2431–2441, 2004.

F. S. Lamb and R. C. Webb. Vascular effects of free radicals generated by electrical stimulation. *American Journal of Physiology-Heart and Circulatory Physiology*, 247(5):H709–H714, 1984.

J. Latikka and H. Eskola. The electrical conductivity of human cerebrospinal fluid in vivo. In *World Congress on Medical Physics and Biomedical Engineering 2018: June 3-8, 2018, Prague, Czech Republic (Vol. 1)*, pages 773–776. Springer, 2019.

S. M. Lawrence, G. Dhillon, W. Jensen, K. Yoshida, and K. W. Horch. Acute peripheral nerve recording characteristics of polymer-based longitudinal intrafascicular electrodes. *IEEE Transactions on Neural Systems and Rehabilitation Engineering*, 12(3):345–348, 2004.

I. Ledezma-Yanez, W. D. Z. Wallace, P. Sebastián-Pascual, V. Climent, J. M. Feliu, and M. Koper. Interfacial water reorganization as a ph-dependent descriptor of the hydrogen evolution rate on platinum electrodes. *Nature Energy*, 2(4):1–7, 2017.

F. Leichsenring, C. Steinert, S. Rabung, and J. P. Ioannidis. The efficacy of psychotherapies and pharmacotherapies for mental disorders in adults: an umbrella review and meta-analytic evaluation of recent meta-analyses. *World Psychiatry*, 21(1):133–145, 2022.

R. T. Leung, M. N. Shivdasani, D. A. Nayagam, and R. K. Shepherd. In vivoandin vitrocomparison of the charge injection capacity of platinum macroelectrodes. *IEEE Transactions on Biomedical Engineering*, 62(3):849–857, 2014.

M. F. Li, L. W. Liao, D. F. Yuan, D. Mei, and Y.-X. Chen. ph effect on oxygen reduction reaction at pt (1 1 1) electrode. *Electrochimica Acta*, 110:780–789, 2013.

L. W. Liao, M. F. Li, J. Kang, D. Chen, Y.-X. Chen, and S. Ye. Electrode reaction induced ph change at the pt electrode/electrolyte interface and its impact on electrode processes. *Journal of electroanalytical chemistry*, 688: 207–215, 2013.

J. C. Lilly, J. R. Hughes, E. C. Alvord Jr, and T. W. Galkin. Brief, noninjurious electric waveform for stimulation of the brain. *Science*, 121(3144):468–469, 1955.

P. P. Lopes, D. Tripkovic, P. F. Martins, D. Strmcnik, E. A. Ticianelli, V. R. Stamenkovic, and N. M. Markovic. Dynamics of electrochemical pt dissolu-

tion at atomic and molecular levels. *Journal of Electroanalytical Chemistry*, 819:123–129, 2018.

K. A. Ludwig, N. B. Langhals, M. D. Joseph, S. M. Richardson-Burns, J. L. Hendricks, and D. R. Kipke. Poly (3, 4-ethylenedioxythiophene)(PEDOT) polymer coatings facilitate smaller neural recording electrodes. *Journal of neural engineering*, 8(1):014001, 2011.

P. J. Mahon and K. B. Oldham. Semioperations and convolutions in voltammetry. *ChemElectroChem*, 5(6):839–848, 2018.

M. Matsumoto, T. Miyazaki, and H. Imai. Oxygen-enhanced dissolution of platinum in acidic electrochemical environments. *The Journal of Physical Chemistry C*, 115(22):11163–11169, 2011.

C. McCallum and D. Pletcher. An investigation of the mechanism of the oxidation of carbon monoxide adsorbed onto a smooth pt electrode in aqueous acid. *Journal of Electroanalytical Chemistry and Interfacial Electrochemistry*, 70(3):277–290, 1976.

H. McCann, G. Pisano, and L. Beltrachini. Variation in reported human head tissue electrical conductivity values. *Brain topography*, 32:825–858, 2019.

G. C. McConnell, H. D. Rees, A. I. Levey, C.-A. Gutekunst, R. E. Gross, and R. V. Bellamkonda. Implanted neural electrodes cause chronic, local inflammation that is correlated with local neurodegeneration. *Journal of neural engineering*, 6(5):056003, 2009.

D. McCreery, W. Agnew, T. Yuen, and L. Bullara. Comparison of neural damage induced by electrical stimulation with faradaic and capacitor electrodes. *Annals of biomedical engineering*, 16(5):463–481, 1988.

D. McCreery, T. Yuen, W. Agnew, and L. Bullara. Stimulus parameters affecting tissue injury during microstimulation in the cochlear nucleus of the cat. *Hearing research*, 77(1-2):105–115, 1994.

D. McCreery, W. Agnew, T. Yuen, and L. Bullara. Relationship between stimulus amplitude, stimulus frequency and neural damage during electrical stimulation of sciatic nerve of cat. *Medical and Biological Engineering and Computing*, 33:426–429, 1995.

D. McCreery, V. Pikov, and P. R. Troyk. Neuronal loss due to prolonged controlled-current stimulation with chronically implanted microelectrodes in the cat cerebral cortex. *Journal of Neural Engineering*, 7(3):036005, may 2010.

D. B. McCreery, W. F. Agnew, T. G. Yuen, and L. Bullara. Charge density and charge per phase as cofactors in neural injury induced by electrical stimulation. *IEEE Transactions on Biomedical Engineering*, 37(10):996–1001, 1990.

D. B. McCreery, T. G. Yuen, W. F. Agnew, and L. A. Bullara. A characterization of the effects on neuronal excitability due to prolonged microstimulation with chronically implanted microelectrodes. *IEEE transactions on biomedical engineering*, 44(10):931–939, 1997.

J. McHardy, L. Robblee, J. Marston, and S. Brummer. Electrical stimulation with Pt electrodes. IV. factors influencing Pt dissolution in inorganic saline. *Biomaterials*, 1(3):129–134, 1980.

C. C. McIntyre and W. M. Grill. Finite element analysis of the current-density and electric field generated by metal microelectrodes. *Annals of biomedical engineering*, 29:227–235, 2001.

D. R. Merrill, M. Bikson, and J. G. Jefferys. Electrical stimulation of excitable tissue: design of efficacious and safe protocols. *Journal of neuroscience methods*, 141(2):171–198, 2005.

J. T. Mortimer and N. Bhadra. Fundamentals of electrical stimulation. In *Neuromodulation*, pages 71–82. Elsevier, 2018.

J. T. Mortimer, D. Kaufman, and U. Roessmann. Intramuscular electrical stimulation: tissue damage. *Annals of biomedical engineering*, 8(3):235–244, 1980.

S. Musa, D. R. Rand, C. Bartic, W. Eberle, B. Nuttin, and G. Borghs. Coulometric detection of irreversible electrochemical reactions occurring at pt microelectrodes used for neural stimulation. *Analytical chemistry*, 83(11): 4012–4022, 2011.

D. J. Myers, X. Wang, M. C. Smith, and K. L. More. Potentiostatic and potential cycling dissolution of polycrystalline platinum and platinum nanoparticle fuel cell catalysts. *Journal of The Electrochemical Society*, 165(6): F3178–F3190, 2018.

J. B. Nadol Jr, J. T. O'Malley, B. J. Burgess, and D. Galler. Cellular immunologic responses to cochlear implantation in the human. *Hearing research*, 318:11–17, 2014.

S. Nagashima, T. Ikai, Y. Sasaki, T. Kawasaki, T. Hatanaka, H. Kato, and K. Kishita. Atomic-level observation of electrochemical platinum dissolution and redeposition. *Nano Letters*, 19(10):7000–7005, 2019.

X. Navarro, T. B. Krueger, N. Lago, S. Micera, T. Stieglitz, and P. Dario. A critical review of interfaces with the peripheral nervous system for the control of neuroprostheses and hybrid bionic systems. *Journal of the Peripheral Nervous System*, 10(3):229–258, 2005.

S. Negi, R. Bhandari, L. Rieth, and F. Solzbacher. In vitro comparison of sputtered iridium oxide and platinum-coated neural implantable microelectrode arrays. *Biomedical materials*, 5(1):015007, 2010.

C. Newbold, R. Richardson, C. Q. Huang, D. Milojevic, R. Cowan, and R. Shepherd. An in vitro model for investigating impedance changes with cell growth and electrical stimulation: implications for cochlear implants. *Journal of neural engineering*, 1(4):218, 2004.

C. Newbold, R. Richardson, R. Millard, C. Huang, D. Milojevic, R. Shepherd, and R. Cowan. Changes in biphasic electrode impedance with protein adsorption and cell growth. *Journal of neural engineering*, 7(5):056011, 2010.

C. Newbold, S. Mergen, R. Richardson, P. Seligman, R. Millard, R. Cowan, and R. Shepherd. Impedance changes in chronically implanted and stimulated cochlear implant electrodes. *Cochlear implants international*, 15(4):191–199, 2014.

J. Newman. Resistance for flow of current to a disk. *J. electrochem. Soc*, 113 (5):501–502, 1966.

T. Niederhoffer, A. Vanhoestenberghe, and H. T. Lancashire. Effect of ph and gel electrolyte on safe charge injection and electrode degradation of platinum electrodes. In *2023 IEEE BioSensors Conference (BioSensors)*, pages 1–4. IEEE, 2023a.

T. Niederhoffer, A. Vanhoestenberghe, and H. T. Lancashire. Methods of poly (3, 4)-ethylenedioxithiophene (pedot) electrodeposition on metal electrodes for neural stimulation and recording. *Journal of neural engineering*, 20(1): 011002, 2023b.

T. Niederhoffer, A. Vanhoestenberghe, and H. T. Lancashire. Extending the understanding of shannon's safe stimulation limit for platinum electrodes: biphasic charge-balanced pulse trains in unbuffered saline at ph= 1 to ph= 12. *Journal of Neural Engineering*, 2024.

K. Obata, L. Stegenburga, and K. Takanabe. Maximizing hydrogen evolution performance on pt in buffered solutions: Mass transfer constrains of h2 and buffer ions. *The Journal of Physical Chemistry C*, 123(35):21554–21563, 2019.

M. Ohashi, T. Hirano, K. Watanabe, H. Shoji, N. Ohashi, H. Baba, N. Endo, and T. Kohno. Hydrogen peroxide modulates neuronal excitability and mem-

brane properties in ventral horn neurons of the rat spinal cord. *Neuroscience*, 331:206–220, 2016.

K. B. Oldham. A gouy–chapman–stern model of the double layer at a (metal)/(ionic liquid) interface. *Journal of Electroanalytical Chemistry*, 613 (2):131–138, 2008.

J. E. O'Reilly. Oxidation-reduction potential of the ferro-ferricyanide system in buffer solutions. *Biochimica et Biophysica Acta (BBA)-Bioenergetics*, 292 (3):509–515, 1973.

J. T. O'Malley, B. J. Burgess, D. Galler, and J. B. Nadol Jr. Foreign body response to silicone in cochlear implant electrodes in the human. *Otology & neurotology*, 38(7):970–977, 2017.

V. Paggi, F. Fallegger, L. Serex, O. Rizzo, K. Galan, A. Giannotti, I. Furfaro, C. Zinno, F. Bernini, S. Micera, et al. A soft, scalable and adaptable multi-contact cuff electrode for targeted peripheral nerve modulation. *Bioelectronic Medicine*, 10(1):6, 2024.

J. Palmer, R. Green, F. Boscher, L. Poole-Warren, P. Carter, Y. Enke, N. Lovell, and M. Lord. Development and performance of a biomimetic artificial perilymph for in vitro testing of medical devices. *Journal of Neural Engineering*, 16(2):026006, 2019.

M. Pałys, T. Korba, M. Bos, and W. E. van der Linden. The separation of overlapping peaks in cyclic voltammetry by means of semi-differential transformation. *Talanta*, 38(7):723–733, 1991.

H. Park, P. Takmakov, and H. Lee. Electrochemical evaluations of fractal microelectrodes for energy efficient neurostimulation. *Scientific reports*, 8 (1):4375, 2018.

H. Park, S. Zhang, A. Steinman, Z. Chen, and H. Lee. Graphene prevents

neurostimulation-induced platinum dissolution in fractal microelectrodes. *2D Materials*, 6(3):035037, 2019.

S. Pimenta, J. A. Rodrigues, F. Machado, J. F. Ribeiro, M. J. Maciel, O. Bondarchuk, P. Monteiro, J. Gaspar, J. H. Correia, and L. Jacinto. Double-layer flexible neural probe with closely spaced electrodes for high-density in vivo brain recordings. *Frontiers in Neuroscience*, 15:663174, 2021.

R. H. Pudenz, L. Bullara, S. Jacques, and F. Hambrecht. Electrical stimulation of the brain. iii. the neural damage model. *Surgical neurology*, 4(4):389–400, 1975.

M. K. Puglia and P. K. Bowen. Cyclic voltammetry study of noble metals and their alloys for use in implantable electrodes. *ACS omega*, 7(38):34200–34212, 2022.

C. Qin, Z. Tan, Y. Pan, Y. Li, L. Wang, L. Ren, W. Zhou, and L. Wang. Automatic and precise localization and cortical labeling of subdural and depth intracranial electrodes. *Frontiers in Neuroinformatics*, 11:10, 2017.

J. E. B. Randles. Kinetics of rapid electrode reactions. *Discussions of the faraday society*, 1:11–19, 1947.

E. Ravagli, S. Mastitskaya, N. Thompson, F. Iacoviello, P. R. Shearing, J. Perkins, A. V. Gourine, K. Aristovich, and D. Holder. Imaging fascicular organization of rat sciatic nerves with fast neural electrical impedance tomography. *Nature communications*, 11(1):6241, 2020.

A. Richardot and E. T. McAdams. Harmonic analysis of low-frequency bioelectrode behavior. *IEEE transactions on medical imaging*, 21(6):604–612, 2002.

L. Robblee, J. McHardy, J. Marston, and S. Brummer. Electrical stimulation with pt electrodes. v. the effect of protein on pt dissolution. *Biomaterials*, 1(3):135–139, 1980.

L. Robblee, J. McHardy, W. Agnew, and L. Bullara. Electrical stimulation with pt electrodes. vii. dissolution of pt electrodes during electrical stimulation of the cat cerebral cortex. *Journal of neuroscience methods*, 9(4):301–308, 1983.

J. T. Rubinstein, F. A. Spelman, M. Soma, and M. F. Suesserman. Current density profiles of surface mounted and recessed electrodes for neural prostheses. *IEEE transactions on biomedical engineering*, (11):864–875, 1987.

R. Sahyouni, D. T. Chang, O. Moshtaghi, A. Mahmoodi, H. R. Djalilian, and H. W. Lin. Functional and histological effects of chronic neural electrode implantation. *Laryngoscope investigative otolaryngology*, 2(2):80–93, 2017.

J. W. Salatino, K. A. Ludwig, T. D. Kozai, and E. K. Purcell. Glial responses to implanted electrodes in the brain. *Nature biomedical engineering*, 1(11): 862–877, 2017.

L. Schaupp, F. Feichtner, R. Schaller-Ammann, S. Mautner, M. Ellmerer, and T. R. Pieber. Recirculation—a novel approach to quantify interstitial analytes in living tissue by combining a sensor with open-flow microperfusion. *Analytical and bioanalytical chemistry*, 406:549–554, 2014.

A. Scheiner, J. T. Mortimer, and U. Roessmann. Imbalanced biphasic electrical stimulation: muscle tissue damage. *Annals of biomedical engineering*, 18(4): 407–425, 1990.

J. Schulte, D. Ashouri, and T. Stieglitz. The longevity of neural interfaces—mechanical oscillation of thin film metal-based neural electrodes determine stability during electrical stimulation. *Advanced Functional Materials*, 34(11):2310130, 2024.

H. Schwan. Linear and nonlinear electrode polarization and biological materials. *Annals of biomedical engineering*, 20(3):269–288, 1992.

D. D. Shah, P. Carter, M. N. Shivdasani, N. Fong, W. Duan, D. Esrafilzadeh, L. Poole-Warren, and U. A. Robles. Deciphering platinum dissolution in neural stimulation electrodes: electrochemistry or biology? *Biomaterials*, page 122575, 2024.

R. V. Shannon. A model of safe levels for electrical stimulation. *IEEE Transactions on biomedical engineering*, 39(4):424–426, 1992.

N. Sharafkhani, A. Z. Kouzani, S. D. Adams, J. M. Long, G. Lissorgues, L. Rousseau, and J. O. Orwa. Neural tissue-microelectrode interaction: Brain micromotion, electrical impedance, and flexible microelectrode insertion. *Journal of Neuroscience Methods*, 365:109388, 2022.

R. Shepherd, M. Murray, M. Hougiton, and G. M. Clark. Scanning electron microscopy of chronically stimulated platinum intracochlear electrodes. *Biomaterials*, 6(4):237–242, 1985.

R. K. Shepherd, P. M. Carter, Y. L. Enke, A. K. Wise, and J. B. Fallon. Chronic intracochlear electrical stimulation at high charge densities results in platinum dissolution but not neural loss or functional changes in vivo. *Journal of neural engineering*, 16(2):026009, 2019.

R. K. Shepherd, P. M. Carter, Y. L. Enke, A. Thompson, B. Flynn, E. P. Trang, A. N. Dalrymple, and J. B. Fallon. Chronic intracochlear electrical stimulation at high charge densities: reducing platinum dissolution. *Journal of neural engineering*, 17(5):056009, 2020.

R. K. Shepherd, P. M. Carter, A. N. Dalrymple, Y. L. Enke, A. K. Wise, T. Nguyen, J. Firth, A. Thompson, and J. B. Fallon. Platinum dissolution and tissue response following long-term electrical stimulation at high charge densities. *Journal of neural engineering*, 18(3):036021, 2021.

B. R. Shrestha, E. Tada, and A. Nishikata. Effect of chloride on platinum dissolution. *Electrochimica Acta*, 143:161–167, 2014.

J. Sobkowski and A. Czerwiński. Kinetics of carbon dioxide adsorption on a platinum electrode. *Journal of Electroanalytical Chemistry and Interfacial Electrochemistry*, 55(3):391–397, 1974.

S. Strbac. The effect of pH on oxygen and hydrogen peroxide reduction on polycrystalline Pt electrode. *Electrochimica Acta*, 56(3):1597–1604, 2011.

M. F. Suesserman, F. A. Spelman, and J. T. Rubinstein. In vitro measurement and characterization of current density profiles produced by nonrecessed, simple recessed, and radially varying recessed stimulating electrodes. *IEEE Transactions on Biomedical Engineering*, 38(5):401–408, 1991.

T. Swiontek, D. Maiman, A. Sances Jr, J. Myklebust, S. Larson, and D. Hemmy. Effect of electrical current on temperature and ph in cerebellum and spinal cord. *Surgical Neurology*, 14(5):365–369, 1980.

R. B. Szlavik and H. de Bruin. The effect of stimulus current pulse width on nerve fiber size recruitment patterns. *Medical engineering & physics*, 21 (6-7):507–515, 1999.

Y. Terasawa, H. Tashiro, Y. Nakano, K. Osawa, and M. Ozawa. Safety assessment of semichronic suprachoroidal electrical stimulation to rabbit retina. In *2013 35th Annual International Conference of the IEEE Engineering in Medicine and Biology Society (EMBC)*, pages 3567–3570. IEEE, 2013.

R. Thakur, F. P. Aplin, and G. Y. Fridman. A hydrogel-based microfluidic nerve cuff for neuromodulation of peripheral nerves. *Micromachines*, 12(12): 1522, 2021.

S. M. Theparambil, P. Hosford, I. Ruminot, O. Kopach, J. R. Reynolds, P. Y. Sandoval, D. Rusakov, L. Barros, and A. Gourine. Astrocytes regulate brain extracellular ph via a neuronal activity-dependent bicarbonate shuttle. *Nature Communications*, 11, 2020. doi: 10.1038/s41467-020-18756-3.

A. A. Topalov, S. Cherevko, A. R. Zeradjanin, J. C. Meier, I. Katsounaros, and K. J. Mayrhofer. Towards a comprehensive understanding of platinum dissolution in acidic media. *Chemical Science*, 5(2):631–638, 2014a.

A. A. Topalov, A. R. Zeradjanin, S. Cherevko, and K. J. Mayrhofer. The impact of dissolved reactive gases on platinum dissolution in acidic media. *Electrochemistry communications*, 40:49–53, 2014b.

M. Tykocinski, R. K. Shepherd, and G. M. Clark. Reduction in excitability of the auditory nerve following electrical stimulation at high stimulus rates. *Hearing research*, 88(1-2):124–142, 1995.

D. J. Tyler and D. M. Durand. Chronic response of the rat sciatic nerve to the flat interface nerve electrode. *Annals of biomedical engineering*, 31(6): 633–642, 2003.

C. van den Honert and J. T. Mortimer. The response of the myelinated nerve fiber to short duration biphasic stimulating currents. *Annals of biomedical engineering*, 7:117–125, 1979.

R. Vatsyayan, D. Cleary, J. R. Martin, E. Halgren, and S. A. Dayeh. Electrochemical safety limits for clinical stimulation investigated using depth and strip electrodes in the pig brain. *Journal of neural engineering*, 18(4): 046077, 2021.

C. Veraart, W. M. Grill, and J. T. Mortimer. Selective control of muscle activation with a multipolar nerve cuff electrode. *IEEE Transactions on biomedical Engineering*, 40(7):640–653, 1993.

W. Watterson, R. Montgomery, and R. Taylor. Fractal electrodes as a generic interface for stimulating neurons. *Scientific reports*, 7(1):6717, 2017.

X. F. Wei and W. M. Grill. Impedance characteristics of deep brain stimulation electrodes in vitro and in vivo. *Journal of neural engineering*, 6(4):046008, 2009.

J. D. Weiland and D. J. Anderson. Chronic neural stimulation with thin-film, iridium oxide electrodes. *IEEE transactions on biomedical engineering*, 47 (7):911–918, 2000.

J. D. Weiland, D. J. Anderson, and M. S. Humayun. In vitro electrical properties for iridium oxide versus titanium nitride stimulating electrodes. *IEEE transactions on biomedical engineering*, 49(12):1574–1579, 2002.

A. Weltin and J. Kieninger. Electrochemical methods for neural interface electrodes. *Journal of Neural Engineering*, 18(5):052001, 2021.

A. Weltin, D. Ganatra, K. König, K. Joseph, U. G. Hofmann, G. A. Urban, and J. Kieninger. New life for old wires: electrochemical sensor method for neural implants. *Journal of Neural Engineering*, 17(1):016007, 2019.

A. C. West and J. Newman. Current distributions on recessed electrodes. *Journal of the Electrochemical Society*, 138(6):1620, 1991.

S. J. Wilks, S. M. Richardson-Burn, J. L. Hendricks, D. Martin, and K. J. Otto. Poly (3, 4-ethylene dioxythiophene)(PEDOT) as a micro-neural interface material for electrostimulation. *Frontiers in neuroengineering*, 2:7, 2009.

L. Xing, M. A. Hossain, M. Tian, D. Beauchemin, K. T. Adjemian, and G. Jerkiewicz. Platinum electro-dissolution in acidic media upon potential cycling. *Electrocatalysis*, 5:96–112, 2014.

L. Xing, X. Song, and P. K. Das. Fuel cell modeling and optimization. In *Fuel Cells for Transportation*, pages 73–101. Elsevier, 2023.

T. G. Yuen, W. F. Agnew, L. A. Bullara, S. Jacques, and D. B. McCreery. Histological evaluation of neural damage from electrical stimulation: considerations for the selection of parameters for clinical application. *Neurosurgery*, 9(3):292–299, 1981.